Tampere University

JENNA TAINIO

Bioactive Borosilicate Glasses for Bone Tissue Engineering Applications

Tampere University Dissertations 990

Tampere University Dissertations 990

JENNA TAINIO

Bioactive Borosilicate Glasses for Bone Tissue Engineering Applications

ACADEMIC DISSERTATION
To be presented, with the permission of
the Faculty of Medicine and Health Technology
of Tampere University,
for public discussion in the auditorium TB109
of Tietotalo, Korkeakoulunkatu 1, Tampere,
on 19th April 2024, at 12 o'clock.

ACADEMIC DISSERTATION
Tampere University, Faculty of Medicine and Health Technology
Finland

Responsible supervisor and Custos	Professor Jonathan Massera Tampere University Finland	
Pre-examiners	Professor Leena Hupa Åbo Akademi Finland	Professor Richard K. Brow Missouri University of Science and Technology USA
Opponent	Professor Pekka Vallittu University of Turku Finland	

The originality of this thesis has been checked using the Turnitin OriginalityCheck service.

Cover design: Roihu Inc.

ISBN 978-952-03-3366-9 (print)
ISBN 978-952-03-3367-6 (pdf)
ISSN 2489-9860 (print)
ISSN 2490-0028 (pdf)
http://urn.fi/URN:ISBN:978-952-03-3367-6

Carbon dioxide emissions from printing Tampere University dissertations have been compensated.

PunaMusta Oy – Yliopistopaino
Joensuu 2024

ACKNOWLEDGEMENTS

The studies presented in this thesis were conducted in the Bioceramics, Bioglasses and Biocomposites research group in the Faculty of Medicine and Health Technology, Tampere University, during the years 2017-2023. I gratefully thank the financial supporters Jane and Aatos Erkko Foundation, the Research Council of Finland and The Doctoral School of Tampere University for enabling my research.

Foremost, I would like to express my deepest gratitude to my supervisor Professor Jonathan Massera, for giving me the opportunity to work under his guidance. Several years ago, doctoral studies in this field were only a dream I casually mentioned to him as a research assistant at our faculty's coffee table. I wish to extend my gratitude to my instructors Professor Susanna Miettinen and PhD Sari Vanhatupa, and additionally Professor Delia S. Brauer, for their support and advice. Additionally, I gratefully acknowledge the official pre-examiners Professor Leena Hupa and Professor Richard K. Brow for their constructive comments for improving the thesis.

This work could not have been possible without my co-authors; Agata Szczodra, Amel Houaoui, Hongfei Liu, Juuso Pohjola, Tomi Anttila, Dahiana A. Avila Salazar, Amy Nommeots-Nomm, Claire Roiland, Bruno Bureau and Daniel R. Neuville. I thank you all for the fruitful collaboration and sharing your expertise with me. My deep appreciation goes additionally to amazing colleagues not yet mentioned; Ayush Mishra, Inari Lyyra, Virginia Alessandra Gobbo, Sonya Ghanavati, Henriikka Teittinen, Mart Kroon, Janne Koivisto, Aleksi Palmroth, Juliane Brandt-Slowik, and all the other co-workers through the years, without forgetting our helpful laboratory and technical personnel. There are too many to mention, really! Thank you for creating a great work atmosphere, I have been lucky to work with all of you.

Lastly, most importantly, my family. My ever-supporting parents Päivi and Heikki. My dearest friends throughout my whole life, Heidi and Milla. My beloved husband year to year, in words and deed, Henri, and our most wonderful and inspiring daughters Amanda and Olivia. You remind me every day about what is important in life.

Kangasala, March 2024

Jenna Tainio

ABSTRACT

In the field of regenerative medicine and tissue engineering, there is a pressing need to develop synthetic alternatives to tissue grafts for reconstruction of bone defects. Bioactive glasses are a promising group of materials due to their ability to form active bonds with bone tissue and stimulate osteogenesis. While a limited number of bioactive glass products have been successfully utilized in clinicals, there is considerable potential to enhance bioactive glasses properties by controlling their compositions.

During this dissertation, a borosilicate glass series with additional incorporations of magnesium and strontium was developed and characterized. The potential for thermal processing and crystallization mechanism of the glasses were studied. 3D structures were then prepared using both the porogen burn-off method and additive manufacturing. Further, glasses *in vitro* reactivity was studied in simulated body fluid, and cytotoxicity was evaluated with human mesenchymal stem cells.

These studies revealed that replacing a portion of the glass's calcium content with magnesium and/or strontium enhanced the hot forming capabilities without undesirable crystallization. The produced 3D-printed scaffolds possessed suitable porosity (pore size and interconnectivity) for tissue infiltration. In addition, the incorporation of Mg and Sr in the composition slowed the reactivity of the glasses, allowing for the customization of the degradation rate. Moreover, the studied glasses degradation products were found beneficial for both osteogenesis and angiogenesis.

In conclusion, the studied bioactive glasses demonstrate significant promise for applications in bone tissue engineering.

TIIVISTELMÄ

Kudosteknologian avulla voidaan kehittää synteettisiä vaihtoehtoja luuvaurioiden korjaamisessa käytettäville kudossiirteille. Bioaktiiviset lasit ovat erittäin lupaava materiaaliryhmä regeneratiivisen lääketieteen sovelluksiin, sillä nämä materiaalit pystyvät muodostamaan aktiivisia sidoksia luukudokseen, sekä stimuloida uuden luun muodostumista. Muutamat kaupalliset lasikoostumukset ovat jo saavuttaneet kliinistä menestystä, mutta muutoksilla perinteisten bioaktiivisten silikaattilasien koostumuksiin on mahdollista parantaa esimerkiksi lasien biohajoavuutta ja prosessoitavuutta.

Tämän väitöskirjan aikana kehitettiin ja karakterisoitiin boorisilikaattilasien sarja, joissa osaan laseista lisättiin magnesiumia ja strontiumia. Lasien lämpöominaisuuksia ja kiteytymismekanismia analysoitiin, sekä niistä valmistettiin kolmiulotteisia (3D) tukirakenteita. Lisäksi tutkittiin lasien *in vitro* -reaktiivisuutta simuloidussa kehon nesteessä, ja sytotoksisuutta arvioitiin ihmisen mesenkymaalisilla kantasoluviljelmillä.

Havaittiin, että kun osa tutkittavien lasikoostumusten kalsiumista korvattiin magnesiumilla ja/tai strontiumilla, lasien lämpökäsiteltävyys parani, sekä lasipartikkeleita oli mahdollista sintrata ilman kiteytymistä. 3D-tulostettujen tukirakenteiden huokoisuus ja huokoskoko olivat lisäksi sopivia kudosinfiltraatiota varten. Magnesium ja strontium myös hidastivat lasien reaktiivisuutta, antaen mahdollisuuden muokata lasien hajoamisnopeutta. Tutkittujen lasien hajoamistuotteet osoittautuivat hyödyllisiksi sekä osteogeneesille että angiogeneesille.

Yhteenvetona voidaan todeta, että nämä uudet bioaktiiviset lasikoostumukset vaikuttavat lupaavilta luukudostekniikan sovelluksiin.

CONTENTS

ABBREVIATIONS AND SYMBOLS

3D	Three-dimensional
α-MEM	α-Minimum Essential Media
aCaP	Amorphous calcium phosphate
ALP	Alkaline phosphatase
ATR	Attenuated total reflectance
β	Heating rate
B	Boron
BM	Basic growth media
bO	bridging oxygen
BSA	Bovine serum albumin
β-TCP	Beta-tricalcium phosphate
Ca	Calcium
CAD	Computer-assisted design
CaP	Calcium phosphate
Col-I	Collagen type-I

DAPI	4',6-diamidino-2-phenylindole
$\frac{d\alpha_i}{dt}$	Transformation rate at a temperature T_i
DLX5	Distal-less homeobox 5
DMEM	Dulbeccos's modified Eagle's medium
DTA	Differential thermal analysis
E_a	Activation energy for viscous flow
E_c	Activation energy for crystallization
$E_{c\alpha}$	Activation energy of crystallization at a specific degree of transformation α
ECM	Extracellular matrix
EDS, EDX	Energy dispersive X-ray spectroscopy – terms are often used interchangeably; EDX refers to the method, while EDS refers to the equipment
F	Fluoride
FTIR	Fourier-transform infrared
HA	Hydroxyapatite
hADSC, hASC	human adipose (derived) stem cell
HCA	Crystallized carbonate substituted hydroxyapatite
JMA	Johnson–Mehl–Avrami
μCT	Micro-computed tomography
M	Molar mass

MAS	Magic angle spinning
Mg	Magnesium
MSC	Mesenchymal stem cell
n	Johnson–Mehl–Avrami exponent
Na	Sodium
nBO	non-bridging oxygen
NMR	Nuclear magnetic resonance
OM	Osteogenic media
ρ	Apparent density
ρ_0	Bulk density
P	Phosphorus
PBS	Phosphate buffered saline
PCL	Poly(ε-caprolactone)
PFA	Paraformaldehyde
PMMA	Polymethyl methacrylate
PLGA	Poly(lactic-*co*-glycolic acid)
PLLA	Poly(L-lactic acid)
Q^n	Represents the structural units of silicate, where n means the number of bridging oxygen atoms found in the silicate system

R	Ideal gas constant
RT	Room temperature
SBF	Simulated body fluid
SD	Standard deviation
SEM	Scanning electron microscopy
Si	Silicon
Si-OH	Silanol
Sr	Strontium
ΔT_{FWHM}	Full width at half maximum of the DTA peak
T_g	Glass transition temperature
T_p	Crystallization peak
T_x	The onset of crystallization
TRIS	Tris(hydroxymethyl)aminomethane
V_M	Molar volume
vWF	Von Willebrand factor
XRD	X-ray crystallography

ORIGINAL PUBLICATIONS

This dissertation is based on the following original peer-reviewed publications, referred to as **Study I-III** in the text. The original publications are reproduced at the end of this thesis with the permission of the copyright holder.

I J. M. Tainio, D. A. Avila Salazar. A. Nommeots-Nomm, C. Roiland, B. Bureau, D. R. Neuvilled, D. S. Brauer, J. Massera. Structure and *in vitro* dissolution of Mg and Sr containing borosilicate bioactive glasses for bone tissue engineering. *Journal of Non-Crystalline Solids* vol. 533, 2020, 119893, ISSN 0022-3093

II J.M. Tainio, T. Anttila, J. Pohjola, D.S. Brauer, J. Massera. Crystallization mechanism of B12.5 bioactive borosilicate glasses and its impact on in vitro degradation. *Journal of the European Ceramic Society,* vol. 44(2), 2024, pp. 1229-1239.

III A. Szczodra†, J. M. Tainio†, A. Houaoui, H. Liu, J. Pohjola, S. Miettinen, D. S. Brauer, J. Massera. Impact of borosilicate bioactive glass scaffold processing and reactivity on in-vitro dissolution properties. *Materials Today Communications* vol. 35, 2023, 105984, ISSN 2352-4928 *

* The contents regarding Tris and dynamic SBF dissolution, as well as scaffolds pre-incubation are not covered in the scope of this dissertation.

† Shared authorship.

UNPUBLISHED MANUSCRIPT

This thesis is also based on the following unpublished manuscript, which is later referred to in the text as **Study IV**.

IV J.M. Tainio, S. Vanhatupa , S. Miettinen, J. Massera. Borosilicate bioactive glasses with added Mg/Sr enhances human adipose stem cells osteogenic/angiogenic commitment. *Submitted for publication on 26th of January.*

AUTHORS CONTRIBUTION

I. Author planned the work and analysed the data with the co-authors. Author was responsible of manufacturing the glasses, and determination of thermal and physical properties. Structural studies were performed mainly by D.A. Avila Salazar, C. Roiland, B. Bureau and D.R. Neuville, and analysed with the author. Further, author performed the *in vitro* dissolution study and post immersion analysis, except SEM/EDX analysis, performed by T. Salminen at the Tampere microscopy centre. SEM/EDX results were analysed by the author. Author wrote the manuscript as first author.

II. Author planned the work with co-authors. The author co-supervised BSc T. Anttila who produced the materials and performed part of the experiments. Author analysed and processed the data and wrote the manuscript as first author.

III. Author planned the work and analysed the data with the co-authors. Production and characterization of the materials were performed by J. Pohjola, H. Liu and A. Szczodra. Cell experiments were performed by H. Liu, A. Houaoui and A. Szczodra. Author co-wrote the manuscript together with shared first authorship with A. Szczodra.

IV. Author planned the work with co-authors. Author was responsible of manufacturing of the materials for the study, cell culturing and execution of the experiments. Further, author conducted the processing and analysis of the data. Author wrote the manuscript as first author.

1 INTRODUCTION

Wars have significantly influenced the trajectory of innovations and technological advancements. In the 1960s, Larry Hench, inspired by a conversation with a US Army colonel returned from the Vietnam War, embarked on a mission to discover a material capable of facilitating the regeneration or repair of injured bones and limbs. Subsequently, Professor Hench successfully developed the first bioactive glasses in 1969. (1). Bioactive glasses are one of the most promising materials for bone tissue engineering. As biodegradable and biomimetic apatite forming materials, they are able to rapidly bond to bone tissue and support the regeneration of the recovering tissue. (2,3). Unfortunately, even though bioactive glasses hold a lot of promise for clinical applications, their usage is still limited (4). While commercial bioactive silicate glasses have been utilized with great success, they still exhibit drawbacks to be overcome. The first drawback lies in their incomplete degradation *in vivo* (5). Additionally, the conventional silicate glasses have a tendency to crystallize upon heating, limiting their usage mostly into powders and putties, while processing the glasses into fibers or complex three-dimensional (3D)-structures with hot forming could widen the scope of applications in bone tissue engineering. (6,7,8).

Efforts to overcome the challenges faced with traditional silicate bioactive glasses have led to the investigation of glasses, where SiO_2 is partially substituted with B_2O_3, as borate glasses exhibit high degradation rates and fast conversion into hydroxyapatite (HA). Additionally, incorporating boron into silicate bioactive glasses has shown significant improvement in thermal properties, particularly in expanding the hot forming domain, thus allowing the production of, for example, 3D porous scaffolds. (9,10,11,12). In addition to boron, many of the alkaline earth ions have been identified to extend glasses thermal working range for hot forming applications. For instance, substituting calcium with magnesium has resulted in improved sintering. (13,14).

The development of new bioactive glasses is interdisciplinary; in addition to compositions effect on material properties, it is important to understand the impact of compositional changes on living cells. For example, while magnesium and strontium have been found to be therapeutic ions that can promote new bone formation (15,16,17), in *in vitro* cell cultures it has been observed that boron may hinder cell proliferation, and even cause cytotoxic effects when released in high concentrations (9,10,18). However, these effects are usually diminished in dynamic culture conditions and *in vivo* (11,19). Moreover, it has been seen with human adipose stem cells (hASC), that while the contact with borosilicate glasses slowed cells proliferation, the release of boron promoted the expression of osteogenic markers and mineralization (20). Furthermore, boron has been found to stimulate angiogenesis, a critical process for bone tissue repair (10). Therefore, while the amount of released boron may need to be controlled, borosilicate bioactive glasses hold great promise for both hard and soft tissue engineering applications (11).

This article-based dissertation consists of a literature review and an experimental section describing the materials and methods used in this work, followed by a presentation of the results. The literature review presents a broad view on strategies for bone regeneration and the biomaterials utilized in bone tissue engineering applications, with a focus on bioactive glasses. In the experimental part of this dissertation, the processing of a borosilicate glass series and characterization techniques employed are described. The developed glass compositions are based on the clinically available glass composition BonAlive® S53P4, where 12.5% (mol-%) of SiO_2 is substituted with B_2O_3, and CaO is substituted with varying amount of MgO and/or SrO. The goal was to study the potential of this borosilicate bioactive glass series for bone tissue engineering. Additionally, aim was to study the tailoring of the glasses reactivity and thermal properties for future processing into three-dimensional (3D) porous scaffolds, and ultimately provide synthetic alternatives for bone defect reconstruction. Furthermore, the impact of ion release as extract and in direct contact, on human adipose-derived stem cells' (hADSCs) viability, proliferation and differentiation was investigated. The obtained data is discussed and compared to previously reported results, and finally, a summary and conclusions of the studies are presented. The original publications of the studies are presented at the end of this thesis.

2 REVIEW OF THE LITERATURE

2.1 Bone tissue engineering

As a standard of care, regenerative medicine currently still utilizes tissue grafts in the reconstruction of bone defects, and as such, bone is one of the most transplanted tissues after blood. However, the use of tissue grafts has many limitations, where one of the most substantial is the inherent limited availability. (21,22). Autologous grafts, harvested typically from the iliac crest of the patient, are utilized in the reconstruction of small-sized defects. These additional harvesting operations cause discomfort and longer recovery time for the patient, with a well-documented risk of complications (23). Large-sized defects are often treated with allogeneic bone tissue, harvested from e.g., donors or cadavers. Especially with children, allografts are used reluctantly due to their high immunologic response and histocompatibility disparities (22,24). Moreover, the need for regenerative medicine increases alongside of the aging population. Therefore, a solution for the ever-increasing need of graft substitutes may lie in engineered biomaterials.

Tissue engineering combines the principles of engineering and life sciences. The subfield of bone tissue engineering focuses on the development of artificial bone substitutes to restore or replace damaged or diseased tissue, and promises new treatments for a range of situations, where loss or failure of bone impairs tissues natural repair mechanism. This includes for example large bone fractures and tumour removals, as well as conditions such as osteoporosis. (25,26). Currently, bio-inert materials are being predominantly used in hard tissue regeneration, while in most of the cases, the damaged tissue only needs temporary support during the time of healing. Ideally, the implanted material should sustain the supportive properties, while giving room to the regenerating tissue by gradual degradation. With the use of biodegradable implants, removal operations can additionally be avoided, which is both cost-effective as well as beneficial for the patient's well-being. (27).

2.1.1 Bone as a tissue

Bone tissue is a hard, dynamic and highly vascularised tissue, that makes up the skeletal system in vertebrates. Bones serve several important functions in the body, such as providing support and protection of internal organs, facilitation of movement, and additionally in mineral reservoir and in homeostatic regulation of blood levels. (24). The extracellular matrix (ECM) of bone tissue consists primarily of a network of collagen (predominantly type I), along with other non-collagenous proteins such as osteocalcin, bone sialoprotein, and osteopontin, a mineral phase, primarily composed of calcium phosphate (CaP) in the form of hydroxyapatite (HA). Initially, the secreted ECM is amorphous and non-crystalline, but gradually mineralizes due to calcium deposition (28,29). The collagen provides a flexible framework for the tissue, while the minerals yield the hardness, structural rigidity and ability to withstand compression. (30,31).

Bones exist in many different shapes and sizes, depending on the anatomical sites. Mature bone tissue can be divided to two subcategories; cortical (compact) bone and trabecular (cancellous) bone. The dense, almost solid cortical bone (with less than 10% porosity) form the protective outer layer of bones and is typically found in long, short, and flat bones. On the other hand, trabecular bone forms a spongy, porous structure (with porosity ranging from 50% to 90%) and can be found in the inner layer of the bone tissue, for example in large parts of bone marrow. (29). Mature bone is largely composed of cylindrical units, i.e. Haversian systems, or osteons. This oriented, composite like structure of the bones results in viscoelastic and anisotropic mechanical characteristic; the tissue's response and capacity vary based on the speed and direction of the applied force, relative to the orientation of the bone structure. Generally, bones can withstand greater forces in the longitudinal direction, which aligns with the natural strain in physical conditions. (28,30).

While severe damage or disease may justify the need for regenerative medicine, healthy bone tissue is capable of self-repair and regeneration to some extent. Bones are dynamic tissues, and constantly reshaped by the cells within it; resorbed by osteoclasts and reformed by the osteoblasts. (30,32).

2.1.2 Bone cells - function and origin

Few types of cells form and maintain bone tissue; mesenchymal stem cell (MSC) originated osteoprogenitor cells, osteoblasts, bone-lining cells and osteoclasts; which all may be regarded as differentiated forms of the same basic cell type, and hematopoietic progenitor cell originated osteoclasts. (Figure 1)

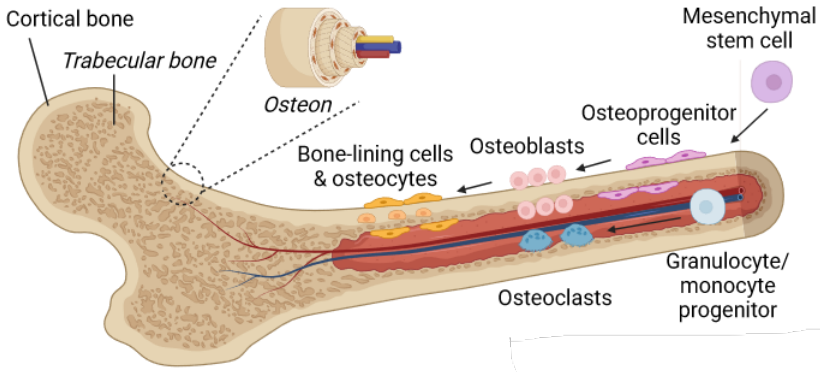

Figure 1. Schematic of biology of the bone - general structure, and the cells of the bone. Created with BioRender.com; adaption from (30).

Mesenchymal stem cells are often utilized in research, and, additionally, successfully in cell therapies due to their bone differentiation capacity *in vitro* and bone regeneration capacity *in vivo*. (33). In the osteogenic differentiation, the cells go through phases of proliferation, matrix maturation and mineralization (34). The osteoprogenitor cells, defined as mesenchymal precursor cells committed to the bone lineage; and differentiate into bone-forming osteoblasts. Osteoblasts secrete the organic ECM, along with enzymes, such as alkaline phosphatase (ALP), that promote calcium and phosphate deposition (thus, mineralization) during bone growth and remodelling. When the ECM deposition ceases, the osteoblasts transform either to bone-lining cells, or when trapped and embedded within the calcified matrix, their structure and function changes to osteocytes. Osteocytes are the most abundant cell type in mature bone tissue. (35,36).

The process of bone resorption by osteoclasts is a critical component of bone remodelling, which is necessary for maintaining the structural integrity and strength of the tissue throughout a person's life. Derived from the fusion of precursor monocytes, osteoclasts are large, multinucleated cells that enable the resorption and

regeneration of the bone tissue by secreting acids and enzymes that dissolve the mineralized matrix and break down the organic components. (27,30,32)

2.1.3 Scaffolds - requirements and manufacturing

In tissue engineering, the three-dimensional (3D) construct built to support the growth and regeneration of the surrounding tissue is called a scaffold. To enable the growth of the regenerating tissue, scaffolds need to fulfil many requirements considering both mechanical and biological aspects. (37). In general, an effective scaffold should provide a suitable porous environment to promote tissue integration; allowing the infiltration, attachment and proliferation of cells and the growth of new bone tissue, as well as vascularization (38). Additionally, the scaffold should maintain appropriate mechanical properties that support stability during the healing process, while similarly gradually degrading, making room for the regenerating tissue. (7,39). Furthermore, scaffolds could be utilized to deliver growth factors, cells and drugs to further favour the recovering of the tissue. However, while the usage and inclusion of the biological components would be potentially valuable, in practise, this could lead to high costs and complex regulatory requirements, and therefore materials-only approaches can be more efficient for the clinical translation and commercialization. (27,40).

Additional aspects to regard are the scaffold usability and productibility. Firstly, scaffolds should be able to undergo sterilization without altering its inherent properties. Moreover, scaffolds should be adaptable for moulding or cutting to match the size of the defect; if possible, already be designed to fit the defect site (i.e., designed for personalized medicine). The ideal scaffold would take into consideration the condition of the target tissue, which is influenced by both patient- and defect- related factors, such as a site of the injury or patient's age. An important factor is, whether the structure needs rigidity, to withstand cyclic forces, in contrast to defects where the site is not under significant loadbearing. (26,27). Moreover, the fabrication method should be reproducible, to be suitable for commercialization. Scaffolds can be produced with multiple different processing methods; e.g., by conventional use of porogens and template-based methods (such as foaming techniques, bio-templating, or freeze casting), as well as additive manufacturing (i.e., computer-assisted design (CAD) and 3D-printing) (41,42,43,44,45). More often

than not, especially ceramic and glass-based scaffolds are formed by thermal processing methods; by sintering of the previously formed green body. (7,46,47).

In the end, even the most promising products are not taken into use if they don't outperform the properties of the previous standard materials or methods. Overall, the scaffold material and design should be carefully selected to meet these requirements and optimize the success of bone tissue regeneration.

2.1.4 Suitable biomaterials

Biomaterials can be defined as any material that are used in direct contact with a living system. The original goal was to find a suitable material with physical properties matching the replaced tissue, that causes a minimal toxic response in the host. (48). Many different types of materials have been utilized in reconstruction of bone defects, from all the common material groups: metals, polymers (natural or synthetic), ceramics (including glasses). Each type of material has their own unique properties and advantages, depending on the specific application and desired outcome, and can additionally be utilized as composites and hybrids. However, one of the main and minimum requirements for biomaterials is biocompatibility, which means that the material does not cause an adverse reaction or rejection by the body's immune system. (27). For bone tissue engineering, it would be highly beneficial if the material supports osteoconduction (growth of bone tissue at the materials surface), or even osteoinduction (stimulation of new bone formation) (49).

The first materials utilized in regenerative curing of bone tissue have been mainly materials that provided mechanical support; being generally inert; enabling the biocompatibility, but have limitations such as poor or no degradation properties and limited ability to promote tissue regeneration. These biomaterials have been widely used in orthopaedic and dental applications, and are still standard approach in many cases, including materials such as metals (e.g., stainless steel, titanium) as screws and plates, and polymers, such as acrylate-based bone cements and fillings (e.g., polymethyl methacrylate; PMMA), to provide high mechanical stability. (24).

More engineered biomaterials have been designed to improve on the limitations of passive inert materials, by being gradually degraded to enable the regeneration of the tissue. For example, biodegradable metals (50); such as magnesium and its alloys (27) are prone to degradation by corrosion, and. e.g., bioresorbable metallic screws

based on magnesium, zinc and calcium (51), have been aimed for load-bearing bone indications, and have shown, in clinical phases, homogenous degradation with a solid bone-to-implant interface (52).

Biodegradable polymers are used widely in tissue engineering applications. The polymers utilized for bone tissue engineering applications include natural polymers of collagen (40), alginate (53,54), silk/fibrin (55,56) and chitosan (57), as well as synthetic polymers, such as poly(L-lactic acid) (PLLA), poly(lactic-*co*-glycolic acid) (PLGA), poly(ε-caprolactone) (PCL) and poly(N-isopropylacrylamide) (27,58,59,60). The polymers are typically utilized in the form of fibers or foams, in some cases also hydrogels. Many of these polymeric materials are able to provide osteoconduction, however, their mechanical properties often are less than those reached with autografts. (61).

Bioceramics have excellent biocompatibility, and often more suitable mechanical properties for hard tissue repair compared to other materials (i.e., not greatly below, or exceeding those of a native bone), and therefore are often regarded as the most promising biomaterials in the field. Bioceramics can be categorized into (crystalline) ceramics, (amorphous) glasses and (partly crystalline) glass-ceramics, and have been reported to be not only osteoconductive, but often osteoinductive. (27). Calcium phosphates compositions, from very slowly degrading hydroxyapatites to resorbable beta-tricalcium phosphates (β-TCP), mimic closely the inorganic phase of bone, and are often used in coatings of implants, or as injectable bone cements (62,63,64). In addition, bioactive glasses are an important class of bioceramics as it was the first synthetic materials shown to form a rapid and direct bonding to bone tissue. Most current commercial products are based on silicates, but multiple different compositions, such as phosphate and borate glasses are also under research. (2,3). Bioactive glasses are discussed in more detail in **chapter 2.2.** Glass-ceramics can be formed, for example, typically by heating a bioactive glass to a specific temperature to induce a crystal nucleation, followed by a further increase in temperature to grow the nuclei. Bioactive glass-ceramics have properties that are intermediate between those of glasses and ceramics. (65). The impact of crystallization on bioactivity is discussed in more detail in **chapter 2.2.3.** However, despite many advantages, the bioceramics are still inherently brittle.

Development of composites and organic-inorganic hybrids has increasingly became the focus of biomaterial development, providing tuneable and synergistic

combinations, to exceed the individual material properties. For example, elastic polymers can be utilized to compensate the brittleness of ceramics, which themselves provide rigidity to the composite. However, different processing conditions are often needed for the different types of materials, which often can complicate the development of such composites. (27). New generation of 'smart' biomaterials have also been proposed; these materials are designed to have dynamic, responsive properties that can adapt to changing biological environments and stimuli (e.g., respond to changes in pH, temperature, or other environmental factors, such as biological/cellular responses they elicit). Smart biomaterials are based on e.g., piezoelectric, magnetic, pH-/thermos- or enzyme-responsive materials, and are still in the early stages of development. (66).

Overall, the continuous evolution and development of biomaterials has allowed for the creation of increasingly advanced materials that can support bone tissue growth and regeneration, with minimal immune response and improved functional outcomes. Although major progress has been achieved over recent years, yet much work remains to develop an ideal synthetic bone graft alternative.

2.2 Bioactive glasses

Glass-making dates back a few millennia, and have been researched for couple of centuries. The main characteristics of a glass are usually considered transparency, and heat, pressure, and corrosion resistance (67). Resistance to hydrolytic attacks is where bioactive glasses majorly differ from traditional glasses. Discovered in 1969 by Larry Hench, bioactive glasses are material group with a network that enables reactivity and degradation in physiological fluids and conditions. This reactivity, discussed in detail in **chapter 2.2.2.**, enables bioactive glasses to form active bonding with bone tissue. (49).

2.2.1 Common compositions

The initial bioactive glass composition discovered by Hench was 45S5, known also as Bioglass®, developed to meet the need of an implant to fill bone voids without causing rejection by the human body (49). Over the years, many compositions have been studied to enhance new bone formation. Glass components can be divided in three categories; network formers, modifiers, and intermediate oxides. Network formers (i.e., silicon dioxide SiO_2, phosphorus pentoxide P_2O_5 and boron trioxide B_2O_3) are the main building unit within the structure, and are able to form glasses without the need of additional elements. Network modifiers (typically alkali or alkaline-earth metal oxides) alter the glass structure by breaking the Si-O-Si bonds to form nonbridging oxygen ($Si\text{-}O^-$), charged balanced by the cations, disrupting thus the stability of the glass network. The intermediate oxides can act both as network modifier or former. (3). Bioactive glasses can be divided based on their glass forming component; e.g., silicate-based glasses (such as 45S5), phosphate-based glasses and borate-based glasses (1).

Traditional silicate bioactive glasses are composed primarily of SiO_2 with addition of P_2O_5 and network modifiers such as calcium oxide (CaO), sodium oxide (Na_2O). Compared to chemically durable silicate glasses, bioactive glasses have lower SiO_2 and higher Na_2O and CaO content, with high CaO/P_2O_5 ratio (9). One of the most well-known bioactive glass composition, S53P4 (known as BonAlive®), was developed in late 1980's in Turku, Finland, followed by 13-39 in the 1990's. (68,69,70,71). Both 45S5 and S53P4 are currently clinically utilized as bone graft substitutes. (4). Bioactive silicate glasses have been widely researched and proved effective clinically, however it has been seen that they do not completely degrade *in vivo*. (72). Additionally, composition such as 45S5 and S53P4 have been found prone to crystallization upon sintering, and thus are difficult to process into 3D structures via heat-treatment. (7,8). 13-93 contains additionally MgO and K_2O in the glass composition, and has been found suitable for e.g. fiber drawing (71).

Phosphate-based bioactive glasses are mainly based on network former P_2O_5, with modifiers, such as CaO, and Na_2O. Phosphate-based bioactive glasses are known to be completely biodegradable, degrading congruently. However, this can also remove the materials ability to form an active bonding with the regenerating tissue, as phosphate-based bioactive glasses do not always exhibit HCA-layer formation. (16,73). They do however possess a wide thermal processing window,

that enables processing by heat-treatment and drawing into fibers, and have been shown promising in several tissue engineering applications (74,75,76,77).

Borate- and borosilicate-based bioactive glasses with B_2O_3 as a network former have gained a lot of interest in the field of tissue engineering., as these glasses have lower chemical durability and possess faster dissolution rate, and additionally, and convert more completely into HA-like material than purely silicate-based glasses. (10,78,79). In suitable amounts boron can stimulate angiogenesis, which is highly necessary for tissue regeneration. Therefore, borate and borosilicate glasses offer great potential for wound healing, and soft and hard tissue engineering (9,10). In some *in vitro* studies the release of boron has been found to possess cytotoxic effects; this however has been seen diminishing in dynamic or *in vivo* conditions. (9,80). Moreover, silicate bioactive glasses hot forming domain, as well as compressive and flexural strength, have drastically improved with incorporations of boron in the structure. (10,81).

Few other bioactive glass compositions have additionally been studied; for example, fluoride bioactive glasses, which contain fluoride (F) in addition to SiO_2, calcium CaO, and Na_2O. Fluoride bioactive glasses have been investigated for dental applications due to their ability to promote remineralization of tooth enamel. (82).

2.2.2 Bioactivity and degradation

Bioactivity is defined as materials ability to evoke a specific biological response at the materials surface, that enables formation of a bond between the tissue and the material. Additionally, there is increasing interest of materials capacity to evoke desired biological effect (such as osteogenesis or angiogenesis) by release of biologically active ions. Bioactive glasses are the first type of biomaterial shown to promote bone tissue regeneration by inducing osteoinductivity. (27,49). The bioactivity is based the glass network; low network connectivity enables exchange and leaching of ions with surrounding solutions, followed by layer formation of calcium phosphate compounds on the surface. The typical chemical reaction of silica-based bioactive glasses in physiological fluids, was proposed by Hench (49) already in 1970's;

1. First, upon immersion starts a **rapid ion exchange** between alkali ions (for example, Ca^{2+}) from the glass network and hydrogen ions (H^{+}) from the physiological fluid, leading to an increase in the solutions pH due to H^{+} consumption.
2. Glass **network starts to degrade**, and increase in the pH further increases the **loss of soluble silica**; leaving behind -silanol (Si-OH) bonds.
3. Then, the silica-gel polymerisation occurs: Si-OH + Si-OH → Si-O-Si; creating cation depleted **silica-rich layer on the surface** of the glass.
4. Migration of Ca^{2+} and $[PO_4]^{3-}$ groups from the glass and surrounding fluid start **forming an amorphous calcium phosphate layer** (aCaP), which grows on the surface of the silica-rich layer.
5. The aCaP is then enriched with OH^{-} and $[CO_3]^{2-}$ from the solution, forming thus the **crystallized carbonate substituted hydroxyapatite** (**HCA)**.

As HCA is similar to the main mineral phase of natural bone tissue, the formation of this layer is crucial to glasses biocompatibility, as well as to promote bone regeneration. The HCA layer formation is frequently studied *in vitro*, and often seen as a sign of compositions bioactivity. (49,83,84,85). It has been proposed that upon implantation, *in vivo*, the following steps to follows the crystallization of HCA;

6. Biochemical adsorption of growth factors on HCA layer
7. Macrophage activation; they participate in the inflammatory reaction that promotes migration of MSCs to a fracture location.
8. Stem cells (osteoprogenitor cell) attachment on the surface (on HCA layer)
9. Induction of stem cells proliferation and differentiation
10. Differentiating (osteoblastic) cells start to form the collagen matrix
11. Crystallization of matrix by mineral deposition
12. Proliferation and growth of bone

In addition to their ability to bond to hard tissue, bioactive glasses have been found to also bond with soft tissues, and could thus be applied in soft tissue engineering and wound healing. (1,86). Notably, studies have indicated that bioactive glasses can impact cellular behaviour through ion release, surface chemistry, and topographical features, playing a significant role in stem cell differentiation (16). One of the key mechanisms by which these ions affect cells, is by activating specific signalling pathways. As an example, bioactive glass 45S5 dissolution products upregulate osteogenic genes, by affecting the expression of

alkaline phosphatase, bone sialoprotein, collagen-I, osteopontin, osteocalcin, osteonectin, RunX2, and bone morphogenic protein. (87). The specific effects of these ions can vary, depending on the type of cells, concentration and duration of ion exposure. (16,17). Some of the most relevant ions regarding bioactive glasses for bone applications are presented in more detail in Table 1. Additionally, over 30 elements (88), such as zinc (89,90), copper (91,92), and silver (93,94), have been studied for their therapeutic effects. (88)

Table 1. Ions that are commonly released from bioactive glass and their overall biological function, and relevance to bone tissue.

Element	Effect	References
Silicon	Important role in connective tissue (bone, cartilage); primary effects in the organic matrix formation. Stimulation of angiogenesis.	(95,96,97,98)
Calcium	Functions as ionic messenger in several signalling pathways and cascades, in wide range of cellular processes. Mainly exists *in vivo* stored in bone minerals. Regulates e.g., bone cell activation and metabolism.	(99,100,101)
Phosphorus	Mediator in great variety of biological processes (incl., in cell membranes, nucleic acids, energy metabolism.) As phosphate, an essential component in bone mineralization; 90% of total P *in vivo* stored in bone as HA. Additionally has a role in regulation of gene expression, related to bone formation (e.g., matrix Gla protein, osteopontin).	(102,103,104)
Boron	Shown to stimulate osteogenesis, angiogenesis, and wound healing, however possibly toxic in high concentrations. Effect not clearly defined, but e.g., B deficiency can lead to bone abnormalities. Suggested to have a significant effect on cell membranes structural integrity and/or function.	(10,11,17,20)
Magnesium	Affects many cellular functions; ion (Ca, K) transport, signal transductions, energy metabolism and cell proliferation. Half of the total physiological Mg stored *in vivo* in bone minerals. Key role in bone remodelling and development.	(105,106,107)
Strontium	Similarly 'bone-seeking' element as Ca, handled very similarly *in vivo*. Toxic doses of Sr can lead to disturbances in normal Ca homeostasis, lower doses have been found to increase bone formation (by increasing osteoblastic activity and decreasing osteoclast activity.) Especially promising as anti-osteoporotic agent.	(15,108)

However, it is also important to note that excessive ion leaching into the surrounding tissue can cause adverse reactions, such as inflammatory response or substantial alteration of local pH, that can for example impair scaffold mineralization (109,110,111). Overall, ion leaching is an important aspect to control and understand to predict the cell fate. By carefully controlling the released ion rate and types, it is possible optimize the biocompatibility and regenerative potential of bioactive glass implants. (1,16,112).

2.2.3 Thermal behaviour, hot forming and crystallization

Glass is a material in a metastable amorphous state, lacking the long-range order found in crystalline materials, and undergoes crystallization when heated at high temperatures (113). To process scaffolds using glass particles, thermal bonding, i.e., sintering, is one of the most common methods. During the sintering, the glass particles undergo viscous flow, which enables fusion and neck growth between the glass particles. As such, pores form between the fusing particles and/or structures. As the contact between the particles grows, the pores shrink and may also be trapped within the structure. (114). If crystallization occurs (i.e., devitrification), sintering might be inhibited. Furthermore, crystallization decreases the overall network molar volume and leads to a shrinkage of the glass network. (65). The reactivity and ion release of bioactive glass, along with the precipitation of the HCA-layer in physiological conditions often depends on the existence and distribution of amorphous- and crystal-phases. In general, crystallization often reduces the bioactivity by inhibiting the formation of the HCA-reaction layer. (3,8,115,116).

The initial stage of glass crystallization starts from nuclei formation, which further grow with time and temperature. The crystallization mechanisms can be divided to either surface crystallization, where the initial nucleation occurs at the glass surface, or bulk crystallization, where the nucleation sites start to form evenly within the material (117). Especially surface crystallization can interfere with the sintering (7).

To analyse thermal behaviour of the glass compositions, differential thermal analysis (DTA) is often utilized. From the thermograph, it is possible to detect characteristic temperatures related to thermal events; such as for example, the glass transition temperature (T_g), at which the material changes from a rigid, glassy state to a softer, viscous state, enabling viscous flow of the material. (113). When the

activation energy to overcome the glass metastability is exceeded, the material starts to crystallize. In the DTA curve, the onset of crystallization (T_x) represents the initiation of the crystallization process, while the crystallization peak (T_p), representing the point at which the crystallization process reaches its peak intensity. (118).

The kinetics of glass crystallization can be studied by adapting mathematical models; commonly, the Kissinger equation (119) is utilized to determine the activation energy of a non-isothermal process; E_a, for viscous flow and E_c, for crystallization. Alternatively, the activation energies can be calculated with the Friedman model (120). The dimensionality (Johnson–Mehl–Avrami (JMA) exponent) of the primary crystallization can be studied with using the model proposed by Augis and Bennet (121). These equations are presented in **chapter 4.3.1**. Other alternative models include e.g., Ozawa method (122).

2.2.4 Modification of glass properties

Alterations in glasses composition can affect the material properties, such as thermal stability, tendency to crystallization, degradation rate, HCA formation and ion release. However, it is as well important to contemporaneously study the effect on cellular processes. With optimal modifications, it could be possible to enhance materials processability, while similarly having a therapeutic effect, that could further tissue recovery. (3,16,71).

The first bioactive glass was based on Na_2O-CaO- P_2O_5-SiO_2 system, and new compositions have been extensively studied. Few other clinically approved compositions, such as S53P4 (68) and 13-93 (71) have originally been statistically selected. The systematic design of the new compositions can be challenging, and therefore a lot of the studies have focused on optimisation of existing, well-known compositions. (88,123). Few models, based on e.g., regression modelling, structural analyses and machine learning have been presented for new design strategies. (3,69,71,88,124,125). As glasses are excellent solvents for almost all elements, changes can be done by several ways, often done by adjusting the quantities, or substituting, some of the oxides in the original compositions. (88,126). Studies by Arstila *et al.* (127) and Groh *et al.* (128) have shown that mixed alkali effect (129,130), or the alkaline earth/alkali ratio may be important, when designing e.g. bioactive

glasses with enhanced hot forming domain. Overall, higher network connectivity, which increases the processing range, additionally reduces the glass reactivity. (3,6,124).

For example, the processing of the successful commercial silicate compositions (i.e., 45S5 and S53P4) to more complex shapes, such as 3D porous structure has been challenging (7,9,131), although possible (132), as these glasses are prone to crystallize before appreciable viscous flow. When compared to these traditional silicate compositions, boron incorporation (i.e., substituting part of the SiO_2 with B_2O_3) has increased the hot forming domain (12,133), while additionally inducing faster reactivity and more complete glass conversion into HCA (9,134,135). This has been utilized, for example, in modifying the bioactive glass 13-93 to obtain clinically successful composition 13-93B3 (19,88). Moreover, it is possible to include other cation, than Na and Ca, within the glass network in order to gain additional beneficial properties (16,88,136). Especially, replacing part of glasses Ca with Mg and Sr, have been studied. These substitutions have been found to improve the hot forming domain and sintering (14,118,137,138), and additionally, have resulted into a slower reactivity and HA precipitation. Moreover, Mg or Sr have been observed to incorporate in the formed HA, possibly benefitting to the overall bioactivity (15,17).

The modification can affect glasses bioactivity, which is not determined only by the glass reactivity, but additionally by their effect on cellular processes. Many of the typical bioactive glass degradation products, as well as commonly used modifiers, are known to partake in bone metabolism and new bone formation. The effect of the released ions has been extensively studied (16,17,87,90,112,139,140,141) and few of the elements and their role and biological functions are briefly discussed in **chapter 2.2.2**.) It is noteworthy, that as the release of ions can easily exceed the limits of toxicity, from a clinical point of view, limited ions release (i.e., controlled surface activity) can be seen as a safety feature (22).

2.3 Glasses in regenerative medicine - state of the art

To replace the mostly allogenic bone graft materials, ceramic products are often used (142,143). Few of the bioactive glass products have successfully found their way on the markets and are used in various bone-filling applications, at present, primarily as granules (1,4), but nowadays also as fiber products for wound healing (144).

The original bioactive glass 45S5, trademarked as Bioglass®, has been approved as middle ear implants (1984), endosseous ridge maintenance implants (1988), and as particulates and granules as bone void fillers (1990), and as PerioGlass® (1993) in dental applications, and as NovaBone® (1999) in orthopedic applications for non-loading-bearing sites, as well as NovaMin® toothpaste-fillers (2011). (1,2,123,126). Other silicate-composition, S53P4, has been approved for usage as bone void filler (2006 in Europe, 2012 in the United States) (22) has in long-term clinical studies shown to be a safe, well-tolerated substitute, showing improvement over autologous and allogeneic bone grafts. (22,72) It is also an effective material for the treatment of osteomyelitis (5,145,146) However, some particles have been seen remaining even over 14 years post operation, due to lack of complete resorption. (72) Additionally, 13-93 (71) has been approved for *in vivo* use in the Europe and US and it's borosilicate derivate 13-93B3 (FDA approved in 2016) (147), as glass nanofibers with high calcium content, has shown ability to heal chronic wounds (such as diabetic ulcers), and been commercialized as Mirragen® (2017) (144,148). Moreover, Na_2O–K_2O–MgO–CaO–B_2O_3–P_2O5–SiO_2 based composition is utilized in Inion BioRestore® synthetic bone graft substitute (149). Several other promising compositions, such as ICIE16 (125) are under research.

Still, there is an unmet need for large, interconnected porous scaffolds for regeneration of large bone defects, and as such, there has been a growing focus on developing constructs with suitable qualities (1,7,9,47,65,131). Fortunately, *in vivo* studies have shown that e.g., sintered S53P4 and PLGA-coated S53P4 scaffolds have potential use as bone substitutes (150,151).Overall, bioactive glasses are a promising material for a wide range of potential applications in tissue regeneration and repair.

3 AIMS OF THE STUDY

The aim of this dissertation was to develop borosilicate bioactive glass compositions suitable for bone tissue engineering applications. The glasses properties were thoroughly studied. Specifically, structural properties, thermal behaviour and *in vitro* bioactivity were assessed in detail. Furthermore, the study aimed to produce 3D scaffolds from these compositions. This dissertation composes of four individual publications, which specific objectives are listed below:

I Preparation of novel glass compositions by modifying the well-known glass composition S53P4 by the substitution of 12.5-mol% of glasses SiO_2 with B_2O_3, as well as with part of the Ca with Mg and/or Sr. These new glasses were known as B12.5-series. The aim was to obtain a thorough understanding of how such substitutions affected the glass properties, by correlating structural and property changes.

II Examination of the crystallization mechanism in B12.5 glasses and assessing the feasibility of sintering glass particles without adverse crystallization. Furthermore, the impact of crystallization on the *in vitro* reactivity of these borosilicate glasses were assessed.

III Preparation of 3D scaffolds from few of the B12.5 glass series compositions. Additionally, the impact of fabrication method on scaffolds characteristics (porosity, mechanical properties), and consequently, on bioactivity, was analysed.

IV Investigation of the material/cell interactions by studying B12.5 glass series' dissolution products effect on human mesenchymal stem cells *in vitro*. The impacts on hADSCs viability and proliferation were observed, as well as the dissolution products osteogenic and angiogenic properties. Moreover, the viability and differentiation of the hADSCs were additionally assessed in direct contact with the material; by culturing on top of glass discs.

4 MATERIALS AND METHODS

4.1 B12.5 glasses – preparation and properties

4.1.1 Glass preparation by melt-deriving

Borosilicate glasses of molar composition of 47.12 SiO_2 – 6.73 B_2O_3 – 21.77 (-x-y) CaO – 22.65 Na_2O – 1.72 P_2O_5 – x MgO – y SrO (mol-%), where x,y = 0, 5 or 10 mol-% were prepared for **Studies I-IV**. The studied glasses were based on composition B12.5, where x,y=0. Glass compositions for all of the B12.5-glass series are presented in Table 2.

Table 2. Nominal oxide compositions of the studied glasses (mol-%).

Glass	SiO_2	B_2O_3	CaO	Na_2O	P_2O_5	MgO	SrO
B12.5	47.12	6.73	21.77	22.66	1.72	-	-
B12.5-Mg5	47.12	6.73	16.77	22.66	1.72	5	-
B12.5-Mg10	47.12	6.73	11.77	22.66	1.72	10	-
B12.5-Sr5	47.12	6.73	16.77	22.66	1.72	-	5
B12.5-Sr10	47.12	6.73	11.77	22.66	1.72	-	10
B12.5-Mg5-Sr10	47.12	6.73	6.77	22.66	1.72	5	10

Raw material batches were prepared from mixtures of sand (99.4 % of pure SiO_2) and analytical grade reagents of H_3BO_3, MgO, $SrCO_3$, $(NH_4)H2PO_4$, Na_2CO_3 and $CaCO_3$, and heated up to 1300°C, in a platinum crucible. Then, molten glass was cast into pre-heated graphite moulds yielding either rectangular blocks or cylindrical rods (with a diameter of 10 mm). Glass was annealed at 500 °C for 5 hours to release the internal stresses. Glass compositions were analysed post melting by EDX (results not reported); within the accuracy of measurement (~1 mol%,) we could not see strong deviation from nominal composition. Glass blocks were crushed and sieved to particle size fractions of < 38, 125-250, 250-500 and 500–1000 μm, and the glass rods were cut to discs (height 2 mm) using a diamond wheel saw and polished up to #4000 grit.

4.1.2 Physical properties – density and molar volume

Glasses densities were measured, in **Study I,** using a gas displacement helium pycnometer (AccuPyc 1330, Micromeritics; accuracy of ± 0.01 g/cm^3). The molar volume, V_M, was calculated using the measured density, with Equation 1:

$$V_M = M/\rho\,, \tag{1}$$

where ρ is the density and M the molar mass of the glass.

4.1.3 Structural properties

Structural analysis, in **Study I,** was performed using Fourier-transform infrared (FTIR) spectrophotometer in attenuated total reflectance (ATR) mode. Spectra were recorded using a Perkin Elmer Spectrum One FTIR in the 600-1600 cm^{-1} domain. Spectra were background corrected and normalized to the band having maximum intensity.

Raman spectroscopy was conducted in the 250 – 1800 domain cm^{-1}, with a T64000 Jobin-Yvon confocal microRaman spectrometer equipped with a CCD detector. All reported spectra were unpolarized, background corrected and normalized to the peak with the highest intensity.

Finally, ^{31}P and ^{11}B magic angle spinning (MAS) nuclear magnetic resonance (NMR) spectra were recorded at room temperature on a Bruker AVANCE III HD NMR spectrometer. ^{31}P pulse solid-state MAS NMR was performed using a commercial 4 mm rotor and magnetic field B_0 = 9.4 T. Chemical shift values (δ_{iso}) were quoted with respect to 85% H_3PO_4, quantitative spectra with 16 accumulations were taken at a spinning frequency of 12.5 kHz and nutation frequency of 69.4 kHz. ^{11}B echo solid-state MAS NMR was performed using a commercial 2.5 mm rotor spun at 30 kHz. The pulse lengths were 1 and 2 μs for P1 and P2, respectively, which corresponded to a flip angle less than 30°. The echo delay was set to 1 rotor period, i.e. 33.33 μs. The recycle delay was 1 s. All δ_{iso} values are quoted with respect to 1M boric acid solution.

4.1.4 Thermal properties

Differential thermal analysis (DTA), in **Studies I and II,** were performed using STA 449 F1 Jupiter, (Netzsch Group, Selb, Germany). From the DTA spectra, the glass transition temperatures (T_g) were taken at the inflection of the first endothermic event. The onset of crystallization (T_x) was defined using the tangent technique on the first exothermic peak (indicative of crystallization), and crystallization peak (T_p) corresponded to the the maximum of the exothermic peak in the DTA thermogram. The ΔT between T_g and T_x, was defined as the processing or sintering window. Measurements were performed in Pt-Rh crucibles in N_2 atmosphere at a heating rate of 10K/min for the measurement of the characteristic temperatures, and at heating rates ranging from 5 to 20 K/min for kinetics studies. All measurement were performed in the temperature range 40 to 1200°C.

4.2 Sintered bodies – preparation and properties

4.2.1 Preparation of bulk sintered bodies – heat treatment

Particles (250-500 μm) were placed in a stainless-steel mould with seven holes (d=10mm, h=10mm) and heated at 20 °C/min to the sintering temperature. Sintering temperature was maintained for one hour and samples then left to cool down to RT. All tested sintering temperatures tested in **Study II**, are presented in Table 3.

The studied temperatures were designed to gain a comparison of amorphous glass (heat treatment at low temperature, 'L', under glasses T_x), to fully crystallized glass (at high temperature 'H'; over glasses T_p at 20 K/min heating rate). Additionally, several sintering temperatures (approximately 25 °C apart) between L and H were studied, where sintered bodies could be obtained with or without partial crystallization based on the DTA and XRD results (**chapter 4.1.4**.)

Table 3. Temperatures (°C) used for heat treatments, to gain amorphous (heating at temperature L), crystallized (heating at temperature H) and sintered bodies in between L and H (temperatures A-E). (**Study II**)

id/composition	B12.5	B12.5-Mg5	B12.5-Sr10	B12.5-Mg5-Sr10
L **'low'**	550	550	550	550
A	650	585	600	575
B	670	610	625	600
C	695	635	650	625
D	720	660	675	650
E	745	685	700	675
H **'high'**	806	821	794	782

4.2.2 Preparation of scaffolds by porogen burn-off method

Burn-off scaffolds, in **Study III,** were prepared by using ammonium bicarbonate (NH_4HCO_3) as porogen, (Sigma-Aldrich, 99.5%, CAS No. 1066-33-7) and < 38 μm glass powders. Compositions labelled B12.5 and B12.5-Mg5-Sr10 (presented in Table 2) were chosen to be tested in the study. The green bodies were prepared by pressing mixture of glass powder (30 vol-%) and porogen (70 vol%) inside a cylindrical mold, followed by sintering, performed in a Nabertherm LT 9/11/SKM electric muffle furnace, in air, using the heating profiles presented in Table 4. During the sintering, the porogen was assumed to fully decompose and evaporate; leaving pores in the formed sintered structure. After the heat treatment, formed scaffolds were taken out of the oven and let to cool down to RT, and afterwards, stored in a desiccator.

Table 4. Heating protocol for scaffold sintering (**Study III**)

Temperature range	Heating rate or time	Step
RT to 300 °C	1°C/min	Slow heating; allowing burning of the porogen
300°C to 545 °C	5°C/min	Slow heating; avoiding sudden shrinkage which might cause cracking of the scaffold
540-545 °C	1h	Holding; fusion of glass particles

4.2.3 Preparation of 3D printed scaffolds

3D printed scaffolds for **Study III** were made from glass powders (< 38 μm) of glass compositions B12.5 and B12.5-Mg5-Sr10, by robocasting using 3Dn-Tabletop printer (nScrypt Inc., Orlando, Florida, USA), and controlled via the Machine Tool 3.0 system software.

Pluronic solution was utilized as a binder for the green body. Pluronic solution was prepared in an ice bath from Pluronic 127 (Sigma-Aldrich, CAS No. 9003-11-6) and distilled water in the ratio of 25:75 wt-%, respectively, and afterwards stored at +4°C. The printable ink was made by mixing the glass powder and Pluronic solution in the ratio of 30:70 wt-%, respectively. Ink was prepared by mixing-cooling cycles at in intervals of 30 seconds mixing (2500 rpm; Vibrofix VF1 electrical shaker, IKA®-Labortechnic, Staufen, Germany), followed by 30 seconds cooling in an ice bath, until the ink was homogenous. The ink was loaded into Optimum® 3cc printing cartridge (Nordson EFD, Bedfordshire, England) and left for 1 hour at RT to achieve proper viscosity for 3D printing.

For the printing, layer patterns were designed with spacing between the filaments being 1.18 mm. Ink was extruded at a feed pressure of 18.0–22.0 psi, through SmoothFlow Tapered Tips with tip diameter of 0.41 mm (Nordson EFD Optimum® SmoothFlow™, Westlake, Ohio, USA) onto acrylic sheets (Folex AG, Seewen, Switzerland). After each layer, the nozzle was elevated (in the z-direction) by 0.45 mm and the pattern of the previous layer was rotated 90°, to gain a cylindrical pattern. To reduce the risk of collapse of the green body, the printed bodies were left to dry in room temperature (RT) at least for 24 h. After drying, heat treatment was performed as for the burn-off scaffolds, presented in Table 4. Similarly, as the porogen and the binder were burned out in the first step of the heating protocol.

4.2.4 Porosity of the sintered bodies and scaffolds

Porosity of the sintered bodies heated at temperatures A-E (Table 3) (**Study II**) and for scaffolds (**Study III**) were obtained by measuring and calculating average heights and masses of samples. The estimation of the scaffolds' porosity was performed assuming that scaffolds are cylinder-shaped. The porosity was estimated using the following Equation 2.

$$Porosity = (1 - \rho/\rho_0) \times 100\% \quad (2)$$

where the ρ_0 was the bulk density, and ρ was the apparent density (specimen mass divided by volume) of each sample. The porosities were obtained from 7 specimens per condition and expressed as mean ± standard deviation (SD).

For **Study III**, micro-computed tomography (μCT) with MicroXCT-400 (Carl Zeiss X-ray Microscopy, Inc., Pleasanton, California, USA) with 80 kV tube voltage and 0.4x objective, resulting pixel size of 16.7 μm, was utilized to gain additional information about the scaffold 3D structures.

4.2.5 Scaffolds mechanical properties

In **Study III**, as the porogen burn-off and 3D printed scaffolds underwent uneven shrinkage during sintering, both top and bottom surfaces were leveled using #P800 SiC paper in 96% ethanol, and air-dried in at 37 °C. Measurements were taken from scaffolds with d≈11-14 mm and h≈5-6 mm.

Compression tests were carried out on an Instron 4411 mechanical tester at a 0.5 mm/min deformation rate. A 5 kN load cell was employed. The highest compression values from individual tests determined the compressive strength. Results represent the mean ± SD of three parallel samples for each scaffold type and glass composition.

4.3 Glasses crystallization

4.3.1 Theoretical determination of activation energies

The activation energies of the glasses of interest were determined in **Study II**. Activation energies associated with the viscous flow and crystallization peak, $E_{c,kis}$ were determined by measuring T_g and T_p at different heating rates and then applying the Kissinger equation (Equation 3) (119)

$$ln\left(\frac{\beta}{T_g^2}\right) = -\frac{E_a}{RT_g} + Constant, \quad (3)$$

where E_a is the activation energy of glass transition, β is the heating rate, T_g the corresponding glass transition temperature at the heating rate , β, and R is the ideal gas constant. The activation energy of crystallization $E_{c,kiss}$ was determined by replacing T_g with T_p.

The apparent activation energy for crystallization $E_{c,fri}$ was also determined using the Friedman isoconversional method (Equation 4) (120)

$$ln\left(\frac{d\alpha_i}{dt}\right) = -\frac{E_{c\alpha}}{RT_i} + Constant, \quad (4)$$

where $E_{c\alpha}$ is the activation energy of crystallization at a specific degree of transformation α, $\frac{d\alpha_i}{dt}$ is the transformation rate at a temperature T_i, and R is the ideal gas constant.

4.3.2 Johnson–Mehl–Avrami factor

The JMA exponent, giving information on the dimensionality of the crystal growth, was determined in **Study II** using the equation proposed by Augis and Bennet (Equation 5); (121)

$$n = \frac{2{,}5}{\Delta T_{FWHM}} \frac{T_p^2}{\frac{E_c}{R}} \ , \quad (5)$$

where n is the JMA exponent, T_p is the crystallization temperature, ΔT_{FWHM} is the full width at half maximum of the DTA peak, and R is the ideal gas constant. E_c is the activation energy of crystallization, determined either by Kissinger Eq.(3) or Friedman Eq.(4) method.

4.3.3 Crystallization after sintering

In **Study II**, scanning electron microscopy (SEM) was utilized to observe the extent of the crystallization in the sintered specimens. The sintered bodies were embedded in resin, then polished to a #4000 grit to unveil their cross sections. Subsequently, carbon coating was applied to the samples, which were then imaged using the Zeiss Crossbeam 540 scanning electron microscope equipped with Oxford Instruments XMaxN 80 energy dispersive X-ray spectroscopy (EDS) detector.

In **Studies II** and **III,** the crystallization of the glasses were evidenced by X-ray crystallography (XRD). Samples were prepared by crushing heat-treated/sintered bodies in a mortar, and analysed for **Study II** using a XRD PANalytical (Siemens) on angles from 20° to 90°, and for **Study III** in the 10–60° 2θ diffraction angle range using MiniFlex™ (Rikagu, Tokyo, Japan).

4.4 *In vitro* reactivity in simulated body fluid

4.4.1 Immersion in simulated body fluid

Glasses and scaffolds reactivity in physiological fluids was tested in simulated body fluid (SBF) in **Studies I, II** and **III,** as suggested in ISO/FDIS 23317 International Standard for Implants for surgery — In vitro evaluation for apatite-forming ability of implant materials. SBF solution was prepared following the protocol described by Kokubo et al. (84). The pH was adjusted to 7.40 ±0.02 at 37°C ±0.2°C. During the experiment, the solution was not refreshed to observe the precipitation of a calcium phosphate (CaP) reactive layer.

In **Study I,** the mass of sample, immersed in 50mL of SBF, ranged from 75 mg to 80.3 mg (±0.5 mg), to maintain the surface area in contact with the solution constant. In addition, polished discs (diameter about 10 mm, height about 2 mm), where the average weight was around 330 ± 50 mg, was also immersed in SBF. For **Study II**, it should be noted that the samples treated at the temperature labelled H had sintered, and therefore were re-crushed before being tested in SBF. Mass was

kept constant at 75 mg ±1 mg per 50 ml SBF. In **Study III** the average sizes of the scaffolds were approximately 14.4 mm x 4.3 mm and 12.6 x 4.0 mm, for B12.5 and B12.5-Mg5-Sr10, respectively, for the porogen burn-off technique. 3D printed scaffolds had sizes of 9.8 mm x 4.5 mm (B12.5) and 8.4 mm x 3.8 mm (B12.5-Mg5-Sr10). Immersion test were performed by maintaining the mass/volume of SBF ratio constant at 20 mg/ml.

Specimens were placed in an incubating shaker at 37°C and 100 rpm, with immersion times ranging from 6 to 336 hours.

4.4.2 Ion dissolution

After immersion, the pH of the solution was measured at 37°C (±0.2°C) with a pH-meter, at each time point. SBF dissolution solution samples were collected for ion concentration determination. ion concentration in solution was quantified by inductively coupled plasma optical emission spectrometry (ICP-OES, Agilent Technologies). In **Studies I, II** and **IV**, 1 ml of solution was collected at each time point and diluted 1:10 in HNO_3. Analysed elements were Si (at wavelength 288.158 nm), B (208.956 nm), Ca (393.366 nm), P (253.561 nm), Mg (279.553 nm) and Sr (407.771 nm).

4.4.3 Structural properties

For **Studies I, II** and **III**, SBF immersed glass specimens were collected, rinsed with acetone (to stop further reactions), and dried. Changes in glasses' surface chemical properties were evidenced with FTIR spectrometry in ATR mode as described in **chapter 3.1.3**. To reveal the samples cross section, specimens were embedded in resin, polished and the composition and structure post immersion were analysed using scanning electron microscopy with energy dispersive X-ray spectroscopy (SEM/EDX) as explained in section **chapter 3.3.3.**

4.5 Cell experiments

4.5.1 Ethical statement and cell cultures

Experiments in **Studies III** and **IV** were performed with donor human adipose-derived stem cell (hADSC) lines, characterized as mesenchymal based stem cells. (152,153) in accordance with the ethical approval granted by the Ethics Committee of Pirkanmaa Hospital District, Tampere, Finland (R15161).

Basic growth media (BM) consisted of α-Minimum Essential Media (α-MEM) with 5% human serum and 1% penicillin/streptomycin in an animal origin free culture conditions. Additionally, supplements of 10 mM β- glycerophosphate, 250 μm L-ascorbic acid 2-phosphate and 1μl/ml dexamethasone were utilized in preparation of osteogenic media (OM).

4.5.2 Material preparation and cell seeding – glass extracts and discs

The glasses in **Study IV** contained all B12.5 series compositions presented in Table 2., with, additionally, composition S53P4 (53.85SiO_2 –21.77 CaO – 22.65 Na_2O – 1.72 P_2O_5 in mol-%), prepared by the melt-quench technique, similarly as glasses described earlier in **chapter 4.1.1**. Polished glass discs, and glass particles of 500-1000 were utilized in the studies. Prior to use in cell culture experiments, discs and glass particles were heated at 200 °C for 1 h, and later disinfected with ethanol in the cell culture laminar hood.

Glass ion-conditioned extracts were prepared from the granules by immersing 87.5 mg/ml of glass particles of fraction size 500-1000 μm in α-MEM, and incubating them 24 hours in a 10 cm diameter cell culture petri dish at 37 °C, as previously described in (20,154). After incubation, the media containing the dissolved ions from the glasses were collected and sterile filtered, before addition of 5% serum, 1% penicillin-streptomycin and OM supplements. New extract batches were prepared weekly, and OM supplements were freshly added before exchange of media.

Discs were preincubated overnight before plating of the cells. Cells were plated in BM and on the following day ('day 0' of experiments), media of interest was introduced (ion extract, or for the disc cultures either BM or OM). Different cell seeding densities were utilized in the experiments, presented in Table 5.

As an addition to the bioactive glass conditions, control cultures were grown without bioactive glass products; controls for ion extract cultures were grown only in presence of pure OM, and controls for discs cultures were cultured on polysterene (cell culture well plate). Cells were cultured in an incubator, at 37 °C, in a humidified atmosphere of 5% CO_2 balanced with 95% air, for up to 21 culturing days. The media (300µl per 48-wellplate well) was changed every 3-4 days.

Table 5. Cell seeding densities for different experiments and culturing conditions in **Study IV**.

Condition / media	**Cell seeding density**	**Experiment / analysis**
Ion extracts (with OM supplements)	~160 cells per cm^2 (48-well plate)	Viability, proliferation, alkaline phosphatase activity, immunocytochemical staining (collagen I), gene expression, mineralization assay.
Glass discs (BM and OM)	3200 cells per cm^2 (48-well plate)	Viability
Glass discs (BM and OM)	2200 cells per cm^2 (48-well plate)	Immunocytochemical staining (collagen I, osteocalcin)

To analyse the ion concentrations, the basic culturing media and glass dissolution extracts were diluted 1:10 in distilled water, then spiked with 50 µl of 70% ultrapure HNO_3 per 10 ml sample and analysed for the ion concentration by ICP-OES Analysed elements were Si (at wavelength 251.611 nm), B (249.772 nm), Ca (317.933 nm), Na (589.592 nm), P (213.618 nm), Mg (285.213 nm) and Sr (216.596 nm).

4.5.3 Material preparation and cell seeding – scaffolds

The samples in **Study III** were bulk, burn-off and 3D printed scaffolds of only B12.5-Mg5-Sr10 composition. Bulk scaffolds were prepared by pressing the glass powder (< 38 μm) into a cylindrical mold with diameter and height of 5 mm. Burn-off and 3D printed scaffolds were prepared with similar methods as described in **chapters 4.2.2** and **4.2.3**, respectively. Scaffolds were sintered for 1h at 545°C in air atmosphere. After sintering, with the average scaffolds height was h= 4.2 ± 0.4 mm and diameter was d= 4.4 ± 0.3 mm. The scaffolds were sterilized by heating them 3 h at 200 °C, and preincubated for 2 days in Tris(hydroxymethyl)aminomethane (TRIS), followed by 24 h in αMEM in incubator at 37 °C with mass/volume ratio constant at 10 mg/ml, to reduce the burst of ions upon immersion. hADSC cell density was 25 000 / well for all scaffold condition.

4.5.4 Cell viability

Cell viability was studied *i*) in **Study III,** for 1, 3 and 7 culturing days and *ii*) in **Study IV,** for up to 21 culturing days, both with ion extracts, and in direct contact (on top of glass discs) in OM and BM. Viability was analysed with Live/Dead staining (Invitrogen, Thermo Fisher Scientific) by incubating the cultures in 0.25 μM Ethidium homodimer-1 (EthD-1) and 0.5 μM Calcein-AM containing solution for 20 to 30 min at RT, followed by immediate imaging with a microscope equipped with a fluorescence unit and a camera.

4.5.5 Cell proliferation

Cell proliferation was evaluated, in **Study IV,** at 7, 14 and 21 culturing days, based on total DNA amount, for extract cultures, with CyQUANT Cell Proliferation Assay (Invitrogen, Thermo Fisher Scientific), by lysing the cells in 0.1% TritonX-100 lysis buffer. Collected supernatant was stored at -80 °C, and after thawed, 20 μl of three parallel replicates of each lysate were mixed with 180 μl of 1:1 CyQUANT GR dye and lysis buffer. The fluorescence was measured with a multiple plate reader (Victor 1420 Multilabel counter, Wallac) at 480/520 nm. Results were statistically analysed with two-way ANOVA.

4.5.6 Immunocytochemical staining

For immunocytochemical staining, cultured cells (7, 14 and 21 culturing days), in **Study IV,** were first fixed with 4 % paraformaldehyde (PFA) for 30 min at RT, and blocked by incubation with 1% bovine serum albumin (BSA), for nonspecific staining, for 60 min at +4 °C. Primary antibody against collagen I (mouse monoclonal anti-collagen-I, 1:2000, for extract and disc cultures) were incubated at +4 °C overnight. Specimens were washed with phosphate buffered saline (PBS) and then incubated with secondary antibodies (donkey anti-mouse Alexa fluor 488 IgG, 1:800) together with actin-staining phalloidin-TRITC (1:500). Additionally, the samples were stained with PBS including nuclei staining 4',6-diamidino-2-phenylindole (DAPI; 1:200), followed by imaging with microscope with fluorescent unit.

4.5.7 Alizarin red mineralization assay

Alizarin red staining assay was performed for extract cultures in **Study IV** (14 and 21 culturing days) to observe CaP mineral formation. Cultures were fixed with iced cold 70% EtOH (90 min incubation at -20 °C) and stained with 2% Alizarin red S solution (pH 4.1–4.3; Sigma-Aldrich) for 10 min at RT. Cultures were then PBS washed and imaged. Then, the attached dye was extracted with 100 mM cetylpyridinium chloride (Sigma-Aldrich) and absorbances were measured at 544 nm (Victor 1420 Multilabel counter).

4.5.8 Gene expression

Expression of human osteogenic markers *RUNX2a*, *OSTERIX, DLX5*, and *OSTEOPONTIN*, as well as of endothelial markers *vWF* and *PECAM-1* were analysed for extract cultures (14 and 21 culturing days) in **Study IV**. RNA was isolated using Macherey-Nagel NucleoSpin-kit by following the manufacturer's protocol, prior to cDNA transcription. qRT-PCR was performed with QuantStudio 12K Flex Real-Time PCR System (Applied Biosystems) and the relative expression were normalized with housekeeping gene *RPLP0*, and calculated by Pfaffl, a mathematical model (155).

5 RESULTS

5.1 Glass compositions - physical and structural properties

5.1.1 Physical properties

Visually, the produced glasses were clear and colourless. Glass network compactness was evaluated by determining the glass density and molar volume, and the results are presented in Table 6. It was seen that within the accuracy of the measurements, partial substitution of Mg for Ca did not lead to changes in the M_V.

Table 6. Measured glass densities and calculated molar volumes for the studied compositions (**Study I**)

Glass	Density (g/cm^3)	Molar volume (cm^3/mol)
B12.5	2.66 ± 0.01	23.2 ± 0.2
B12.5-Mg5	2.65 ± 0.01	23.1 ± 0.2
B12.5-Mg10	2.62 ± 0.01	22.9 ± 0.2
B12.5-Sr5	2.75 ± 0.01	23.3 ± 0.2
B12.5-Sr10	2.84 ± 0.01	23.4 ± 0.2
B12.5-Mg5-Sr10	2.81 ± 0.01	23.3 ± 0.2

5.1.2 Structural properties

Structural properties were analysed by FTIR, Raman and MAS-NMR spectroscopy. Both the FTIR and the Raman spectra (Figure 2A and B, respectively) of all glasses exhibit similar vibrations, indicating features characteristic of borosilicate glasses. However, with further analysis, it was observed that with Mg/Sr substituted compositions, Raman spectra obtained from different parts of glass discs did not overlap (as seen in **Study I -** Figure 2). The band assignments are reported for FTIR spectra, in Table 7 and for Raman spectra, in Table 8.

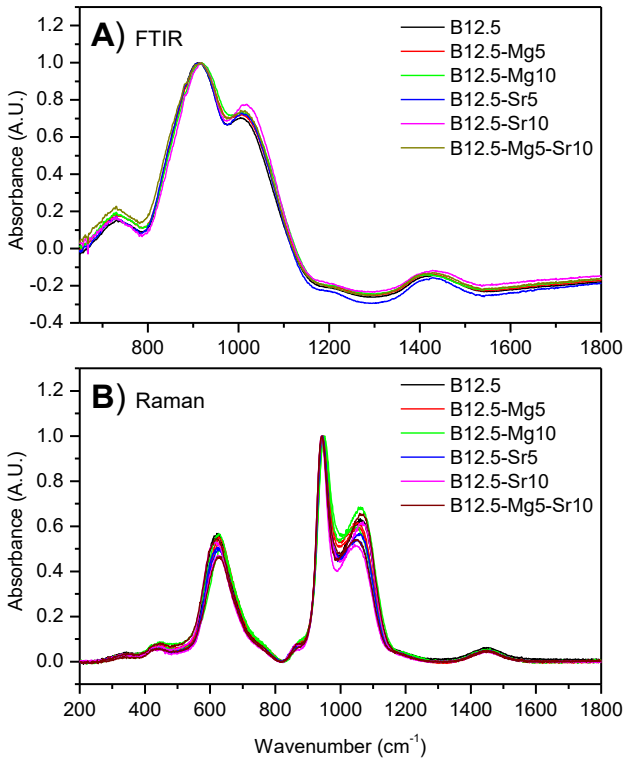

Figure 2 . Normalized and background corrected (**A**) FTIR and (**B**) Raman spectra for all studied glass compositions (analysed from particle sizes in the range 125-250 µm.) (Modified from **Study I**)

Table 7. FTIR spectra band assignments (**Study I**)

Band region	**Attribution**	**Reference**
750 cm^{-1}	Si-O bending	(13,14,156)
950, 1100-1150 cm^{-1}	Si-O- & Si-O-Si asymmetric stretching of the silicate network	(13,14,156)
850-1150 cm^{-1}	B-O stretching vibration in BO_4 units	(157)
1227 cm^{-1}	Boron in the form of BO_2O-	(157)
1400 cm^{-1}	B-O vibration in borate triangles formed by BO_3	(157)

Table 8. Raman spectra band assignments (**Study I**)

Band region	Attribution	Reference
300-500 cm^{-1}	Mixed stretching and bending modes of Si-O-Si bonds	(158)
630 cm^{-1}	Breathing mode of borosilicate rings	(158,159)
950-980 cm^{-1}	Symmetric P-NBO stretching modes associated with Q^0-P tetrahedra (narrow peak), or Si-O stretching with two nbO per silicon atom (Q^2 structural units) (broader peak).	(159,160,161,162)
1050-1100 cm^{-1}	Si-O stretching with three nbO per silicon atom (Q^3 structural units)	(159,160,161,162)
1250-1500 cm^{-1}region	B-O stretching vibration	(163,164,165)
1410 cm^{-1} peak	BO_3 units bonding to BO_4	(163,164,165)
1480 cm^{-1}	BO_3 units connected to another BO_3 unit	(163,164,165)

^{31}P and ^{11}B MAS NMR were recorded for compositions B12.5, B12.5-Mg10, B12.5-Sr10 and B12.5-Mg5-Sr10 to clarify the role of phosphorus and boron in the network. Spectra are presented in Figure 3 and peaks attribution are listed in Table 9.

^{31}P NMR spectra was similar for B12.5, B12.5-Mg10 and B12.5-Sr10 and only a slight chemical shift was observed in the spectra of the B12.5-Mg5-Sr10 glass. NMR peaks were mainly assigned to orthophosphate groups, with a tail, at -3 ppm, possibly indicating phosphate groups connected to the silicate network. ^{11}B spectra presented peaks related to the presence of BO_3 and BO_4 units. After deconvolution of the peaks, it was seen that in composition B12.5, BO_3 and BO_4 units are present in equal amount (52 and 48 ±1%, respectively), while in the Mg/Sr substituted compositions, an increase in BO_3 units at the expense of the BO_4 units, was observed (62 to 38 ±1%, respectively.) Furthermore, the peak assigned to BO_4 units shifted from ~0.4 ppm for B12.5 to ~-2 ppm for all substituted glasses.

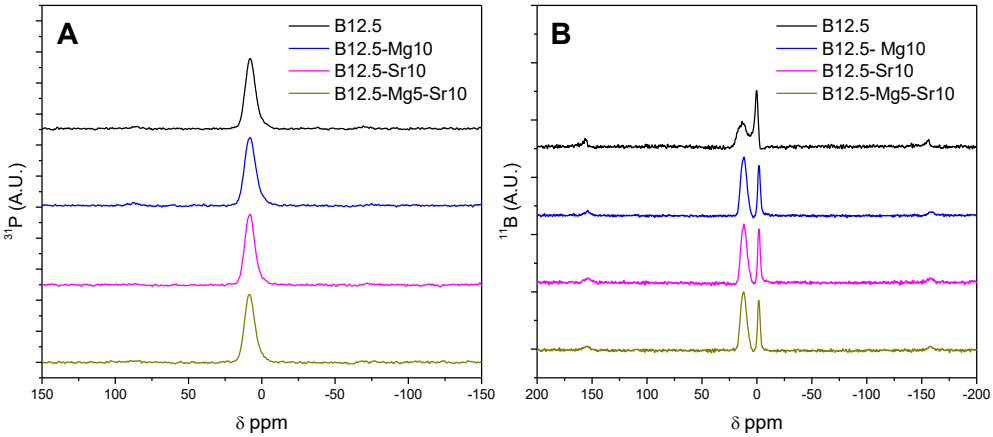

Figure 3. (**A**) 31P and (**B**) 11B MAS NMR spectra for compositions B12.5, B12.5-Mg10, B12.5-Sr10 and B12.5-Mg5-Sr10 (Modified from **Study I**)

Table 9. Observed peaks in the recorded 31P and 11B MAS NMR spectra. (**Study I**)

31P MAS NMR		
Peak at 8-9 ppm	Phosphorus present in Q_P^0 (orthophosphate) groups	(166,167)
Tail at -3 ppm	Possibly related to Q_P^1 phosphate units, i.e. phosphate groups connected to the silicate network	(166,167)
11B MAS NMR		
Peak at 11.8-12.4 ppm	BO_3 units	(168)
Peak in the ~0 to -3 ppm	BO_4 units	(163,168,169)

5.2 Processability

5.2.1 Thermal properties

DTA was conducted for both < 38 μm (fine particles) and [250-500] μm (coarse particles. Example of a thermograph, where temperatures of interest (T_g, T_x and T_p) are labelled, is presented in Figure 4. Characteristic temperatures, determined at a heating rate of 10 K/min, are presented in Table 10. The glass transition temperature of the B12.5 glass series was found to gradually decrease upon increasing Mg/Sr for Ca substitution. The DTA curve for glass composition B12.5-Mg5-Sr10, containing both Mg and Sr, exhibited two T_g's; indicating phase separation. Substitution of Mg for Ca additionally led to an increase in T_p and ΔT, however, no clear trend with Sr substitutions for T_x, T_p or ΔT could be observed. Mixture glass, B12.5-Mg5-Sr10, exhibited overall lower temperatures for T_g, T_x and T_p.

Processing window, determined in **Study I** for particles size 250-500 μm (Table 10) was found to be around 150 °C or higher. When thermal analysis was performed for finer particles in **Study II** (Table 3: T_g, T_x and T_p of the investigated glasses with particle size < 38 μm and recorded at 10 K/min heating rate), it was seen that composition exhibited similar T_g, but lower temperatures for crystallization (both onset and peak temperature), resulting in smaller working range.

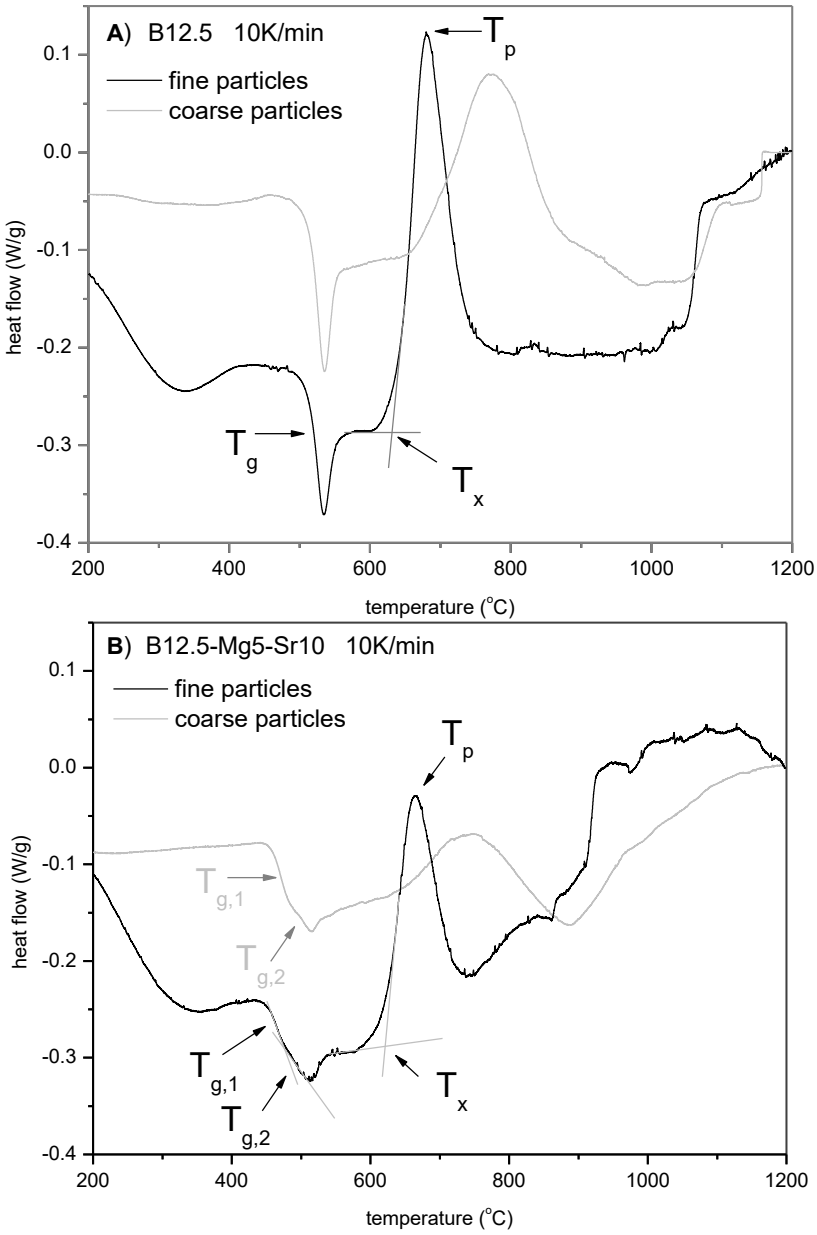

Figure 4. Example of DTA thermograph (modified from **Study II**) determined with 10 K/min heating rate for (**A**) B12.5 and (**B**) B12.5-Mg5-Sr10, respectively, as < 38 µm (fine particles) and [250-500] µm (coarse particles.) The glass transition temperature (T_g) was taken at the inflection point of first endothermic event. The onset of crystallization (T_x) was taken at the beginning of the crystallization peak (tangent method) and the crystallization at the maximum (T_p) of exothermic peak. Processing window (ΔT) was determined between T_g and T_x.

Table 10. DTA results for T_g, T_x and T_p of the investigated glass particles sieved to 250-500 µm (10K /min). ΔT (T_x-T_g) presents the hot forming domain, i.e., working range of the B12.5-glass series. (Modified from **Study I)**

Glass	T_{g1} (±3°C)	T_{g2} (±3°C)	T_x (±3°C)	T_p (±3°C)	$\Delta T = T_g - T_x$ (±6°C)
B12.5	529		691	772	162
B12.5-Mg5	513		678	781	165
B12.5-Mg10	500		687	795	187
B12.5-Sr5	512		659	780	147
B12.5-Sr10	502		675	772	173
B12.5-Mg5-Sr10	472	507	647	725	140/175

5.2.2 Crystallization mechanism

5.2.2.1 Activation energies and the JMA exponent

With increasing heating rate, T_g and additionally T_p shifted toward higher temperatures due to thermal lag (119). The shift of this characteristics temperature, in relation to the heating rate can be used to calculate the activation energy for viscous flow. Additionally, the crystallization kinetic parameters, i.e. the activation energy for crystallization and the Johnson-Mehl-Avrami exponent were calculated.

The activation energy for viscous flow was calculated utilizing the Kissinger equation, while both the Kissinger and Friedman methods were employed to estimate the activation energies for crystallization (Eq. 3&4, respectively) and Augis-Bennett method (Eq. 5) was used to calculate the JMA exponent. Calculated values for two glass particle sizes are reported in Table 11. All the studied glass compositions exhibited similar E_a, within the accuracy of the measurements, around 500 kJ/mol, however minor E_a increase could be associated with Sr addition. Additionally, E_c were found on similar level on all compositions, except with B12.5-

Sr10 and B12.5-Mg5-Sr10, slight difference was noted between values determined with Kissinger and Friedman methods. All JMA exponent, "*n*" values for each glass compositions, with both fine and coarse particles, were found to be close to 1 (ranging from 0.6 to 1.3; as seen in **Study II**)

Table 11. Activation energies for glass transition E_a and crystallization E_c(kis) determined by Kissinger method (Eq.3), and additionally E_c(fri) determined additionally using the Friedman method (Eq.4), determined for both fine (<38 μm) and coarse (250-500 μm) particles. (Modified from **Study II**)

		E_{a1} (±30 kJ/mol)	E_{a2} (±30 kJ/mol)	E_c(kis) (±30 kJ/mol)	E_c(fri) (±10%)
B12.5	coarse	493		210	261
	fine	477		260	286
B12.5-Mg5	coarse	486		237	266
	fine	483		296	350
B12.5-Sr10	coarse	491		302	242
	fine	548		409	296
B12.5-Mg5-Sr10	coarse	550	392	185	286
	fine	665	516	394	344

5.2.2.2 Crystallization and sintering

In order to assess the impact of crystallization on the processing of sintered bodies, glass particles [250-500 μm], were heat treated between 550 °C and 821 °C, as shown in Table 3.

XRD analysis (Figure 5) was conducted on heat treated particles, to detect crystallization occurring during the sintering process. Notably, when visual inspection of the sintered specimens was conducted to assess their handling ability, B12.5 sintered bodies were found fragile and prone to breakage at temperatures lower than 645-650 °C.

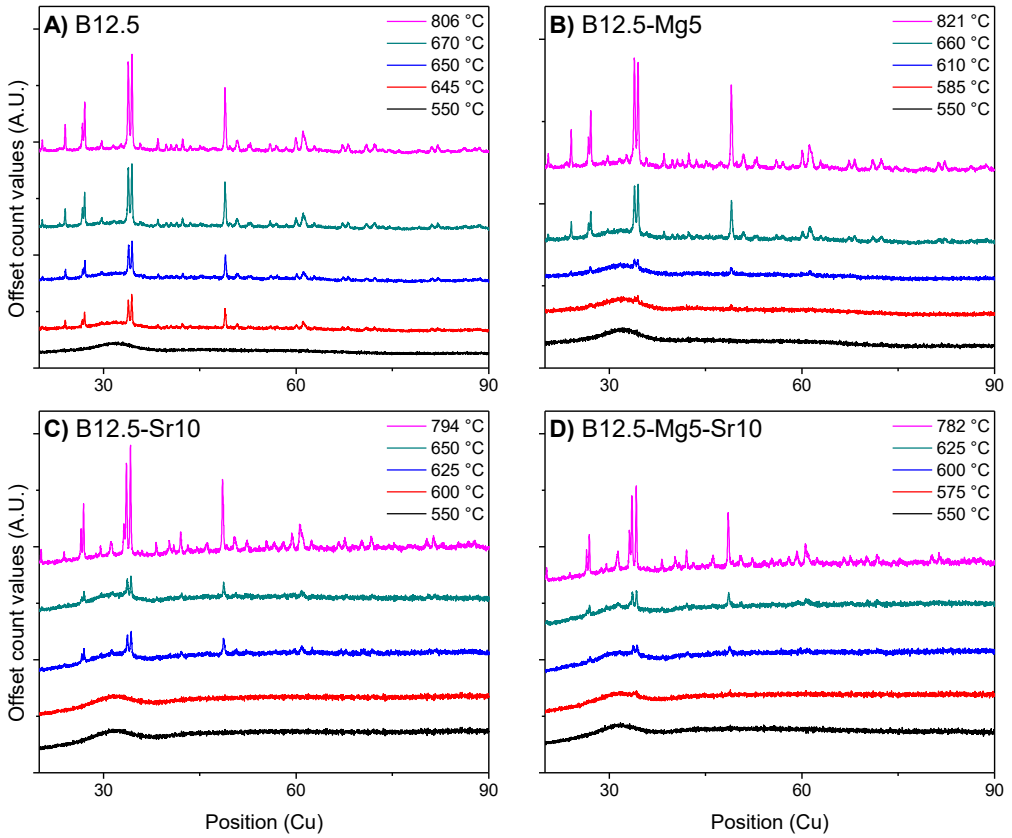

Figure 5. XRD patterns of the glass particles (250-500 µm) after heat treatments at varied temperatures. (**A**) B12.5 (**B**) B12.5-Mg5 (**C**) B12.5-Sr10 (**D**) B12.5-Mg5-Sr10. (Modified from **Study II**)

At 550 °C, XRD analysis revealed that all glasses initially displayed a broad hallow in the 27°-35° range, indicating their amorphous nature. Upon heat treatment, diffraction peaks indicating crystallization emerged, intensifying with increasing temperatures. At the highest temperatures (heated at over compositions respective T_x) all materials are expected to be nearly fully crystallized. From Fig.5A it was seen that for, B12.5 in this study, mechanically stable sintered bodies were not obtained in the temperature range where glasses would have remained amorphous, as it was with other studied compositions. The best fit for the formed crystalline phase corresponded to combeite $Na_{5.27}Ca_3Si_6O_{18}$ (ICDD:01-078-1650), regardless of the glass compositions.

5.2.3 Particles sintering

Cross sections of sintered 250-500 μm particles were imaged by SEM (Figure 4); for B12.5 (A, 650 °C and B, 720 °C), B12.5–Mg5 (C, 610 °Cand D, 660 °C) B12.5–Sr10 (E, 600 °C and F, 675 °C) and B12.5-Mg5-Sr10 (G, 600 °C and H, 650 °C). The initial temperatures mentioned represent the minimum sintering temperature at which the sintered body could be manipulated without experiencing premature, spontaneous, failure.

At this temperature, notable crystallization occurred on the surface of the sintered B12.5 particles (as depicted in Fig. 4A). In contrast, other examined compositions with Mg/Sr additions, exhibited minimal crystal formation along the grain boundaries, appearing as a very thin layer of crystallization, while the glass predominantly retained its amorphous nature (Fig. 4C, E, G). Furthermore, the sintering of Mg/Sr containing glasses could be carried out at temperatures 40-50 °C lower compared to that of B12.5. In general, it was observed that in all the investigated glasses, crystallization initiated from the surface, in agreement with the JMA exponent calculation. With increasing the sintering temperature, more pronounced crystallization was observed.

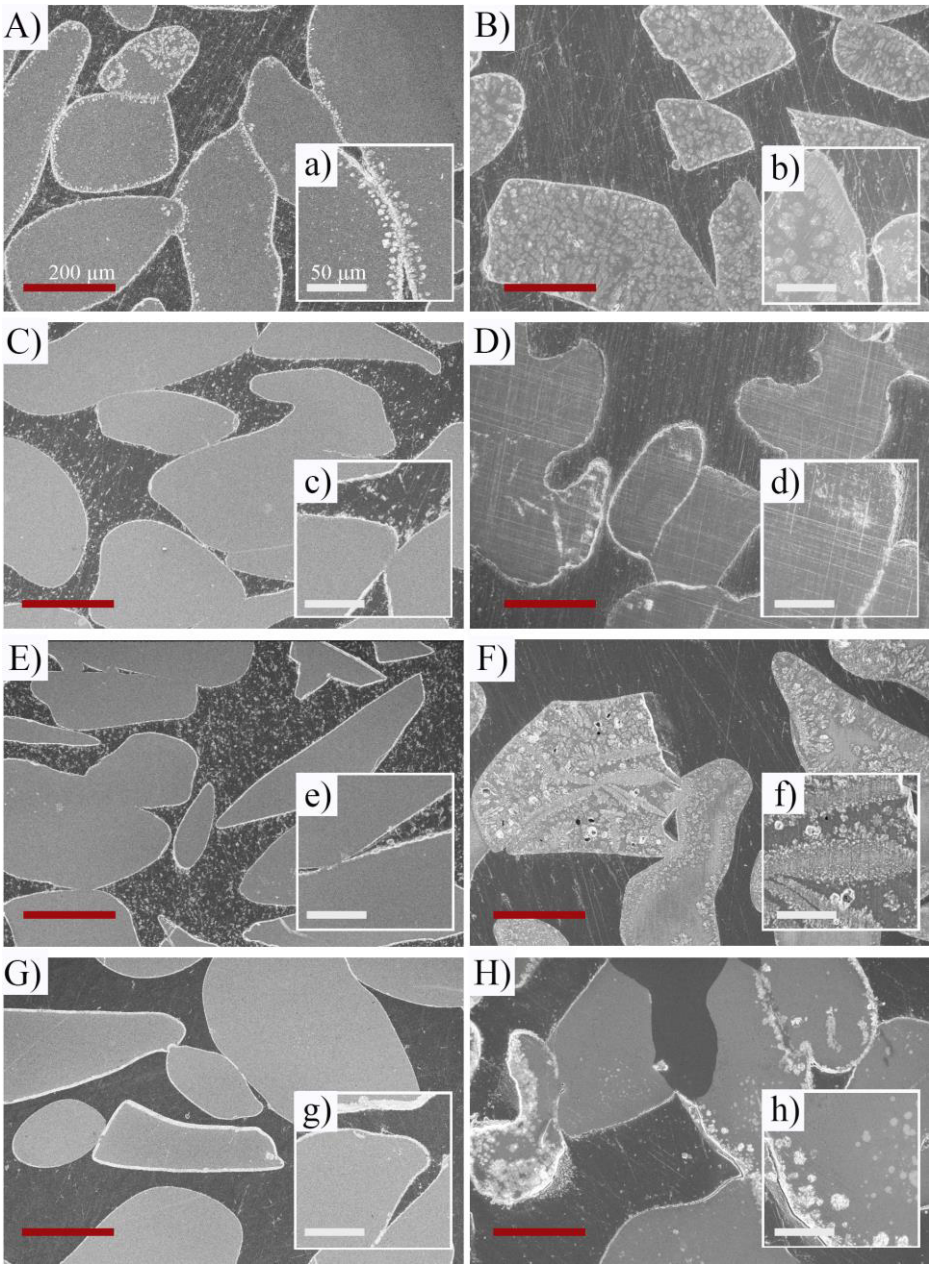

Figure 6. SEM-images of polished cross sections of the sintered specimens – darker epoxy-phase surrounds the glass particles. (**A,B**) B12.5 sintered 1h at 650 °C and 720 °C, respectively. (**C,D**) B12.5-Mg5 sintered 1h at 610 °C and 660 °C, respectively. (**E,F**) B12.5-Sr10 sintered 1h at 600 °C and 674 °C, respectively. (**G,H**) B12.5-Mg5-Sr10 sintered 1h at 600 °C and 650 °C, respectively. Scale bars: red 200 µm (100x magnification), white 50 µm (250x magnification). (Modified from **Study II**)

5.2.4 Scaffold processing – porosity

Initially, the sintering ability of the various glass composition was assessed by pressing glass particles and heat treating the green body (particles with size 250-500 μm) as presented in **Study II**. The sintering temperatures are reported in Table 3. Post sintering, B12.5 porosity varied from 48–54%, and 14-36% for B12.5-Mg5, 46-52%, for B12.5-Sr10 and around 20-49% for B12.5-Mg5-Sr10.

Successively bulk sintered body as well as porous scaffold using the porogen burn off and robocasting were produced from glass B12.5 and B12.5-Mg5-Sr10 (**Study III)**. As expected, sintering smaller particles yielded lower porosity (as seen in Figure 7.). Sintered bulk specimens yielded porosity under 50% and as seen with bigger particles size the porosity of B12.5 specimens were found higher than that of B12.5-Mg5-Sr10. Employing the burn-off and 3D printing methods resulted in a porosity of 50-70%. It was observed (as seen in micro-CT image presented in Figure 8) that scaffolds produced via porogen burn-off had randomly sized and positioned round pores, while those created through 3D printing were composed of parallel filaments with uniform spacing, leading to interconnected porosity. The average pore sizes were measured for the 3D-printed scaffolds with optical microscope, and found to be around 280±70 μm in width and 290±60 μm in length for B12.5, and 192±46 μm in width and 208±57 μm in length for B12.5-Mg5-Sr10, respectively.

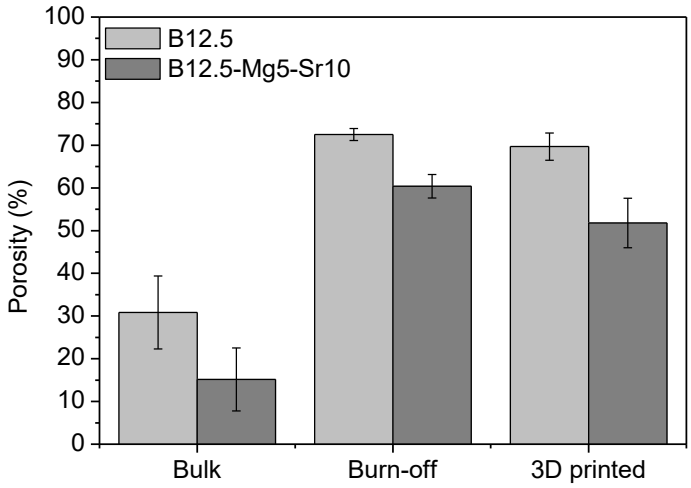

Figure 7. Average porosity of sintered specimens and scaffolds, produced from <38 µm particles sintered 1h at 540-545 °C (Modified from **Study III**)

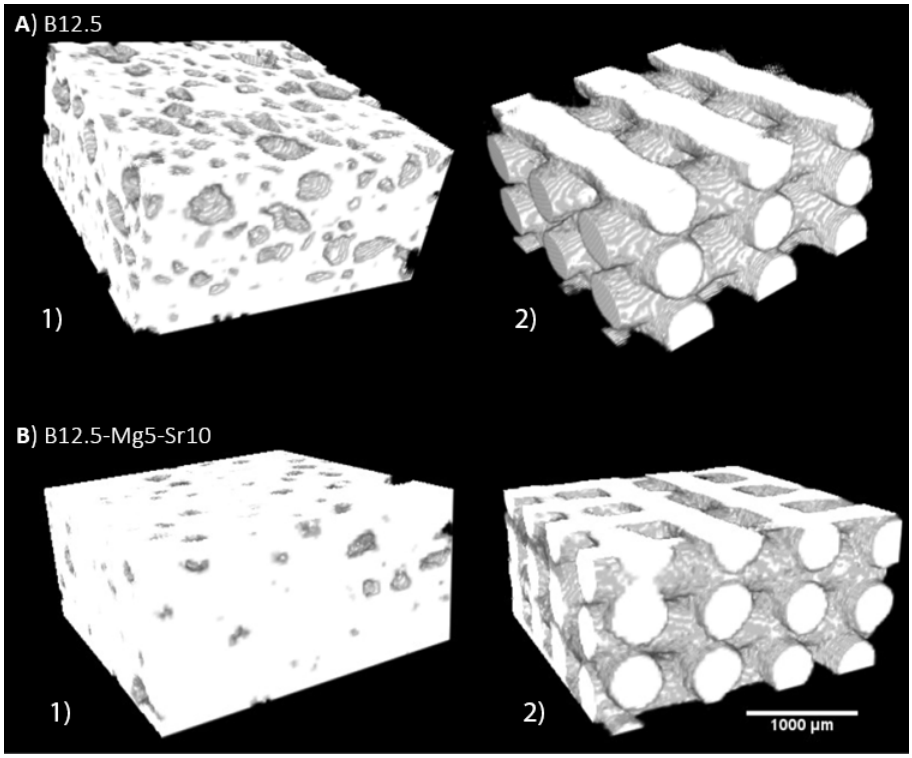

Figure 8. micro-CT imaging of 3D structures of the scaffolds produced via 1) burn-off, 2) 3D printing of (**A**) B12.5, (**B**) B12.5-Mg5-Sr10 compositions. Scale bar 1 mm. (Modified from **Study III**)

5.2.5 Scaffold mechanical properties

The compressive strengths of B12.5 scaffolds, fabricated using the burn-off method and 3D printing, were measured in **Study III** at 1.5±0.2 and 2.5±0.7 MPa, respectively. Notably, B12.5-Mg-Sr composition demonstrated substantially higher strengths, at 8.9±2.4 and 6.1±1.8 MPa for scaffolds produced via burn-off and 3D printing, respectively. Example of the stress-strain curves are presented in Appendix I Supplementary Figure 1.

5.3 *In vitro* reactivity in SBF

Immersion in SBF lasted up to 2 weeks and was performed on various particle sizes (in **Study I**, weight varying from 75 mg to 80.3 mg per 50 ml SBF when surface area was kept constant between the compositions. In **Study II**, mass was kept constant at 75 mg to per 50 ml SBF), polished discs (in **Study I**, 10 mm x 2 mm, weight 330 ± 50 mg per 50 ml SBF), porogen burn-off and 3D printed scaffolds (in **Study III**, around 13.5 mm x 4 mm and 9 mm x 4 mm, respectively; keeping mass/SBF volume ratio constant at 20 mg/ml). The changes in the dissolution solutions pH and ion concentrations, caused by glass degradation, were analysed. Additionally, structural and compositional changes at the glass surface, after immersion, were assessed with FTIR and EDX/SEM. The results presented here are limited to the compositions B12.5 and B12.5-Mg5-Sr10; results for the other compositions are presented in the original publications (**Studies I** and **II)**.

5.3.1 Changes in pH

The initial pH of SBF was set at a physiologically relevant level (pH 7.40 ±0.2). Figure 9. presents the pH measurement results for multiple amorphous glass particles and structures (**Studies I** and **III**), after up to two weeks immersion. With glass particles, it was seen that the final pH increased with decreasing particle size. Additionally, highest pH changes were observed with 3D-printed and porogen scaffolds, respectively. In the pH profiles between compositions, it was clearly seen that the replacement of Ca for Mg and Sr led to a progressive decrease in the pH change.

Figure 10. presents the pH changes for amorphous (particles size 250-500 µm heat treated at 550 °C) and crystallized particles (particles size 250-500 µm heat treated at 806 °C and 782 °C for B12.5 and B12.5-Mg5-Sr10, respectively) (**Study II**), upon immersion for two weeks in SBF. It was seen, that crystallized particles induced higher pH change than their amorphous counterpart.

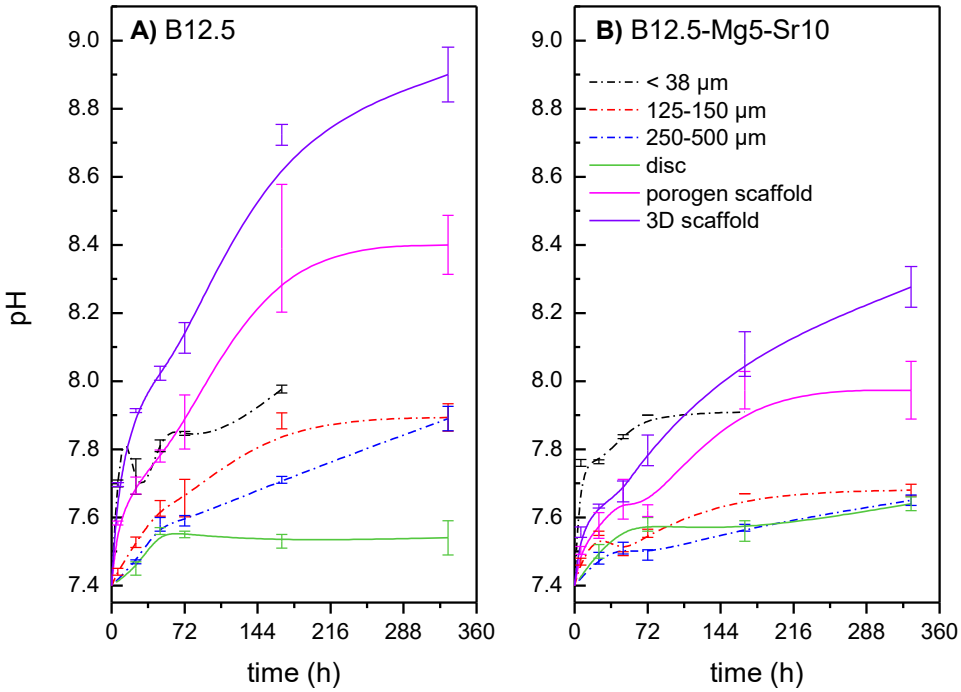

Figure 9. pH of SBF solution after glass particles (<38, 125-250, 250-500 µm, S_A between compositions constant), discs and scaffolds (mass per V_{SBF} kept constant) immersion up to two weeks. **(A)** amorphous B12.5 and **(B)** amorphous B12.5-Mg5-Sr10. (Combined from **Studies I** and **III**)

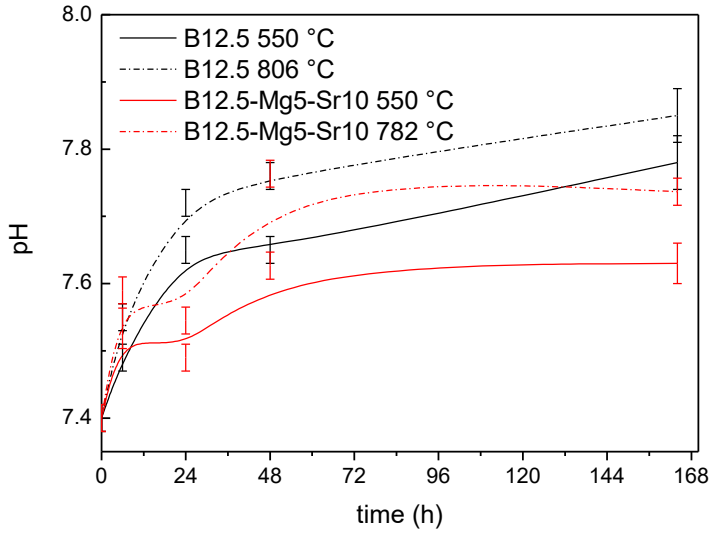

Figure 10. Comparison of the SBF solution pH changes between amorphous (550 °C) and crystallized 250-500 µm (806 °C and 782 °C) B12.5 and B12.5-Mg5-Sr10 particles (mass per V_{SBF} kept constant), respectively. Immersion in SBF lasted up to one week. (Modified from **Study II**)

5.3.2 Ion release

The ion release due to glasses degradation in SBF is presented in Figure 11 (for B and Si), Figure 12 (for Ca and P) and Figure 13 (for Mg and Sr). The results for Na exceed the calibration levels, and were therefore not presented. The ion concentrations of the initial SBF was 93 ppm of Ca, 30 ppm of P, and 35 ppm of Mg. It is worth noting, that elements of B, Si and Sr are not present in the initial SBF composition, and were only present in the solution due to the glass dissolution.

Fig.11 presents the dissolution solutions levels for the glass network formers boron and silicon. It can be seen that, as expected, upon immersion the ion concentration in solution increased, following the same trend as the pH curves in Fig.9. Boron release (Fig. 11A and B) significantly decreased when part of the calcium was replaced with magnesium and strontium in the glass's composition. The effect was not as substantial for silicon release (Fig. 11C and D). It was seen (in Appendix II: Supplementary Figure 2), that upon immersion in SBF, the glass particles released up to 20 wt-% of their theoretical maximum of silica, while boron release was up to 80 wt-% and depended highly on the composition; amount of released B was notably lower in Mg and Sr containing glasses.

Fig.12 present calcium and phosphate concentrations. It was observed that after an initial increase, calcium release (Fig. 12A and B) either started to stabilize, or even decreased. This happened simultaneously, as phosphorus (Fig. 12C and D) levels in the dissolution solution decreased. With apatite-forming materials, this phenomena is typically linked to Ca-P precipitation (83). The phosphorus levels decreased more with B12.5, compared to Mg/Sr substituted glass, and with samples with more reactive surface area (i.e., scaffolds or small particles).

Fig.13 presents the results for magnesium and strontium levels. The glass B12.5 did not contain magnesium in B12.5 composition, however SBF solution does. Decrease in magnesium levels upon immersion of the B12.5 specimens (Fig. 13A) was similarly observed, as with phosphate (Fig. 9C). Neither SBF nor B12.5 contained any Sr, therefore the levels (Fig. 13C) remained at zero. B12.5-Mg5-Sr10 specimens released both magnesium (Fig. 13B) and strontium (Fig. 13D) with gradual, yet stabilizing trend.

Figure 14. presents the comparison between amorphous and crystallized B12.5 and B12.5-Mg5-Sr10 particles of 250-500 μm. Boron release (Fig. 14A) appears faster in the crystallized glasses, whereas silicon release (Fig.14B) appears to be similar in both the crystallized and amorphous samples. The release of the cations of calcium, magnesium and strontium (Fig. 14C, E, F, respectively) express higher concentration in solutions containing the crystallized glasses, with similar trend as the release of boron. Phosphorus levels (Fig. 14D) for B12.5 stabilise for the crystallized samples after 72h, while continuing to decrease for amorphous specimens. For B12.5-Mg5-Sr10 specimens, P levels seem rather stable for the observation period.

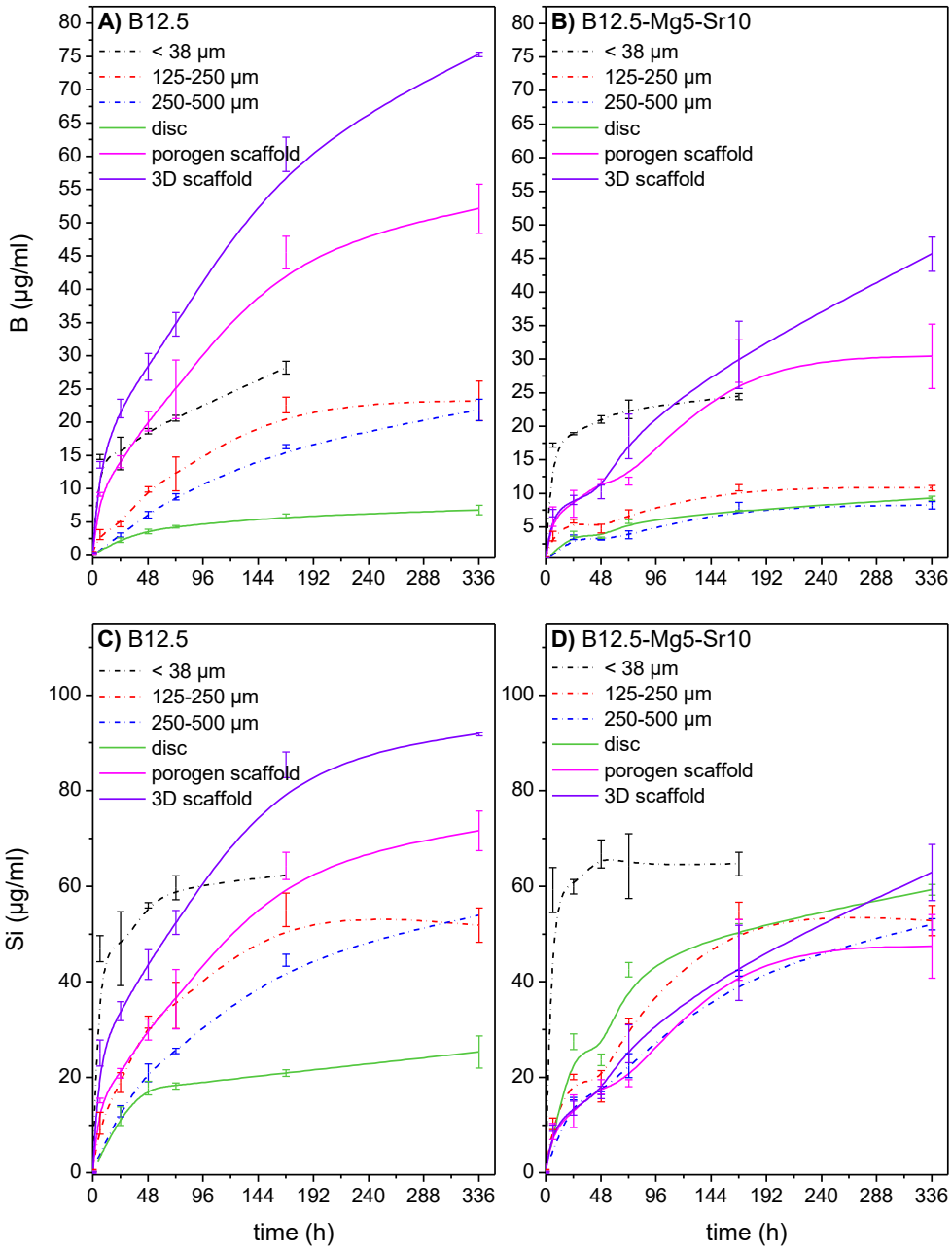

Figure 11. Dissolution of different particle sizes (S_A between compositions constant), discs and sintered constructs (mass per V_{SBF} kept constant) immersed in SBF - ICP (ppm) analysed for the following elements in SBF solution; boron (**A, B**) and silicon (**C, D**) for B12.5 and B12.5-Mg5-Sr10, respectively. (Combined from **Studies I** and **III**).

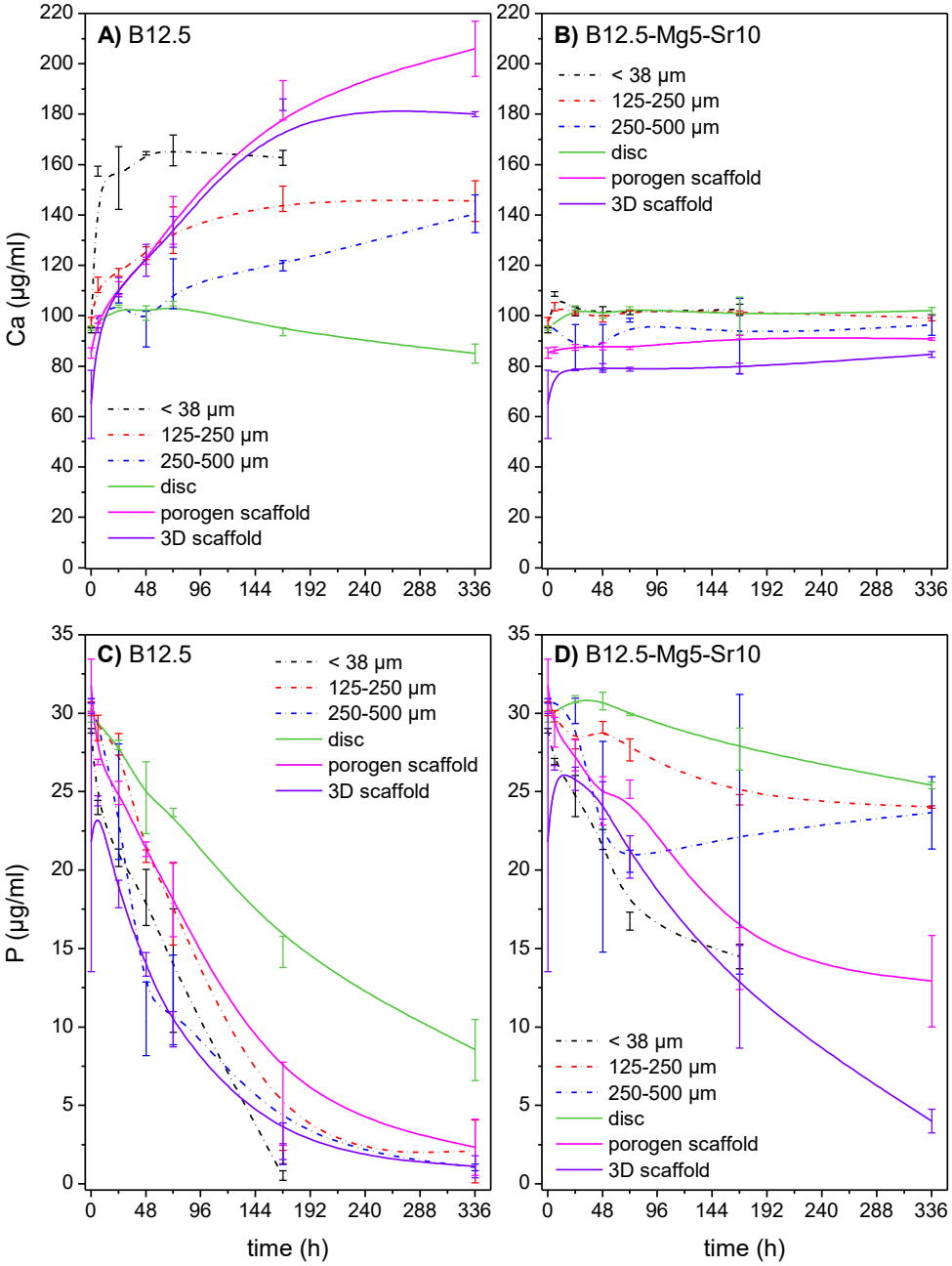

Figure 12. Dissolution of different particle sizes (SA between compositions constant), discs and sintered constructs (mass per VSBF kept constant) immersed in SBF - ICP (ppm) analysed for the following elements in SBF solution; calcium (**A, B**) and phosphate (**C, D**) for B12.5 and B12.5-Mg5-Sr10, respectively. (Combined from **Studies I** and **III**).

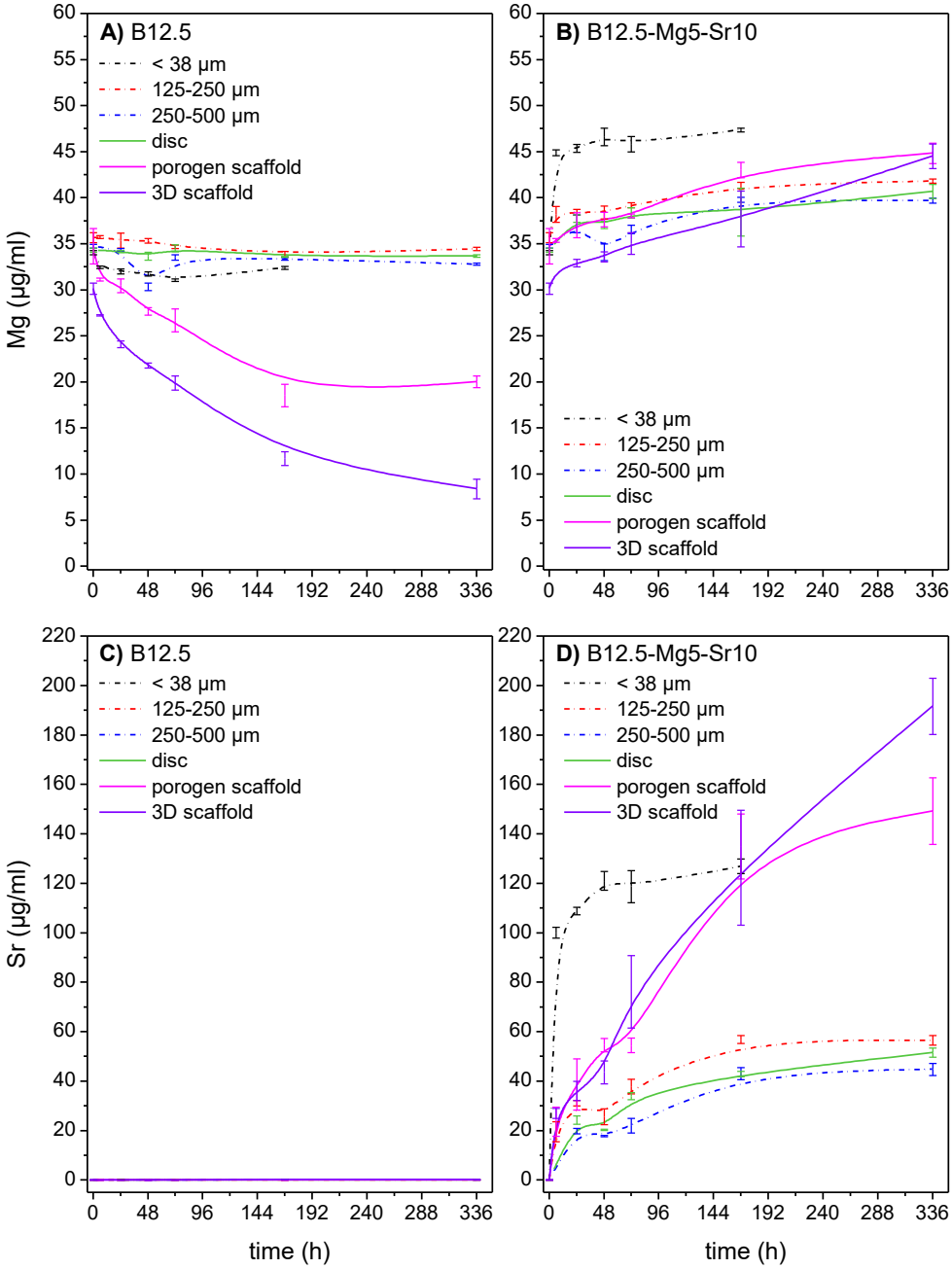

Figure 13. Dissolution of different particle sizes (SA between compositions constant), discs and sintered constructs (mass per VSBF kept constant) immersed in SBF - ICP (ppm) analysed for the following elements in SBF solution; magnesium (**A, B**) and strontium (**C, D**) for B12.5 and B12.5-Mg5-Sr10, respectively. (Combined from **Studies I** and **III**).

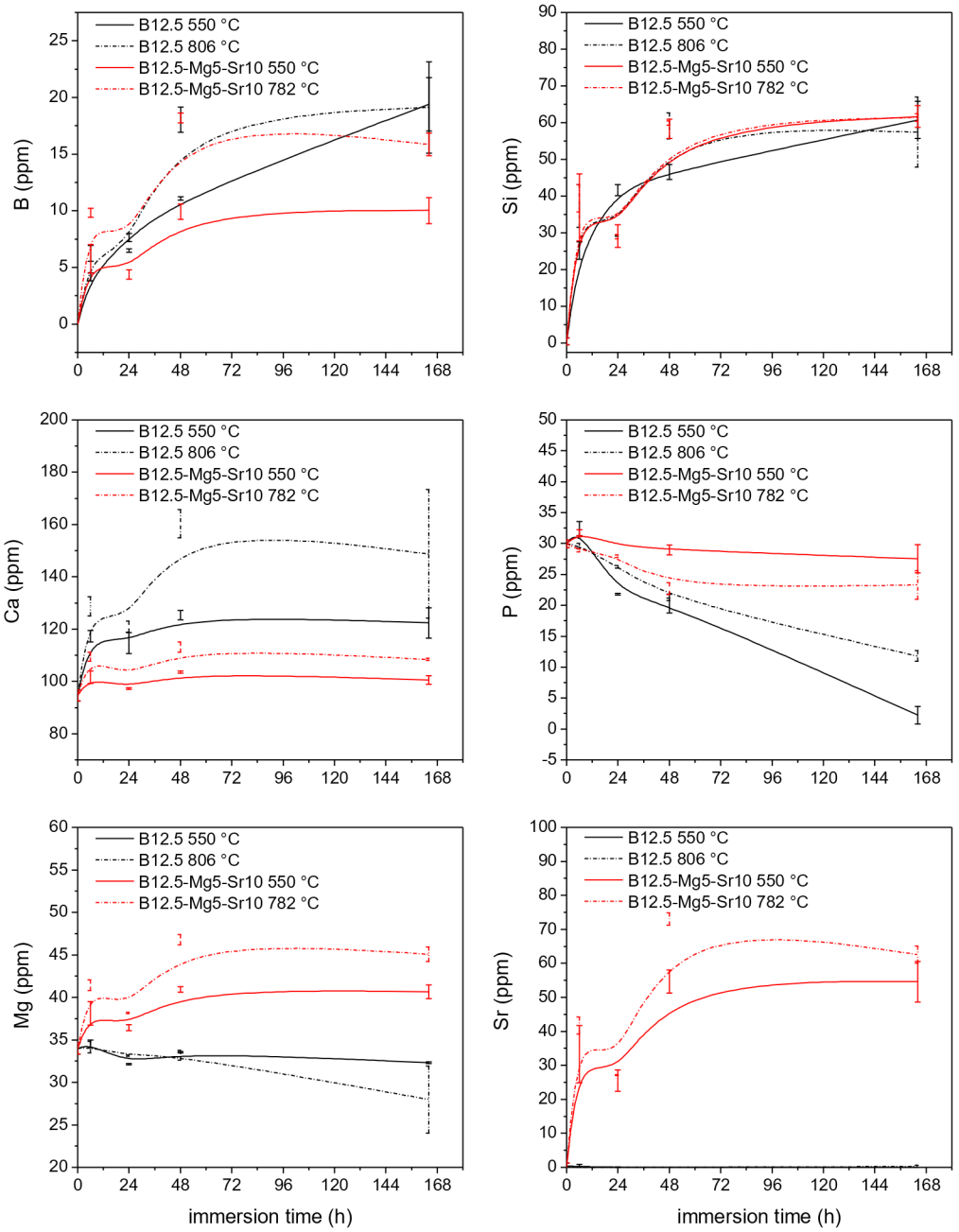

Figure 14. Comparison of released elements from amorphous and crystallized glass particles into SBF. ICP analysis for elements (ppm) of **(A)** boron, **(B)** silicon, **(C)** calcium, **(D)** phosphorus, **(E)** magnesium and **(F)** strontium, over immersion time ranging from 6 hours to 1 week. (Modified from **Study II**)

5.3.3 Structural changes

Changes in glass surface composition as a function of immersion time in SBF were assessed using FTIR (presented in Figure 15) and compared to structure before immersion (Fig.2 in **chapter 5.1.2**). The details of the changes have been summarized in Table 13.

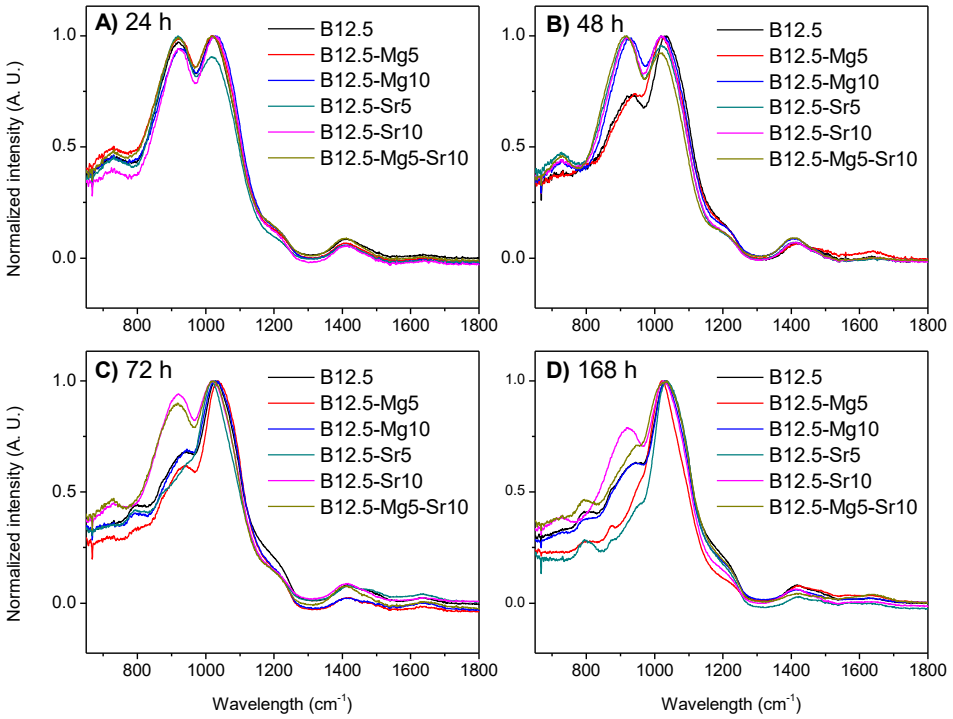

Figure 15. FTIR spectra of the investigated glasses (125-250 µm particles) after (**A**) 24 h, (**B**) 48 h, (**C**) 72 h and (**D**) 168 h immersion in SBF (**Study I**)

In summary, the analysis of the structure, after immersion, indicates the characteristic behaviour of bioactive glasses. First the breakage and partial degradation of the glass network (10,156), followed by the silica-gel formation (~1200 cm^{-1}) (170) and precipitation of a calcium phosphate surface layer containing carbonates (i.e., HCA; bands around 1017 cm^{-1} and 1420 cm^{-1}.) (171). It was additionally noted that Sr and/or Mg in the glass composition led to a decrease in the rate of network changes (for example seen in Fig.15B and C), as well as in the speed of reactive layer formation. Moreover, the introduction of Sr appears to induce a subtle shift in the bands associated with PO_4^{3-} vibrations (1000-1100 cm^{-1} region.) (14,172).

Table 12. Notable changes in FTIR spectra due to immersion in SBF (**Study I**)

Band region	Changes and attribution	Reference
918 cm^{-1}	Bands decreased in intensity – can correspond to Si-O and B-O vibrations; indication of metal cations connected to nbO being released (ion exchange) and a silica gel forming (Si-OH). Additionally, after a long immersion, possibly linked to phosphate vibration.	(10,156)
1017 cm^{-1}	Bands increase in intensity and shift to ~1024 cm^{-1}; along with the band centred at 918 cm^{-1}, this has been seen to be related to phosphate vibration.	(14,172)
~1200 cm^{-1}	A shoulder increased in intensity – can be related to the presence of SiO_4 as Q4 units (in the silica gel)	(170)
1420 cm^{-1}	Post immersion, appearance of double band at around the region 1300-1500 cm^{-1} is attributable to CO-vibrations.	(173)
1640 cm^{-1}	Appearance of a new band – along with the broad band in the 2600-3600 cm-1 range (not presented) is an indications of absorbed water in the structure and at the glass surface.	(170)

Figure 16. presents the FTIR spectra for crystallized specimens, immersed in SBF for up to one week. The results are discussed in comparison to the results obtained on amorphous particles (Figure 15 and Table 12), the changes in the FTIR spectra are presented in Table 14.

A noticeable distinction between the amorphous and crystallized samples was evident in the range of 700-730 cm^{-1}. In the case of the crystalline specimens, a double band was observed, while their amorphous counterparts initially displayed only a single band. This region has been associated with the borate network or could be attributed to Si-O-Si bending. (174). Additionally, for borosilicate glasses, 850–1200 cm^{-1} region has been linked with B-O of BO_4 (12,157) and Si–O–NBO stretching vibrations (115). The decrease in intensity of this band is likely due to the release of soluble silicate, or to the degradation of the borate phase.

Another distinct difference between the specimens can be observed in the formation of peaks around 1420 cm^{-1}. In this spectral region, the glasses exhibit a peak associated with [BO_3] triangles (12,157) before immersion. However, upon closer examination during immersion, it becomes apparent that in the region of 1300-1500 cm^{-1}, amorphous B12.5 and B12.5-Mg5 samples start to exhibit a doublet, which can be attributed to CO_3^{2-} groups (115,171).

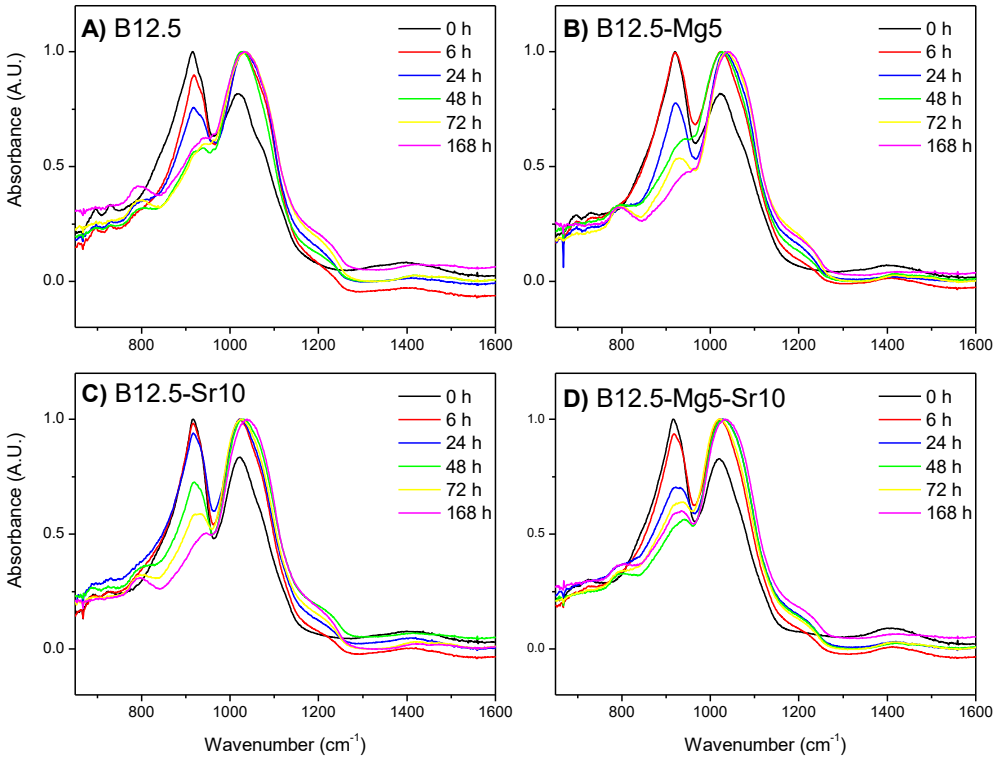

Figure 16. Background corrected and normalized FTIR spectra up to 1600 cm^{-1} for crystallized glass particles, up to one week SBF immersion; (**A**) B12.5 (**B**) B12.5-Mg5 (**C**) B12.5-Sr10 (**D**) B12.5-Mg5-Sr10. (**Study II**)

Table 13. Notable changes in FTIR spectra after immersion – comparison of crystallized specimens to their amorphous counterparts (**Study II**)

Band region	Changes and attribution	Reference
700 – 730 cm^{-1}	Double bands for crystallized specimens, when amorphous glasses exhibited only one band. After immersion, bands disappeared. Linked to either B-O-B linkages of the borate network in borosilicate and borate glasses, or could be attributed to Si-O-Si bending, or vibrations of various Q^n silicate units containing NBOs	(13,174)
800 cm^{-1}	After longer immersion, formation of a new band –bands falling within the 800–1300 cm^{-1} range have been assigned to the asymmetric vibrations of SiO_4 tetrahedra. The specific wavenumber of the peak depends on the quantity of NBO's constituting the tetrahedron.	(174)
918 cm^{-1}	Bands were sharper, and decreased faster for crystallized specimens, than for amorphous glasses –region has been linked with B-O stretching vibration of BO_4, also associated to Si–O(s) with non-bridging oxygen (Si–O–NBO) stretching vibrations.	(12,115,157)
1017 cm^{-1}	Similarly as for amorphous glasses, bands increase in intensity and shifted to ~1024 cm^{-1}; phosphate vibration.	(14,172)
~1200 cm^{-1}	A shoulder increased in intensity – can be related to the presence of SiO_4 as Q4 units (in the silica gel)	(170)
1420 cm^{-1}	Crystallized specimens did not exhibit notable bands, attributable to CO-vibrations.	(173)

5.3.4 Precipitation of a surface layer

SEM images of the cross-sections of the immersed glass particles are presented in Figure 17. Three distinguished layers were observed, and their compositions were determined with EDX. The composition of the particles' cores corresponded to the expected nominal glass composition, followed by a silica-rich layer. The outermost layer was composed primarily of calcium and phosphorus.

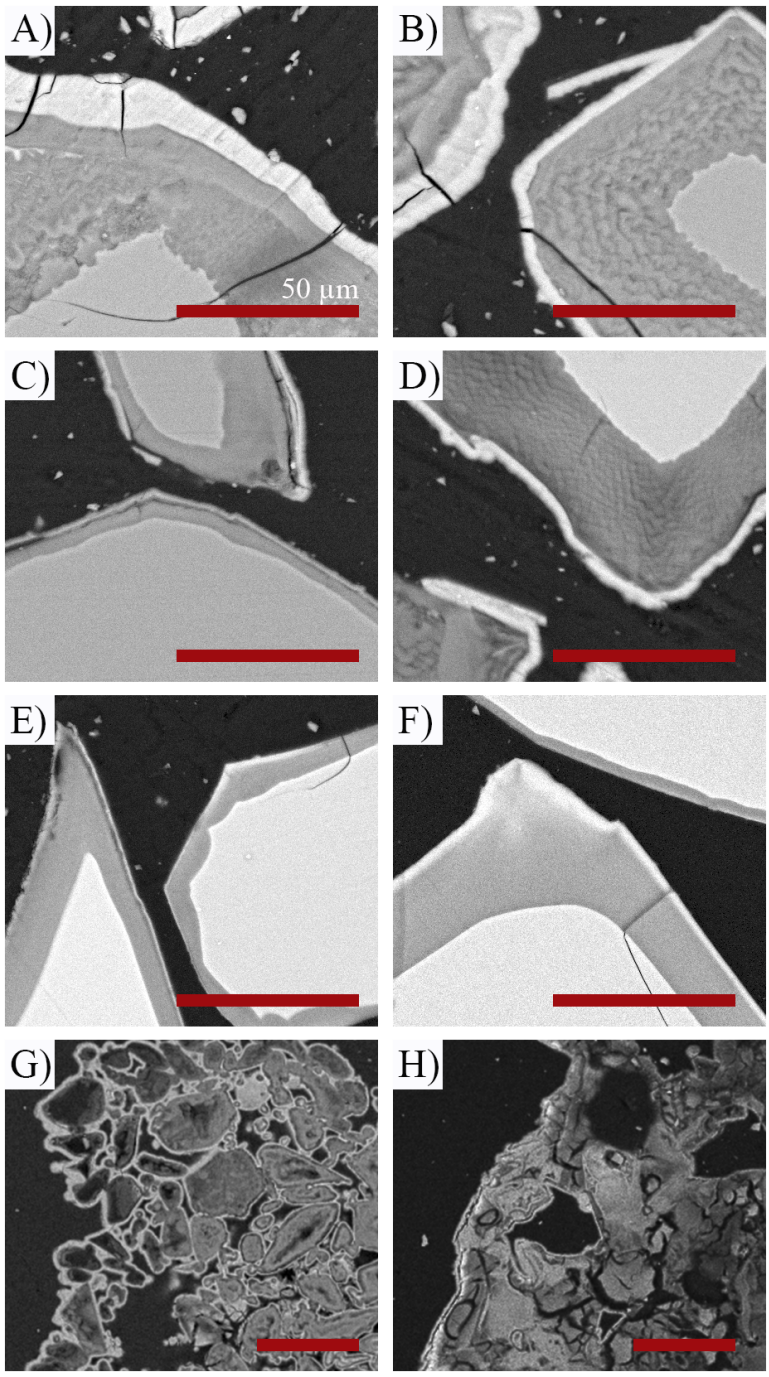

Figure 17. SEM images of specimens after SBF immersion; (**A**) B12.5, (**B**) B12.5-Mg5, (**C**) B12.5-Mg10, (**D**) B12.5-Sr5, (**E**) B12.5-Sr10, (**F**) B12.5-Mg5-Sr10 glass particles (125-250 µm) after 1 week (Modified from **Study I**) and (**G**) B12.5 and (**H**) B12.5-Mg5-Sr10 burn off scaffolds (sintered from < 38 µm particles) (Modified from **Study III**) after 2 weeks. Scale bar 50 µm for all images.

On the outermost layer EDX analysis revealed that for B12.5 glass particles, the Ca/P ratio was ~1.6, agreeing with the formation of a hydroxyapatite-like phase at the surface of the bioactive glass particles (175). The glasses containing Mg and/or Sr) showed similar compositions of the surface layer, the ratio (Ca+Mg+Sr)/P was maintained at ~1.6, indicating Mg/Sr incorporation in the HA-layer (14). The thickness of the Ca-P layer (Fig. 17A-F) was observed to decrease with increasing substitution, which can be related to the observed slower degradation rate of the glasses, resulting in a delay in HCA precipitation (13,14).

Similarly, with scaffolds (**Study III**; Fig.17G, H) a bright layer appeared at the surface of the grains exposed to the SBF solution. The layer was found to be rich in calcium and phosphorus and assigned to the precipitation of a reactive layer (83). At the surface of the B12.5 scaffold the Ca/P ratio was ~1.76, and for the B12.5-Mg-Sr, the reactive layer on exhibited a (Ca+Mg+Sr)/P ratio of ~1.35-1.4 Additionally, precipitated layers on B12.5-Mg-Sr scaffolds were found significantly thinner than on B12.5 scaffolds.

5.4 Cell/material interactions

5.4.1 Cytotoxicity

5.4.1.1 Viability

Cell viability was investigated via live/dead staining, and results after 7 culturing days are presented in Figure 18. hADSCs, in **Study IV,** were highly viable in presence of all glass's degradation products (Fig. 18A), as well as in direct cell/material contact (on top of glass discs; Fig.18B). Additionally, with hADSCs in contact with 3D structures from **Study III** (Fig.18C), the density of viable cell on the scaffolds increased during the observation period, while the cells in indirect contact (e.g., at the bottom of the culturing well; smaller images in Fig.18C) formed highly confluent cultures It is noteworthy, that the structures themselves gave autofluorescence on the wavelength, where necrotic cells were imaged; the red seen in Fig.18C indicates mainly this autofluorescence.

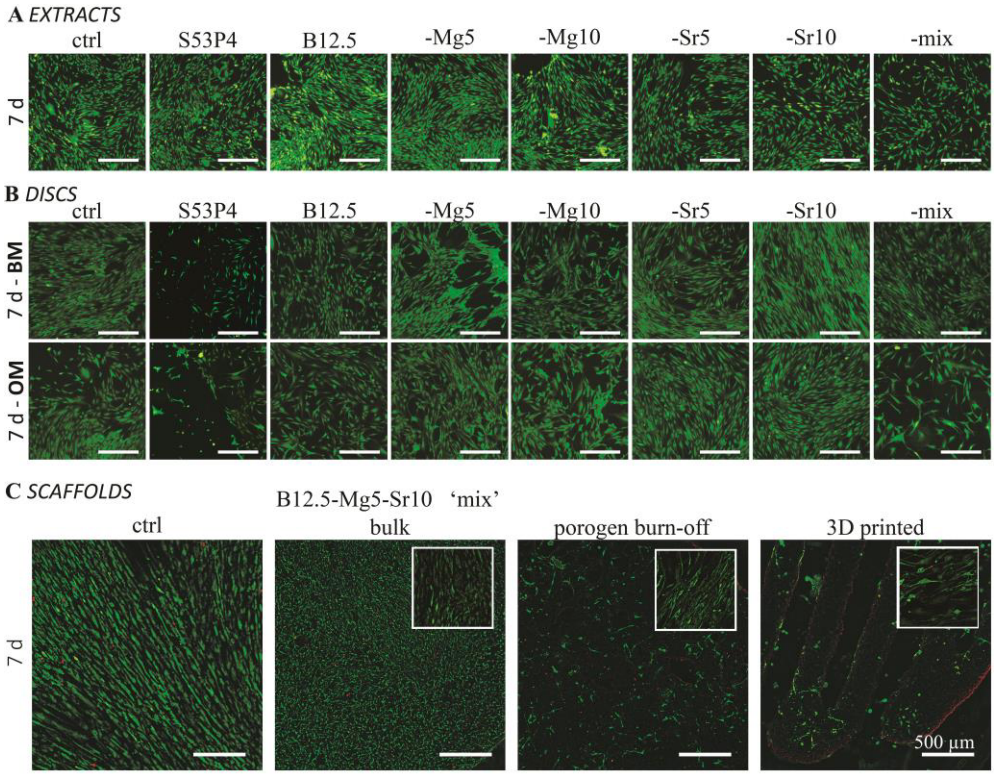

Figure 18. hADSC viability determined via live-dead staining on culturing day 7 (**A**) in extracts (with OM supplements) (**B**) on top of discs; both BM (upper row) and OM (lower row) medias and (**C**) on top of sintered 3D structures (smaller image from well bottom). Calcein-AM staining (viable cells) presented as green, EthD-1 (necrotic cells) as red. Additionally, autofluorescence from the scaffolds was observed on wavelength presented as red. Scale bar 500 µm for all images. (Modified from **Studies III** and **IV**.)

5.4.1.2 Proliferation

In all conditions in **Study IV**, cell proliferation increased over the course of the observation period (as seen from Figure 19). After one week of culturing, no statistically significant differences were observed among the conditions. However, after two weeks, cultures exposed to B12.5 extract showed lower proliferation, while those with B12.5-Sr5 extract exhibited higher proliferation compared to the control. By the end of the third week of culturing, there were no statistically significant differences in proliferation between the control, B12.5, and B12.5-Mg5-Sr10 conditions while other bioactive glass exposed cultures exhibited significantly higher proliferation.

When comparing borosilicate extracts to silicate extract, proliferation on S53P4 was notably higher on days 14 and 21 of culturing compared to pure borosilicate B12.5. In magnesium-doped cultures (B12.5-Mg5, B12.5-Mg10, and B12.5-Mg5-Sr10, referred as "mix"), proliferation levels reached a similar level as S53P4 extract after 21 days of culturing. In cultures where calcium was substituted solely by strontium (B12.5-Sr5 and B12.5-Sr10) proliferation was not significantly different from S53P4 cultures for up to two weeks. However, at 21 days, these cultures exhibited the highest levels of proliferation.

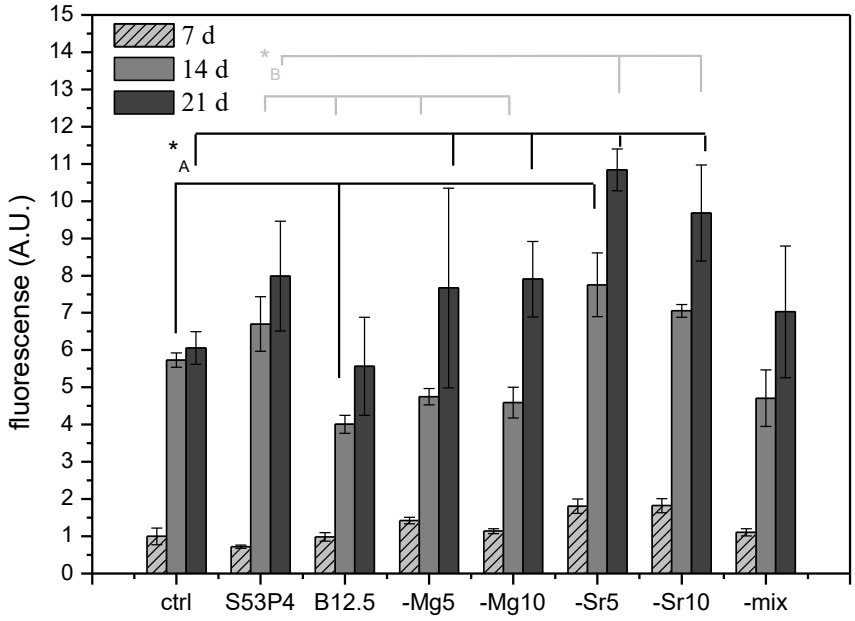

Figure 19. The proliferation of hADSCs measured with CyQuant cell proliferation assay, on control condition and exposed to glass extracts, after 7, 14 and 21 days of culturing. The proliferation was analysed with two-way ANOVA; statistically significant difference ($p < 0.0021$) was observed when studied glasses compared to control condition (marked with $*_A$), and with borosilicate's when compared with S53P4 extract (marked with $*_B$). **(**Modified from **Study IV**)

5.4.2 Maturation of the extracellular matrix

5.4.2.1 Collagen-I formation

Collagen-I expression could be observed in ion extract cultures (Figure 20), with all conditions in intracellular space after 14 days of culturing, and after 21 days, extensive extracellular matrixes could be detected. Similarly, in contact with bioactive glass discs (Figure 21), hADCs, after 14 days of culturing, the BM cultures expressed intracellular Col-I formation, while on OM cultures the collagen-I was already secreted into the extracellular space.

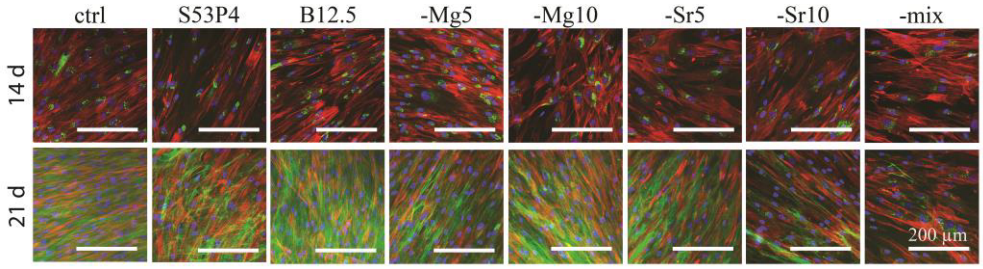

Figure 20. Immunocytochemical staining for observation of collagen-I network formation in ion extract cultures after 14 and 21 days of culturing. Staining's presented for col-I (green), actin network (red) and cell nuclei (blue). Scale bar 200 µm for all images. (Modified from **Study IV**)

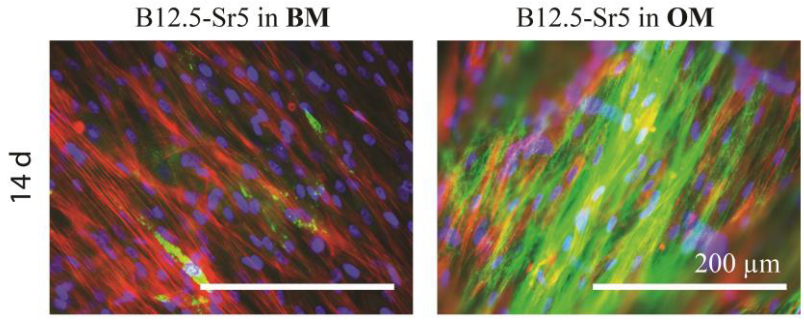

Figure 21. Immunocytochemical staining for observation of collagen-I network formation om disc cultures - examples from B12.5-Sr5 glass cultures in BM (left) and OM (right) media after 14 days of culturing. Staining's presented for col-I (green), actin network (red) and cell nuclei (blue). Scale bar 200 µm for both images. (Modified from **Study IV**)

5.4.2.2 Mineralization

Alizarin red staining was conducted to visualize the mineral formation in the cultures (presented in Figure 22). Following imaging, the stain was extracted and and quantitively analysed (presented in Figure 23). Cultures exposed to a medium containing strontium began to clearly exhibit mineralization after 14 days of culturing. By the end of 21 days, mineralization was also observed in other borosilicate cultures.

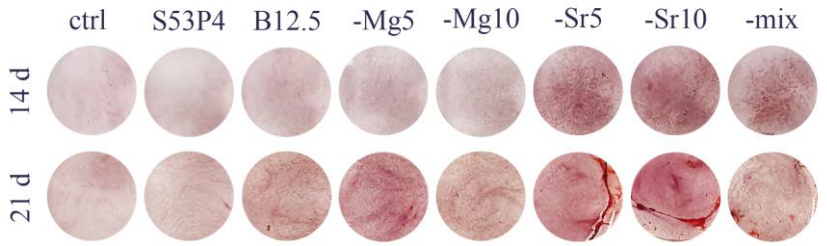

Figure 22. Images of Alizarin red stained ion extract cultures after 14 and 21 days of culturing - reddish stain binding on calcium deposits in the cultures. (Modified from **Study IV**)

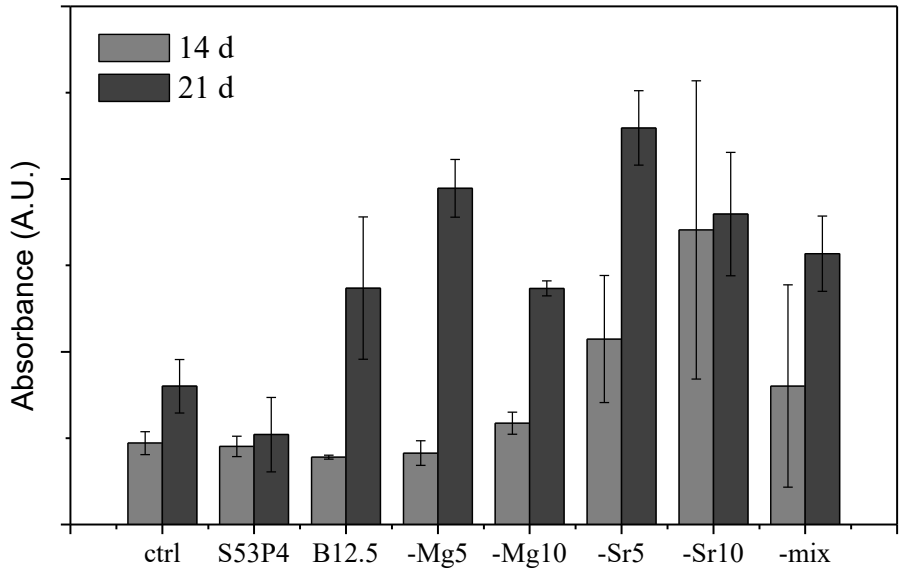

Figure 23. Quantified results from Alizarin red stained ion extract cell cultures (Modified from **Study IV**)

5.4.3 Gene expression

5.4.3.1 Osteogenic markers

The relative expression of few key osteogenic markers (*RUNX2a, OSTERIX*, *DLX5* and *OSTEOPONTIN*) were analysed to evaluate the later stage of osteogenic commitment. The results are presented on an arbitrary scale that has been normalized to the control levels at the initial time point (Figure 24).

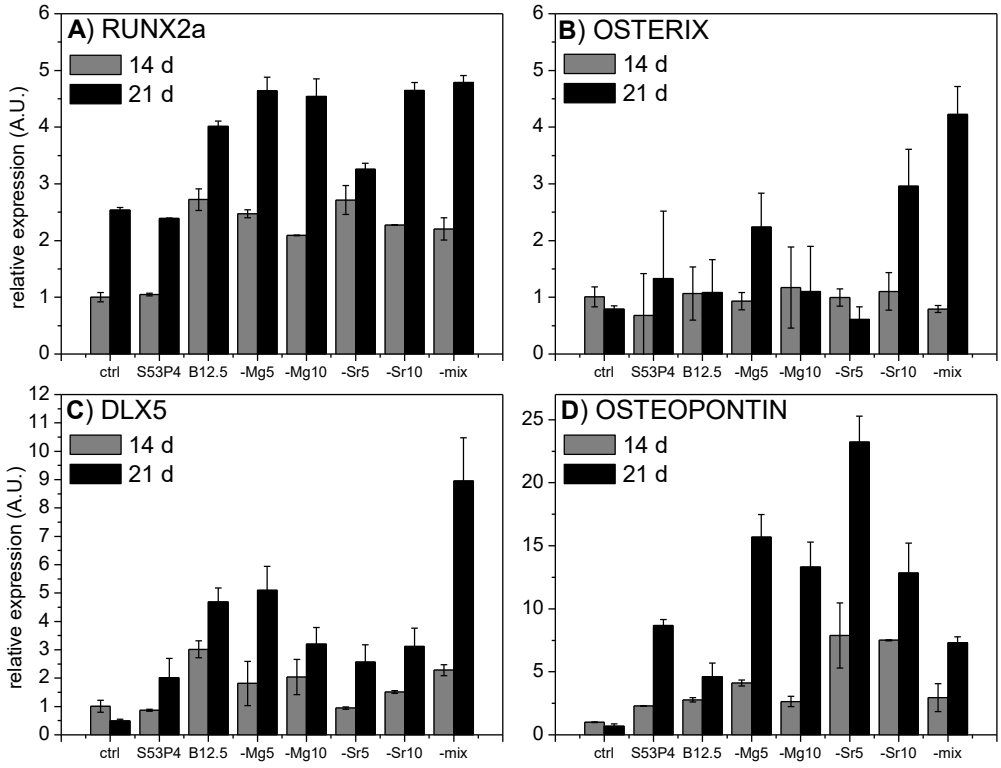

Figure 24. Adjusted relative expression of (**A**) RUNX2a, (**B**) DLX5, (**C**) OSTERIX, and (D) OSTEOPONTIN for glass ion extract studies up to 21 culturing days, determined with qRT-PCR. (Modified from **Study IV**)

RUNX2a expression (Fig.24A) was upregulated for the whole borosilicate series after both 14 and 21 culturing days, when compared to control and S53P4 exposed cultures. All studied bioactive glasses enhanced higher expression of homeobox

protein *DLX5* (Fig.24B) than on control conditions after 21 culturing days. At the 14 days' time point, the expression of *OSTERIX* (Fig.24C) was on similar level with all conditions. After 21 days of culturing, variations between the cultures were observed; upregulation was observed for B12.5-Mg5, B12.5-Sr10 and B12.5-Mg5-Sr10 cultures. All bioactive glasses demonstrated a notable higher *OSTEOPONTIN* (Fig.24D) expression than on control conditions on both studied time points. After 21 days of culturing, expression was slightly downregulated on control condition.

5.4.3.2 Endothelial markers

The degradation products' effect on expression of endothelial marker genes *vWF* and *PECAM-1* is presented in Figure 25. With control, S53P4 and B12.5 cultures, the *vWF* expression (Fig. 25A) decreased between 14 and 21 days of culturing, while expression increased in the Mg/Sr substituted glass extract cultures. Additionally, while expression of *PECAM-1* (Fig.25B) was upregulated by S53P4 and B12.5 cultures after 21 culturing days, the Mg/Sr substituted compositions had a notably higher upregulating effect on the *PECAM-1* expression, increasing with increasing Mg/Sr for Ca substitution in the glass and extract composition.

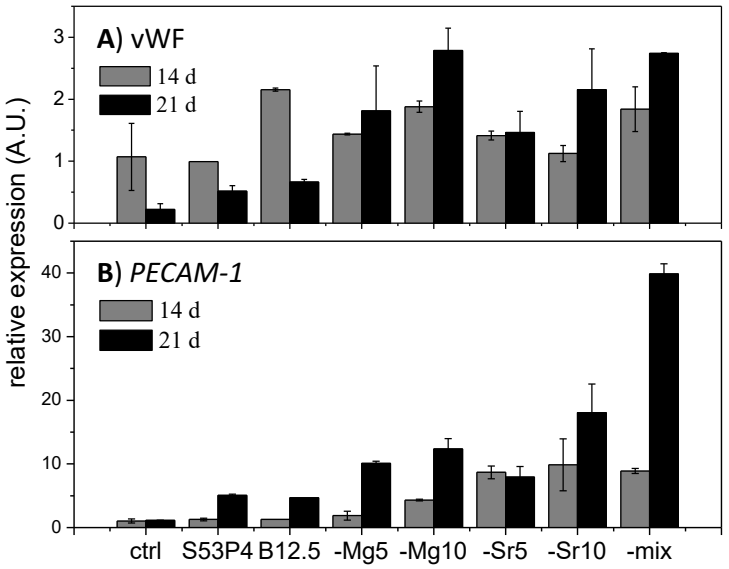

Figure 25. Endothelial marker qRT-PCR results; (**A**) vWF and (**B**) PECAM-1 expression after 14 and 21 culturing days. (**Study IV**)

6 DISCUSSION

6.1 Glass properties

The newly developed, melt-derived B12.5 borosilicate glass series were characterized by their physical, structural and thermal properties in **Study I**. It was observed that the properties of the borosilicate glass were indeed modified by the introduction of Mg and/or Sr in place of Ca.

Density and molar volume give an indication of the compactness of the glass network. When comparing the studied glasses with each other, it was seen that partial substitution of Mg for Ca led to a slight decrease, while substitution by Sr led to an increase in density (presented in Table 6). These changes in compositions in the densities were assigned to the lower atomic mass of Mg, and to the larger atomic mass of Sr, when compared to Ca, respectively. However, no significant change in the molar volume were observed within the accuracy of the measurement, indicating that the glass network did not appear to either expand or contract upon substitution. (14).

Structural properties were analysed with FTIR, Raman and MAS NMR spectroscopy. FTIR and Raman analysis (Figure 2) featured characteristic of borosilicate glasses (as described in Table 7 and 8). While FTIR analysis did not reveal significant difference between the studied glass compositions, in the case of borosilicate, the overlapping of the BO_3, BO_4, bridging and non-bridging oxygen atoms in the silicate network makes it challenging to effectively draw conclusion on the glass structure. Raman spectroscopy, however, allows clarification of the impact of modifiers on the borate and silicate structure. When Raman spectra were recorded from different parts of a polished specimens (as presented in **Study I** Figure 2 – Normalized Raman spectra), it was seen that while all spectra tend to overlap in the case of glass B12.5, this was not necessarily the case for the other glass compositions, which makes comparisons between glass compositions challenging. It seemed that replacing Ca with either Mg or Sr might lead to structural inhomogeneity within the melt-derived glass. While the boron network did not seem to be greatly affected,

significant variations were recorded in the Q_2/Q_3 ratio for SiO_2, indicating changes in the ratio between bridging and non-bridging oxygen atoms in the silicate structure. (159,160,162,161). In previous studies, it has been observed that the B-O-Si bond in Na_2O-B_2O_3-SiO_2 glasses can be easily broken, making these glasses indeed prone to significant phase separation. (10,176). MAS NMR (presented in Figure 3) revealed more detailed information about the connectivity of phosphorus and boron within the glass network. The ^{11}B analysis indicated that substitution of MgO and/or SrO for CaO results in changes in the BO_3/BO_4 ratio, in the borate network; often the increase in the BO_3 at expense of BO_4 could be expected to increase the glasses reactivity. However, quite the opposite was observed Mg/Sr substituted glasses; therefore it is likely that the modification changes the network in more complex degrees. (177). This is potentially assigned to a change in the number of Si-O-. In previous studies, it has been observed that the B-O-Si bond in Na2O-B2O3-SiO2 glasses are hydrolically less resistant than Si-O-Si. (10,176). However, Si-O-B are more stable than B-O-B bonds. The absence of any changes in ^{31}P chemical shift in the first three compositions (B12.5, B12.5-Mg10 and B12.5-Sr10), with substitution of Mg or Sr for Ca, might suggest that P_2O_5 reacts preferentially with CaO and Na_2O instead of MgO or SrO. (178,179). The slight change in the mixed Mg/Sr glasses ^{31}P chemical shift indicated a de-shielding effect in the glass network. (166).

The glass transition temperature of the B12.5 was found to be around 530 °C, decreasing to ~513 °C with 5% Mg/Sr substitution and to around ~500 °C with 10% Mg/Sr substitution regardless of the particle size studied (Table 10). The onset and peak of crystallization depended on the analysed particle size; smaller particles undergo crystallization at lower temperatures compared to larger particles due to a higher surface energy. Therefore, smaller particles are more prone to crystallization during sintering. (117). When studying the substitutions effects on the thermal properties, it was seen that both increasing Mg and Sr for Ca led to a decrease in T_g, agreeing with previous studied on Mg and Sr substituted bioactive glasses (13,14). While Mg addition resulted in an increase in T_p and ΔT. No clear trend for substitution of Sr for Ca on T_x, T_p or ΔT could be observed. The DTA curve for glass composition B12.5-Mg5-Sr10, containing both Mg and Sr, exhibited two T_g's, indicating phase separation, in agreement with inhomogeneity observed with Raman spectroscopy. ΔT over 100 °C is promising toward glass sintering without risk of uncontrolled crystallization. (180)

6.2 Crystallization and processability

It is well known that glass crystallization can negatively affect not only the bioactivity (8), but also inhibit proper particles sintering (7). Crystallization of the B12.5 series was studied in more detail in **Study II**. Activation energies of glass transition were determined with the Kissinger method, and activation energies for crystallization peak were determined with additionally with Friedman method (Eq. 3&4, respectively; results presented in Table 11.) Augis-Bennett method (Eq. 5) was utilized for studying the dimensionality of the primary crystallization with the JMA exponent. Additionally, the processability of the investigated glasses was analysed by heat-treatments at various temperatures to evaluate the potential of sintering of glass particles without adverse crystallization. Moreover, the crystallization mechanism and type of formed primary crystal phase were studied. Lastly, in **Study III,** 3D sintered structures were prepared, and evaluated for their potential for bone tissue engineering applications.

Activation energy values are a measure of the energy, that must be overcome for a particular process to occur. B12.5 borosilicate glass was observed to exhibit lower activation energy for viscous flow (E_a ~ 480 kJ/mol), i.e., higher tendency to sinter, when compared to S53P4 (E_a around 800 kJ/mol) (118). This demonstrates that boron significantly enhanced the sintering ability, as also observed in other studies (9,181). While the Kissinger equation remains appropriate in the case of homogeneous reactions and follows the first order kinetics, the Friedman method makes no mathematical assumption and can be applied to heterogeneous reactions, enabling to evidence changes in crystallization mechanism across the entire crystallization domain (182). While additionally the determined E_c values were similar for the studied specimens in the accuracy of measurement, a slight decrease of E_c can be seen with increasing particle size. This may indicate that the number of nucleation sites at the material surface decreases with the surface area, giving slightly decreasing crystallization tendency; possibly indicating bulk crystallization. (183) Moreover, slight variations in $E_{c,kis}$ and $E_{c,fri}$ values of B12.5-Sr10 and B12.5-Mg5-Sr10 could indicate more complex crystallization mechanism within the glass, such as an overlapping or competitions between different crystallization mechanisms (183). All JMA exponent n values for each glass compositions, however, with both fine and coarse particles, were found to be close to 1 (ranging from 0.6 to 1.3), suggesting surface crystallization mechanism (118). Therefore, as the theoretical analysis indicated complex crystallization mechanism, to assess the mechanism in

more detail, larger particles (250-500 μm) were studied (**Study II**), as finer particles are generally more prone to surface crystallization. (184).

XRD (Figure 5) were performed to observe signs of crystallization occurring at different sintering temperatures. Upon heat treatment, partial crystallization emerged, intensifying with higher temperatures. In this study (II), mechanically stable sintered bodies of B12.5 (Fig.5A) were not obtained in the temperature range where glasses would have remained amorphous. However, additions of Mg and Sr (Fig.5B, C& D) improved the thermal properties, allowing sintering without adverse crystallization. Moreover, it seemed that one new peak in the B12.5-Sr10 and B12.5-Mg5-Sr10 emerged in the data, suggesting the presence of another phase. The best fit for the formed crystalline phase on all of the investigated glasses corresponded to combeite $Na_{5.27}Ca_3Si_6O_{18}$ (ICDD:01-078-1650.) This phase is similar, yet slightly Na deficient, to one observed upon crystallization of traditional silicate bioactive glasses, 45S5 and S53P4, Na_2O-CaO-$2SiO_2$ (PDF 01-077-2189), i.e., sodium calcium silicate (8). Additionally, Na_2O-CaO-$2SiO_2$ crystals have been evidenced when sintering fine particles of B12.5 glasses, additionally attributed to one of the main crystal phases in similar glass composition, i.e. B25 (12,185). Nevertheless, the literature is far from consensus in identifying a primary crystal phase in silicate bioactive glasses (186) and indeed, additionally combeites ($Na_2Ca_2Si_3O_9$) as a primary crystalline phase have been observed e.g. with 45S5 (9,116). EDS analysis, performed on the thin crystallized layers shown in SEM (Figure 6), was in agreement with the crystal composition observed by XRD.

SEM (Figure 6) was utilized to visually inspect the cross-sections of the sintered specimens, both in lowest temperature at which the holding sintered body could be obtained, and in temperature where specimens were expected to be partially crystallized. At this temperature, significant surface crystallization was observed on the sintered B12.5 particles (Fig. 6A). Additionally, poor sintering was evident. This might suggest that the crystallization interfered with the viscous flow sintering (9,187). With increasing sintering temperature (Fig.6B), it can be seen that particles show complete crystallization without significant neck growth. This indicates that crystallization inhibits particle sintering. Indeed, it has additionally been found by Fagerlund *et al.* that crystallization of the glass S53P4 inhibited proper glass sintering (8). B12.5-Mg5 (Fig. 5C) and B12.5-Sr10 (Fig. 5E), where parts of CaO was replaced with either MgO or SrO, showed barely any crystal formation following the grain boundaries (very thin layer of crystallization), and the glass seemed to remain mostly

amorphous. Additionally, the sintering could be performed at temperatures 40-50 °C lower than for B12.5. Moreover, the imaged Mg containing bioactive glasses (Fig. 6D,H) demonstrate to have slower crystallization rate with significant neck growth between particles, indicating partial sintering prior to crystallization. Overall, it was observed that all the studied glasses started to initially crystallize from the surface, which is in agreement with the calculated JMA exponent.

From porosity of specimens sintered from coarse particles (250-500 μm), it was seen that the inclusion of magnesium, in the composition, resulted in greater shrinkage and higher densification. Surprisingly, increasing the sintering temperature did not yield bodies with higher density, which may be attributed to the concomitant crystallization and sintering (187).

From scaffolds produced from < 38 μm particles, it was observed that the scaffold did remain amorphous after the heat processing (see **Study III** supplementary file S2 – XRD diffraction pattern of post sintering.) However, slight discoloration (as seen in **Study III** Supplementary File S1) was observed upon sintering of the 3D printed scaffold, likely caused by incomplete evaporation of carbon. Regardless of the technique used, the porosities of the obtained B12.5 scaffolds were found higher than that of B12.5-Mg5-Sr10 scaffolds. This could be explained by enhanced sinterability of B12.5-Mg5-Sr10, caused by the addition of Mg and Sr (13,14). Most importantly, the produced scaffolds had porosity over 50% (Figure 7) and pore size over 100 μm, aligning with recommended criteria for facilitating tissue and cell infiltration (9). In this study, the produced 3D printed scaffolds offered better pore size homogeneity when compared to those obtained by porogen burn-off. Moreover, the interconnective porosity observed in the 3D printed scaffolds (Figure 8) could be suitable for enabling cell migration within the scaffolds, as well as the diffusion of nutrients and the metabolic waste products (188).

In the **Study III**, significantly higher compressive strengths were obtained with B12.5-Mg5-Sr10 composition compared to B12.5. Addition of Mg to the glass composition lowers the glass viscosity which, consequently, improves the sintering properties and improves scaffolds strength (189,190). Moreover, the strength is greatly affected by the porosity. Thus, the increase in strength can also be linked to the lower porosities of B12.5-Mg5-Sr10 scaffolds (Figure 7) (12).

Overall, the compressive strengths of the produced sintered glass scaffolds were measured to be mostly within the 2–12 MPa strength of trabecular bone (191). It is evident that these values by themselves remain insufficient for load-bearing applications, if compared to the compressive strength of cortical bone, that has been reported to be in the range of 100–150 MPa. (191). While it should be noted, the measured scaffold surfaces were not processed (polished), resulting in uneven surfaces and thus also load distribution not uniformly distributed, it additionally must be considered that as test were performed in air atmosphere, scaffolds were unaffected by fatigue effects (192) that significantly reduce glass strength in the aqueous environments of *in vivo* applications. From materials scientists' point of view, the materials used for orthopaedic implants are often expected to possess a combination of high strength, low modulus, and high fatigue and wear resistance (193). However, if the materials were to be utilized as a replacement for the void filling products (e.g., bone grafts, glass/ceramic particles or putties), the bearing of the load could also be carried by e.g. plate fixation; therefore, even lower mechanical strength could be sufficient for certain bone tissue engineering applications. (194,195).

6.3 *In vitro* reactivity

The *in vitro* reactivity of the B12.5 glasses was tested in SBF, solution designed to mimic the chemical composition of human blood plasma and interstitial fluid (84). The studies were performed with different particle sizes, and hot-formed structures. In **Study I**, the theoretical surface area between compositions was kept constant (following principle of ISO / FDIS 23317: bioactivity of powders based on surface area, i.e., mass of the immersed particles was adjusted based on compositions density), to enable more accurate comparison of reactivity between the glass compositions. In **Study II**, as well as in **Study III** the protocol developed by the Technical committee for Bioglasses (TC04 of the International Commission on Glass) (85) was followed. As such, the mass of glass to volume of SBF ratio was kept constant.

As expected, the rate of degradation and ion release was directly linked to the samples surface area (as seen in pH changes in Figure 9), owing to dissolution occurring by an ion exchange process. (83). Overall, it was seen that the replacement of Ca with Mg and/or Sr led to a progressive decrease in glass reactivity rate, as

suggested by the pH analysis (Fig. 9). Additionally, both the ion release (Figures 11-13) and the post-immersion FTIR analysis (Figure 15) indicated, that, glasses with Sr and/or Mg exhibit lower rate of borate degradation and a decrease in the speed of reactive layer formation (as also observed in Figure 17). Therefore, the Mg/Sr substitutions were linked to stabilization of the glass network; and, especially, a stabilization of the boron network. These results were in strong agreement with previous studies reporting the slower dissolution rate of Mg and Sr-containing silicate bioactive glasses, along with a delayed hydroxyapatite precipitation. (13,14). Additionally, as expected, the borate network seemed to dissolve faster than the silicate (Supplementary Figure 1.) It is to be noted, that in SBF, the dissolution behaviour of the glasses is affected by the available hydrogen ions for ion exchange; therefore, for example the release of Si is lower in SBF, than it would be expected to be for example in TRIS solution. (196,197)

To better understand the nature of the formed reactive layer upon immersion, EDX/SEM analysis was conducted on both glass particles (**Study I**) as well as for scaffolds (**Study III**), as depicted in Figure 17. Several layers were observed at the particles' surfaces. Firstly, on the outermost layer EDX analysis revealed that, in the case of the B12.5 glass particles (Fig.17A) the Ca/P ratio was ~1.6 agreeing with the formation of a hydroxyapatite-like phase at the surface of the bioactive glass particles. With other investigated glass compositions, the ratio (Ca+Mg+Sr)/P was maintained at ~1.6, assigned to the precipitation of Mg/Sr-substituted HCA. Secondly, under the outermost layer, a SiO_2 rich layer was distinguished. Formation of a silica-rich layer has been discussed in detail by many authors, as typical for silica-based bioactive glasses. (1). Lastly, the composition of the particles' cores corresponded to the expected nominal glass composition, indicating that the particles had not fully reacted during the immersion period.

In **Study II**, the effect of crystallization on particles the reactivity in SBF was analysed. Interestingly, crystallized specimens seemed to be more reactive than their amorphous counterparts; during the observation period (up to 1 week of immersion) based both on the pH changes (Figure 10) and ion release (Figure 14), indicating greater reactivities for the residual glass phases. Upon closer inspection of the ion release (as seen in **Study II** Figure 5. Dissolution products from amorphous and crystallized B12.5-series glass particles), it was seen that glass composition B12.5-Mg5 exhibited similar trend as B12.5, and B12.5-Sr10 similarly as B12.5-Mg5-Sr10 for with their P levels in the dissolution solution. Results indicated, that while B, Ca,

Mg and Sr were released faster in crystallized specimens B12.5 and B12.5-Mg5 the P was initially consumed faster, before stabilizing. P consumption, upon immersion of amorphous specimens, was steady during the entire testing period. This could be attributed to Ca-P formation stopping earlier for the crystallized B12.5 and B12.5-Mg5, than for their amorphous counterparts. Similar trend was not observed with Sr containing glasses. Overall, the Sr-containing glasses reacted significantly slower in SBF, than other studied compositions. This has been linked to the stabilizing effect of Sr in the glass composition. (198).

The structural changes upon immersion were compared between amorphous and crystallized specimens with FTIR (Figure 16). Most interestingly, while all B12.5 and B12.5-Mg5 samples showed presence of phosphate vibrations, attributable to Ca-P formation, crystallized specimens lacked bands attributable to CO-vibrations. In general, appearance of phosphate vibration together with the carbonate vibration are typical of the presence of carbonated HA at the materials surface after the immersion in SBF. It is well accepted that the dissolution of bioactive glasses leads to the precipitation of an amorphous calcium phosphate layer, which then crystallize into HCA (178). The lack of carbonate vibration may indicate that the layer is still, at the ACP stage. Moreover, the lack of carbonate vibration at the surface of Sr-containing glasses was again linked to slower reactivity during the observation period. Overall, the delay in HCA formation itself, caused by the crystallization, is a well-known phenomena with bioactive glasses (199).

The results acquired in **Study II** suggested that with the B12.5 glass family, the partially crystallized matrixes degraded in SBF more rapidly. The overall fast reactivity of the crystallized specimens could perhaps be assigned to the presence of a borate phase, remaining post heat-treatment. Indeed, the only crystals evidenced by XRD were combeite, which does not contain boron. Therefore, it is likely that the remaining amorphous phase is a borate-rich phase. It has been seen that depending on the forming crystal phases and composition of the remaining glass phase, certain glass-ceramics can be highly bioactive (117).

6.4 Cells response

The cytotoxicity of B12.5-glass series was assessed via cell viability (as extracts, and 2D and 3D structures) and proliferation studies (for extract cultures). As mesenchymal stem cells have often been used successfully in research and cell therapies, due to their ability to differentiate into multiple mesenchymal and non-mesenchymal lineages *in vitro* (33,80), the glasses effects on cells differentiation (as extracts and 2D structure), ECM maturation (Figure 20-23) and cells osteogenic commitment (Figure 24) as well as endothelial marker expression (Figure 25) was additionally assessed. Osteogenic media supplements were utilized with the extracts, and in part of the direct cell/material culturing conditions.

In general, the ability of borate and borosilicate glass to support cell viability has often been reported as poorer compared to corresponding silicate glasses (20,19,200). However, in **Study IV,** we observed high viability of hADSC cultures in the presence of B12.5 glass degradation products (undiluted ion extracts; Figure 18A) and in direct cell/material contact on top of glass discs (Fig.18B). Ojansivu *et al.* (20) have seen that S53P4-based borosilicate glasses B50 and B25 decreased the proliferation of hADSC cultures. In contrast, in **Study III**, while proliferation on pure borosilicate B12.5 was lower than on S53P4 (Figure 19), the Mg/Sr modifications notably improved cell proliferation. Importantly, there were no indications of glasses cytotoxicity on cells (with ~27-36 ppm of B). In **Study III**, a pre-incubation for the produced scaffolds was however necessary to decrease burst release of ions for the cultured cells. Moreover, this effect is usually diminished in dynamic culturing conditions and *in vivo* experiments (9,201). After pre-incubation, the cell density of viable cells increased throughout the seven days of culturing (Fig. 18C), and there was no significant difference between the studied B12.5-Mg5-Sr10 burn-off and 3D printed scaffolds. It did not seem that the incomplete removal of residual carbon from the scaffolds had a significant effect on cell viability.

Bone is a connective tissue characterized by a mineralized ECM, which major structural components consists of type I collagen fiber network and a mineral phase mainly as calcium phosphate, in the form of hydroxyapatite crystals (30). In this respect, immunocytochemical staining for collagen-I (Figure 20 and 21) and mineralization assays (Figure 22 and 23) were utilized to evaluate the osteogenic differentiation as well as the maturation of the ECM. Collagen-I expression was observed with all studied conditions. When comparing the effect of direct contact

culturing (Fig.21) to ion extract conditions (Fig.20) to the col-I expression, it could be observed that after 14 days of culturing, the col-I was in similar stage in BM media cultures as seen in OM supplemented ion extracts, while the OM supplemented disc cultures showed even more enhanced collagen production and ECM secretion. It indeed has been seen in previous studies that the role of direct cell-bioactive glass interactions could have more significant effect in cellular changes, than ions present in the extracts, as in absence of cell-biomaterial contact bioactive glass ions stimulate osteogenesis only when OM-supplements are present (154). Moreover, in study by Ojansivu *et al.* (202) it was observed that, upon immersion a porous, coral-like structure developed at the surface of the glass. Additionally, the cells attached on these surfaces were covered with a CaP precipitate. (202)

Alizarin red staining was performed to evidence the mineral formation on culture to assess the late osteogenesis of hADSCs cultured in glass extracts. Cells cultured on discs were not characterized, as the mineral formed by the cells cannot be discriminated from the HA formed due to the glass reactivity. Mineral formation on the cultures was observed during the observation period. Moreover, strontium-containing medium promoted the mineralization process, as also seen in human osteoblast cultures. (108,203).

Summarising the osteogenic marker expression, at the studied timepoints, increasing *RUNX2a* expression (Fig.24A) was evidenced in all conditions. The expression of this gene has been attributed to be essential for osteoblast formation, but for the osteogenic differentiation to proceed, the upregulated expression diminishes to enable mineralization. (204). *OSTERIX* (Fig.24B) expression was clearly stimulated only by B12.5-Mg5, -Sr10 and B12.5-Mg5-Sr10. OSTERIX, is a transcription factor that plays a critical role in osteoblast differentiation and bone formation. It is expressed primarily in osteoblasts and chondrocytes, as well as in preosteoblasts and mesenchymal stem cells that are committed to the osteoblast lineage. (205). *DLX5* is a protein coding gene involved in osteoblast differentiation and induction of mineralization. (206). The *DLX5* (Fig.24C) upregulation by all bioactive glass extracts indicates osteoblast differentiation and induction of mineralization. For *OSTEOPONTIN* (Fig.24D), the upregulation in the presence of bioactive glass ions was even over 20-fold when compared to the control conditions; as the expression was highly stimulated, it could be attributable to peaking during mineralization phase. The expression of osteopontin changes during the differentiation phases; *OSTEOPONTIN* is upregulated in proliferation phase, after

which it declines, and peaks during mineralization. (34). While it should additionally be kept in mind that the mesenchymal stem cells differentiation towards osteogenic lineages were supported by supplementing the media with L-ascorbic acid 2-phosphate, dexamethasone and beta-glycerophosphate (153), overall, results suggested that the bioactive glass extracts initiated osteoblast differentiation, moving into mineralisation phase.

Von Willebrand factor (*vWF*) encodes a glycoprotein, secreted by endothelial cells, that partakes in haemostasis and regulates blood vessel formation (207). *PECAM-1*, in the other hand, is expressed in endothelial cell-cell junctions, where the protein has an important role restoring vascular permeability barrier (208). Therefore, as both *vWF* and *PECAM-1* were upregulated by the borosilicate extracts, it seems that the degradation products could additionally support the angiogenesis of the surrounding tissue. In study by Ojansivu *et al.* (20), the borosilicate bioactive glasses B25 and B50 had an upregulating effect on these markers, and indeed, B12.5-series seems to have a similar effect.

6.5 Practical implications

Based on these studies, B12.5 glass-series exhibits promising bioactive properties, while simultaneously having a relatively large hot forming window. The partial substitution of Ca with Sr and/or Mg can enable controlling of the glasses reactivity and boron release by stabilizing the borate network. Furthermore, the incorporation of Mg and Sr into the reactive layer may impart additional functionality to these glasses. The results additionally indicated that the introduction of boron enhanced the sintering ability compared to the original S53P4 composition. While the optimal temperature range for sintering the base borosilicate B12.5 approached the compositions crystallization temperature and crystallization interfered with viscous flow sintering, the additions of both Mg and Sr slightly improved the sintering ability. Interestingly, it was found that crystallization seemed to increase the glasses initial reactivity. Although surface crystallization can pose challenges to sintering, the partial crystallization of the glasses could enable tailoring the glasses chemical stability and degradation rate even further.

Amorphous 3D scaffolds were fabricated using finer (< 38 μm) glass particles, resulting in structures with large pores (50 - 500 μm) and porosity ranging from 50-

90%. This porosity is essential for scaffold osteoconductivity, allowing tissue infiltration and regeneration crucial for effective bone tissue engineering (38,65). Therefore, the studied scaffolds could be promising to promote and support new bone growth in non-bearing applications.

6.6 Study limitations and future perspectives

The structural and thermal analysis revealed (**Study I**), that the melt-derived Mg/Sr containing glasses indicated possible inhomogeneity and phase separation within their structure. This could perhaps be improved with changes in the melting protocol, such as by longer melting time, or multiple consecutive meltings. Still, however it is possible that the studied compositions are within domain of immiscibility of silicate and borate phase. (209).

In the scope of this dissertation, the glasses reactivity was thoroughly tested in SBF (**Studies I, II** and **III**). From the scientific point of view, it could have been interesting to study the reactivity and ion release, additionally, in other buffer solutions, such as TRIS. However, *in vitro* studies with SBF are more useful for evaluation of apatite-forming ability of material intended for implants, prior to *in vivo* studies (ISO/FDIS 23317). As the crystallization studies (**Study II**) indicated that the crystallization did not seem to inhibit the bioactivity of the B12.5-glass series, it would have been perhaps warranted to study the properties of the produced glass-ceramics, as well as the nature of the remaining residual glass phases after immersion, further.

In **Study III**, amorphous and porous scaffold structures were produced with different thermal processing methods. However, the mechanical properties of these scaffolds remained low. While the achievable information from this one study is ultimately limited, results gave an indication of the effect of Mg/Sr substitution on the scaffold properties. It is still to be said, that with changing of the processing parameters, further optimisation of the scaffolds properties is possible.

Based on studies with mesenchymal stem cells (**Study IV**), the glasses seem promising for bone tissue engineering applications. However, as a result of multiple elements in the studied glass compositions, specific trends linked to

composition/property relationships are challenging to establish. Additionally, multiple cell lines would be needed to provide statistically holding results. Moreover, dynamic testing conditions (e.g., flow-through or bioreactor conditions) would more accurately mimic the physiological environment. While the results obtained during this dissertation have given a broad view of the B12.5 borosilicate glasses potential for bone tissue engineering applications, further studies, such as *in vivo* would be needed to confirm the cytocompatibility and functionality of the materials.

7 SUMMARY AND CONCLUSIONS

The aim of this dissertation was to develop and characterize new bioactive borosilicate glass compositions, suitable for bone tissue engineering. The studies focused on understanding the properties of the newly developed compositions, and the effect of Mg/Sr additions to the glass's properties and reactivity. The compositions bioactivity was estimated via *in vitro* SBF immersion and cell culturing. Further, the effects on crystallization to the composition's properties and behaviour were analysed. Finally, scaffolds were produced of the most interesting compositions, and tested for their properties and bioactivity. The main conclusions of the four studies included in this thesis are described below:

Study I: Six borosilicate glass compositions, based on the commercial bioactive S53P4 glass, were developed and characterized for their physical and structural properties. Mg and/or Sr were introduced to modify the glasses properties, replacing part of the Ca content.

Thermal analysis revealed that Mg/Sr substitution for Ca expanded the glasses hot forming range. Mg substitution reduced glass viscosity, while Sr appeared to slow crystallization kinetics. Mixed Mg/Sr glasses exhibited phase separation, confirmed by DTA and Raman spectroscopy. Overall, B12.5 borosilicate's seemed to offer improved thermal properties over the original composition. Changes in boron network connectivity were observed, with an increase in BO_3 at the expense of BO_4 when Mg/Sr were added to the composition. The combined presence of Ca, Mg, and Sr affected additionally the phosphate environment in the glass network. Ion release and post-immersion structural analysis indicated typical bioactive glass reaction mechanism. Moreover, results showed that replacing Ca with Sr and/or Mg helped to control boron release, by stabilizing the borate network. All glasses demonstrated rapid apatite formation, with slightly slower reactivity linked for higher substitution. Mg and Sr were found to be incorporated into the apatite, consistent with previous studies. Furthermore, it was suspected that the release and incorporation of Mg and Sr may enhance the functionality of these new bioactive glasses.

Study II: Deeper thermal analysis and calculated JMA exponents suggested dominant surface crystallization in all B12.5-variants, supported by SEM analysis. B12.5-glass series showed, in theory, superior sintering ability compared to S53P4, yet without Mg or Sr additions risked devitrification due to proximity to its crystallization temperature. This led to partially crystallized, mechanically weak sintered bodies. Mg and Sr in the composition improved sintering and enabled amorphous structure formation.

Post-immersion analysis indicated that the partial crystallization initially boosted reactivity in SBF. This altered the behaviour was attributed to the remaining amorphous phase, that was suspected to impact on dissolution kinetics. Silicate network participation in crystal formation left borate-rich areas amorphous, enhancing reactivity. Apatite precipitation occurred in both amorphous and crystallized glasses, with crystallized samples lacking carbonate formation.; HCA formation was hindered by crystallization, while HA still precipitated. While surface crystallization poses challenges for the sintering, however, partial crystallization offers opportunities for tailored chemical stability and degradation rates.

Study III: Bioactive borosilicate glass scaffolds, produced from B12.5 and B12.5-Mg5-Sr10 compositions, were successfully manufactured and sintered using 3D printing, and porogen burn-off methods. The formed scaffolds met porosity and pore size requirements for bone tissue engineering. The 3D printed scaffolds showed superior interconnected porosity, more uniform pore sizes, and better reproducibility.

Immersion in SBF indicated the formation of a HA-like layer. Similarly, as previously seen, B12.5-Mg5-Sr10 scaffolds exhibited slower dissolution and HA precipitation in SBF compared to B12.5, attributed to the stabilizing effect of Mg and Sr substitution. In cell culture, B12.5 scaffolds exhibited some toxicity to the cells due to high ion release in static culture, that could be mitigated with dynamic culture. Additionally, preincubation of scaffolds in TRIS and αMEM effectively reduced burst release of ions during cell culture. hADSCs survival with B12.5-Mg5-Sr10 scaffolds was comparable to control cultures without scaffolds. Migration of hADSCs beneath the top layer in 3D printed scaffolds was also observed.

Overall, 3D printed B12.5-Mg5-Sr10 scaffolds exhibited bioactivity, high interconnected porosity, suitable pore size, and optimal dissolution rate, enhancing hADSCs survival. They met structural property requirements and demonstrated good reproducibility.

Study IV: In prior studies, it has been seen that borosilicate bioactive glasses can hinder cell proliferation. Overall, the dissolution products of B12.5 glasses were well-tolerated; all hADSC-cultures remained viable and reached high cell densities. While B12.5 extracts led to slower cell proliferation compared to S53P4 cultures, Mg/Sr substitution in B12.5 slightly increased cells proliferation. Viability assays additionally confirmed high cell viability when in direct contact with the borosilicate glasses.

The ion extracts were observed to significantly influence cell behaviour, regulating ALP activity and osteogenic gene expression markers. While major ECM mineralization wasn't achieved in 21 days, the degradation products accelerated hADSC differentiation and ECM maturation. Direct contact with bioactive glasses alone induced hADSC differentiation, highlighting the importance of glass surface properties in promoting osteogenesis. Furthermore, boron-containing bioactive glasses, including the B12.5 series, are known to support angiogenesis. This glass series notably upregulated endothelial markers *vWF* and *PECAM-1* expression. The effect was more pronounced with higher Mg/Sr substitution for Ca, suggesting the role of Mg and/or Sr in angiogenic factor upregulation.

Overall, all the studied glasses and their dissolution products positively influenced hADSCs' osteogenic commitment while supporting angiogenic factors. It was observed that in this glass series, Mg and Sr substitution for Ca had a slightly more prominent effect on cells than pure borosilicate.

8 REFERENCES

1. Jones JR. Review of bioactive glass: From Hench to hybrids. Acta Biomaterialia. 2013; 9(1): 4457-4486.

2. Hench LL, Jones JR. Bioactive Glasses: Frontiers and Challenges. Frontiers in Bioengineering and Biotechnology. 2015; 3: 1-12.

3. Brauer DS. Bioactive glasses - Structure and properties. Angewandte Chemie - International Edition. 2015; 54(14): 4160-4181.

4. Jones JR, Brauer DS, Hupa L:GDC. Bioglass and Bioactive Glasses and Their Impact on Healthcare. International Journal of Applied Glass Science. 2016; 7: 423-434.

5. Lindfors NC, Hyvönen P, Nyyssönen M, Kirjavainen M, Kankare J, Gullichsen E, et al. Bioactive glass S53P4 as bone graft substitute in treatment of osteomyelitis. Bone. 2010; 47(2): 212-218.

6. Baino F. Bioactive glasses – When glass science and technology meet regenerative medicine. Ceramics International. 2018; 44(13): 14953-14966.

7. Baino F, Fiume E, Barberi J, Kargozar S, Marchi J, Massera J, et al. Processing methods for making porous bioactive glass-based scaffolds—A state-of-the-art review. International Journal of Applied Ceramic Technology. 2019; 16(5): 1762-1796.

8. Fagerlund S, Massera J, Moritz N, Hupa L, Hupa M. Phase composition and in vitro bioactivity of porous implants made of bioactive glass S53P4. Acta Biomaterialia. 2012; 8(6): 2331-2339.

9. Rahaman MN, Day DE, Bal BS, Fu Q, Jung SB, Bonewald LF, et al. Bioactive glass in tissue engineering. Acta Biomaterialia. 2011; 7(6): 2355-2373.

10. Balasubramanian B, Büttner T, Miguez Pacheco V, Boccaccini AR. Boron-containing bioactive glasses in bone and soft tissue engineering. Journal of the European Ceramic Society. 2018; 38(3): 855-869.

11. Ege D, Zheng K, Boccaccini AR. Borate Bioactive Glasses (BBG): Bone Regeneration, Wound Healing Applications, and Future Directions. ACS Applied Bio Materials. 2022; 5(8): 3608-3622.

12. Fabert M, Ojha N, Erasmus E, Hannula M, Hokka M, HJ, et al. Crystallization and sintering of borosilicate bioactive glasses for application in tissue engineering. Journal of Materials Chemistry B. 2017; 5(23): 4514-4525.

13. Massera J, Hupa L, Hupa M. Influence of the partial substitution of CaO with MgO on the thermal properties and in vitro reactivity of the bioactive glass S53P4. Journal of Non-Crystalline Solids. 2012; 358(18-19): 2701 - 2707.

14. Massera J, Hupa L. Influence of SrO substitution for CaO on the properties of bioactive glass S53P4. Journal of Materials Science: Materials in Medicine. 2014; 25: 657–668.

15. Gentleman E, Fredholm YC, Jell G, Lotfibakhshaiesh N, O'Donnell MD, Hill RG, et al. The effects of strontium-substituted bioactive glasses on osteoblasts and osteoclasts in vitro. Biomaterials. 2010; 31(14): 3949-3956.

16. Hoppe A, Güldal NS, Boccaccini AR. A review of the biological response to ionic dissolution products from bioactive glasses and glass-ceramics. Biomaterials. 2011; 32(11): 2757-2774.

17. Hoppe A, Mouriño V, Boccaccini A. Therapeutic inorganic ions in bioactive glasses to enhance bone formation and beyond. Biomaterials Science. 2013; 1(3): 254-256.

18. Fu Q, Rahaman MN, Fu H, Liu X. Silicate, borosilicate, and borate bioactive glass scaffolds with controllable degradation rate for bone tissue engineering applications. I. Preparation and in vitro degradation. Journal of Biomedical Materials Research Part A. 2010; 95A(1): 164-171.

19. Brown RF, Rahaman MN, Dwilewicz AB, Huang W, Day DE, Li Y, et al. Effect of borate glass composition on its conversion to hydroxyapatite and on the proliferation of MC3T3-E1 cells. Journal of Biomedical Materials Research - Part A. 2009; 88A(2): 392-400.

20. Ojansivu M, Mishra A, Vanhatupa S, Juntunen M, Larionova A, Massera J, et al. The effect of S53P4-based borosilicate glasses and glass dissolution products on the osteogenic commitment of human adipose stem cells. PLoS ONE. 2018; 13(8).

21. Langer R, Vacanti JP. Tissue engineering. Science. 1993; 260(5110): 920 - 926.

22. Aro HT, Välimäki VV, Strandberg N, Lankinen P, Löyttyniemi E, Saunavaara V, et al. Bioactive glass granules versus standard autologous and allogeneic bone grafts: a randomized trial of 49 adult bone tumor patients with a 10-year follow-up. Acta Orthopaedica. 2022; 93: 519–527.

23. Younger EM, Chapman MW. Morbidity at bone graft donor sites. Journal of Orthopaedic Trauma. 1989; 3(3): 192-195.

24. Kneser U, Schaefer DJ, Polykandriotis E, Horch RE. Tissue engineering of bone: The reconstructive surgeon's point of view. Journal of Cellular and Molecular Medicine. 2006; 10(1): 7-19.

25. Dimitriou R, Jones E, McGonagle D, Giannoudis PV. Bone regeneration: current concepts and future directions. BMC Medicine. 2011;(9): 66.

26. Amini AR, Laurencin CT, Nukavarapu SP. Bone tissue engineering: Recent advances and challenges. Critical Reviews in Biomedical Engineering. 2012; 40(5): 363-408.

27. Koons GL, Diba M, Mikos AG. Materials design for bone- tissue engineering. Nature Reviews. Materials. 2020; 5(8): 584-603.

28. van Gaalen S, Kruyt M, Meijer G, Mistry A,MA,vdBJ, Jansen J, de Groot K, et al. Tissue engineering of bone. In van Blitterswijk C, editor. Tissue Engineering. 1st ed.: Academic Press; 2008. p. 776.

29. Schroeder JE, Mosheiff R. Tissue engineering approaches for bone repair: Concepts and evidence. Injury. 2011; 42(6): 609-613.

30. Ross MH, Pawlina W. Bone. In Ross MH, Pawlina W. Histology - A Text and Atlas with Correlated Cell. 6th ed.: Lippincott Williams & Wilkins; 2011. p. 974.

31. Salgado AJ, Coutinho OP, Reis RL. Bone tissue engineering: State of the art and future trends. Macromolecular Bioscience. 2004; 4(8): 743-765.

32. Alberts B, Johnson A, Lewis J, Raff M, Roberts K, Walter P. Molecular biology of the cell. 5th ed. New York, NY: Garland Science; 2008.

33. Tsuji W, Rubin JP, Marra KG. Adipose-derived stem cells: Implications in tissue regeneration. World journal of stem cells. 2014; 6(3): 312-321.

34. Lian JB, Stein GS. Development of the osteoblast phenotype: molecular mechanisms mediating osteoblast growth and differentiation. The Iowa Orthopaedic Journal. 1995; 15: 118–140.

35. Kassem M, Abdallah BM,SH. Osteoblastic cells: differentiation and trans-differentiation. Archives of Biochemistry and Biophysics. 2008; 472(2): 183-187.

36. Lian JB, Stein GS, Van Wijnen AJ, Stein JL, HMQ, Gaur T, et al. MicroRNA control of bone formation and homeostasis. Nature Reviews Endocrinology. 2012; 8(4): 212-227.

37. Hutmacher DW. Scaffolds in tissue engineering bone and cartilage. Biomaterials. 2000; 21(24): 2529-2543.

38. Karageorgiou V, Kaplan D. Porosity of 3D biomaterial scaffolds and osteogenesis. Biomaterials. 2005; 26(27): 5474-5491.

39. Bose S, Roy M, Bandyopadhyay A. Recent advances in bone tissue engineering scaffolds. Trends in biotechnology. 2012; 30(10): 546–554.

40. Lee CH, Singla A, Lee Y. Biomedical applications of collagen. International Journal of Pharmaceutics. 2001; 221(1-2): 1-22.

41. Qian J, Kang Y, Zhang W. Fabrication and characterization of biomorphic 45S5 Bioglass scaffold from sugarcane. Materials Science and Engineering: C. 2009; 29: 1361–1364.

42. Boccardi E, Philippart A, Juhasz-Bortuzzo JA, Novajra G, Vitale-Brovarone C, Boccaccini AR. Characterisation of Bioglass based foams developed via replication of natural marine sponges. Advances in Applied Ceramics. 2015; 114: S56–S62.

43. Ohji T, Fukushima M. Macro-porous ceramics: Processing and properties. International Materials Reviews. 2012; 57(2).

44. Haaparanta AM, Järvinen E, Cengiz IF, Ellä V, Kokkonen HT, Kiviranta I, et al. Preparation and characterization of collagen/PLA, chitosan/PLA, and collagen/chitosan/PLA hybrid scaffolds for cartilage tissue engineering. Journal of Materials Science: Materials in Medicine. 2014; 25(4): 1129 - 1136.

45. Zhang L, Yang G, Johnson BN, Jia X. Three-dimensional (3D) printed scaffold and material selection for bone repair. Acta Biomaterialia. 2019; 84: 16-33.

46. Chocholata P, Kulda V, Babuska V. Fabrication of scaffolds for bone-tissue regeneration. Materials. 2019; 12(4).

47. Turnbull G, Clarke J, Picard F, Riches P, Jia L, Han F, et al. 3D bioactive composite scaffolds for bone tissue engineering. Bioactive Materials. 2018; 3(3): 278-314.

48. Hench LL, Polak JM. Third-generation biomedical materials. Science. 2002; 295(5557): 1014-1017.

49. Hench LL, Splinter RJ, Allen WC, Greenlee TK. Bonding mechanisms at the interface of ceramic prosthetic materials. Journal of Biomedical Materials Research. 1971; 5(6): 117-141.

50. Zheng YF, Gu XN, Witte F. Biodegradable metals. Materials Science and Engineering: R: Reports. 2014; 77: 1-34.

51. Hofstetter J, Becker M, Martinelli E, Weinberg AM, Mingler B, Kilian H, et al. High-Strength Low-Alloy (HSLA) Mg–Zn–Ca Alloys with Excellent Biodegradation Performance. JOM. 2014; 66(4): 566-572.

52. Holweg P, Labmayr V, Schwarze U, Sommer NG, Ornig M, Leithner A. Osteotomy after medial malleolus fracture fixed with magnesium screws ZX00 - A case report. Trauma Case Reports. 2022; 42.

53. Lee KY, Mooney DJ. Alginate: Properties and biomedical applications. Progress in Polymer Science (Oxford). 2012; 37(1): 106-126.

54. Sun J, Tan H. Alginate-based biomaterials for regenerative medicine applications. Materials. 2013; 6(4): 1285-1309.

55. Ahmed TAE, Dare EV, Hincke M. Fibrin: A versatile scaffold for tissue engineering applications. Tissue Engineering - Part B: Reviews. 2008; 14(2): 199-215.

56. Kundu B, Rajkhowa R, Kundu SC, Wang X. Silk fibroin biomaterials for tissue regenerations. Advanced Drug Delivery Reviews. 2013; 65(4): 457-470.

57. Di Martino A, Sittinger M, Risbud MV. Chitosan: A versatile biopolymer for orthopaedic tissue-engineering. Biomaterials. 2005; 26(30): 5983-5990.

58. Zhang R, Ma PX. Poly(α-hydroxyl acids)/hydroxyapatite porous composites for bone- tissue engineering. I. Preparation and morphology. Journal of Biomedical Materials Research. 1999; 44(4): 446-455.

59. Mikos AG, Temenoff JS. Formation of highly porous biodegradable scaffolds. Electronic Journal of Biotechnology. 2000; 3(2): 114-119.

60. Bhattarai DP, Aguilar LE, Park CH, Kim CS. A Review on Properties of Natural and Synthetic Based Electrospun Fibrous Materials for Bone Tissue Engineering. Membranes. 2018; 8(3).

61. Agrawal CM, Ray RB. Biodegradable polymeric scaffolds for musculoskeletal tissue engineering. Journal of Biomedical Materials Research. 2001; 55(2): 141-150.

62. LeGeros RZ. Properties of osteoconductive biomaterials: Calcium phosphates. Clinical orthopaedics and related research. 2002; 395: 81-98.

63. Campana V,MG, Pagano E, Barba M, Cicione C, Salonna G, Lattanzi W, et al. Bone substitutes in orthopaedic surgery: from basic science to clinical practice. Journal of Materials Science: Materials in Medicine. 2014; 25(10): 2445-2461.

64. Bohner M, Le Gars Santoni B, Döbelin N. β-tricalcium phosphate for bone substitution: Synthesis and properties. Acta Biomaterialia. 2020; 1: 23-41.

65. Gerhardt LC, Boccaccini AR. Bioactive glass and glass-ceramic scaffolds for bone tissue engineering. Materials. 2010; 3(7): 3867-3910.

66. Montoya C, Du Y, Gianforcaro AL, Orrego S, Yang M, Lelkes PI. On the road to smart biomaterials for bone research: definitions, concepts, advances, and outlook. Bone research. 2021; 9.

67. Mauro JC, Zanotto ED. Two Centuries of Glass Research: Historical Trends, Current Status, and Grand Challenges for the Future. International Journal of Applied Glass Science. 2014; 5(3): 313 - 327.

68. Andersson ÖH, Karlsson KH, Kangasniemi K, Yliurpo A. Models for physical properties and bioactivity of phosphate opal glasses. Glastechnische berichte. 1988; 61(10): 300-305.

69. Andersson ÖH, Liu GZ, Karlsson KH, Niemi L, Miettinen J, Juhanoja J. In vivo behavior of glasses in the SiO–NaO–CaO–PO–AlO–BO system. Journal of Materials Science: Materials in Medicine. 1990; 1: 219–227.

70. Brink M, Turunen T, Happonen RP, Yli-Urpo A. Compositional dependence of bioactivity of glasses in the system Na2O- K2O-MgO-Cao-B2O3-P2O5-SiO2. Journal of Biomedical Materials Research. 1997; 37(1): 144-121.

71. Brink M. The influence of alkali and alkaline earths on the working range for bioactive glasses. Journal of Biomedical Materials Research. 1997; 36(1): 109-117.

72. Lindfors NC, Koski I, Heikkilä JT, Mattila K, Aho AJ. A prospective randomized 14-year follow-up study of bioactive glass and autogenous bone as bone graft substitutes in benign bone tumors. Journal of Biomedical Materials Research Part B: Applied Biomaterials. 2010; 94B(1): 157-164.

73. Islam MT, Felfel RM, Abou Neel EA, Grant DM, I. A, Hossain KMZ. Bioactive calcium phosphate-based glasses and ceramics and their biomedical applications: A review. Journal of Tissue Engineering. 2017; 8.

74. Abou Neel EA, Ahmed I, Blaker JJ, Bismarck A, Boccaccini AR, Lewis MP, et al. Effect of iron on the surface, degradation and ion release properties of phosphate-based glass fibres. Acta Biomaterialia. 2005; 1(5): 553-563.

75. Brauer DS, Rüssel C, Vogt S, Weisser J, Schnabelrauch M. Degradable phosphate glass fiber reinforced polymer matrices: Mechanical properties and cell response. Journal of Materials Science: Materials in Medicine. 2008; 19(1): 121-127.

76. Abou Neel EA, Pickup DM, Valappil SP, Newport RJ, Knowles JC. Bioactive functional materials: A perspective on phosphate-based glasses. Journal of Materials Chemistry. 2009; 19(6): 690-701.

77. Ahmed I, Jones IA, Parsons AJ, Bernard J, Farmer J, Scotchford CA, et al. Composites for bone repair: Phosphate glass fibre reinforced PLA with

varying fibre architecture. Journal of Materials Science: Materials in Medicine. 2011; 22(8): 1825-1834.

78. Liang W, Rahaman MN, Day DE, Marion NW, Riley GC, Mao JJ. Bioactive borate glass scaffold for bone tissue engineering. Journal of Non-Crystalline Solids. 2008; 354(15-16): 1690-1696.

79. Bi L, Rahaman MN, Day DE, Brown Z, Samujh C, Liu X, et al. Effect of bioactive borate glass microstructure on bone regeneration, angiogenesis, and hydroxyapatite conversion in a rat calvarial defect model. Acta Biomaterialia. 2013; 9(8): 8015-8026.

80. Thyparambil NJ, Gutgesell LC, Bromet BA, Flowers LE, Greaney S, Day DE, et al. Bioactive borate glass triggers phenotypic changes in adipose stem cells. Journal of Materials Science: Materials in Medicine. 2020; 32.

81. Yang X, Zhang L, Chen X, Sun X, Yang G, Guo X, et al. Incorporation of B 2O 3 in CaO-SiO 2-P 2O 5 bioactive glass system for improving strength of low-temperature co-fired porous glass ceramics. Journal of Non-Crystalline Solids. 2012; 358(9): 1171-1179.

82. Chen H, Hill R, Baysan A. The effect of different concentrations of fluoride in toothpastes with or without bioactive glass on artificial root caries. Journal of dentistry. 2023; 133.

83. Hench LL, Clark DE. Physical chemistry of glass surfaces. Journal of Non-Crystalline Solids. 1978; 28(1): 83-105.

84. Kokubo T, Kushitani H, Sakka S, Kitsugi T, Yamamuro T. Solutions able to reproduce in vivo surface-structure changes in bioactive glass-ceramic A-W3. Journal of Biomedical Materials Research. 1990; 24(6): 721-734.

85. Maçon AL, Kim TB, Valliant EM, Goetschius K, Brow RK, Day DE, et al. A unified in vitro evaluation for apatite-forming ability of bioactive glasses and

their variants. Journal of Materials Science: Materials in Medicine. 2015; 26(2): 1-10.

86. Miguez-Pacheco V, Hench LL, Boccacini AR. Bioactive glasses beyond bone and teeth: Emerging applications in contact with soft tissues. Acta Biomaterialia. 2015; 13: 1-15.

87. Jell G, Stevens MM. Gene activation by bioactive glasses. Journal of Materials Science: Materials in Medicine. 2006; 17: 997-1002.

88. Brauer DS, Hupa L. Glass as a biomaterial: strategies for optimising bioactive glasses for clinical applications. Comptes Rendus. Géoscience. 2022; 354(S1): 185-197.

89. Yamaguchi M. Role of zinc in bone formation and bone resorption. Journal of Trace Elements in Experimental Medicine. 1998; 11: 119-135.

90. Cacciotti I. Bivalent cationic ions doped bioactive glasses: the influence of magnesium, zinc, strontium and copper on the physical and biological properties. Journal of Materials Science. 2017; 52(15): 8812 - 8831.

91. Rodríguez JP, Ríos S, González M. Modulation of the proliferation and differentiation of human mesenchymal stem cells by copper. Journal of Cellular Biochemistry. 2002; 85(1): 92-100.

92. Bari A, Bloise N, Fiorilli S, Novajra G, Vallet-Regí M, Bruni G, et al. opper-containing mesoporous bioactive glass nanoparticles as multifunctional agent for bone regeneration. Acta Biomaterialia. 2017; 55: 493-504.

93. Bellantone M, Williams HD, Hench LL. Broad-spectrum bactericidal activity of Ag2O-doped bioactive glass. Antimicrobial Agents and Chemotherapy. 2002; 46(6): 1940 - 1945.

94. Miola M, Verné E, Vitale-Brovarone C, Baino F. Antibacterial Bioglass-Derived Scaffolds: Innovative Synthesis Approach and Characterization. International Journal of Applied Glass Science. 2016; 7(2): 238-247.

95. Carlisle EM. Silicon: a possible factor in bone calcification. Science. 1970; 167(3916): 270-280.

96. Carlisle EM. Silicon as a trace nutrient. Science of the Total Environment. 1988; 73(1-2): 95-106.

97. Henstock JR, Canham LT, Anderson SI. Silicon: The evolution of its use in biomaterials. Acta Biomaterialia. 2015; 11(1): 17-26.

98. Dashnyam K, El-Fiqi A, Buitrago JO, Perez RA, Knowles JC, Kim HW. A mini review focused on the proangiogenic role of silicate ions released from silicon-containing biomaterials. Journal of Tissue Engineering. 2017; 8(1-13).

99. Jaiswal JK. Calcium – how and why? Journal of Biosciences. 2001; 26(3): 357-363.

100. Marie PJ. The calcium-sensing receptor in bone cells: a potential therapeutic target in osteoporosis. Bone. 2010; 46(3): 571-576.

101. Berridge MJ, Bootman MD, Roderick HL. Calcium signalling: Dynamics, homeostasis and remodelling. Nature Reviews Molecular Cell Biology. 2003; 4(7): 517-529.

102. Michigami T, Kawai M, Yamazaki M, Ozono K. Phosphate as a Signaling Molecule and Its Sensing Mechanism. Physiological Reviews. 2018; 98(4): 2317-2348.

103. Michigami T, Ozono K. Roles of Phosphate in Skeleton. Frontiers in Endocrinology (Lausanne). 2019; 10.

104. Beck GRJ, Zerler B, Moran E. Phosphate is a specific signal for induction of osteopontin gene expression. Proceedings of the National Academy of Sciences. 2000; 97(15): 8352-8357.

105. Diba M, Goudouri O, Tapia F, Boccaccini AR. Magnesium-containing bioactive polycrystalline silicate-based ceramics and glass-ceramics for biomedical applications. Current Opinion in Solid State and Materials Science. 2014; 18(3): 147-167.

106. Saris NL, Mervaala E, Karppanen H, Khawaja JA, Lewenstam A. Magnesium: An update on physiological, clinical and analytical aspects. Clinica Chimica Acta. 2000; 294(1-2): 1-26.

107. Okuma T. Magnesium and bone strength. Nutrition. 2001; 17(7-8): 679 - 680.

108. Marx D, Rahimnejad Yazdi A, Papini M, M. T. A review of the latest insights into the mechanism of action of strontium in bone. Bone Reports. 2020; 12.

109. Mahony O, Tsigkou O, Ionescu C, Minelli C, Ling L, Hanly R, et al. Silica-Gelatin Hybrids with Tailorable Degradation and Mechanical Properties for Tissue Regeneration. Advanced Functional Materials. 2010; 20(22): 3835-3845.

110. Atala A, Kasper FK, Mikos AG. Engineering complex tissues. Science Translational Medicine. 2012; 4(160): 160rv12.

111. Feng P, Wu P, Gao C, Yang Y, Guo W, Yang W, et al. A Multimaterial Scaffold With Tunable Properties: Toward Bone Tissue Repair. Advanced Science. 2018; 5(6): 1700817.

112. Xynos ID, Hukkanen MVJ, Batten JJ, Buttery LD, Hench LL, Polak JM. Bioglass ®45S5 stimulates osteoblast turnover and enhances bone formation in vitro: Implications and applications for bone tissue engineering. Calcified tissue international. 2000; 67(4): 321-329.

113. Zanotto ED&MJC. The glassy state of matter: Its definition and ultimate fate. Journal of Non-Crystalline Solids. 2017; 471: 490-495.

114. Nommeots-Nomm A, Massera J. Glass and Glass-Ceramic Scaffolds: Manufacturing Methods and the Impact of Crystallization on In-Vitro Dissolution. In Baino F, editor. Scaffolds in Tissue Engineering - Materials, Technologies and Clinical Applications.: InTech; 2017. p. 31-47.

115. Magallanes-Perdomo M, Meille S, J.-M. C, Pacard E, Chevalier J. Bioactivity modulation of Bioglass® powder by thermal treatment. Journal of the European Ceramic Society. 2012; 32(11): 2765-2775.

116. Filho OP, La Torre GP, Hench LL. Effect of crystallization on apatite-layer formation of bioactive glass 4S55. Journal of Biomedical Materials Research. 1996; 30: 509-514.

117. Clupper DC, Hench LL. Crystallization kinetics of tape cast bioactive glass 45S5. Journal of Non-Crystalline Solids. 2003; 315(1-2): 43-48.

118. Massera J, Fagerlund S, Hupa L, Hupa M. Crystallization Mechanism of the Bioactive Glasses, 45S5 and S53P4. Journal of the American Ceramic Society. 2012; 95: 607-613.

119. Kissinger HE. Reaction kinetics in differential thermal analysis. Analytical Chemistry. 1957; 29(11): 1702-1706.

120. Friedman HL. Kinetics of thermal degradation of char-forming plastics from thermogravimetry. Application to a phenolic plastic. Journal of Polymer Science. 1964; 6(1): 183-195.

121. Augis JA, Bennett JE. Calculation of the avrami parameters for heterogeneous solid state reactions using a modification of the kissinger method. Journal of Thermal Analysis. 1978; 13(2): 283-292.

122. Ozawa T. Kinetics of non-isothermal crystallization. Polymer. 1971; 12(3): 150-158.

123. Hench LL. Chronology of Bioactive Glass Development and Clinical Applications. New Journal of Glass and Ceramics. 2013; 3(2): 67-73.

124. Hill RG, Brauer DS. Predicting the bioactivity of glasses using the network connectivity or split network models. Journal of Non-Crystalline Solids. 2011; 357(24): 3884 - 3887.

125. Elgayar I, Aliev AE, Boccaccini AR, Hill RG. Structural analysis of bioactive glasses. Journal of Non-Crystalline Solids. 2005; 351(2): 173-183.

126. Fiume E, Barberi J, Verné E, Baino F. Bioactive Glasses: From Parent 45S5 Composition to Scaffold-Assisted Tissue-Healing Therapies. Journal of Functional Biomaterials. 2018; 9(24).

127. Arstila H, Vedel E, Hupa L, Hupa M. Factors affecting crystallization of bioactive glasses. Journal of the European Ceramic Society. 2007; 27(2-3): 1543 - 1546.

128. Groh D, Döhler F, Brauer DS. Bioactive glasses with improved processing. Part 1. Thermal properties, ion release and apatite formation. Acta Biomaterialia. 2014; 10(10): 4465-4473.

129. Tylkowski M, Brauer DS. Mixed alkali effects in Bioglass® 45S5. Journal of Non-Crystalline Solids. 2013; 376: 175 - 181.

130. Brückner R, Tylkowski M, Hupa L, Brauer DS. Controlling the ion release from mixed alkali bioactive glasses by varying modifier ionic radii and molar volume. Journal of Materials Chemistry B. 2016; 4(28): 3121-3134.

131. Chen QZ, Thompson ID, Boccaccini AR. 45S5 Bioglass-derived glass-ceramic scaffolds for bone tissue engineering. Biomaterials. 2006; 27(11): 2414-2425.

132. Aalto-Setälä L, Uppstu P, Sinitsyna P, Lindfors NC, Hupa L. Dissolution of Amorphous S53P4 Glass Scaffolds in Dynamic In Vitro Conditions. Materials. 2021; 14(17): 4834.

133. Erasmus EP, Johnson OT, Sigalas I, Massera J. Effects of Sintering Temperature on Crystallization and Fabrication of Porous Bioactive Glass Scaffolds for Bone Regeneration. Scientific Reports. 2017; 7: 6046.

134. Huang W, Day DE, Kittiratanapiboon K, Rahaman MN. Kinetics and mechanisms of the conversion of silicate (45S5), borate, and borosilicate glasses to hydroxyapatite in dilute phosphate solutions. Journal of Materials Science: Materials in Medicine. 2006; 17(7): 583-596.

135. Yao A, Wang D, Huang W, Fu Q, Rahaman MN, Day DE. In vitro bioactive characteristics of borate-based glasses with controllable degradation behavior. Journal of the American Ceramic Society. 2007; 90(1): 303-306.

136. Pantulap U, Arango-Ospina M, Boccaccini AR. Bioactive glasses incorporating less-common ions to improve biological and physical properties. Journal of Materials Science: Materials in Medicine. 2022; 33(1): 3.

137. Bellucci D, Sola A, Salvatori R, Anesi A, Chiarini L, Cannillo V. Role of magnesium oxide and strontium oxide as modifiers in silicate-based bioactive glasses: Effects on thermal behaviour, mechanical properties and in-vitro bioactivity. Materials Science and Engineering: C. 2017; 72: 566-575.

138. Wetzel R, Blochberger M, Scheffler F, Hupa L, Brauer DS. Mg or Zn for Ca substitution improves the sintering of bioglass 45S5. Scientific Reports. 2020; 10(1).

139. Xynos ID, Edgar AJ, Buttery LDK, Hench LL, Polak JM. Gene-expression profiling of human osteoblasts following treatment with the ionic products of Bioglass® 45S5 dissolution. Journal of Biomedical Materials Research. 2001; 55(2): 151-157.

140. Wu C, Chang J. Multifunctional mesoporous bioactive glasses for effective delivery of therapeutic ions and drug/growth factors. Journal of Controlled Release. 2014; 193: 282-295.

141. Rabiee SM, Nazparvar N, Azizian M, Vashaee D, Tayebi L. Effect of ion substitution on properties of bioactive glasses: A review. Ceramics International. 2015; 41(6): 7241-7251.

142. Roberts TT, Rosenbaum AJ. Bone grafts, bone substitutes and orthobiologics - The bridge between basic science and clinical advancements in fracture healing. Organogenesis. 2012; 8(4): 114-124.

143. Bow AADE, Dhar M. Commercially available bone graft substitutes: the impact of origin and processing on graft functionality. Drug Metabolism Reviews. 2019; 51(4): 533-544.

144. Naseri S, Lepry WC, Nazhat SN. Bioactive glasses in wound healing: hope or hype?. Journal of Materials Chemistry B. 2017; 5(31): 6167-6174.

145. Malat TA, Glombitza M, Dahmen J, Hax PM, Steinhausen E. The Use of Bioactive Glass S53P4 as Bone Graft Substitute in the Treatment of Chronic Osteomyelitis and Infected Non-Unions - a Retrospective Study of 50 Patients. Zeitschrift fur Orthopadie und Unfallchirurgie. 2018; 156(02): 152-159.

146. Lindfors N,GJ, Drago L, Arts JJ, Juutilainen V, Hyvönen P, Suda AJ, et al. Antibacterial Bioactive Glass, S53P4, for Chronic Bone Infections - A

Multinational Study. In Drago L, editor. Advances in Experimental Medicine and Biology.: Springer, Cham; 2017. p. 81-92.

147. Armstrong DG, Orgill DP, Galiano RD, Glat PM, DiDomenico LA, Carter MJ, et al. A multi-centre, single-blinded randomised controlledclinical trial evaluating the effect of resorbable glass fibrematrix in the treatment of diabetic foot ulcers. International Wound Journal. 2022; 19(4): 791 - 801.

148. Buck DWI. Innovative Bioactive Glass Fiber Technology Accelerates Wound Healing and Minimizes Costs: A Case Series. Advances in Skin & Wound Care. 2020; 33(8): 1-6.

149. Moimas L, Biasotto M, Di Lenarda R, Olivo A, Schmid C. Rabbit pilot study on the resorbability of three-dimensional bioactive glass fibre scaffolds. Acta Biomaterialia. 2006; 2(2): 191-199.

150. Björkenheim R, Strömberg G, Ainola M, Uppstu P, Aalto-Setälä L, Hupa L, et al. Bone morphogenic protein expression and bone formation are induced by bioactive glass S53P4 scaffolds in vivo. Journal of Biomedical Materials Research - Part B Applied Biomaterials. 2019; 107(3): 847-857.

151. Eriksson E, Björkenheim R, Strömberg G, Ainola M, Uppstu P, Aalto-Setälä L, et al. S53P4 bioactive glass scaffolds induce BMP expression and integrative bone formation in a critical-sized diaphysis defect treated with a single-staged induced membrane technique. Acta Biomaterialia. 2021; 126: 463-476.

152. Lindroos B, Boucher S, Chase L, Kuokkanen H, Huhtala H, Haataja R, et al. Serum-free, xeno-free culture media maintain the proliferation rate and multipotentiality of adipose stem cells in vitro. Cytotherapy. 2009; 11(7): 958-972.

153. Kyllönen L, Haimi S, Mannerström B, Huhtala H, Rajala KM, Skottman H, et al. Effects of different serum conditions on osteogenic differentiation of human adipose stem cells in vitro. Stem Cell Research & Therapy. 2013; 4(17).

154. Ojansivu M, Vanhatupa S, Björkvik L, Häkkänen H, Kellomäki M, Autio R, et al. Bioactive glass ions as strong enhancers of osteogenic differentiation in human adipose stem cells.. Acta Biomaterialia. 2015; 21: 190-203.

155. Pfaffl MW. A new mathematical model for relative quantification in real-time RT-PCR. Nucleic acids research. 2001; 29(9).

156. Serra J, González P, Liste S, Serra C, Chiussi S, León B, et al. FTIR and XPS studies of bioactive silica based glasses. Journal of Non-Crystalline Solids. 2003; 332(1-3): 20-27.

157. Pascuta P, Bosca M, Rada S, Culea M, Bratu I, Culea E. FTIR spectro-scopic study of Gd2O3-Bi2O3-B2O3 glasses. Journal of Optoelectronics and Advanced Materials. 2008; 10: 2416-2419.

158. Bunker BC, Tallant DR, Kirkpatrick RJ, Turner GL. Multinuclear nuclear nuclear magnetic resonance and Raman investigation of sodium borosilicate glass structures. Physics and chemistry of glasses. 1990; 31(1): 30–41.

159. Fukumi K, Hayakawa J, Komiyama T. Intensity of raman band in silicate glasses. Journal of Non-Crystalline Solids. 1990; 119(3): 297-302.

160. Manara D, Grandjean A, Neuville DR. Advances in understanding the structure of borosilicate glasses: A Raman spectroscopy study. American Mineralogist. 2009; 94(5-6): 777-784.

161. Neuville DR. Viscosity, structure and mixing in (Ca, Na) silicate melts. Chemical geology. 2006; 229(1-3): 28-41.

162. Mysen BO, Frantz JD. Raman spectroscopy of silicate melts at magmatic temperatures: Na2O-SiO2, K2O-SiO2 and Li2O-SiO2 binary compositions in the temperature range 25–1475 C. Chemical geology. 1992; 96(3-4): 321-332.

163. Fujikura K, Karpukhina N, Kasuga T, Brauer DS, Hill RG, Law RV. Influence of strontium substitution on structure and crystallisation of Bioglass® 45S5. Journal of Materials Chemistry. 2012; 22(15): 7395-7402.

164. Akagi R, Ohtori N, N. U. Raman spectra of K2O-B2O3 glasses and melts. Journal of Non-Crystalline Solids. 1990; 126: 224-230.

165. Meera BN, Sood AK, Chandrabhas N, Ramakrishna J. Raman study of lead borate glasses. Journal of Non-Crystalline Solids. 1990; 126(3): 224-230.

166. Yu Y, Edén M. Structure–composition relationships of bioactive borophosphosilicate glasses probed by multinuclear 11B, 29Si, and 31P solid state NMR. RSC Advances. 2016; 6: 101288-101303.

167. Pedone A, Charpentier T, Malavasi G, Menziani MC. New Insights into the Atomic Structure of 45S5 Bioglass by Means of Solid-State NMR Spectroscopy and Accurate First-Principles Simulations. Chemistry of Materials. 2010; 22: 5644–5652.

168. Angeli F, Villain O, Schuller S, Charpentier T, de Ligny D, Bressel L, et al. Effect of temperature and thermal history on borosilicate glass structure. Physical Review B. 2012; 85(5): 054110.

169. Howes AP, Vedishcheva NM, Samoson A, Hanna JV, Smith ME, Holland D, et al. Boron environments in Pyrex® glass—a high resolution, Double-Rotation NMR and thermodynamic modelling study. Physical Chemistry Chemical Physics. 2011; 13(25): 11919-11928.

170. Raynaud S, Champion E, Bernache-Assollant D, Thomas P. Calcium phosphate apatites with variable Ca/P atomic ratio I. Synthesis, characterisation and thermal stability of powders. Biomaterials. 2002; 23(4): 1065-1072.

171. Queiroz AC, Santos JD, Monteiro FJ, Prado da Silva MH. Dissolution studies of hydroxyapatite and glass-reinforced hydroxyapatite ceramics. Materials Characterization. 2003; 50(2-3): 197-202.

172. Berzina-Cimdina L, Borodajenko N. Research of Calcium Phosphates Using Fourier Transform Infrared Spectroscopy. In Theophanides T, editor. Infrared Spectroscopy - Materials Science, Engineering and Technology.: InTech; 2012. p. 123-148.

173. Fredholm YC, Karpukhina N, Law RV, Hill RG. Strontium containing bioactive glasses: glass structure and physical properties. Journal of Non-Crystalline Solids. 2010; 356(44-49): 2546-2551.

174. Agathopoulos S, Tulyaganov DU, Ventura JMG, Kannan S, Saranti A, Karakassides MA, et al. Structural analysis and devitrification of glasses based on the CaO–MgO–SiO2 system with B2O3, Na2O, CaF2 and P2O5 additives. Journal of Non-Crystalline Solids. 2006; 352(4): 322-328.

175. Liu H, Yazici H, Ergun C, Webster TJ, Bermek H. An in vitro evaluation of the Ca/P ratio for the cytocompatibility of nano-to-micron particulate calcium phosphates for bone regeneration. Acta Biomaterialia. 2008; 4(5): 1472-1479.

176. Du WF, Kuraoka K, Akai T, Yazawa T. Study of Al2O3 effect on structural change and phase separation in Na2O-B2O3-SiO2 glass by NMR. Journal of Materials Science. 2000; 35(19): 4865 - 4871.

177. Massera J, Claireaux C, Lehtonen T, Tuominen J, Hupa L, Hupa M. Control of the thermal properties of slow bioresorbable glasses by boron addition. Journal of Non-Crystalline Solids. 2011; 357(21): 3623-3630.

178. Yu Y, Bacsik Z, Edén M. Contrasting In Vitro Apatite Growth from Bioactive Glass Surfaces with that of Spontaneous Precipitation. Materials (Basel, Switzerland). 2018; 11(9).

179. Stevensson B, Mathew R, Edén M. Assessing the Phosphate Distribution in Bioactive Phosphosilicate Glasses by 31P Solid-State NMR and Molecular Dynamics Simulations. The Journal of Physical Chemistry B. 2014; 118(29): 8863–8876.

180. Massera J, Haldeman A, Milanese D, Gebavi H, Ferraris M, Foy P, et al. Processing and characterization of core–clad tellurite glass preforms and fibers fabricated by rotational casting. Optical Materials. 2010; 32(5): 582-588.

181. Massera J, Claireaux C, Lehtonen T, Tuominen J, Hupa L, Hupa M. Control of the thermal properties of slow bioresorbable glasses by boron addition. Journal of Non-Crystalline Solids. 2011; 357(21): 3623-3630.

182. Starink MJ. The determination of activation energy from linear heating rate experiments: a comparison of the accuracy of isoconversion methods. Thermochimica Acta. 2003; 404(1-2): 163-176.

183. Massera J, Mayran M, Rocherullé J, Hupa L. Crystallization behavior of phosphate glasses and its impacton the glasses' bioactivity. Journal of Materials Science. 2015; 50: 3091–3102.

184. Clupper DC, Hench LL. Crystallization kinetics of tape cast bioactive glass 45S5. Journal of Non-Crystalline Solids. 2003; 315(1-2): 43-48.

185. Pohjola J. Borosilicate Scaffold Processingfor Bone Tissue Engineering. Tampere:; 2017.

186. Bellucci D, Cannillo V, Sola A. An Overview of The Effects of Thermal Processing on Bioactive Glasses. Science of Sintering. 2010; 42: 307-320.

187. Blaeß C, Müller R, Poologasundarampillai G, Brauer DS. Sintering and concomitant crystallization of bioactive glasses. International Journal of Applied Glass Science. 2019; 10: 449– 462.

188. Iordache F. Chapter 2 - Bioprinted scaffolds. In Holban AM, Grumezescu AM, editors. Materials for Biomedical Engineering: Hydrogels and Polymer-based Scaffolds.: Elsevier; 2019. p. 35-60.

189. Diba M, Tapia F, Boccaccini AR, Strobel LA. Magnesium-Containing Bioactive Glasses for Biomedical Applications. International Journal of Applied Glass Science. 2012; 3(3): 221 - 253.

190. Souza MT, Crovace MC, Schröder C, Eckert H, Peitl O, Zanotto ED. Effect of magnesium ion incorporation on the thermal stability, dissolution behavior and bioactivity in Bioglass-derived glasses. Journal of Non-Crystalline Solids. 2013; 382: 57-65.

191. Fu Q, E S, Tomsia AP. Bioinspired Strong and Highly Porous Glass Scaffolds. Advanced functional materials. 2011; 21(6): 1058–1063.

192. Liu Y, Wang YM, Pang HF, Zhao Q, Liu L. A Ni-free ZrCuFeAlAg bulk metallic glass with potential for biomedical applications. Acta Biomaterialia. 2013; 9(6): 7043-7053.

193. Liu X, Rahaman MN, Hilmas GE, Bal BS. Mechanical properties of bioactive glass (13-93) scaffolds fabricated by robotic deposition for structural bone repair. Acta Biomaterialia. 2013; 9(6): 7025-7034.

194. Perren SM. Evolution of the internal fixation of long bone fractures. Journal of Bone and Joint Surgery - Series B. ; 84(8): 1093 - 1110.

195. Schemitsch EH. Size Matters: Defining Critical in Bone Defect Size! Journal of Orthopaedic Trauma. 2017; 31: S20 - S22.

196. Siekkinen M, Karlström O, Hupa L. Dissolution of bioactive glass S53P4 in a three-reactor cascade in continuous flow conditions. Open Ceramics. 2023; 13: 100327.

197. Taipale S, Ek P, Hupa M, Hupa L. Continuous measurement of the dissolution rate of ions from glasses. Advanced Materials Research. 2008; Glass(39-40): 341–346.

198. Tainio JM, Avila Salazar DA, Nommeots-Nomm A, Roiland C, Bureau B, Neuville DR, et al. Structure and in vitro dissolution of Mg and Sr containing borosilicate bioactive glasses for bone tissue engineering. Journal of Non-Crystalline Solids. 2020; 533: 119893.

199. Filho OP, G.P. LT, Hench LL. Effect of crystallization on apatite-layer formation of bioactive glass 4S55. Journal of Biomedical Materials Research. 1996; 30: 509-514.

200. Fu Q, Rahaman M, Bal B, Huang W, Day D. Preparation and bioactive characteristics of a porous 13–93 glass, and fabrication into the articulating surface of aproximal tibia. Journal of Biomedical Materials Research - Part A. 2007; 82(1): 222-229.

201. Kaur G, Pandey OP, Singh K, Homa D, Scott B, Pickrell G. A review of bioactive glasses: Their structure, properties, fabrication and apatite formation. Journal of Biomedical Materials Research part A. 2014; 102A: 254– 274.

202. Ojansivu M, Wang X, Hyväri L, Kellomäki M, Hupa L, Vanhatupa S, et al. Bioactive glass induced osteogenic differentiation of human adipose stem cells is dependent on cell attachment mechanism and mitogen-activated protein kinases. European Cells and Materials. 2018; 35: 54-72.

203. Rybchyn MS, Slater M, Conigrave AD, Mason RS. An Akt-dependent increase in canonical Wnt signaling and a decrease in sclerostin protein levels are involved in strontium ranelate-induced osteogenic effects in human osteoblasts. The Journal of Biological Chemistry. 2011; 286(27): 23771-23779.

204. Komori T. Roles of Runx2 in Skeletal Development. In Groner Y, Ito Y, Liu P, Neil J, Speck N, van Wijnen A, editors. RUNX Proteins in Development and Cancer. Advances in Experimental Medicine and Biology, vol 962. Singapore: Springer; 2017. p. 83–93.

205. Nakashima K, Zhou X, Kunkel G, Zhang Z, Deng JM, Behringer RR, et al. The novel zinc finger-containing transcription factor osterix is required for osteoblast differentiation and bone formation. Cell. 2002; 108(1): 17-29.

206. Lee MH, Kim YJ, Yoon WJ, Kim JI, Kim BG, Hwang YS, et al. Dlx5 specifically regulates Runx2 type II expression by binding to homeodomain-response elements in the Runx2 distal promoter. Journal of Biological Chemistry. 2005; 280(42): 35579-35587.

207. Randi AM, Laffan MA. Von Willebrand factor and angiogenesis: basic and applied issues. Journal of Thrombosis and Haemostasis. 2017; 15(1): 13-20.

208. Lertkiatmongkol P, Liao D, Mei H, Hu Y, Newman PJ. Endothelial functions of PECAM-1 (CD31). Current opinion in hematology. 2016; 23(3): 253–259.

209. Clare AG. The Unique Nature of Glass. In Jones JR, Clare AG, editors. Bio-Glasses: An Introduction.: John Wiley & Sons, Ltd.; 2012. p. 1-12.

APPENDIX I – SCAFFOLD STRESS-STRAIN CURVES

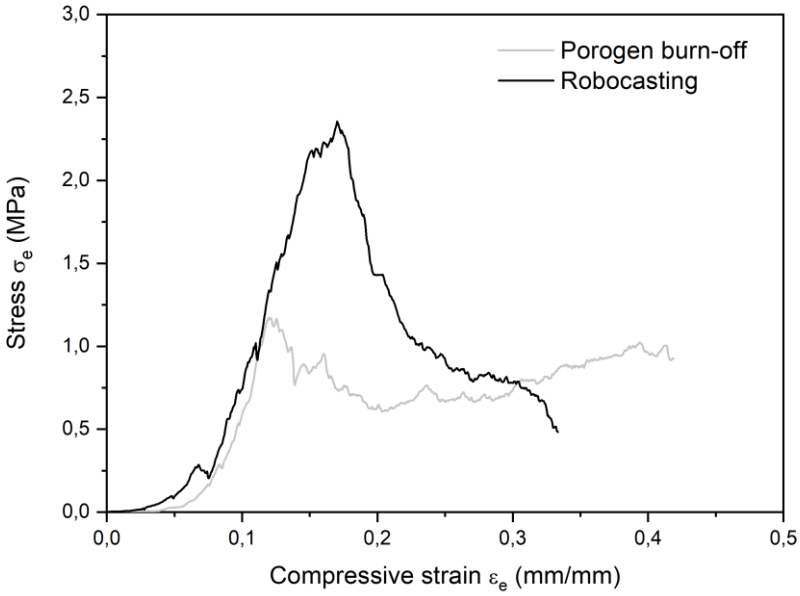

Supplementary Figure 1. Examples of stress-strain curves for scaffolds prepared both by porogen burn-off and 3D-printing (robocasting.)

APPENDIX II – SI AND B RELEASE UPON SBF IMMERSION

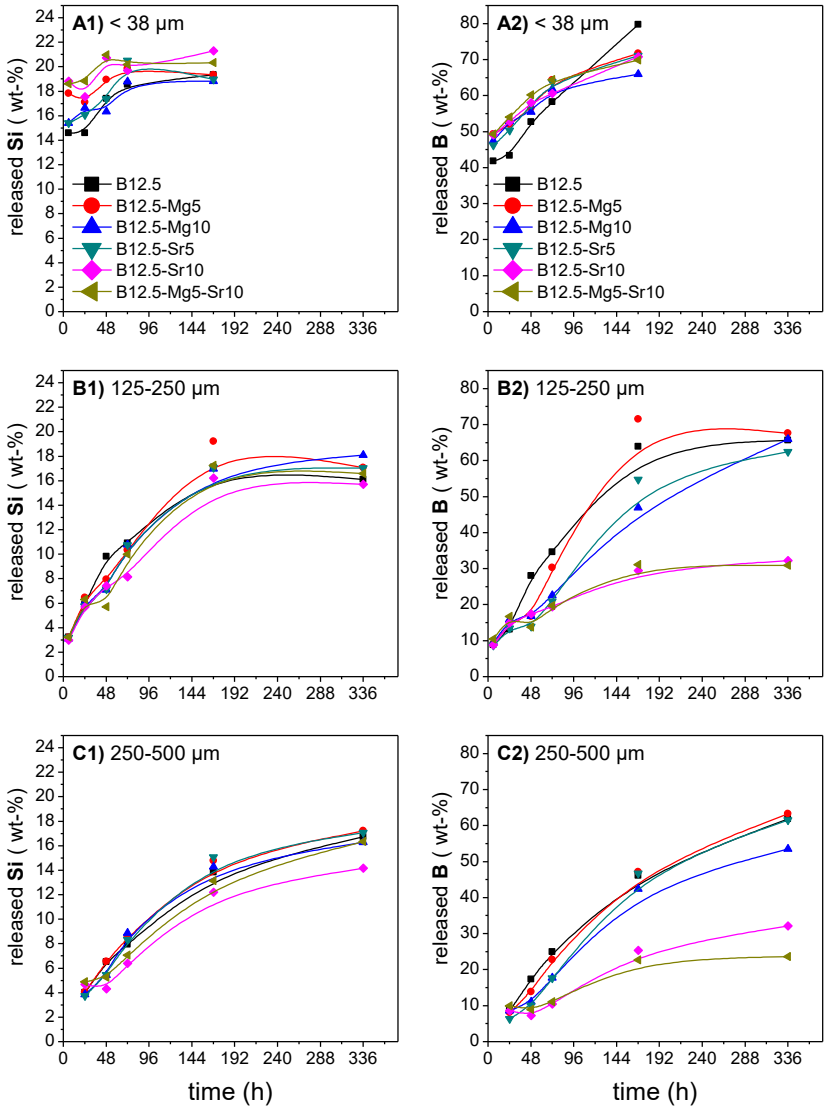

Supplementary Figure 2. Amount of released **1**) silicon and **2**) boron from the theoretical maximum in the studied glass composition (weight-%). Particle size immersed in SBF **A**) < 38 µm, **B**) 125-250 µm and **C**) 250-500 µm.

I

STRUCTURE AND IN VITRO DISSOLUTION OF MG AND SR CONTAINING BOROSILICATE BIOACTIVE GLASSES FOR BONE TISSUE ENGINEERING

by

Jenna M. Tainio, Diana A. Avila Salazar, Amy Nommeots-Nomm, Claire Roiland, Bruno Bureau, Daniel R. Neuville, Delia S. Brauer and Jonathan Massera

Journal of Non-Crystalline Solids Vol 533, Article ID 119893, 1 April 2020.

Contents lists available at ScienceDirect

Journal of Non-Crystalline Solids

journal homepage: www.elsevier.com/locate/jnoncrysol

Structure and in vitro dissolution of Mg and Sr containing borosilicate bioactive glasses for bone tissue engineering

J.M. Tainio[a,*], D.A. Avila Salazar[b], A. Nommeots-Nomm[a], C. Roiland[c], B. Bureau[c], D.R. Neuville[d], D.S. Brauer[b], J. Massera[a]

[a] Faculty of Medicine and Health Technology, Tampere University, Korkeakoulunkatu 10, FI-33720 Tampere, Finland
[b] Otto-Schott-Institut, Friedrich-Schiller-Universität, Fraunhoferstr. 6, 07743 Jena, Germany
[c] Institut Sciences Chimiques de Rennes, UMR-CNRS 6226, Campus de Beaulieu, Université de Rennes 1, 35042 Rennes Cedex, France
[d] Géomatériaux, CNRS-IPGP, 1 rue Jussieu, Paris 75005, France

ARTICLE INFO

Keywords:
Borosilicate glasses
Bioactive glasses
Tissue engineering
Structural properties
In vitro dissolution

ABSTRACT

Borosilicate bioactive glasses are promising for bone tissue engineering. The objective was to assess the impact of magnesium and/or strontium, when substituted for calcium on the glasses' thermal and dissolution properties. Both Mg and Sr substitution appeared to enhance the hot forming domain, i.e. the ability to hot process (sinter, draw fibres) without adverse crystallization. Structural analysis indicated that substitution of MgO and/or SrO for CaO results in changes in the BO_3/BO_4 ratio as well as in the ratio between bridging and non-bridging oxygen atoms in the silicate structure. Additionally, a de-shielding effect was noticed when Ca, Mg and Sr are present together in the glass network, possibly owing to PO_4^{3-} charge-balanced preferentially by Na^+. The Mg and/or Sr substitution resulted in a lower ion release in simulated body fluid and delayed formation of hydroxyapatite. However, once this layer formed it consisted of a Mg/Sr-substituted apatite. This work highlights the effect of combined ionic substitutions on bioactive glass structure and properties.

1. Introduction

Currently, regenerative medicine still utilizes tissue grafts as the gold standard in the reconstruction of bone defects. However, tissue grafts have many limitations, where lack of availability is one of the most substantial. Although major progress in the field of bone tissue engineering has been achieved over recent years, much work is needed to develop an ideal synthetic alternative. One promising biomaterial group for this intention are bioactive glasses, which are able to rapidly bond to bone tissue, and have osteostimulating properties [1,2].

The commercial silicate bioactive glass S53P4 is used successfully in clinical applications, but the composition still has some drawbacks, such as its incomplete degradation in vivo [3]. In addition, many melt-derived silicate bioactive glasses have high tendency to crystallize upon heat-treatment, thereby limiting the use of hot forming processes necessary in obtaining glass 3D-scaffold structures [4–7].

To improve dissolution of traditional silicate bioactive glasses, substitution of SiO_2 with B_2O_3 has been studied. When compared to silicate glasses, borate glasses have higher degradation rates, and they have been found to convert more completely into hydroxyapatite (HA)-like material [8]. The release of boron during in vitro cell culture testing has been found to negatively affect cell proliferation [9–11]. However, in a study with human adipose stem cells (hASC) it was seen that while the hASC showed slower proliferation rates with borosilicate glasses than on the silicate counterpart, the release of boron (both in contact and elution test) promoted expression of osteogenic markers and mineralization [12]. Additionally, in suitable amounts boron has been seen to stimulate angiogenesis, which is necessary for the repair of bone tissue [9,13]. In addition, borosilicate bioactive glasses have been found promising for soft tissue engineering applications and wound healing [14]. Therefore, borosilicate glasses offer great potential for tissue engineering applications.

Boron incorporation into silicate bioactive glasses has also been found to drastically improve thermal properties as seen an increase in the hot forming domain [15–17]. However, boron is not the only element to improve glass against crystallization. In general, alkaline earth ions have been found to increase the working range for hot forming applications [18]. For example, the substitution of MgO for CaO leads to a shift of the viscosity vs. temperature curve, resulting in improved sintering [19]. It has been seen that substituting SrO for CaO increases the hot forming domain, if the SrO content remained below 10 mol% in S53P4 [20]. MgO and SrO are of particular interest for bioactive glass

* Corresponding author.
E-mail address: jenna.tainio@tuni.fi (J.M. Tainio).

https://doi.org/10.1016/j.jnoncrysol.2020.119893
Received 17 October 2019; Received in revised form 3 January 2020; Accepted 6 January 2020
Available online 23 January 2020

applications since these elements are known to promote new bone formation and the formation of Mg- or Sr-substituted HA. Sr-substituted HA has additionally been shown to be successful for the treatment of bone defects in osteoporotic patients. [21–23]. In bioactive glasses, when Ca is substituted with Sr, a slower dissolution rate and slower HA precipitation is observed. Despite this, the presence of Sr has been found to enhance the proliferation of human gingival fibroblasts on both silicate and phosphate bioactive glasses [24].

In the present study, the clinically utilized commercial glass composition BonAlive® S53P4 was modified by the substitution of B_2O_3 for SiO_2, as well as with replacing varying amounts of the Ca with Mg and/or Sr. This was to enhance the hot forming domain as well as promote the precipitation of a Mg/Sr-substituted HA layer. The aim was to obtain a thorough understanding of how such substitutions can be used to optimise glass properties, by correlating structural and property changes. The impact of Ca substitution with Mg and/or Sr on the precipitation of hydroxyapatite upon immersion in simulated body fluid was also ascertained. The goal was to develop new bioactive glasses with tailored glass dissolution and optimum thermal properties for future processing into 3D porous scaffolds.

2. Materials and methods

2.1. Glass preparation

Borosilicate bioactive glasses were prepared with a molar composition of 47.12 SiO_2 – 6.73 B_2O_3 – 21.77 (-x-y) CaO – 22.65 Na_2O – 1.72 P_2O_5 – x MgO – y SrO (mol-%), where x,y = 0, 5 or 10 mol-%. Glass compositions are presented in Table 1. The base glass of this study (x,y = 0) will be referred to as B12.5.

Batches were prepared from mixtures of sand (99,4% of pure SiO_2) and analytical grade reagents from Sigma Aldrich (H_3BO_3, MgO, $SrCO_3$, $(NH_4)H_2PO_4$, Na_2CO_3) and ThermoFisher ($CaCO_3$). The raw materials were melted in a platinum crucible in an electric furnace (P310, Nabertherm GmbH, Lilienthal, Germany) under air atmosphere at 1300 °C, for 1 h Melts were poured into pre-heated graphite moulds to obtain either rectangular blocks or cylindrical rods (diameter 10 mm). Annealing was performed at 15–40 K below the glasses' respective glass transition temperature for 5–12 h. Glass blocks were crushed and sieved to particle size fractions < 38, 125–250 and 250–500 μm. The particle size distribution of the ground glasses was analysed by dynamic light scattering using a Mastersizer 2000 with Hydro 2000S module (Malvern Instruments, Worcestershire, United Kingdom). The glass rods were cut to discs (height 2 mm) using a diamond wheel saw (650 CE, South Bay Technology Inc, California, USA) and wet polished (using water) by hand (Knuth-Rotor 2, Struers, Denmark) to 4000 grit silicon carbide grinding paper (Struers).

2.2. Thermal, physical and structural properties

Glass transition (T_g) (taken at midpoint), onset of crystallization (T_x) and crystallization peak (T_p) temperatures were determined using differential thermal analysis (STA 449 F1 Jupiter, Netzsch Group, Selb, Germany) in Pt-Rh crucibles at a heating rate of 10 K/min from 40 to 1200 °C in N_2 atmosphere. Glass density was measured using a gas displacement helium pycnometer (AccuPyc 1330, Micromeritics, Georgia, USA) with an accuracy of ± 0.01 g/cm^3. Using the measured density, the molar volume, V_M, was calculated as following: $V_M = M/\rho$ where ρ is the density and M the molar mass of the glass.

Structural analysis was performed using Fourier-transform infrared (FTIR) and Raman spectroscopy as well as ^{31}P and ^{11}B MAS NMR. FTIR was performed using a Perkin Elmer Spectrum One FTIR spectrophotometer in attenuated total reflectance (ATR) mode. Spectra were recorded in the range of 600–1600 cm^{-1}, corrected for Fresnel losses, background corrected and normalized to the band having maximum intensity. All presented spectra are an average of 8 scans and have a resolution of 1 cm^{-1}. Raman measurements were performed using a T64000 Jobin-Yvon confocal microRaman spectrometer equipped with a CCD detector. The 488.01 nm line of a coherent 70-C5 Ar^+ laser operating at 100 mW at the sample was used for sample excitation. For the samples examined here, this excitation and CCD system result in a signal-to-noise ratio of 80/1. The integration time was 300 s. All reported spectra are unpolarized, background corrected and normalized to the peak with the highest intensity. ^{31}P single pulse solid-state MAS NMR spectra were recorded at room temperature on a Bruker AVANCE III HD NMR spectrometer with magnetic field B_0 = 9.4 T. Magic angle spinning (MAS) was performed using a commercial 4 mm rotor. All chemical shift values (δ_{iso}) were quoted with respect to 85% H_3PO_4. Quantitative spectra with 16 accumulations were taken at a spinning frequency of 12.5 kHz and nutation frequency of 69.4 kHz after adjusting the delay time (D_1) to five times the longest spin-lattice relaxation time (T_1). The latter was calculated after the measurement of a 2-scan (T_1) saturation recovery experiment followed by further processing such as the fitting of the line-shape of the pseudo 2D spectrum (Bruker NMR Software, Top-spin, Version 3.5 pl 7, April 3, 2017). ^{11}B spin echo solid-state MAS NMR spectra were recorded at room temperature on a Bruker AVANCE III NMR spectrometer with magnetic field B_0 = 14 T. MAS was performed using a commercial 2.5 mm rotor spun at 30 kHz. The pulse lengths were 1 and 2 μs for P1 and P2, respectively, which corresponded to a flip angle less than 30°. The echo delay was set to 1 rotor period, i.e. 33.33 μs. The recycle delay was 1 s. The probe signal was removed from ^{11}B spectra. T_2 measurements were performed using a 2D spin-echo pulse program. All δ_{iso}values are quoted with respect to 1 M boric acid solution. Spectra were fitted using Dmfit software [25].

Table 1
Oxide compositions of the studied glasses in mol%.

Glass	SiO_2	B_2O_3	CaO	Na_2O	P_2O_5	MgO	SrO
B12.5	47.12	6.73	21.77	22.66	1.72	–	–
B12.5-Mg5	47.12	6.73	16.77	22.66	1.72	5	–
B12.5-Mg10	47.12	6.73	11.77	22.66	1.72	10	–
B12.5-Sr5	47.12	6.73	16.77	22.66	1.72	–	5
B12.5-Sr10	47.12	6.73	11.77	22.66	1.72	–	10
B12.5-Mg5-Sr10	47.12	6.73	6.77	22.66	1.72	5	10

2.3. In vitro dissolution

Dissolution tests were performed in simulated body fluid (SBF) ranging from 6 h to two weeks (approximately 336 h). SBF solution was prepared following the protocol presented in reference [26]. Reagents used were NaCl, $NaHCO_3$, KCl, K_2HPO_4, MgCl, CaCl, Na_2SO_4 (VWR Chemicals) and Tris ultra pure (MP Biomedicals). Glass samples were immersed in 50 ml of SBF solution and placed in an incubating shaker (Multitron AJ 118 g, Infors, Bottmingen, Switzerland) at 37 °C and 100 rpm for 6, 24, 48, 72, 168 and 336 h. The ratio of surface area to volume of SBF was kept constant by taking into account the change in average particle size (assuming spherical particles) as well as changes in density induced by changes in composition. The amount of immersed glass particles ranged therefore from 75 mg to 80.3 mg (± 0.5 mg). Polished discs (diameter about 10 mm, height about 2 mm) had an average weight around 330 ± 50 mg.

At each time point, the pH of the dissolution medium was measured at 37 °C (± 0.2 °C) with a pH-metre (SevenMulti MP 225, Mettler Toledo International Inc., Greifensee, Switzerland). For ion concentration analysis, 1 ml of solution was diluted with 9 ml of 1 M nitric acid, and measured using inductively coupled plasma optical emission spectrometry (ICP-OES, Agilent Technologies, USA). Analysed elements were Si (at wavelength 288.158 nm), B (208.956 nm), Ca (393.366 nm), P (253.561 nm), Mg (279.553 nm) and Sr (407.771 nm). The immersed glass specimens were filtrated and rinsed with acetone to

stop further reactions, then dried. The specimens were analysed using FTIR spectrometry (range 600–4000 cm^{-1}, further details mention in previous section). Some of the glass particles were embedded in resin and polished to reveal the particles' cross section. Composition and structure of the glass powders post immersion were analysed using scanning electron microscopy with energy dispersive X-ray spectroscopy (SEM/EDX Leo 1530 Gemini, Zeiss, and EDXA UltraDry, Thermo Scientific). The accuracy of the elemental analysis was 0.1 wt%.

3. Results and discussion

Density and molar volume give an indication of the compactness of the glass network. The density and molar volume of the base glass B12.5 were found to be 2.66 ± 0.01 g/cm^3 and 23.2 ± 0.2 cm^3/mol, respectively. Partial substitution of Mg for Ca led to a slight decrease in both density (down to 2.62 ± 0.01 g/cm^3) and molar volume (22.9 ± 0.2 cm^3/mol). This decrease in density is related to the lower atomic mass and higher field strength of Mg compared to Ca. The smaller size of Mg^{2+} also leads to compaction of the network [19]. The change in density and molar volume can also be assigned to the change in coordination number [27] and possibly the intermediate role that Mg has been reported to play [28]. Substitution by Sr led to an increase in density (up to 2.84 ± 0.01 g/cm^3) owing to the larger mass of Sr compared to Ca. No significant impact on the molar volume was observed (23.4 ± 0.2 cm^3/mol) within the accuracy of the measurements. This means that despite the larger ionic radius of Sr^{2+} and lower ionic strength compared to Ca^{2+}, the glass network does not appear to either expand or contract upon substitution [20]. For the glass containing both Mg and Sr, density was 2.81 ± 0.01 g/cm^3 and molar volume 23.3 ± 0.2 cm^3/mol.

T_g, T_x and T_p, as well as ΔT ($\Delta T = T_x - T_g$), the hot forming domain, are presented in Table 2. Substitution of Mg for Ca led to a decrease in T_g and an increase in T_p and ΔT. Substitution of Sr for Ca led to a decrease in T_g; however, no clear trend for T_x, T_p or ΔT could be observed. The DTA curve for glass composition B12.5-Mg5-Sr10, containing both Mg and Sr, exhibited two T_g's. ΔT was calculated using the higher T_g. This mixed glass exhibited lower T_g, T_x, T_p and a smaller ΔT than the base glass B12.5. ΔT increased by up to 25 K with 10% Ca for Mg substitution, as expected from the literature [19]. The glass composition with 10 mol% Sr exhibited an extended ΔT, therefore making it the most suitable for hot forming processes. This agrees with our previous study, where we found that when the molar content of SrO in a bioactive glass exceeds 5 mol%, crystallization rate and peak intensity decreased [20]. However, for the glasses studied here, this did not narrow the working range as in our previous study [20]. The presence of two T_g's in the Mg/Sr substituted glass may indicate significant phase separation, possibly suggesting that Ca, Sr and Mg have different affinities to the P_2O_5, SiO_2 or B_2O_3 sub-networks. The large ΔT recorded for the glasses of investigation are promising toward glass sintering without risk of uncontrolled crystallization.

Structural properties were analysed by FTIR, Raman and MAS NMR spectroscopy. Fig. 1 presents the FTIR spectra of all glasses investigated here. The spectra all look very similar, and they show features characteristic for borosilicate glasses. The band around 750 cm^{-1} is assigned to Si-O bending. The bands at 950 cm^{-1} and in the 1100–1150 cm^{-1} region correspond to Si-O^- and Si—O—Si asymmetric stretching of the silicate network. [19,20,29]. Additionally, B—O stretching vibration in BO_4 units also appear in the 850–1150 cm^{-1} range, and the broad band around 1400 cm^{-1} corresponds to B—O vibration in borate triangles formed by BO_3. Boron in the form of BO_2O^- is expected to lead to a band of low intensity at 1227 cm^{-1}. [30]. One should note that, in the case of borosilicate, the overlapping of the BO_3, BO_4, bridging (bO) and non-bridging oxygen atoms (nbO) in the silicate network makes it challenging to effectively draw conclusion on the glass structure. Raman spectroscopy, however, should allow elucidation of the impact of modifiers on the borate and silicate structure.

Table 2
Tg, Tx and Tp of the investigated glasses. ΔT presents the hot forming domain, i.e. working range of the B12.5-glass series. DTA performed on glass particles sieved to 250–500 μm.

Glass	T_g (± 2 °C)	T_x (± 2 °C)	T_p (± 2 °C)	$\Delta T = T_g - T_x$ (± 4 °C)
B12.5	529	691	772	162
B12.5-Mg5	513	678	781	165
B12.5-Mg10	500	687	795	187
B12.5-Sr5	512	659	780	147
B12.5-Sr10	502	675	772	173
B12.5-Mg5-Sr10	472/507	647	725	140/175

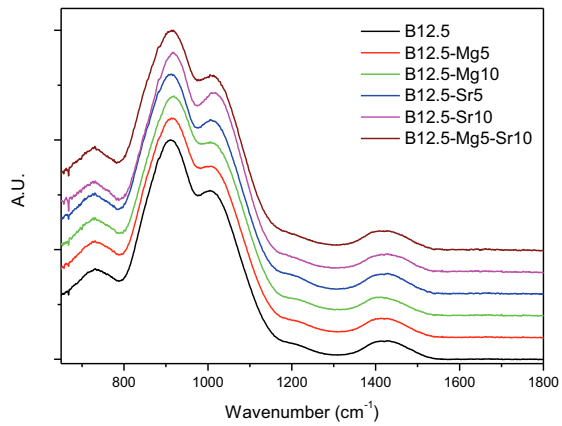

Fig. 1. Stacked FTIR spectra of the investigated glasses of particle sizes in the range 125–250 μm.

Fig. 2 presents the Raman spectra of all glasses, measured from various areas per specimen (side and centre of the disc) and on two different specimens from different batches. All spectra exhibit similar vibrations. The bands in the 300–500 cm^{-1} region are related to mixed stretching and bending modes of Si—O—Si bonds [31]. The peaks around 950–980 cm^{-1} and 1050–1100 cm^{-1} are characteristic for Si—O stretching with two and three nbO per silicon atom (i.e. Q^2 and Q^3 structural units), respectively [32–35]. Peaks around the 550–850 cm^{-1} region are typically indicative of breathing ring modes of borate- and borosilicate ring units. Therefore, the band seen at 630 cm^{-1} can be attributed to a breathing mode of borosilicate rings. [31–33]. Within the 1250–1500 cm^{-1} region the B-O stretching vibration can be found. The peak at around 1410 cm^{-1} is assigned to BO_3 units bonding to BO_4, and the one at around 1480 cm^{-1} to BO_3 units connected to another BO_3 unit. [36–38].

While all spectra tend to overlap in the case of glass B12.5, this was not necessarily the case for the other glass compositions, which makes comparisons between glass compositions challenging. It suggests that replacing Ca with either Mg or Sr led to structural inhomogeneity. The variation in structure within one sample or between samples were greater in the case of Mg substitution than for Sr substitution. While the boron network did not seem to be greatly affected, significant variations were recorded in the Q_2/Q_3 ratio for SiO_2. This is not yet fully understood and further investigations are ongoing to clarify this point. However, one hypothesis could be a non-uniform distribution of Ca, Sr and Mg within the borate and silicate thereby, owing to some elements possibly having a higher affinity to one forming units than the others [39].

To clarify the role played by phosphorus and boron in the network, ^{31}P (Fig. 3a) and ^{11}B (Fig. 3b) MAS NMR spectra were recorded. In

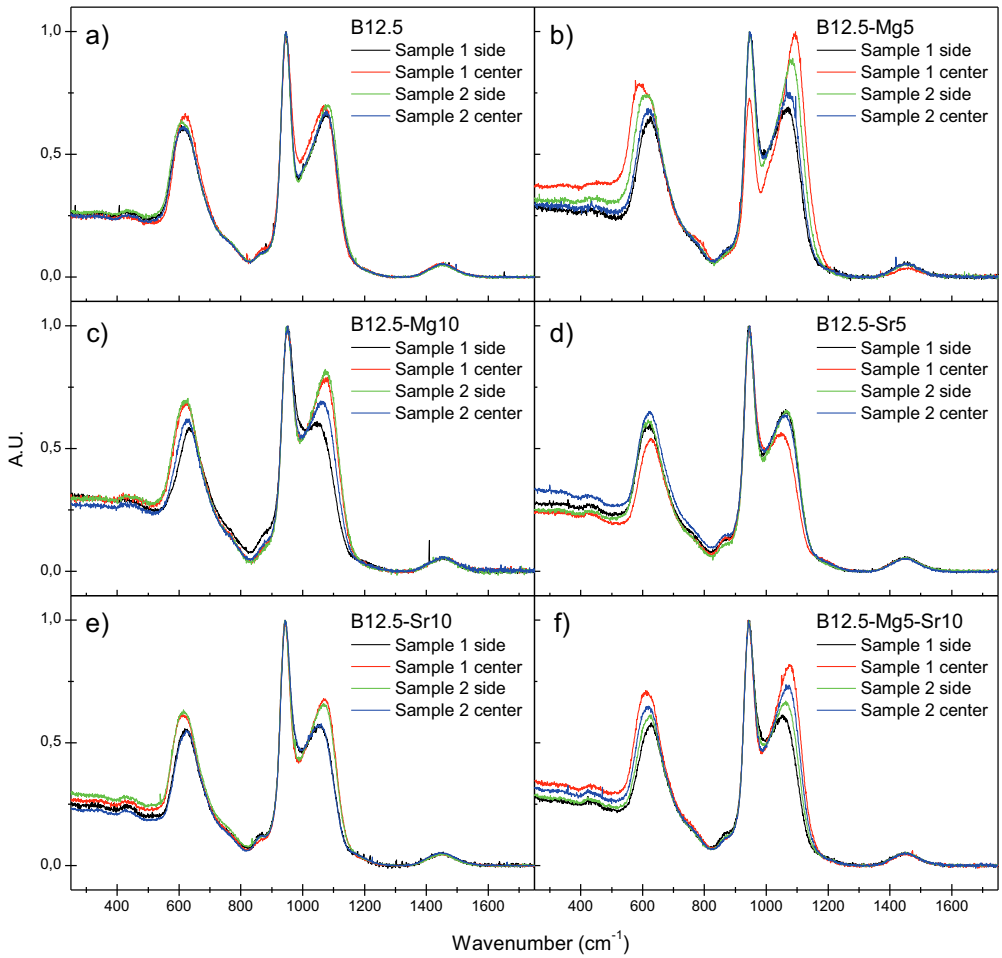

Fig. 2. Normalized Raman spectra of the investigated borosilicates: (a) base borosilicate B12.5, (b,c) magnesium containing glasses, (d,e) strontium containing glasses and (f) mixed glass with both Mg and Sr.

Fig. 3a, the peak at 8–9 ppm indicates phosphorus present in Q_P^0 (orthophosphate) groups, while the tail at -3 ppm may [40] or may not [41] be related to Q_P^1 phosphate units, i.e. phosphate groups connected to the silicate network. As expected from previous work on bioactive glasses, Q_P^0 tetrahedra are dominant over the whole range of glass compositions, while a low amount (if any) of Q_P^1 tetrahedra can be only seen as a shoulder of the main peak [42]. he absence of any changes in ^{31}P chemical shift in the first three compositions (B12.5, B12.5-Mg10 and B12.5-Sr10), i.e. with substitution of Mg or Sr for Ca, might suggest that P_2O_5 reacts preferentially with CaO and Na_2O instead of MgO or SrO. In bioactive phosphosilicate glasses, where with a P_2O_5 content <6 mol%, orthophosphate anions are charge-balanced by Na^+/Ca^{2+} distributed randomly [40]. In the current system (1.72 mol% P_2O_5) P might only be surrounded by Na^+/Ca^{2+} in all glasses except the mixed Mg/Sr glass. The de-shielding effect observed for the mixed Mg/Sr glass (Fig. 3a) might be interpreted as an increased Na/Ca ratio surrounding PO_4^{3-} groups.

In ^{11}B MAS NMR spectra (Fig. 3b), the peak at 11.8–12.4 ppm can be assigned to BO_3 units while the peak in the ~0 to -3 ppm region can be assigned to BO_4 [43]. Transversal relaxation time, T_2, was measured for each composition. T_2 values obtained are 42 ms and 27 ms for BO_3 and BO_4, respectively, and showed no variation with glass composition. Moreover, the echo delay (1 μs) can be neglected compared to T_2. Therefore, the ratio of the two chemically distinct boron sites (BO_3 and BO_4) can be determined directly by fitting ^{11}B NMR spectra without any correction of T_2 relaxation. The ratios obtained are presented in Table 3. In glass composition B12.5, approximately equal amount of BO_3 and BO_4 are detected (51.5 and 48.5%, respectively). However, when Ca is replaced, a clear increase in the proportion of BO_3 units at the expense of BO_4 units can be seen. Furthermore, while the position of the peak assigned to BO_3 units does not change drastically, the peak related to BO_4 shifts from ~0.4 ppm for B12.5 to ~−2 ppm for all substituted glasses. The peak at ~0.4 ppm can be attributed to BO_4 [1B, 3Si] or to BO_4 units in borate superstructural rings [43,44]. The peak, when centred at ~−2 ppm, is often allocated to BO_4 [0B, 4Si] [36]. A more systematic study will be performed to better understand the role of each cation in the borosilicate structure. Similarly, the presence of the two T_g's in the case of the mixed Sr/Mg containing glass will be further investigated to clarify whether it is caused by phase separation or a change in the percolation pathways [45].

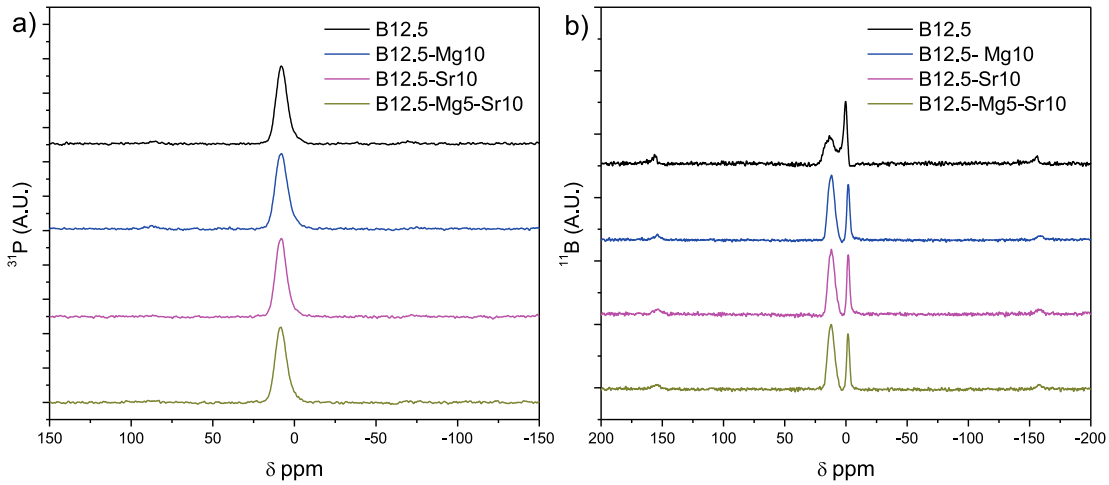

Fig. 3. (a) ^{31}P and (b) ^{11}B MAS NMR for compositions B12.5, B12.5-Mg10, B12.5-Sr10 and B12.5-Mg5-Sr10.

Table 3
The ratio of two chemically distinct boron sites (BO_3 and BO_4) in the studied glasses, obtained from ^{11}B NMR spectra.

Glass	T2 (ms)		%	
	BIII	BIV	BIII	BIV
B12.5	59	38	51.5	48.5
B12.5-Mg5	48	41	62	38
B12.5-Mg10	40	36	62	38
B12.5-Sr5	53	37	63	37
B12.5-Sr10	48	37	61	39
B12.5-Mg5-Sr10	45	57	63	37

Dissolution of the glasses (using samples of various particle size) in SBF was analysed by means of pH and ion concentration measurements. The changes in the glasses' structure upon immersion were analysed by FTIR and SEM/EDX. Fig. 4 presents the change in pH with varying particle size as well as discs. The pH was observed to increase with increasing immersion time and to stabilize at long immersion times. This behaviour was seen regardless of the particles size studied and has been extensively reported upon dissolution of silicate and borosilicate glasses [46].

However, from Fig. 4 it can be observed that the maximum final pH decreased with increasing particle size (Fig. 4e). This has to be expected as the rate of dissolution is directly linked to the specific surface area, owing to dissolution occurring by an ion exchange process. It is also of interest to point out that not all particle sizes were equally suited to detect differences between glass compositions, as the smallest particle size (<38 μm) and the bulk (disc) samples results did not show much variation between compositions, and pH changes as a function of immersion time are identical within the accuracy of the measurements for all compositions in Fig. 4a and d. This suggests that the glasses dissolved in a similar fashion. By contrast when using coarse particles, clear differences in the pH profiles between compositions can be seen, where the replacement of Ca for Mg and/or Sr led to a progressive decrease in the pH change. The effect is more pronounced when the borosilicate glass contains Sr ions. This is in strong agreement with previous articles reporting the slower dissolution rate of Mg and Sr-containing silicate bioactive glasses along with a delayed hydroxyapatite precipitation [19,20].

Si, B, P and Ca ion concentration in the immersion solution were quantified using ICP-OES and are presented in Fig. 5. As expected, upon immersion of the glasses the ion concentration in solution increased, following the same trend, i.e. saturation at long immersion time, as the pH curve in Fig. 4b. The Si release did not drastically change between compositions (Fig. 5a), as the solubility of Si species in solution is limited in the pH range studied here [47]. By contrast, B release was drastically decreased when Ca was replaced with Mg and even more so when replaced with Sr or both Mg and Sr. Such ion release behaviour confirms the hypothesis drawn from Raman and MAS NMR analyses, that Mg, Ca and Sr, have variable affinity towards the silicate or borate sub-networks. It seems clear from these dissolution results that Mg and Sr tend to stabilize the borate sub-network. The decrease in B release into the medium is also well correlated with the increase in BO_3 at the expense of BO_4 units when part of the Ca is replaced by Mg and/or Sr. The increased glass stability might be imparted to an increase in Si−O−B and/or cation interaction with the borate structure.

With increasing substitution, Ca releases decreased. This is most likely only assigned to the lower Ca content in the substituted glasses. Furthermore, as expected form bioactive glasses, the P content decreased with increasing immersion time, suggesting the precipitation of a phosphate-rich phase. Such consumption is typically linked to the precipitation of HA on bioactive silicate and borosilicate glasses. It is noteworthy that the P consumption decreased with increasing substitution. This can be linked to a delayed HA precipitation as reported in silicate glass. [19,20]

While the trends were similar for all particle size ranges investigated here, ion release was slower with decreasing relative surface area, in agreement with the pH changes discussed above.

Changes in glass surface composition as a function of immersion time in SBF were assessed using FTIR (Fig. 6a and b; particle size 125–250 μm taken as an example). With increasing immersion time, (i) the band located around 918 cm^{-1} decreased in intensity, (ii) the band located at 1017 cm^{-1} increased in intensity and shifted to ~1024 cm^{-1}, (iii) a shoulder at ~1200 cm^{-1} increased in intensity, and (vi) a band at 1640 cm^{-1} appeared. As mentioned earlier, the band at 918 cm^{-1}, where observed change was most prominent, corresponds to Si−O and B−O vibrations. [14,29] The changes in these bands are indicative of metal cations connected to nbO being released (ion exchange) and a silica gel forming (Si−OH). The bands centred at 1024 and 918 cm^{-1} for longer immersion times are related to phosphate vibration, and the shoulder at 1200 cm^{-1} can be related to the presence of SiO_4 as Q^4 units (in the silica gel), respectively. [20,48,49]

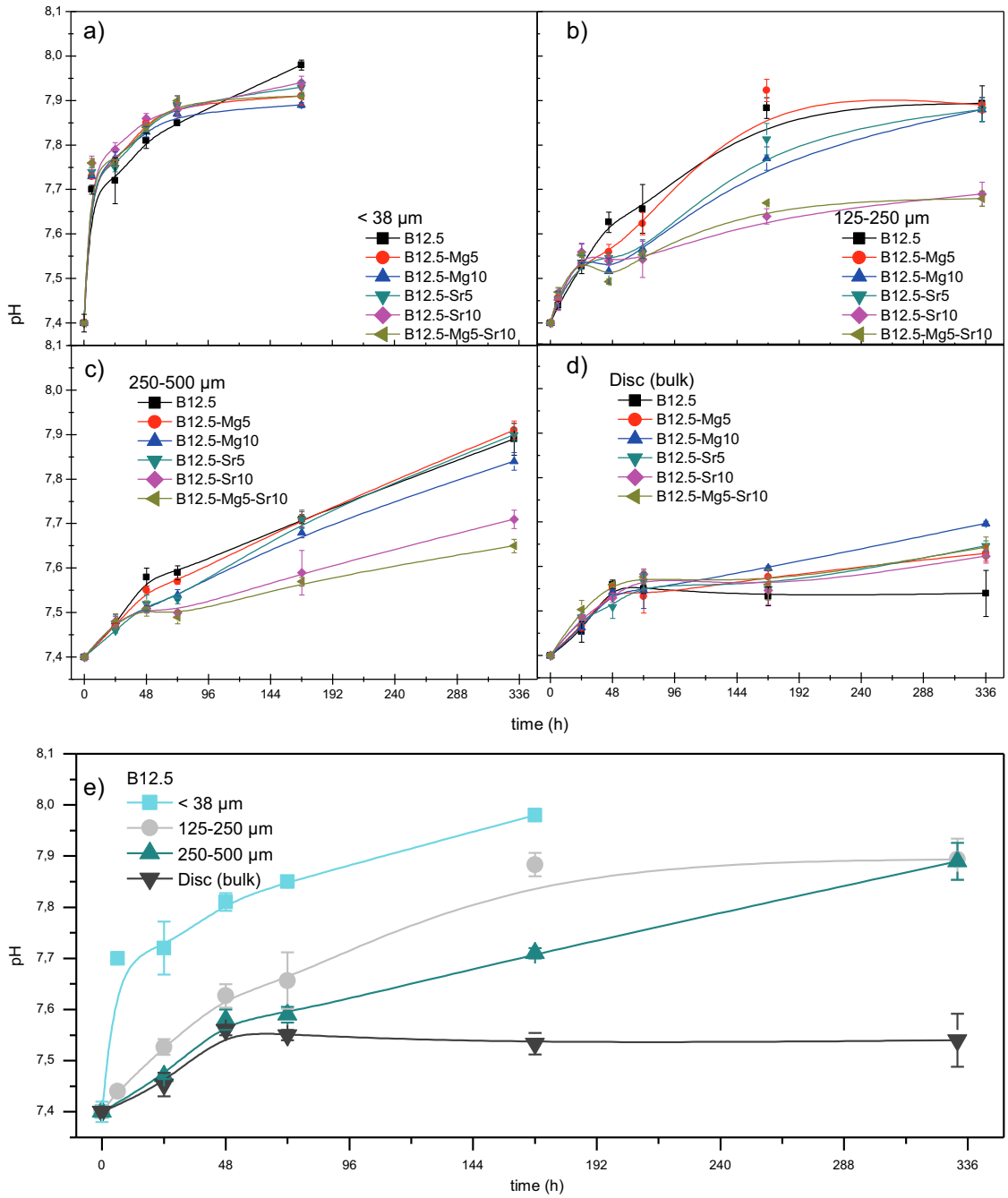

Fig. 4. pH of SBF after immersion of glasses with particle sizes in the range (a) <38 µm, (b) 125–250 µm or (c) 250–500 µm, (d) polished glass discs (d = 10 mm, h = 2 mm). (e) pH changes related to different particle sizes presented for glass B12.5.

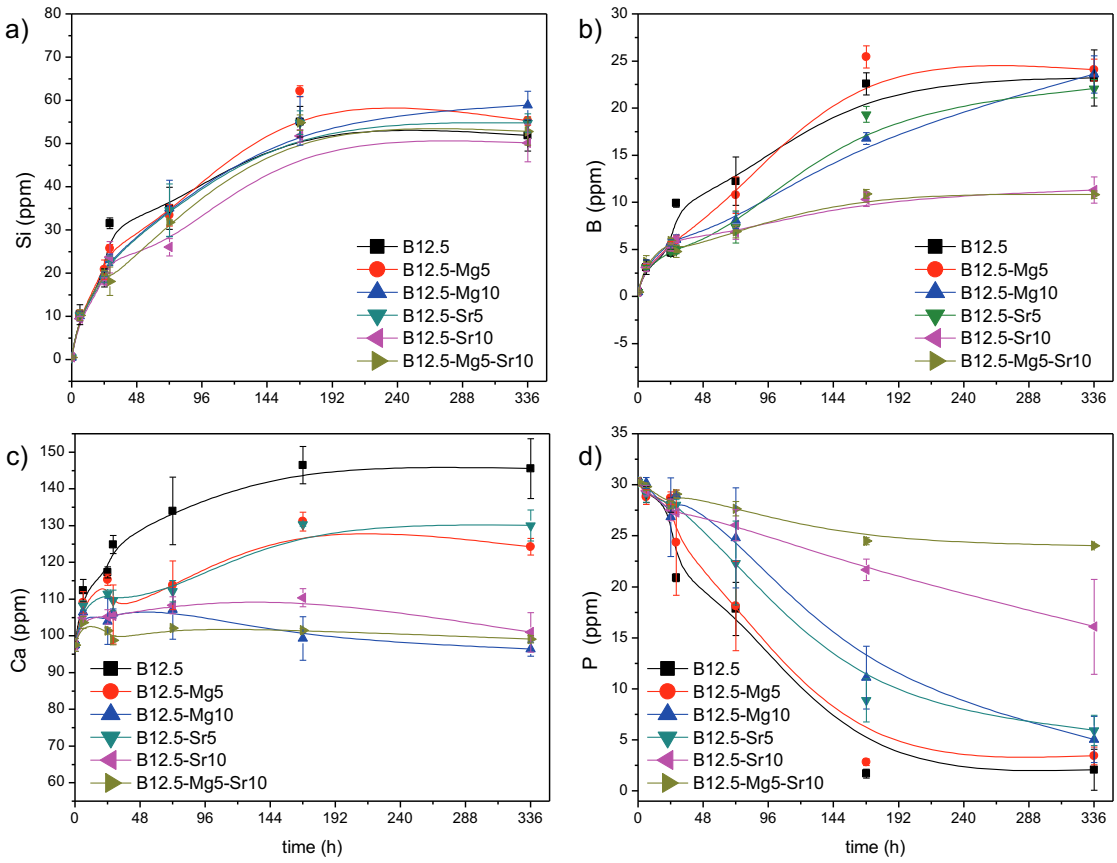

Fig. 5. (a) Si, (b) B, (c) Ca and (d) P ion concentration as a function of immersion time. Glass particles in the particle size range from 125–250 μm.

The bands around 1640 cm^{-1} and the broad band in the 2600–3600 cm^{-1} range (not presented) are indications of absorbed water in the structure and at the glass surface[49]. Finally, a double band at around 1420 cm^{-1}, attributable to CO vibrations [50], appears post immersion. Overall, the structural analysis post dissolution indicates that the typical ion exchange occurs, while possibly also the borate part of the network breaks down and partly dissolves. This is followed by the precipitation of a calcium phosphate surface layer containing carbonates, likely to be a carbonate-substituted apatite. From FTIR analysis, and in agreement with ICP analysis, the presence of Sr and/or Mg led to a decrease in the rate of borate dissolution and a decrease in the speed of reactive layer formation. The addition of Sr seems to cause a slight shift in the bands related to PO_4^{3-} vibrations.

To better understand the nature of the formed reactive layer, EDX/SEM analysis was conducted. Fig. 7 presents SEM images of the immersed glass particles. Several layers can be observed at the particles' surfaces. The composition of the particles' cores corresponds to the expected nominal glass composition. This indicates that the particles have not fully dissolved in SBF during the course of the dissolution study. Successively a SiO_2 rich layer can be distinguished. Formation of a silica-rich layer has been discussed in detail by many authors, and it originates from modifier ions being released in exchange for protons from the solution, Si-OH groups forming from nbO and, subsequently, re-polymerizing [51]. This is also in agreement with FTIR absorption band at 1200 cm^{-1} discussed earlier. On the outermost layer EDX analysis revealed that, in the case of the B12.5 glass particles (Fig. 7a) the Ca/P ratio was ~1.6 as seen in Table 4.

This agrees with the formation of a hydroxyapatite-like phase at the surface of the bioactive glass particles, typically described as a biomimetic apatite. The carbonate bands detected in the FTIR analysis further confirmed the precipitation of hydroxycarbonated apatite (HCA, usually in B-type substitution). [52]. Increasing substitution of Ca with Mg and/or Sr led to an increasing amount of those elements on the reactive layer [53–55]. The layer was assigned to the precipitation of Mg/Sr-substituted HCA, thus explaining the reason for the shifted phosphate peaks in the FTIR spectra [20]. The ratio (Ca + Mg + Sr)/P was found to decrease with increasing the substitution, most likely due to the retarding effect of Mg and Sr on the precipitation of a CaP reactive layer, as well as the slower dissolution rate of those glasses [19,20].

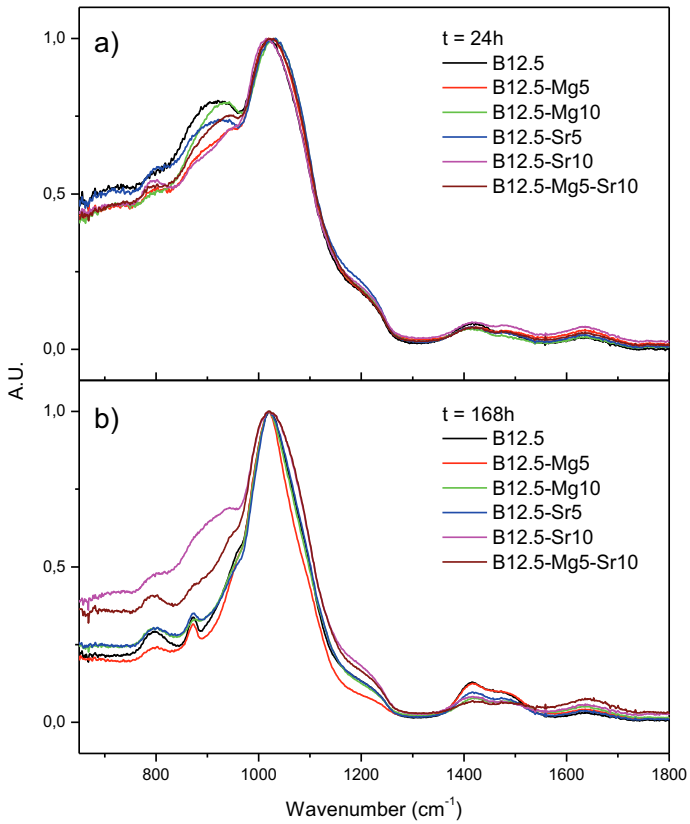

Fig. 6. FTIR spectra of the investigated glasses on (a) 24 h and (b) 168 h of SBF immersion of 125–250 μm particles.

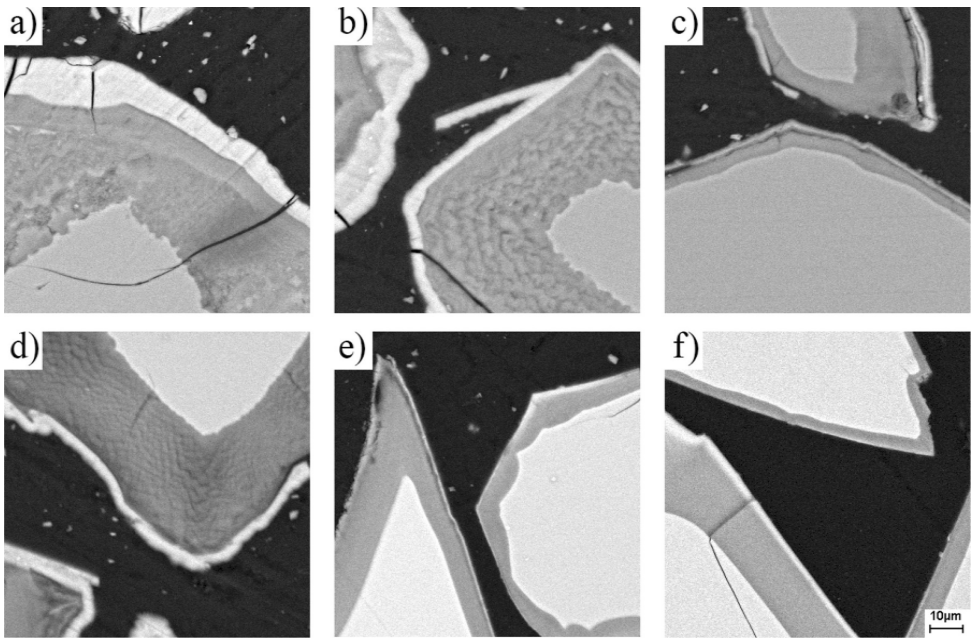

Fig. 7. SEM images of cross sections of particles (d = 125–250 μm) immersed for 168 h in SBF: (a) B12.5, (b) B12.5-Mg5, (c) B12.5-Mg10, (d) B12.5-Sr5, (e) B12.5-Sr10 and (f) B12.5-Mg5-Sr10. Scale bar for all images 10 μm (500× magnification).

Table 4
Composition of the outermost reactive layer formed at 168 h of immersion in SBF.

Composition	Ca (at%)	Mg (at%)	Sr (at%)	P (at%)	(Ca+Mg+Sr)/P
B12.5	22.0 ± 1.6	0.5 ± 0.1		13.9 ± 0.9	1.62 ± 0.03
B12.5-Mg5	20.1 ± 1.9	1.1 ± 0.1		13.7 ± 1.6	1.55 ± 0.04
B12.5-Mg10	20.0 ± 1.9	1.5 ± 0.5		14.2 ± 0.7	1.51 ± 0.07
B12.5-Sr5	18.6 ± 0.1	1.1 ± 0.1	1.1 ± 0.1	14.5 ± 0.2	1.43 ± 0.02
B12.5-Sr10	11.8 ± 0.4	1.3 ± 0.1	2.1 ± 0.2	12.1 ± 1.3	1.26 ± 0.13
B12.5-Mg5-Sr10	15.2 ± 0.9	2.1 ± 0.3	3.7 ± 0.4	15.4 ± 1.1	1.32 ± 0.17

4. Conclusions

In this study, six borosilicate glass compositions based on the commercial bioactive glass S53P4 were developed and characterized for their physical and structural properties. The properties of the borosilicate glass were modified by the introduction of Mg and/or Sr in place of Ca.

The thermal analysis showed that Mg/Sr for Ca substitution slightly increased the hot forming domain (ΔT). Based on DTA and Raman spectroscopy results, phase separation occurred in the mixed Mg/Sr glasses. Ion release and structural analysis results showed that Sr had a higher affinity for the boron sub-network. From the structural analysis, it was also observed that the boron network connectivity changed, with higher presence of BO_3 at the expense of BO_4. The phosphate environment was also affected when Ca, Mg and Sr were all present in the glass network.

Rapid apatite formation was seen for all investigated glasses, with apatite forming rates being slightly slower for higher substitution. Results suggest that Mg and Sr were incorporated into the apatite, as seen in previous studies. In addition to apatite formation, dissolution of ions is of utmost importance when selecting bioactive glasses for in vivo applications. In the present study, it was found that replacing part of Ca with Sr and/or Mg helps in controlling the boron release, owing to stabilization of the borate network. This is of particular interest since borosilicate glasses have been shown to have a promoting effect on mesenchymal stem cell differentiation towards osteogenic lineages, but the release of boron from the glasses has been found to inhibit cell proliferation. Therefore, stabilizing effect could be utilized to control the release of boron and maintaining it at a level where it enhances bone formation and angiogenesis without impeding cell proliferation. Furthermore, the release of Mg and Sr, as well as their incorporation into the reactive layer, may confer added functionality to these new bioactive glasses. These glasses are therefore of interest in bone tissue engineering. Improved thermal properties, when compared to the S53P4 composition, would especially be beneficial for scaffold manufacturing

CRediT authorship contribution statement

J.M. Tainio: Conceptualization, Methodology, Validation, Formal analysis, Investigation, Data curation, Writing - original draft, Writing - review & editing, Visualization. **D.A. Avila Salazar:** Methodology, Formal analysis, Data curation. **A. Nommeots-Nomm:** Methodology, Formal analysis, Data curation. **C. Roiland:** Methodology, Formal analysis, Data curation. **B. Bureau:** Methodology, Formal analysis, Data curation. **D.R. Neuville:** Supervision, Project administration, Funding acquisition, Writing - original draft, Writing - review & editing. **D.S. Brauer:** Supervision, Project administration, Funding acquisition, Writing - original draft, Writing - review & editing. **J. Massera:** Supervision, Project administration, Funding acquisition, Writing - original draft, Writing - review & editing.

Declaration of Competing Interest

The authors declare that they have no known competing financial interests or personal relationships that could have appeared to influence the work reported in this paper.

Acknowledgments

Authors gratefully acknowledge the support of the Jane & Aatos Erkko Foundation (AGATE project) for financial support of JT. Academy of Finland is also acknowledged for financial support of JM through the Academy research Fellow Grant. Academy of Finland and the DAAD are acknowledge for supporting the Finnish and German team through the bilateral mobility programme. The authors would like to thank Henriikka Teittinen (Tampere University), Roland Wetzel and Thilo Grammes (Friedrich-Schiller-Universität) for their help performing measurements and for fruitful discussions.

References

[1] D.S. Brauer, Bioactive glasses-structure and properties, Angew. Chemie - Int. Ed. (2015) 4160–4181, https://doi.org/10.1002/anie.201405310.
[2] L.L. Hench, J.R. Jones, Bioactive glasses: frontiers and challenges, Front. Bioeng. Biotechnol. 3 (2015) 1–12, https://doi.org/10.3389/fbioe.2015.00194.
[3] N.C. Lindfors, I. Koski, J.T. Heikkilä, K. Mattila, A.J. Aho, A prospective randomized 14-year follow-up study of bioactive glass and autogenous bone as bone graft substitutes in benign bone tumors, J. Biomed. Mater. Res. - Part B Appl. Biomater (2010) 94.
[4] J. Massera, S. Fagerlund, L. Hupa, M. Hupa, Crystallization mechanism of the bioactive glasses, 45S5 and S53P4, J. Am. Ceram. Soc. 95 (2012) 607–613, https://doi.org/10.1111/j.1551-2916.2011.05012.x.
[5] L. Hupa, S. Fagerlund, J. Massera, L. Björkvik, Dissolution behavior of the bioactive glass S53P4 when sodium is replaced by potassium, and calcium with magnesium or strontium, J. Non. Cryst. Solids. 432 (2016) 41–46, https://doi.org/10.1016/j.jnoncrysol.2015.03.026.
[6] C. Blaeß, R. Müller, G. Poologasundarampillai, D.S. Brauer, Sintering and concomitant crystallisation of bioactive glasses, Int. J. Appl. Glas. Sci. (2019) 1–14, https://doi.org/10.1111/ijag.13477.
[7] A. Nommeots-Nomm, C. Ligorio, A.J. Bodey, B. Cai, J.R. Jones, P.D. Lee, G. Poologasundarampillai, Four-dimensional imaging and quantification of viscous flow sintering within a 3D printed bioactive glass scaffold using synchrotron X-ray tomography, Mater. Today Adv. 2 (2019) 100011, , https://doi.org/10.1016/j.mtadv.2019.100011.
[8] M.N. Rahaman, D.E. Day, B. Sonny Bal, Q. Fu, S.B. Jung, L.F. Bonewald, A.P. Tomsia, Bioactive glass in tissue engineering, Acta Biomater 7 (2011) 2355–2373, https://doi.org/10.1016/j.actbio.2011.03.016.
[9] Q. Fu, M.N. Rahaman, H. Fu, X. Liu, Silicate, borosilicate, and borate bioactive glass scaffolds with controllable degradation rate for bone tissue engineering applications. I. Preparation and in vitro degradation. J. Biomed. Mater. Res. Part A. 95A (2010) 164–171.
[10] R.F. Brown, M.N. Rahaman, A.B. Dwilewicz, W. Huang, D.E. Day, Y. Li, B.S. Bal, Effect of borate glass composition on its conversion to hydroxyapatite and on the proliferation of MC3T3-E1 cells, J. Biomed. Mater. Res. - Part A. 88 (2009) 392–400, https://doi.org/10.1002/jbm.a.31679.
[11] X. Ying, S. Cheng, W. Wang, Z. Lin, Q. Chen, W. Zhang, D. Kou, Y. Shen, X. Cheng, F.A. Rompis, L. Peng, C.Z. Lu, Effect of boron on osteogenic differentiation of human bone marrow stromal cells, Biol. Trace Elem. Res. 144 (2011) 306–315, https://doi.org/10.1007/s12011-011-9094-x.
[12] M. Ojansivu, S. Vanhatupa, M. Juntunen, A. Larionova, S. Miettinen, A. Mishra, J. Massera, The effect of S53P4-based borosilicate glasses and glass dissolution products on the osteogenic commitment of human adipose stem cells, PLoS ONE 13 (2018) 1–20, https://doi.org/10.1371/journal.pone.0202740.
[13] P. Balasubramanian, L. Hupa, B. Jokic, R. Detsch, A. Grünewald, A.R. Boccaccini, Angiogenic potential of boron-containing bioactive glasses: in vitro study, J. Mater. Sci. 52 (2017) 8785–8792, https://doi.org/10.1007/s10853-016-0563-7.
[14] P. Balasubramanian, T. Büttner, V. Miguez Pacheco, A.R. Boccaccini, Boron-containing bioactive glasses in bone and soft tissue engineering, J. Eur. Ceram. Soc. (2018), https://doi.org/10.1016/j.jeurceramsoc.2017.11.001.
[15] M. Fabert, N. Ojha, E. Erasmus, M. Hannula, M. Hokka, J. Hyttinen, J. Rocherullé,

I. Sigalas, J. Massera, Crystallization and sintering of borosilicate bioactive glasses for application in tissue engineering, J. Mater. Chem. B. 5 (2017) 4514–4525, https://doi.org/10.1039/c7tb00106a.
[16] E.P. Erasmus, O.T. Johnson, I. Sigalas, J. Massera, Effects of sintering temperature on crystallization and fabrication of porous bioactive glass scaffolds for bone regeneration, Sci. Rep. (2017) 7, https://doi.org/10.1038/s41598-017-06337-2.
[17] E.P. Erasmus, R. Sule, O.T. Johnson, J. Massera, I. Sigalas, In vitro evaluation of porous borosilicate, borophosphate and phosphate bioactive glasses scaffolds fabricated using foaming agent for bone regeneration, Sci. Rep. 8 (2018) 1–13, https://doi.org/10.1038/s41598-018-22032-2.
[18] M. Brink, The influence of alkali and alkaline earths on the working range for bioactive glasses, J. Biomed. Mater. Res. 36 (1997) 109–117 doi:10.1002/(SICI)1097-4636(199707)36:1<109::AID-JBM13>3.0.CO;2-D.
[19] J. Massera, L. Hupa, M. Hupa, Influence of the partial substitution of cao with mgo on the thermal properties and in vitro reactivity of the bioactive glass S53P4, J. Non. Cryst. Solids. 358 (2012) 2701–2707, https://doi.org/10.1016/j.jnoncrysol.2012.06.032.
[20] J. Massera, L. Hupa, Influence of SrO substitution for CaO on the properties of bioactive glass S53P4, J. Mater. Sci. Mater. Med. 25 (2014) 657–668, https://doi.org/10.1007/s10856-013-5120-1.
[21] E. Gentleman, Y.C. Fredholm, G. Jell, N. Lotfibakhshaiesh, M.D. O'Donnell, R.G. Hill, M.M. Stevens, The effects of strontium-substituted bioactive glasses on osteoblasts and osteoclasts in vitro, Biomaterials 31 (2010) 3949–3956, https://doi.org/10.1016/j.biomaterials.2010.01.121.
[22] A. Goel, R.R. Rajagopal, J.M.F. Ferreira, Influence of strontium on structure, sintering and biodegradation behaviour of CaO-MgO-SrO-SiO 2-P 2O 5-CaF 2 glasses, Acta Biomater 7 (2011) 4071–4080, https://doi.org/10.1016/j.actbio.2011.06.047.
[23] A. Hoppe, V. Mouriño, A.R. Boccaccini, Therapeutic inorganic ions in bioactive glasses to enhance bone formation and beyond, Biomater. Sci. 1 (2013) 254–256, https://doi.org/10.1039/c2bm00116k.
[24] J. Massera, A. Kokkari, T. Närhi, L. Hupa, The influence of SrO and CaO in silicate and phosphate bioactive glasses on human gingival fibroblasts, J. Mater. Sci. Mater. Med. 26 (2015) 196.
[25] D. Massiot, F. Fayon, M. Capron, I. King, S. Le Calvé, B. Alonso, J.O. Durand, B. Bujoli, Z. Gan, G. Hoatson, Modelling one- and two-dimensional solid-state NMR spectra, Magn. Reson. Chem. 40 (2002) 70–76, https://doi.org/10.1002/mrc.984.
[26] T. Kokubo, H. Kushitani, S. Sakka, T. Kitsugi, T. Yamamuro, Solutions able to reproduce in vivo surface-structure changes in bioactive glass-ceramic A-W3, J. Biomed. Mater. Res. 24 (1990) 721–734.
[27] A. Pedone, G. Malavasi, M.C. Menziani, Computational insight into the effect of CaO/MgO substitution on the structural properties of phospho-silicate bioactive glasses, J. Phys. Chem. C. 113 (2009) 15723–15730, https://doi.org/10.1021/jp904131t.
[28] S.J. Watts, R.G. Hill, M.D. O'Donnell, R.V. Law, Influence of magnesia on the structure and properties of bioactive glasses, J. Non. Cryst. Solids. 356 (2010) 517–524, https://doi.org/10.1016/j.jnoncrysol.2009.04.074.
[29] J. Serra, P. González, S. Liste, C. Serra, S. Chiussi, B. León, M. Pérez-Amor, H.O. Ylänen, M. Hupa, FTIR and XPS studies of bioactive silica based glasses, J. Non. Cryst. Solids. 332 (2003) 20–27, https://doi.org/10.1016/j.jnoncrysol.2003.09.013.
[30] P. Pascuta, M. Bosca, S. Rada, M. Culea, I. Bratu, E. Culea, FTIR spectro-scopic study of Gd2O3-Bi2O3-B2O3 glasses, journal of optoelectronics and advanced materials, J. Optoelectron. Adv. Mater. 10 (2008) 2416–2419.
[31] B.C. Bunker, D.R. Tallant, R.J. Kirkpatrick, G.L. Turner, Multinuclear nuclear magnetic resonance and Raman investigation of sodium borosilicate glass structures, Phys. Chem. Glas. (1990) 30–41.
[32] K. Fukumi, J. Hayakawa, T. Komiyama, Intensity of Raman band in silicate glasses, J. Non. Cryst. Solids. (1990) 297–302.
[33] D. Manara, A. Grandjean, D.R. Neuville, Advances in understanding the structure of borosilicate glasses: a raman spectroscopy study, Am. Mineral 94 (2009) 777–784, https://doi.org/10.2138/am.2009.3027.
[34] B.O. Mysen, J.D. Frantz, Raman spectroscopy of silicate melts at magmatic temperatures: sodium oxide-silica, potassium oxide-silica, and lithium oxide-silica binary compositions in the temperature range 25-1475°C, Chem. Geol. 96 (1992) 321–332.
[35] D.R. Neuville, Viscosity, structure and mixing in (Ca, Na) silicate melts, Chem. Geol. 229 (2006) 28–41, https://doi.org/10.1016/j.chemgeo.2006.01.008.
[36] K. Fujikura, N. Karpuknhina, T. Kasuga, D.S. Brauer, R.G. Hill, R.V. L.aw, Influence of strontium substitution on structure and crystallisation of Bioglass® 45S5, J. Mater. Chem. 22 (2012) 7395–7402, https://doi.org/10.1039/c2jm14674f.
[37] R. Akagi, N. Ohtori, N. Umesaki, Raman spectra of K2O-B2O3 glasses and melts, J. Non. Cryst. Solids. 126 (1990) 224–230.
[38] B.N. Meera, A.K. Sood, N. Chandrabhas, J. Ramakrishna, Raman study of lead borate glasses, J. Non. Cryst. Solids. 126 (1990) 224–230, https://doi.org/10.1016/0022-3093(90)90823-5.
[39] R. Mathew, B. Stevensson, M. Edén, Na/Ca intermixing around silicate and phosphate groups in bioactive phosphosilicate glasses revealed by heteronuclear solid-state NMR and molecular dynamics simulations, J. Phys. Chem. B. 119 (2015) 5701–5715, https://doi.org/10.1021/acs.jpcb.5b01130.
[40] Y. Yu, M. Edén, Structure–composition relationships of bioactive borophosphosilicate glasses probed by multinuclear ^{11}B, ^{29}Si, and ^{31}P solid state NMR, RSC Adv. 6 (2016) 101288–101303, https://doi.org/10.1039/C6RA15275A.
[41] A. Pedone, T. Charpentier, G. Malavasi, M.C. Menziani, New insights into the atomic structure of 45S5 bioglass by means of solid-state NMR spectroscopy and accurate first-principles simulations, Chem. Mater. 22 (2010) 5644–5652, https://doi.org/10.1021/cm102089c.
[42] D.S. Brauer, N. Karpukhina, R.V. Law, R.G. Hill, Structure of fluoride-containing bioactive glasses, J. Mater. Chem. 19 (2009) 5629–5636, https://doi.org/10.1039/b900956f.
[43] F. Angeli, O. Villain, S. Schuller, T. Charpentier, D. De Ligny, L. Bressel, L. Wondraczek, Effect of temperature and thermal history on borosilicate glass structure, Phys. Rev. B - Condens. Matter Mater. Phys. (2012) 85, https://doi.org/10.1103/PhysRevB.85.054110.
[44] A.P. Howes, N.M. Vedishcheva, A. Samoson, J.V. Hanna, M.E. Smith, D. Holland, R. Dupree, Boron environments in Pyrex® glass - A high resolution, double-rotation NMR and thermodynamic modelling study, Phys. Chem. Chem. Phys. 13 (2011) 11919–11928, https://doi.org/10.1039/c1cp20771g.
[45] C. Le Losq, D.R. Neuville, W. Chen, P. Florian, D. Massiot, Z. Zhou, G.N. Greaves, Percolation channels: a universal idea to describe the atomic structure and dynamics of glasses and melts, Sci. Rep. 7 (2017) 1–12, https://doi.org/10.1038/s41598-017-16741-3.
[46] L. Bingel, D. Groh, N. Karpukhina, D.S. Brauer, Influence of dissolution medium pH on ion release and apatite formation of Bioglass® 45S5, Mater. Lett. 143 (2015) 279–282, https://doi.org/10.1016/j.matlet.2014.12.124.
[47] R.K. Iler, The Chemistry of Silica: Solubility, Polymerization, Colloid and Surface Properties, and Biochemistry, Wiley, New York, 1979.
[48] L. Berzina-Cimdina, N. Borodajenko, Research of calcium phosphates using Fourier transform infrared spectroscopy, in: InTech (Ed, Infrared Spectrosc. - Mater. Sci. Eng. Technol. (2012).
[49] S. Raynaud, E. Champion, D. Bernache-Assollant, P. Thomas, Calcium phosphate apatites with variable Ca/P atomic ratio I. Synthesis, characterisation and thermal stability of powders, Biomaterials 23 (2002) 1065–1072.
[50] B. Ratner, A. Hoffman, F. Schoen, J.E. Lemons, Biomaterials Science. An Introduction to Materials in Medicine, second ed., Academic Press, London, UK, 2014.
[51] J.R. Jones, Reprint of: review of bioactive glass: from Hench to hybrids, Acta Biomater 23 (2015) S53–S82, https://doi.org/10.1016/j.actbio.2015.07.019.
[52] D.S. Brauer, N. Karpukhina, M.D. O'Donnell, R.V. Law, R.G. Hill, Fluoride-containing bioactive glasses: effect of glass design and structure on degradation, pH and apatite formation in simulated body fluid, Acta Biomater 6 (2010) 3275–3282, https://doi.org/10.1016/J.ACTBIO.2010.01.043.
[53] I. Mayer, R. Schlam, J.D.B. Featherstone, Magnesium-containing carbonate apatites, J. Inorg. Biochem. 66 (1997) 1–6, https://doi.org/10.1016/S0162-0134(96)00145-6.
[54] N. Kanzaki, K. Onuma, G. Treboux, S. Tsutsumi, A. Ito, Inhibitory effect of magnesium and zinc on crystallization kinetics of hydroxyapatite (0001) face, J. Phys. Chem. B. 104 (2000) 4189–4194 https://www.scopus.com/inward/record.uri?eid=2-s2.0-0000723585&partnerID=40&md5=00ac897aef1bf3a23512404e0540d11c.
[55] Y.C. Fredholm, N. Karpukhina, D.S. Brauer, J.R. Jones, R.V. Law, R.G. Hill, Influence of strontium for calcium substitution in bioactive glasses on degradation, ion release and apatite formation. J. R. Soc. Interface. 9 (2012) 880–889, https://doi.org/10.1098/rsif.2011.0387.

II

CRYSTALLIZATION MECHANISM OF B12.5 BIOACTIVE BOROSILICATE GLASSES AND ITS IMPACT ON IN VITRO DEGRADATION

by

Jenna M. Tainio, Tomi Anttila, Juuso Pohjola, Delia S. Brauer and Jonathan Massera

Journal of the European Ceramic Society Vol 44, Issue 2, pp. 1229-1238, February 2024.

Journal of the European Ceramic Society 44 (2024) 1229–1238

Contents lists available at ScienceDirect

Journal of the European Ceramic Society

journal homepage: www.elsevier.com/locate/jeurceramsoc

Crystallization mechanism of B12.5 bioactive borosilicate glasses and its impact on *in vitro* degradation

J.M. Tainio [a,*], T. Anttila [a], J. Pohjola [a,1], D.S. Brauer [b], J. Massera [a]

[a] Faculty of Medicine and Health Technology, Tampere University, Korkeakoulunkatu 10, FI-33720 Tampere, Finland
[b] Otto-Schott-Institut, Friedrich-Schiller-Universität, Fraunhoferstr. 6, 07743 Jena, Germany

ARTICLE INFO

Keywords:
Borosilicate glasses
Bioactive glasses
Bone tissue engineering
Crystallization

ABSTRACT

Understanding the thermal properties and crystallization mechanisms are crucial upon sintering of bioactive glasses. In this study, crystallization mechanism and sintering ability of S53P4-based B12.5 borosilicate glass series, containing varying amounts of magnesium and/or strontium, was assessed. Additionally, the effect of crystallization onto these glasses bioactive properties was investigated.

Glasses were composed of 47.12 SiO_2 - 6.73 B_2O_3 - 21.77-x-y CaO - 22.65 Na_2O - 1.72 P_2O_5 - x MgO - y SrO, where x,y = 0, 5 or 10 (mol%). Thermal properties were analysed with DTA, and glass transition temperatures and onset of crystallization were determined to gain an overview of temperature range suitable for heat treatments, and for calculation of activation energies related to viscous flow and crystallization. Further, sintered bodies were formed by heat-treating coarse glass particles in large temperature range; their porosity was assessed, cross section were analysed by SEM and crystallinity was studied with XRD. To evaluate the impact of crystallization on the in vitro reactivity, dissolution studies were executed in SBF-solution up to one week, with pH and ion content of solution measured at the end of immersion. Immersed particles were studied with FTIR to observe changes in the glasses structure.

The main crystallization mechanism of B12.5-based glasses was determined to be surface crystallization. While the crystallization interfered with viscous flow sintering of the pure borosilicate glass, Mg and Sr addition enabled sintering of amorphous bodies more easily and with wider temperature range. Mg in the composition especially enabled densification. In vitro studies presented that surprisingly, partially crystallized specimen were initially more reactive than the amorphous specimen.

1. Introduction

Regenerative medicine and tissue engineering have rapidly progressed over the years, and continue to advance in assembling functional constructs to restore or improve damaged tissues and organs. Although major progress has been achieved, much work is needed to develop more available and suitable synthetic alternatives for the current gold standard; transplants and tissue grafts [1]. Bioactive glasses are especially promising material group for the reconstruction of bone defects, as they are biodegradable and able to form active bonding with bone tissue, due to the precipitation of hydroxycarbonated apatite (HCA) at their surface, when in physiological conditions [2]. Few commercial bioactive glass compositions are utilized successfully in clinical applications, although in limited forms, mainly as powders and granules. There is evident clinical need of a more complex shaped, even load-bearing, implant materials, that could be utilized in bone tissue engineering for patient-specific reconstructive surgery [3,4].

To be able to hot-form bioactive glasses into complex shapes, understanding the thermal behaviour of glasses is highly important. Glass is a ceramic material in a metastable amorphous state. Glass will undergo crystallization, when the activation energy to overcome the metastability is exceeded. Bioactive glass's tendency to react in physiological conditions, resulting in materials bioactivity, is dependent on the existence and distribution of amorphous- and crystal-phases [5,6]. In general, crystallization can inhibit the formation of essential HCA-reaction layer [7]. Furthermore, it has also been demonstrated that the process of crystallization inhibits proper sintering [6,8]. This limits the use of hot forming processes utilized via well-established techniques

* Corresponding author.
E-mail address: jenna.tainio@tuni.fi (J.M. Tainio).
[1] Now at University of Turku, FI-20014 Turun yliopisto, Finland.

https://doi.org/10.1016/j.jeurceramsoc.2023.09.043
Received 28 June 2023; Received in revised form 13 September 2023; Accepted 15 September 2023
Available online 16 September 2023

for 3D-scaffold production methods [9]. Differential thermal analysis (DTA) or differential scanning calorimetry (DSC) can be used to assess materials' thermal behavior. A variety of models have been developed to determine activation energies (E_a, for glass transition / viscous flow and E_c, for crystallization), as well as the dimensionality of the primary crystallization (surface vs. bulk crystallization) from DTA or DSC thermograms. The kinetics of glass crystallization are often based on the Avrami equation, which assumes isothermal heating. This parameter has been further evaluated for non-isothermal analysis as proposed by Kissinger et al., Augis and Bennet and Ozawa et al. [10–12]. The Johnson–Mehl–Avrami (JMA) exponent, a parameter that also can be extracted form thermal analysis in isothermal or non-isothermal, giving information about the crystal growth dimensionality [13].

Alterations in glasses composition majorly affect the material properties. Modifications, such additions of network modifiers can enhance materials processability, as well as including therapeutic ions could further tissue recovery [5,14,15]. For example, borosilicate bioactive glasses are highly interesting as borate in glass structure increases the hot forming domain [16,17], while additionally inducing faster glasses dissolution and more complete glass conversion into hydroxycarbonated apatite than silicate bioactive glasses [18,19]. Additionally, they are suitable for both soft and hard tissue engineering [20,21]. Further substitutions, such as replacing part of glasses CaO with, MgO and/or SrO, have additionally been found to improve the hot forming domain and sintering [22–25].

Here, commercial glass composition (BonAlive®) S53P4 has been modified by the substitution of B_2O_3 for SiO_2, with additional replacement of part of the Ca for Mg and/or Sr. The glass structure and in vitro degradation of these B12.5 glasses has been reported in Tainio et al., 2020 [25]. Aim of this study is to understand the crystallization mechanism of these glasses, to evaluate the potential of sintering of glass particles without adverse crystallization. Furthermore, the impact of crystallization on the in vitro dissolution of these borosilicate glasses has been assessed.

2. Materials and methods

2.1. Glass preparation

Borosilicate bioactive glasses were prepared with a molar composition of 47.12 SiO_2 – 6.73 B_2O_3 – (21.77 -x-y) CaO – 22.65 Na_2O – 1.72 P_2O_5 – x MgO – y SrO (mol%), where x,y = 0, 5 or 10 mol%; the compositions studied in this work are presented in.

Table 1. Glasses were melted as previously described by Tainio et al. [25] and crushed and sieved to particle fraction size < 38 μm and 250–500 μm.

2.2. Thermal properties

The glass transition temperature (T_g) was measured as the inflection of the first endothermic event, and the onset of crystallization (T_x) was measured by the tangent technique on the first exothermic peak, indicative of crystallization. The temperature range between T_g and the T_x, was defined as the processing or sintering window. T_p, defined as the maximum of the exothermic peak in the DTA thermogram, corresponds to the crystallization temperature. Temperatures were determined as described in [26] using differential thermal analysis (STA 449 F1 Jupiter, Netzsch Group, Selb, Germany) in Pt-Rh crucibles at a heating rate of 5, 10, 15 and 20 °C/min from 40° to 1200°C in N_2 atmosphere. The thermal properties were measured on powders with particles size fractions; < 38 μm ('fine') and 250–500 μm ('coarse').

The activation energies for viscous flow (E_a) and crystallization (E_c) were determined by measuring T_g and T_p at the different heating rates, and then applying the Kissinger equation (Eq. (1)) [10,27].

$$\ln\left(\frac{\beta}{T_g^2}\right) = -\frac{E_a}{RT_g} + Constant, \tag{1}$$

where E_a is the activation energy of glass transition, β is the heating rate, T_g the glass transition temperature at the heating rate β, and R is the ideal gas constant. The activation energy of crystallization E_c was determined by replacing T_g with T_p. The apparent activation energy for crystallization E_c was also determined using the Friedman isoconversional method (Eq. (2)) [27].

$$\ln\left(\frac{d\alpha_i}{dt}\right) = -\frac{E_{c\alpha}}{RT_i} + Constant, \tag{2}$$

where $E_{c\alpha}$ activation energy of crystallization at a specific degree of transformation α, $\frac{d\alpha_i}{dt}$ is the transformation rate at a temperature T_i, and R is the ideal gas constant.

To gain information about the dimensionality of the crystal growth, the JMA exponent was determined using the equation proposed by Augis and Bennet (Eq. (3)); [11].

$$n = \frac{2,5}{\Delta T_{FWHM}} \frac{T_p^2}{\frac{E_c}{R}}, \tag{3}$$

where n is the JMA exponent, T_p is the crystallization temperature, ΔT_{FWHM} is the full width at half maximum of the DTA peak, and R is the ideal gas constant. E_c is the activation energy of crystallization, determined either by Kissinger Eq. (1) or Friedman Eq. (2) method.

2.3. Heat treatment; sintering, porosity and crystallization

Heat treatments were focused on coarse glass particles, with 20 °C/min heating rate to prevent significant nucleation during the heating process. Glass particles (250–500 μm) were placed in a stainless-steel mould with seven holes (d = 10 mm, h = 10 mm). Based on the DTA results (gained at 20 °C/min heating rate), the samples were heated up to specific temperatures (see Table 2 for the temperature tested for all glass compositions.) The aim was to gain (*i*) one heat treated sample which remained fully amorphous (heat treatment at low temperature, 'L'), (*ii*) one which was fully crystallized (high temperature 'H'), and (*iii*) sintered bodies with possible partial crystallization (gained from several sintering temperatures approximately 35 °C apart.) The temperature was maintained for one hour, and afterwards, the samples were left to cool down to room temperature.

Porosity of the sintered bodies was obtained by measuring and calculating average heights and masses of parallels heated at temperatures A–E (Table 2). The estimation of the sintered samples' porosity was

Table 1
Oxide compositions of the studied glasses in mol%.

Glass	SiO_2	B_2O_3	CaO	Na_2O	P_2O_5	MgO	SrO
B12.5	47.12	6.73	21.77	22.66	1.72	–	–
B12.5-Mg5	47.12	6.73	16.77	22.66	1.72	5	–
B12.5-Sr10	47.12	6.73	11.77	22.66	1.72	–	10
B12.5-Mg5-Sr10	47.12	6.73	6.77	22.66	1.72	5	10

Table 2
Temperatures (°C) used for heat treatments, to gain amorphous (heating at temperature L), crystallized (heating at temperature H) and sintered bodies in between L and H (temperatures A-E).

id/composition	B12.5	B12.5-Mg5	B12.5-Sr10	B12.5-Mg5-Sr10
L 'low'	550	550	550	550
A	650	585	600	575
B	670	610	625	600
C	695	635	650	625
D	720	660	675	650
E	745	685	700	675
H 'high'	806	821	794	782

performed assuming that specimens are cylinder-shaped. The porosity was estimated using the following Eq. (4).

$$Porosity = (1 - \rho/\rho 0) \times 100\% \quad (4)$$

where the ρ_0 was the bulk density, and ρ was the apparent density (specimen mass divided by volume) of each sintered sample. The porosities were obtained from 7 specimen per condition and expressed as mean ± standard deviation (SD).

Scanning electron microscopy (SEM) was performed on sintered specimen to observe the stage of the formed bodies' crystallization. Formed sintered bodies were cast to resin and polished up to 4000 grit to reveal cross section. The samples were coated with carbon and imaged using Zeiss Crossbeam 540 scanning electron microscope. The system was equipped with Oxford Instruments XMaxN 80 Energy dispersive X-ray Spectroscopy (EDS) detector.

Stage of glasses crystallization were confirmed by X-ray crystallography (XRD). Samples were prepared by crushing heat-treated/sintered bodies in a mortar, and analysed using a XRD PANalytical (Siemens) on angles from 20° to 90°. Approximately 0.2 g of glass was used for each analysis.

2.4. In vitro degradation

The impact of crystallization on in vitro degradation properties was conducted in simulated body fluid (SBF). SBF was first described by Kokubo et al. [28]. The pH of the solution was adjusted to 7.40 ± 0.02 at 37 °C ± 0.2 °C. Approximately 75 mg ± 1 mg of 250–500 μm glass particles, that were heat treated at the temperatures labelled L and H (Table 2) were weighted in 120 ml cylindrical containers and submerged by 50 ml of SBF-solution, pre-heated at 37 °C. It should be noted that the samples treated at the temperature labelled H had sintered during the heat treatments, and therefore were re-crushed and sieved before being tested in SBF. Samples were then placed for 6, 24, 48, 72 and 168 h in a shaking incubator, set at 100 rpm and 37 °C. At each time point, the pH was measured with a Mettler Toledo seven multi or Thermo Orion Star A3 at 37 °C ± 0,2 °C. Glass particles were then filtered from the solution, rinsed with acetone and dried to stop further hydrolysis reactions. 1 ml of dissolution solution was taken from each sample and diluted in 9 ml of 1 M HCl (1:10) for inductively coupled plasma optical emission spectrometry (ICP-OES, Agilent Technologies, USA). Measured elements were Si (at wavelength 288.158 nm), B (208.956 nm), Ca (393.366 nm), P (253.561 nm), Mg (279.553 nm) and Sr (407.771 nm). Sodium was excluded due the high content initially present in the SBF.

Fourier transform infra-red (FTIR) Spectrum One FTIR (PerkinElmer, Inc., USA) in attenuated total reflectance (ATR) mode was used observe any structural changes at the glasses' surfaces. All FTIR spectra were recorded within the range 600–4000 cm^{-1}, corrected for Fresnel losses and normalized to the absorption band showing the maximum intensity.

3. Results and discussion

3.1. Glass transition and crystallization temperatures

Thermal properties were analysed with DTA. Table 3 presents results gained from DTA performed on glass particles sieved to < 38 μm at heating rate of 10 °C/min. Corresponding values for the coarse particle size (250–500 μm) have been previously determined and published by Tainio et al. [25].

Overall, magnesium is known to decrease the crystallization tendency, and indeed, also in this study, the presence of Mg caused a decrease in T_g, that resulted in slight increase of the sintering window. This effect has been previously linked to a mixed cation effect that decreases the glass viscosity [29], or often depends on the configurational entropy variations of the mixed melts [30]. Strontium substitution for calcium reduced the T_g, T_x and T_p temperatures, however not causing any significant change in the hot forming range. It was observed, that while the T_g was similar for both particle sizes, as expected, DTA traces of the fine particles exhibited a shift towards lower crystallization temperatures [31]. Moreover, in the DTA thermograph (Fig. 1) peaks associated to crystallization were sharper and more intense with fine particles, than with coarse particles. Decrease in crystallization temperature simultaneously with increase in the intensity of the exothermic peak, associated with increasing surface-to-volume ratio, suggesting a predominant surface crystallization mechanism.

Hot forming range for all compositions in fine particle size was determined to be around or over 100 K Typically a hot forming domain of over 100 K is promising towards sintering of the glass [31,32], however the kinetics of the crystallization process must be evaluated to confirm this. For coarse particles, hot forming range was around 150 K or higher [25]. DTA were additionally determined with heating rates of 5, 15 and 20 K/min for both particle sizes. As the heating rate increased, T_g and T_p shifted toward higher temperatures due to thermal lag [33].

3.2. Activation energies and the JMA exponent

The Kissinger and Friedman methods were employed to estimate the activation energies (Eq. (1)&(2), respectively) and Augis-Bennett method (Eq. (3)) for the JMA exponent. These results are presented in Table 4. While the Kissinger equation remains appropriate in the case of

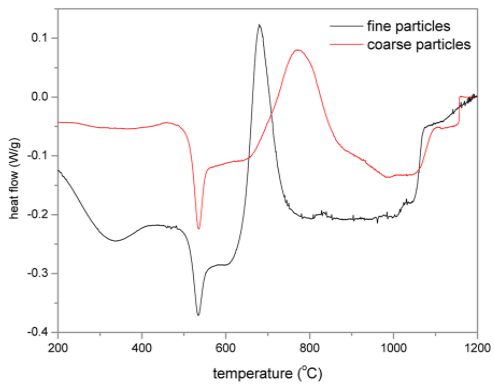

Fig. 1. DTA thermograph determined with 10 K/min heating rate for B12.5 < 38 μm (fine particles) and [250−500] μm (coarse particles).

Table 3
T_g, T_x and T_p of the investigated glasses < 38 μm with 10 K/min heating rate. ΔT presents the hot forming domain, i.e. sintering window of the B12.5-glass compositions; ***ΔT*** values have been compared to the ones for [250–500] μm particle size, published previously in [25].

Glass	T_{g1} (± 3 °C)	T_{g2} (± 3 °C)	T_x (± 3 °C)	T_p (± 3 °C)	$\Delta T = T_g\text{-}T_x$ (± 6 °C)	ΔT compared to [250,500] μm sintering window
B12.5	528		644	684	116	- 46 °C
B12.5-Mg5	510		641	688	131	- 34 °C
B12.5-Sr10	495		606	664	111	- 62 °C
B12.5-Mg5-Sr10	467	500	620	675	120 / 153	- 20 °C

Table 4
Activation energies for glass transition E_a and crystallization E_c(kis) determined by Kissinger method (Eq. (1)), and additionally E_c(fri) determined additionally using the Friedman method (Eq. (2)), followed by JMA-values n(kis) and n(fri), respectively.

		E_{a1} ± 30 kJ/mol	E_{a2} ± 30 kJ/mol	E_c (kis) ± 30 kJ/mol	E_c (fri) 10 %	n (kis) ± 0.1	n (fri) ± 0.1
B12.5	coarse	493		210	261	1.0	0.8
	fine	477		260	286	1.3	1.2
B12.5-Mg5	coarse	486		237	266	0.7	0.6
	fine	483		296	350	1.1	0.9
B12.5-Sr10	coarse	491		302	242	0.7	0.8
	fine	548		409	296	0.6	0.8
B12.5-Mg5-Sr10	coarse	550	392	185	286	1.0	0.6
	fine	665	516	394	344	0.8	0.9

homogeneous reactions and follows the first order kinetics, the Friedman method makes no mathematical assumption and can be applied to heterogeneous reactions, enabling to evidence changes in crystallization mechanism across the entire crystallization domain [34].

The crystallization of bioactive glass S53P4, the composition where the B12.5-series was originally based on, has been studied in detail [31]. B12.5 borosilicate glass was observed to exhibit lower activation energy for viscous flow ($E_a \sim 480$ kJ/mol), i.e., higher tendency to sinter, when compared to S53P4 (E_a around 800 kJ/mol). This demonstrates that boron significantly enhanced the sintering ability, as also observed in other studies [19,26]. While the presence of boron had a clear effect, varying amounts Mg and Sr for Ca substitutions had smaller impact on activation energies. Additionally, while E_a and E_c did not differ, within the accuracy of the measurement, with addition of Mg when comparing with B12.5, slight E_a increase was associated with Sr addition for B12.5-Sr10 fine particles, and in mixture glass B12.5-Mg5-Sr10. Additionally, observed from the results gained with Kissinger method, that presence of Sr seemed to exhibit an increase in the activation energy for crystallization; this could be attributable to delayed crystallization. However, E_c were quite similar with all compositions and both particle sizes; in detail, values determined with Friedman method for all compositions were similar as the ones obtained using the Kissinger equation. Slight variations with B12.5-Sr10 and B12.5-Mg5-Sr10 E_c values could indicate more complex crystallization mechanism within the glass, such as overlapping or competitions between different crystallization mechanisms.

One aspect to define crystallization is to assess the dimensionality of the crystal growth using the JMA exponent. The *n* values for each glass compositions, with both fine and coarse particles, were found to be close to 1. This suggests surface crystallization, similarly as it has been shown for the S53P4 [31].

3.3. Cross section and porosity of sintered specimen

To assess the crystallization mechanism, we chose to focus on large particles, as finer particles are generally more prone to surface crystallization [13]. Fig. 2 present SEM images of sintered 250–500 μm particles, heat treated at 650 °C for B12.5, 610 °C for B12.5-Mg5 and 600 °C

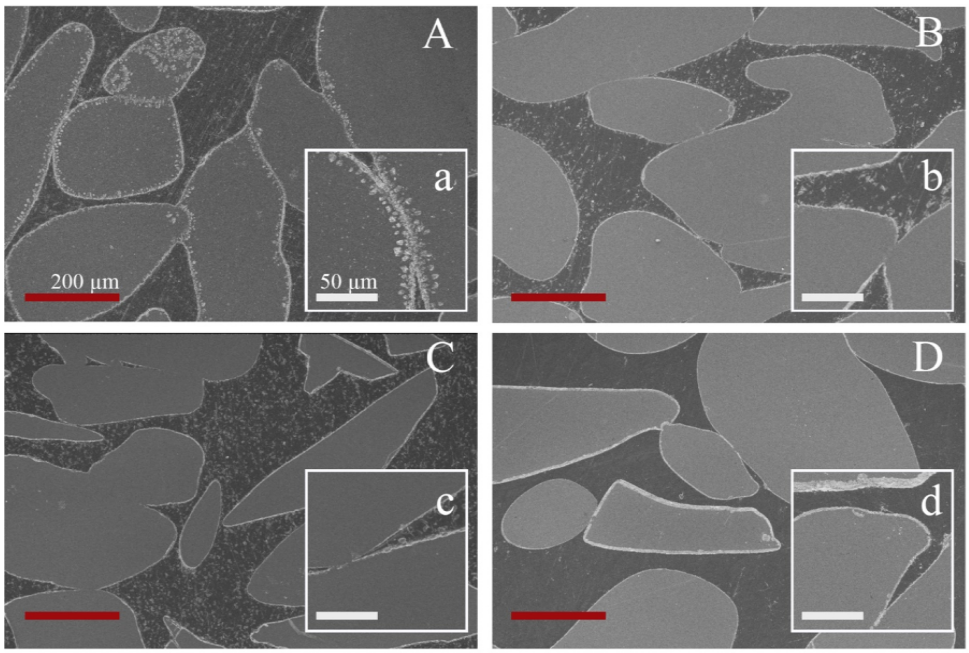

Fig. 2. SEM-image of polished cross sections of the sintered specimen. Darker epoxy-phase surrounds the glass particles. (A) B12.5 sintered 1 h at 650 °C. (B) B12.5-Mg5 sintered 1 h at 610 °C. (C) B12.5-Sr10 sintered 1 h at 600 °C. (D) B12.5-Mg5-Sr10 sintered 1 h at 600 °C. Scale bars: red 200 μm (100x magnification), white 50 μm (250x magnification).

for B12.5-Sr10 and B12.5-Mg5-Sr10. These temperatures were the lowest temperature at which the sintered body could be handled, without premature, spontaneous failure of the specimen. At this temperature, significant surface crystallization was observed on the sintered B12.5 particles (Fig. 2A). Additionally, poor sintering was evident. This might suggest that the crystallization interfered with the viscous flow sintering [9]. Indeed, it has additionally been found by Fagerlund et al. that crystallization of the glass S53P4 inhibited proper glass sintering [6]. B12.5-Mg5 (Figs. 2B) and B12.5-Sr10 (Fig. 2C), where parts of CaO was replaced with either MgO or SrO, showed barely any crystal formation following the grain boundaries (very thin layer of crystallization), and the glass seemed to remain mostly amorphous. Additionally, the sintering could be performed at temperatures 40–50 °C lower than for B12.5. Overall, it was observed that all the studied glasses crystallized from the surface, which is in agreement with the calculation of JMA exponent.

With increasing sintering temperature (temperatures labelled D in Table 2.), SEM micrographs shown in supplementary file S1, it can be seen that, in the case of the B12.5 glass, particles show complete crystallization without significant neck growth. This indicates that crystallization inhibits particle sintering. Mg containing bioactive glass demonstrate to have slower crystallization rate with significant neck growth between particles, indicating partial sintering prior to crystallization.

Table 5. presents the estimated porosity of the sintered specimen. The porosity for B12.5 sintered specimen ranged around 48–54 %, B12.5-Mg5 in the range of 14–36 %, B12.5-Sr10 in the range of 46–52 % and B12.5-Mg5-Sr10 around 20–49 %. Although magnesium in the composition resulted in greater shrinkage and higher densification, interestingly increasing the sintering temperature did not lead to bodies with higher density. This can be related to the concomitant crystallization-sintering [8].

3.4. Stages of crystallization in different sintering temperatures

Fig. 3. presents XRD were performed on coarse particles (250–500 μm), heated at temperatures 'H′ (~ 100 K above T_p determined from DTA with heating rate of 2 K/min), 'L′ (550 °C; above T_g's but under all T_x) and various temperatures between, where sintered bodies, that did not collapse on their own weight, could be obtained. The aim was to observe any signs of crystallization occurring during the sintering stage.

The nature of the crystalline phase was assessed by XRD. As shown in Fig. 3, all glasses exhibit a broad halo in the 27–35° region. This hallow is characteristic of an amorphous material. Upon heat treatment diffraction peaks appeared, which increased with increasing the heat treatment temperature. Peaks were associated to crystallization, with best fit for the most prominent peak being attributable as combeite ($Na_{5.27}Ca_3Si_6O_{18}$; PDF 98-006-2827). This phase is similar to one observed upon crystallization of traditional silicate bioactive glasses, 45S5 and S53P4, i.e. sodium calcium silicate, Na_2O-CaO-2SiO_2 (PDF 01–077–2189) [6]. Additionally, Na_2O-CaO-2SiO_2 crystals have been evidenced when sintering B12.5 glasses as finer particles [35]. Moreover, this also has been attributed to one of the main crystal phases in similar glass composition of B25 [17]. Nevertheless, the literature is far from consensus in identifying a primary crystal phase in silicate bioactive glasses [36] and indeed, additionally combeites ($Na_2Ca_2Si_3O_9$) as a primary crystalline phase have been observed e.g. with 45S5 [19,37]. Furthermore, previous studies have shown that cations might have preferential affinity with the borate phase, thus decreasing the Na content within the silicate phase in phase separated borosilicate glasses, this may also account for small discrepancy in the Na content within the crystal phase [25]. EDS analysis, performed on the thin crystallized layers shown in Fig. 2, was in agreement with the crystal composition observed by XRD.

From Fig. 3A it can be noted, that for B12.5 crystallization occurs simultaneously with sintering, and in this study, mechanically stable sintered bodies were not obtained in the temperature range where glasses would have remained amorphous (i.e., produced specimen were impossible to handle without breakage of the sintered body). On the other hand, it has been demonstrated that with finer glass particles, these glasses could be sintered at their respective T_x–95 °C without inducing crystallization [35,38]. Furthermore, with careful optimization of sintering parameters, manufacturing of porous amorphous bodies could be additionally possible from the coarser particles [39]. However, additions of Mg and Sr (Fig. 3B, C& D) did improve the thermal properties.

While the addition of boron at the expense of SiO_2 clearly enhances the sintering ability of the bioactive glass [20], the substitution of CaO with SrO further, in agreement with the thermal analysis, delayed the crystallization (Fig. 3C, D). And, while Mg effect on E_a was not significant, it is known that Mg, when replaced for Ca tend to shift the viscosity curve toward lower temperature [22], allowing partial sintering of specimen without adverse crystal formation.

While the decrease in bioactivity in crystallized 45S5 and S53P4 has been assigned to the crystal formation [31], it should be kept in mind that the remaining amorphous phase and secondary crystals (not always visible in the XRD pattern) will also impact the bioactivity of the crystallized glasses. Therefore, it is of paramount importance to assess the impact of crystallization on the bioactivity of the glasses. In this study, this was assessed by the precipitation of HCA layer upon immersion in SBF, as seen in [25]. If the crystallization is expected to occur at a fast rate and from the surface, it is extremely difficult to prepare materials with similar degree of crystallinity, or to prepare materials with controlled crystallinity.

3.5. Crystallizations effect on in vitro reactivity

As such, two sets of samples were analysed for each glass composition: *(i)* glasses heat treated at temperature higher than their glass transition, but below the onset of crystallization, labelled 'L′ and *(ii)* glasses heat treated at temperature corresponding to the maximum of their crystallization peak in the DTA thermogram to ensure close to full crystallization, labelled 'H′. All glass particles were then immersed in SBF.

The pH was measured at each time points between 6 and 168 h (Fig. 4). All glasses, irrespective of their composition or heat treatment, led to an increase in pH, as it is characteristic for the dissolution of bioactive glasses [40]. When SrO was present in the composition, a lower pH change was recorded; confirming the stabilizing effect of Sr on

Table 5
Porosity and SD of the sintered specimen calculated using Eq. (4). Temperatures A-E are previously presented in Table 2.

	B12.5		B12.5-Mg5		B12.5-Sr10		B12.5-Mg5-Sr10	
T	porosity (%)	SD	porosity (%)	SD	porosity (%)	SD	porosity (%)	SD
A	-	-	36.2	2.2	46.7	0.9	39.6	2.0
B	54.4	2.0	26.8	0.9	45.7	1.5	34.7	0.8
C	48.7	0.7	24.8	3.9	50.8	3.0	49.0	4.4
D	48.1	0.7	14.2	3.5	50.2	2.8	41.1	3.1
E	47.5	0.8	26.8	5.1	52.1	3.3	20.2	3.3

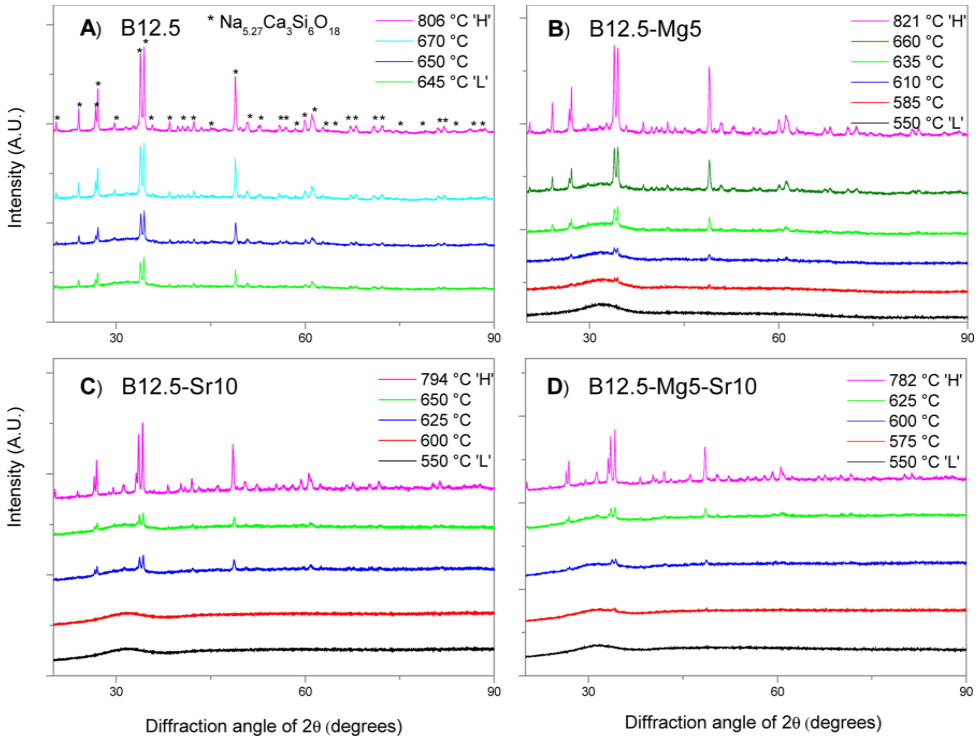

Fig. 3. XRD patterns of the glasses after heat treatments at varied temperatures. (A) B12.5 (B) B12.5-Mg5 (C) B12.5-Sr10 (D) B12.5-Mg5-Sr10.

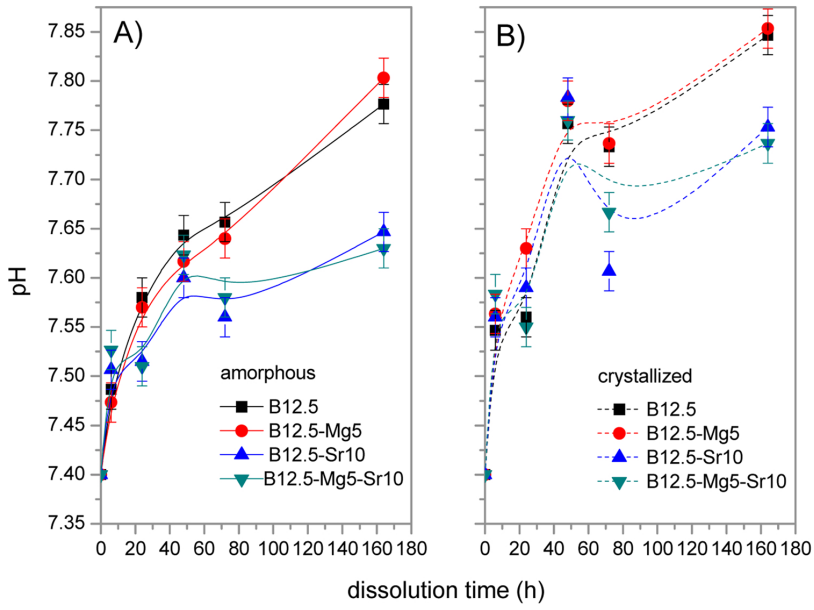

Fig. 4. pH of SBF solution after dissolution time, for specimen sintered at **(A)** low temperatures 'L' and **(B)** high temperatures 'H'.

the glasses' dissolution [25]. At each timepoint, crystallized particles were associated with higher pH than their amorphous counterparts.

Aside, it is worth mentioning that in this experiment the protocol developed by the Technical committee for Bioglasses (TC04 of the International Commission on Glass) was followed [41]. As such, the mass of glass to volume of SBF ratio was kept constant. Therefore, while the pH increase appears similar for B12.5 and B12.5-Mg5, it should be mentioned that the density [25] and therefore the number of particles and overall surface area in contact with the solution is higher in the case of the B12.5-Mg5, thus indicating a slower dissolution from this glass

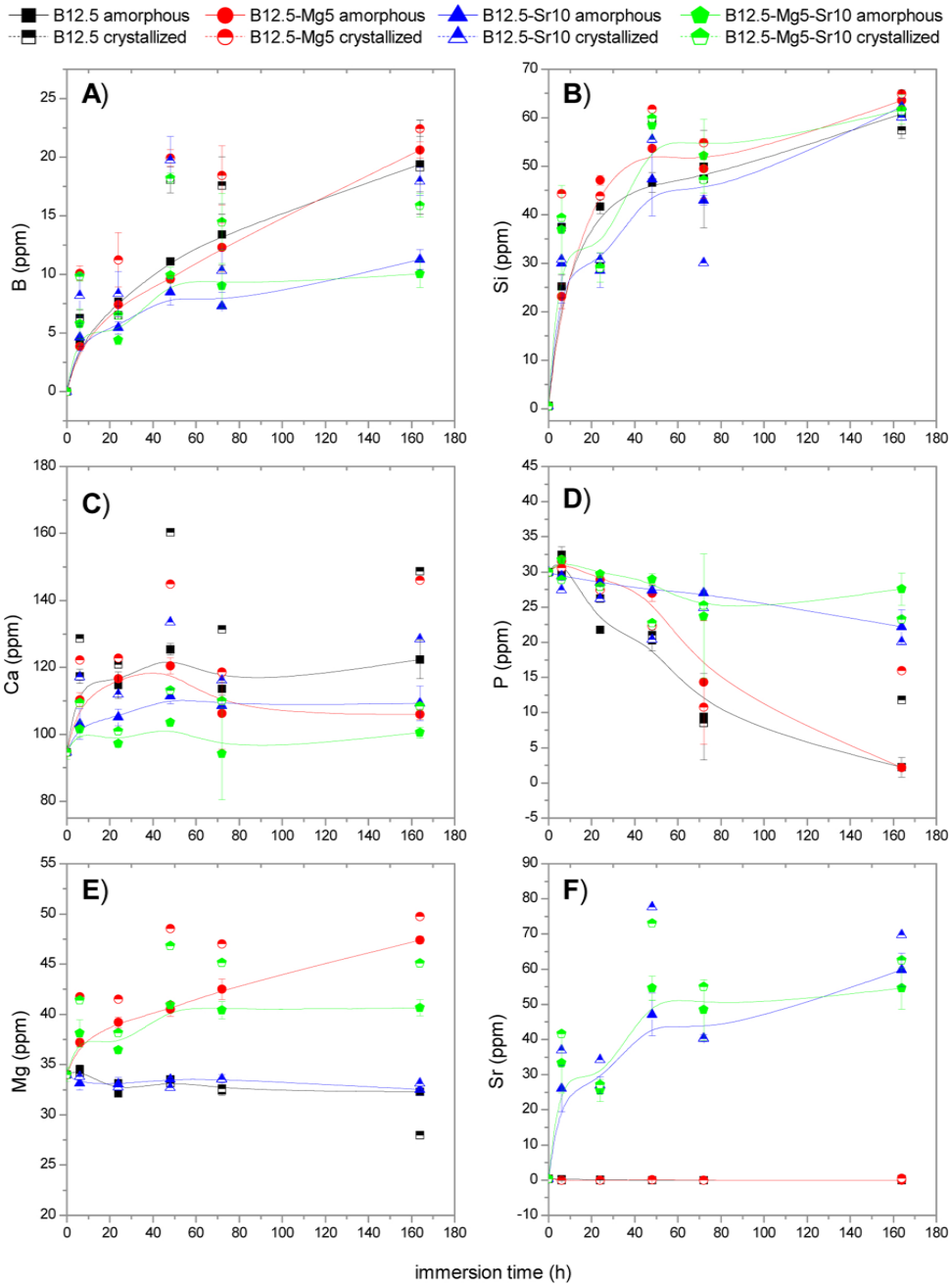

Fig. 5. Dissolution products from amorphous and crystallized B12.5-series glass particles (sintering temperatures L and H in Table 2, respectively) immersed in SBF. ICP (ppm) for dissolution in SBF elements (A) boron, (B) silicon, (C) calcium, (D) phosphorus, (E) magnesium and (F) strontium over immersion time from 6 h to 2 weeks.

compared to B12.5. This is expected, since Mg^{2+} ions are smaller than Ca^{2+}, resulting in larger field strength. Similarly, the replacement of part of the CaO with SrO, leads to glasses with higher density and, thus, maintain the m/V constant leads to lower number of particles immersed and lower surface area, consequently reducing the dissolution rate [23].

ICP-OES was used to assess the ion concentration in solution, post immersion (Fig. 5). When first looking at the glass former, i.e. Si and B; boron appears to be released faster in the crystallized glasses, whereas silicon release appears to be similar in both the crystallized and amorphous samples. Ca, Mg and Sr, all considered as modifiers, exhibit higher concentration in solutions containing the crystallized glasses. Overall, the release of the cation seems correlated with the release of boron. This could indicate that, while the silicate phase crystallizes, the borate phase remains predominantly amorphous and dissolve rapidly in SBF, leading to the increase pH change seen in Fig. 4.

Finally, the consumption of phosphorus is a clear indication of the precipitation of a CaP layer. It has been demonstrated that crystallization of S53P4 bioactive glass led to a decrease in the rate of precipitation of HCA [6]. Here, according to the ion release, the crystallization of the borosilicate glasses does not seem to lead to a significant change in the

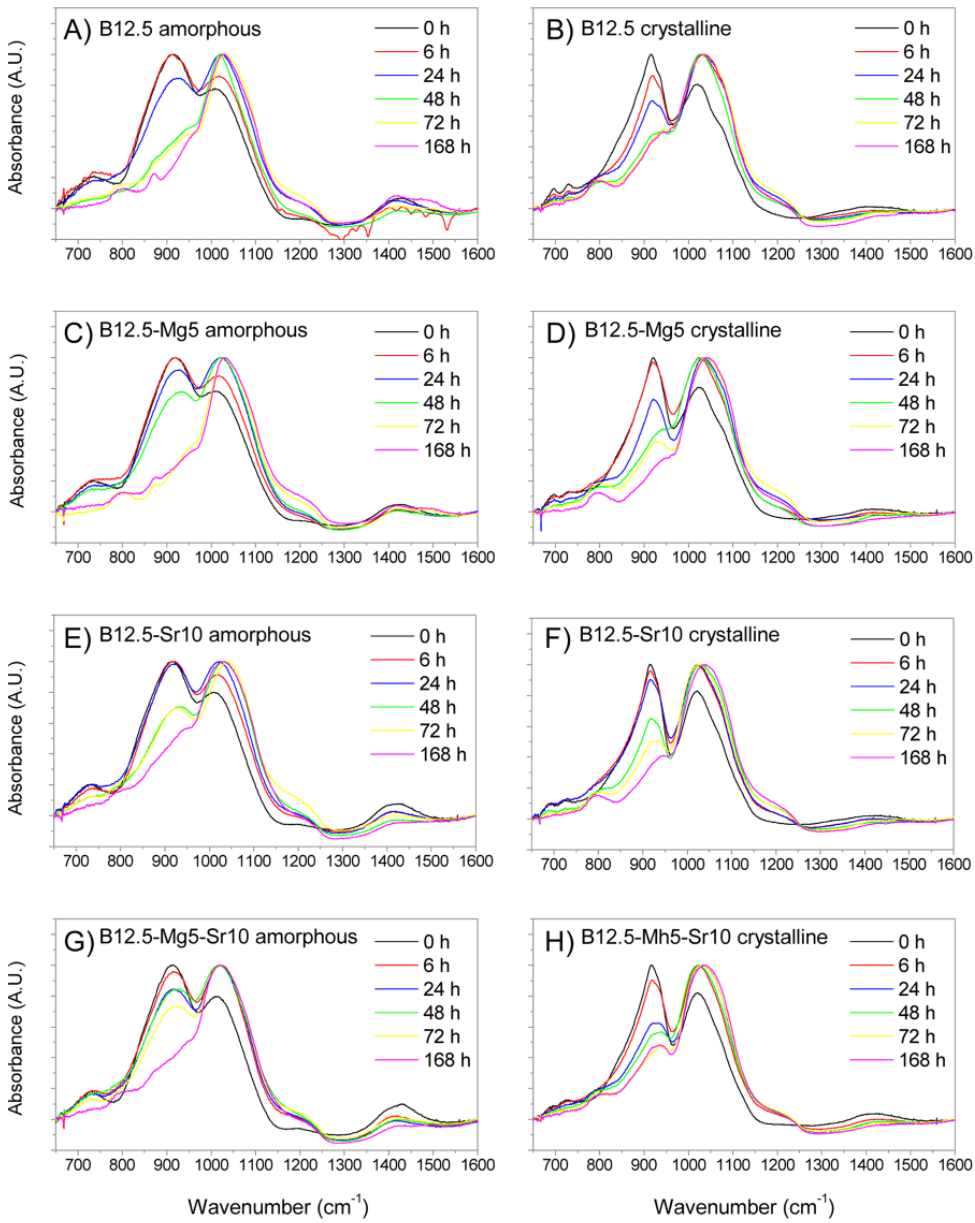

Fig. 6. Background corrected and normalized FTIR curves up to 1600 cm^{-1} for both amorphous and crystallized B12.5 particles, sintered at low and high temperatures, respectively; (A,B) B12.5 (C,D) B12.5-Mg5 (E,F) B12.5-Sr10 (G,H) B12.5-Mg5-Sr10.

speed of CaP formation, until after 72 h immersion. After this, we could observe that for B12.5 and B12.5-Mg5, the P levels stabilise for the crystallized samples, while continuing to decrease for amorphous specimen. This indicates CaP formation stopping earlier for the crystallized B12.5 and B12.5-Mg5, than for their amorphous counterparts. Similar trend was not observed with Sr containing glasses. Overall, the Sr-containing glasses dissolved (and formed precipitate) significantly slower, than other studied compositions. This has been linked to the stabilizing effect of Sr in the glass composition. [25]. Though in this study Mg additions did not seem to have an effect on the degradation rate. Overall, substitution of calcium by magnesium has been linked to slower degradation of bioactive glasses, as well as to delayed apatite formation [22,42–44].

The dissolution study suggests that with these glass compositions, partially crystallized matrixes dissolve more rapidly. Indeed, it has been seen that depending on the forming crystal phases and composition of the remaining glass phase, certain glass-ceramics are highly bioactive [13].

Changes in glass surface composition as a function of immersion time in SBF were assessed using FTIR (Fig. 6). The original untreated glass FTIR for the studied glasses have been discussed by Tainio et al. [25]. For amorphous glasses, these results indicated ion exchange as a result of metal cations being released due to breakage of the borate network, with additional indicators of water absorption and a silica gel formation. Additionally, phosphate and CO-vibration appeared post immersion, indicating the precipitation of a calcium phosphate surface layer containing carbonates, likely as HCA.

With increasing immersion time, for the crystallized specimen (*i*) bands at around 700 – 730 cm^{-1} disappeared; (*ii*) band at 800 cm^{-1} formed after longer immersion period, *(iii)* the band located around 918 cm^{-1} was sharper, and decreased faster for crystallized than for amorphous *(iv)* the band located around 1017 cm^{-1} increased in intensity and shifted to slightly higher wavenumber (around 1024 cm^{-1}), similarly as has been seen with amorphous glasses, *(v)* for all samples, a shoulder at ~1200 cm^{-1} was evident after immersion.

Notable difference between amorphous and crystallized samples was observed around 700–730 cm^{-1}, where a double band could be observed for the crystalline specimen, whereas their amorphous counterparts exhibited initially only one band. This region has been linked to bending of B-O-B linkages of the borate network in borosilicate and borate glasses, or could be attributed to vibrations of various Q^n silicate units containing NBOs, suggesting of a high modification degree of the silicate network [45]. Other prominent change was observed at 918 cm^{-1}. In general, for borosilicate glasses, 850–1200 cm^{-1} region has been linked with B-O stretching vibration of BO_4 [17,46], but could also be associated to Si–O(s) with non-bridging oxygen (Si–O–NBO) stretching vibrations [7]. Decrease in this band intensity is likely due to the release of the soluble silicate and to the dissolution of the borate phase. Intensity increasing of resonances at 1024 and 1243 cm^{-1} corresponding to symmetric vibration of P-O stretching of a phosphate group [7,47]. One additional difference between the specimen was observed at peak formation at around 1420 cm^{-1}. In this area, glasses exhibited a peak attributable to [BO_3] triangles [17,46] before immersion. Upon immersion, with close inspection it could be observed that to the region 1300–1500 cm^{-1}, amorphous B12.5 and B12.5-Mg5 started to form of a doublet, attributable to CO_3^{2-} groups [7,48].

Appearance of phosphate vibration together with the carbonate vibration are typical of the presence of carbonated hydroxyapatite (HA) at the materials surface after the immersion in SBF. Indeed, it is well accepted that the dissolution of bioactive glasses leads to the precipitation of an amorphous calcium phosphate layer (ACP) which then crystallize into HCA [49]. In this study, while both the phosphate and CO_3^{2-} peak are clearly visible upon immersion of amorphous and Sr-free samples, the carbonate vibration is not clearly seen at the surface of Sr-containing glasses. From both ICP and FTIR analysis it appears that the studied amorphous B12.5-Sr10 and B12.5-Mg5-Sr10 exhibit delayed CaP precipitation and delayed crystallization into HCA, when compared to B12.5 and B12.5-Mg5. This could be expected, as seen in previous study [25], higher levels of Sr and/or Mg substitutions in B12.5 compositions led to a decrease both in the rate of borate degradation and in the speed of reactive layer formation. Moreover, in the interest of this study, it was seen that when glasses crystallized, the HCA precipitation and crystallization was further delayed, as the lack of carbonate vibration may indicate that the layer is still, at the ACP stage. The overall fast reactivity of the crystallized specimen could perhaps be assigned to the presence of the borate amorphous phase, remaining post heat-treatment; significant ion release upon immersion could supports the precipitation process. However, overall the delay in HCA formation itself, caused by the crystallization, is a well-known phenomena with bioactive glasses [50].

4. Conclusions

Thermal analysis and JMA exponents for B12.5 and its variants implied dominant surface crystallization for both studied size fractions. This was additionally backed by SEM analysis. The calculated activation energies suggested that the B12.5-glass series exhibited enhanced sintering ability when compared to the commercial composition S53P4. However, the optimal temperature range to sinter the B12.5 is very close to its crystallization temperature, thus easily causing devitrification of the system; as crystallization interfered with viscous flow sintering, the formed sintered bodies were partially crystallized and possessed low mechanical properties. Additions of both Mg and Sr slightly improved the sintering ability, and enabled forming of amorphous, holding structures.

Based on the in vitro dissolution, crystallization seemed to increase the glasses initial reactivity. The main type of crystal was attributable to either combeite, or slightly sodium deficient Na_2O-CaO-2SiO_2. The type of crystals formed can alter the behaviour of the remaining amorphous phase, and thus partly crystallized glass can behave in unexpected ways. Post immersion structural analysis indicated that the typical glass bioactive glass reaction mechanism was maintained. Based on the ion release, it is likely that while the silicate parts of the network partake in the crystal formation, it left more borate rich areas amorphous, with faster reactivity than the completely amorphous glass. This leads to the precipitation of an apatite layer in both amorphous and crystallized glasses, where crystallized samples lacked the carbonate formation. Therefore, results indicated that crystallization inhibited the formation of HCA, while HA was still precipitated.

Overall, while the surface crystallization mechanism can make the sintering challenging, the partial crystallization of the glasses could enable tailoring the glasses chemical stability and degradation rate even further.

Declaration of Competing Interest

The authors declare that they have no known competing financial interests or personal relationships that could have appeared to influence the work reported in this paper.

Acknowledgements

Authors gratefully acknowledge the support of the Jane & Aatos Erkko Foundation (AGATE project) and Tampere University Doctoral School Programme for their funding of the study. Academy of Finland (331924, 295962) and the German Academic Exchange Service (DAAD) are also acknowledged for financial support. This work made use of Tampere Microscopy Center facilities at Tampere University. Authors would like to thank Dr. Turkka Salminen for technical assistance with SEM/EDS imaging and analysis, and prof. Mikko Hokka for EDX analysis.

Appendix A. Supporting information

Supplementary data associated with this article can be found in the online version at doi:10.1016/j.jeurceramsoc.2023.09.043.

References

[1] J.R. Jones, Review of bioactive glass: from Hench to hybrids, Acta Biomater. 9 (1) (2013) 4457–4486.
[2] L.L. Hench, R.J. Splinter, W.C. Allen, T.K. Greenlee, Bonding mechanisms at the interface of ceramic prosthetic materials, J. Biomed. Mater. Res. 5 (6) (1971) 117–141.
[3] L.L. Hench, J.R. Jones, Bioactive glasses: frontiers and challenges, Front. Bioeng. Biotechnol. 3 (2015) 1–12.
[4] J.R. Jones, D.S. Brauer, L:G.D.C. Hupa, Bioglass and Bioactive Glasses and Their Impact on Healthcare, Int. J. Appl. Glass Sci. 7 (2016) 423–434.
[5] D.S. Brauer, Bioactive glasses - structure and properties, Angew. Chem. - Int. Ed. 54 (14) (2015) 4160–4181.
[6] S. Fagerlund, J. Massera, N. Moritz, L. Hupa, M. Hupa, Phase composition and in vitro bioactivity of porous implants made of bioactive glass S53P4, Acta Biomater. 8 (6) (2012) 2331–2339.
[7] M. Magallanes-Perdomo, S. Meille, C. J.-M, E. Pacard, J. Chevalier, Bioactivity modulation of Bioglass® powder by thermal treatment, J. Eur. Ceram. Soc. 32 (11) (2012) 2765–2775.
[8] C. Blaeß, R. Müller, G. Poologasundarampillai, D.S. Brauer, Sintering and concomitant crystallization of bioactive glasses, Int. J. Appl. Glass Sci. 10 (2019) 449–462.
[9] F. Baino, E. Fiume, J. Barberi, S. Kargozar, J. Marchi, J. Massera, et al., Processing methods for making porous bioactive glass-based scaffolds—a state-of-the-art review, Int. J. Appl. Ceram. Technol. 16 (5) (2019) 1762–1796.
[10] H.E. Kissinger, Reaction kinetics in differential thermal analysis, Anal. Chem. 29 (11) (1957) 1702–1706.
[11] J.A. Augis, J.E. Bennett, Calculation of the avrami parameters for heterogeneous solid state reactions using a modification of the kissinger method, J. Therm. Anal. 13 (2) (1978) 283–292.
[12] T. Ozawa, Kinetics of non-isothermal crystallization, Polymer 12 (3) (1971) 150–158.
[13] D.C. Clupper, L.L. Hench, Crystallization kinetics of tape cast bioactive glass 45S5, J. Non-Cryst. Solids 315 (1–2) (2003) 43–48.
[14] A. Hoppe, N.S. Gueldal, A.R. Boccaccini, A review of the biological response to ionic dissolution products from bioactive glasses and glass-ceramics, Biomaterials 32 (11) (2011) 2757–2774.
[15] M. Brink, The influence of alkali and alkaline earths on the working range for bioactive glasses, J. Biomed. Mater. Res. 36 (1998) 109–117.
[16] E.P. Erasmus, O.T. Johnson, I. Sigalas, J. Massera, Effects of sintering temperature on crystallization and fabrication of porous bioactive glass scaffolds for bone regeneration, Sci. Rep. 7 (2017) 6046.
[17] M. Fabert, N. Ojha, E. Erasmus, M. Hannula, M. Hokka, J. Massera, et al., Crystallization and sintering of borosilicate bioactive glasses for application in tissue engineering, J. Mater. Chem. B 5 (23) (2017) 4514–4525.
[18] W. Huang, D.E. Day, K. Kittiratanapiboon, M.N. Rahaman, Kinetics and mechanisms of the conversion of silicate (45S5), borate, and borosilicate glasses to hydroxyapatite in dilute phosphate solutions, J. Mater. Sci.: Mater. Med. 17 (7) (2006) 583–596.
[19] M.N. Rahaman, D.E. Day, B.S. Bal, Q. Fu, S.B. Jung, L.F. Bonewald, et al., Bioactive glass in tissue engineering, Acta Biomater. 7 (6) (2011) 2355–2373.
[20] B. Balasubramanian, T. Büttner, V. Miguez Pacheco, A.R. Boccaccini, Boron-containing bioactive glasses in bone and soft tissue engineering, J. Eur. Ceram. Soc. 38 (3) (2018) 855–869.
[21] D. Ege, K. Zheng, A.R. Boccaccini, Borate bioactive glasses (BBG): bone regeneration, wound healing applications, and future directions, ACS Appl. Biol. Mater. 5 (8) (2022) 3608–3622.
[22] J. Massera, L. Hupa, M. Hupa, Influence of the partial substitution of CaO with MgO on the thermal properties and in vitro reactivity of the bioactive glass S53P4, J. Non-Cryst. Solids 358 (18–19) (2012) 2701–2707.
[23] J. Massera, L. Hupa, Influence of SrO substitution for CaO on the properties of bioactive glass S53P4, J. Mater. Sci.: Mater. Med. 25 (2014) 657–668.
[24] R. Wetzel, M. Blochberger, F. Scheffler, L. Hupa, D.S. Brauer, Mg or Zn for Ca substitution improves the sintering of bioglass 45S5, Sci. Rep. 10 (1) (2020).
[25] J.M. Tainio, D.A. Avila Salazar, A. Nommeots-Nomm, C. Roiland, B. Bureau, D. R. Neuville, et al., Structure and in vitro dissolution of Mg and Sr containing borosilicate bioactive glasses for bone tissue engineering, J. Non-Cryst. Solids 533 (2020), 119893.
[26] J. Massera, C. Claireaux, T. Lehtonen, J. Tuominen, L. Hupa, M. Hupa, Control of the thermal properties of slow bioresorbable glasses by boron addition, J. Non-Cryst. Solids 357 (21) (2011) 3623–3630.
[27] H.L. Friedman, Kinetics of thermal degradation of char-forming plastics from thermogravimetry. Application to a phenolic plastic, J. Polym. Sci. 6 (1) (1964) 183–195.
[28] T. Kokubo, H. Kushitani, S. Sakka, T. Kitsugi, T. Yamamuro, Solutions able to reproduce in vivo surface-structure changes in bioactive glass-ceramic A-W3, J. Biomed. Mater. Res. 24 (6) (1990) 721–734.
[29] M.T. Souza, M.C. Crovace, C. Schröder, H. Eckert, O. Peitl, E.D. Zanotto, Effect of magnesium ion incorporation on the thermal stability, dissolution behavior and bioactivity in Bioglass-derived glasses, J. Non-Cryst. Solids 382 (2013) 57–65.
[30] D. Neuville, L. Cormier, V. Montouillout, P. Florian, F. Millot, J.C. Rifflet, et al., Structure of Mg- and Mg/Ca aluminosilicate glasses: 27Al NMR and Raman spectroscopy investigations, Am. Mineral. 93 (2008) 1721–1731.
[31] J. Massera, S. Fagerlund, L. Hupa, M. Hupa, Crystallization mechanism of the bioactive glasses, 45S5 and S53P4, J. Am. Ceram. Soc. 95 (2012) 607–613.
[32] J. Massera, M. Mayran, J. Rocherullé, L. Hupa, Crystallization behavior of phosphate glasses and its impact on the glasses' bioactivity, J. Mater. Sci. 50 (8) (2015) 3091–3102.
[33] H.E. Kissinger, Variation of peak temperature with heating rate, J. 0 F. Res. Natl. Bu reau Stand. 57 (4) (1956).
[34] M.J. Starink, The determination of activation energy from linear heating rate experiments: a comparison of the accuracy of isoconversion methods, Thermochim. Acta 404 (1–2) (2003) 163–176.
[35] J. Pohjola, Borosilicate Scaffold Processingfor Bone Tissue Engineering. Tampere, 2017.
[36] D. Bellucci, V. Cannillo, A. Sola, An overview of the effects of thermal processing on bioactive glasses, Sci. Sinter. 42 (2010) 307–320.
[37] O.P. Filho, G.P. Latorre, L.L. Hench, Effect of crystallization on apatite-layer formation of bioactive glass 45S5, J. Biomed. Mater. Res. 30 (4) (1996) 509–514.
[38] A. Szczodra, J.M. Tainio, A. Houaoui, H. Liu, J. Pohjola, S. Miettinen, et al., Impact of borosilicate bioactive glass scaffold processing and reactivity on in-vitro dissolution properties, Mater. Today Commun. (2023) 35.
[39] L. Aalto-Setälä, P. Uppstu, P. Sinitsyna, N.C. Lindfors, L. Hupa, Dissolution of amorphous S53P4 glass scaffolds in dynamic in vitro conditions, Materials 14 (17) (2021) 4834.
[40] L.L. Hench, D.E. Clark, Physical chemistry of glass surfaces, J. Non-Cryst. Solids 28 (1) (1978) 83–105.
[41] A.L. Maçon, T.B. Kim, E.M. Valliant, K. Goetschius, R.K. Brow, D.E. Day, et al., A unified in vitro evaluation for apatite-forming ability of bioactive glasses and their variants, J. Mater. Sci.: Mater. Med. 26 (2) (2015) 1–10.
[42] M. Diba, O. Goudouri, F. Tapia, A.R. Boccaccini, Magnesium-containing bioactive polycrystalline silicate-based ceramics and glass-ceramics for biomedical applications, Curr. Opin. Solid State Mater. Sci. 18 (3) (2014) 147–167.
[43] M. Blochberger, L. Hupa, D.S. Brauer, Influence of zinc and magnesium substitution on ion release from Bioglass 45S5 at physiological and acidic pH, Biomed. Glass (2015) 1.
[44] N. Kanzaki, K. Onuma, G. Treboux, S. Tsutsumi, A. Ito, Inhibitory effect of magnesium and zinc on crystallization kinetics of hydroxyapatite (0001) face, J. Phys. Chem. B 104 (17) (2000) 4189–4194.
[45] S. Agathopoulos, D.U. Tulyaganov, J.M.G. Ventura, S. Kannan, A. Saranti, M. A. Karakassides, et al., Structural analysis and devitrification of glasses based on the CaO–MgO–SiO2 system with B2O3, Na2O, CaF2 and P2O5 additives, J. Non-Cryst. Solids 352 (4) (2006) 322–328.
[46] P. Pascuta, M. Bosca, S. Rada, M. Culea, I. Bratu, E. Culea, FTIR spectro-scopic study of Gd2O3-Bi2O3-B2O3 glasses, J. Optoelectron. Adv. Mater. 10 (2008) 2416–2419.
[47] Q. Fu, M. Rahaman, B. Bal, W. Huang, D. Day, Preparation and bioactive characteristics of a porous 13–93 glass, and fabrication into the articulating surface of aproximal tibia, J. Biomed. Mater. Res. Part A 82 (1) (2007) 222–229.
[48] A.C. Queiroz, J.D. Santos, F.J. Monteiro, M.H. Prado da Silva, Dissolution studies of hydroxyapatite and glass-reinforced hydroxyapatite ceramics, Mater. Charact. 50 (2–3) (2003) 197–202.
[49] Y. Yu, Z. Bacsik, M. Edén, Contrasting in vitro apatite growth from bioactive glass surfaces with that of spontaneous precipitation, Materials 11 (9) (2018).
[50] O.P. Filho, L.T. G.P, L.L. Hench, Effect of crystallization on apatite-layer formation of bioactive glass 4S55, J. Biomed. Mater. Res. 30 (1996) 509–514.

III

IMPACT OF BOROSILICATE BIOACTIVE GLASS SCAFFOLD PROCESSING AND REACTIVITY ON IN-VITRO DISSOLUTION PROPERTIES

by

Agata Szczodra*, Jenna M. Tainio*, Amel Houaoui, Hongfei Liu, Juuso Pohjola, Susanna Miettinen, Delia S. Brauer and Jonathan Massera

Materials Today Communications, Volume 35, Article ID 105984, June 2023.

Materials Today Communications 35 (2023) 105984

Contents lists available at ScienceDirect

Materials Today Communications

journal homepage: www.elsevier.com/locate/mtcomm

Impact of borosilicate bioactive glass scaffold processing and reactivity on in-vitro dissolution properties

Agata Szczodra [a,*,1], Jenna M. Tainio [a,1], Amel Houaoui [a], Hongfei Liu [a], Juuso Pohjola [a], Susanna Miettinen [a,b], Delia S. Brauer [c], Jonathan Massera [a]

[a] Tampere University, Faculty of Medicine and Health Technology, Tampere, Finland
[b] Research, Development and Innovation Centre, Tampere University Hospital, Tampere, Finland
[c] Otto-Schott-Institut, Friedrich-Schiller-Universität, Jena, Germany

ARTICLE INFO

Keywords:
Borosilicate bioactive glasses
Scaffolds
In vitro dissolution
3D printing
Human cells

ABSTRACT

In this study, bulk borosilicate glasses and 3D scaffolds (processed by the burn-off technique and by robocasting) were synthesized to investigate the impact of the manufacturing method, glass composition and preincubation time on in vitro dissolution and cell response. The studied compositions are based on commercial bioactive glass S53P4 (BonAlive) where 12.5% SiO_2 has been replaced by B_2O (labelled B12.5), and part of the CaO is replaced with MgO and SrO (labelled B12.5-Mg-Sr). First, the impact of the processing and glass composition, on the dissolution rate, was assessed. As expected, scaffolds were found to exhibit faster dissolution, due to the increased surface area, when compared to the bulk glass. Furthermore, the 3D printed scaffolds were found to dissolve faster than the burn-off scaffolds. Moreover, scaffolds made from B12.5-Mg-Sr glass composition exhibited slower ion release and precipitation of calcium phosphate (CaP) layer, when compared to B12.5, due to the stabilizing effect of Mg and Sr. Finally, dynamic condition produces lower ion releases that static condition and could be more optimal for in vitro cell growth. Secondly, in culture with murine MC3T3-E1 cells, it was shown that 3 days preincubation would be optimal to decrease the burst of ions that is known to lead to cell death. However, it was found that MC3T3-E1 survived and proliferated only in presence of B12.5-Mg-Sr scaffolds. Finally, it was shown that despite scaffolds having different porosities, they had no significant difference on human adipose-derived stem cells (hADSCs) survival. This manuscript brings new information on 1) the impact of material design (porosity) and composition on dissolution kinetic sand reactivity, 2) the impact of static vs dynamic testing on in-vitro dissolution and 3) the impact of materials' pre-incubation on cell behavior.

1. Introduction

Current BAG bone substitutes are limited to powders, granules, and putties. No porous 3D scaffolds are currently commercialized. Indeed, commercial silicate BAG e.g., S53P4 demonstrate crystallization tendencies during sintering, thus inhibiting the processing of porous construct [1-4]. For 3D scaffold to be osteoconductive, large pores (50–500 μm) and highly interconnected porosity (> 50 μm) with overall porosity over 50% are needed to allow tissue infiltration and regeneration [5,6]. Additionally, it is crucial for proper bone repair that scaffold would provide mechanical support, with properties close to the natural bone [5,7].

To overcome the high crystallization tendency of traditional silicate bioactive glasses, borosilicate glasses were developed [4,8]. High boron content was found efficient in producing glasses with fast and more complete conversion into hydroxyapatite and with thermal properties allowing sintering into 3D scaffolds without crystallization [9,10,4,8]. However, high porosity of porous scaffolds, and fast dissolution of borosilicate glasses lead to extensive ion release, in vitro, often resulting in cells death [11,12]. However, this is not a problem in vivo where ions get constantly flushed away [4,13]. Consequently, it is difficult to evaluate the true potential of borosilicate 3D porous scaffolds as bone replacement based on in vitro studies. Thus, understanding how different parameters can affect ion release and dissolution rate, would allow for better control over their final performance in vitro and easier translation into in vivo and clinical studies.

* Corresponding author.
E-mail address: agata.szczodra@tuni.fi (A. Szczodra).
[1] Shared authorship.

https://doi.org/10.1016/j.mtcomm.2023.105984
Received 20 October 2022; Received in revised form 30 March 2023; Accepted 11 April 2023
Available online 11 April 2023

Table 1
Nominal glass composition (%).

Glass	mol%						
	SiO_2	B_2O_3	CaO	Na_2O	P_2O_5	MgO	SrO
B12.5	47.12	6.73	21.77	22.66	1.72	0	0
B12.5-Mg-Sr	47.12	6.73	6.77	22.66	1.72	5	10

To gain better understanding on the impact of borosilicate glass composition and porosity on the in-vitro dissolution and cell behaviour, two borosilicate glasses based on the S53P4 composition were developed; B12.5: 47.12 SiO_2–6.73 B_2O_3–21.77 CaO–22.66 Na_2O–1.72 P_2O_5 (mol%) and B12.5-Mg-Sr: 47.12 SiO_2–6.73 B_2O_3–6.77 CaO–22.66 Na_2O–1.72 P_2O_5–5 MgO–10 SrO (mol%). In the study by Tainio et al. the initial characterization of B12.5 glasses modified, where Mg and/or Sr where partially substituted for Ca, has been done [14]. Based on the results, the B12.5 and B12.5-Mg-Sr glass compositions, with respectively fastest and slowest dissolution rate, were chosen for this study. The idea was 1) to assess which aqueous solution better mimics the dissolution/reaction of bioactive glasses in culture medium, 2) to assess if an increased pre-incubation time can decrease the initial burst release, of a fast degrading bioactive glass, while maintaining a significant release of therapeutic ions, 3) to better understand the changes in ion release when the dissolution is in dynamic rather than static, 4) to study the impact of scaffolds structure on the release of ions, and 5) assess the impact of ions release and pre-incubation time on cell behavior.

Generally, the replacement of CaO with SrO and/or MgO has stabilizing effect on borate network and helps to reduce the dissolution rate of the glass [14]. Moreover, substitution of SrO and/or MgO for CaO increases the hot forming domain in S53P4, thus allows better sinterability with suppressed crystallization tendencies [15,16]. Additionally, SrO has been shown to stimulate an osteogenic response from hBMSCs [17,18] and MC3T3-E1 (J. [19]; [20]. Furthermore, Sr was reported to promote the proliferation and differentiation of osteoblasts [21-23]. Magnesium is also essential for bone development and homeostasis, and it has been shown to stimulate osteogenesis in human osteoblasts [24, 25]. Furthermore, addition of MgO and SrO in the composition of the glass promotes bone repair and remodeling [26-28].

Moreover, due to improved thermal properties, these glass compositions were used to produce 3D porous scaffolds using the porogen burn-off or 3D printing (robocasting) manufacturing methods. Porogen burn-off is a relatively easy technique that does not require advanced or expensive equipment. The porogen burn-off also allows fabrication of scaffolds with high porosity (>90%) and macropores having dimension up to 500 μm [29,30]. However, this technique usually leads to low pore interconnectivity with, often, interconnection too small to favour cell migration. [29,31]. 3D printing technique allows a precise control over the object structures such as the interconnectivity, shape, orientation, and pore size which can be customized through a 'layer-by-layer' manufacturing [29,32,33]. Computer-aided-design (CAD) is used and allows the development of fully interconnected porous networks that cannot be easily built using conventional techniques.

Finally, an effect of manufacturing method and glass composition on static/dynamic in vitro dissolution in TRIS and SBF was studied by Inductively Coupled Plasma – Optical Emission Spectroscopy (ICP-OES) and SEM. The effect of glass composition and preincubation time in TRIS and αMEM culture medium on murine MC3T3-E1 cell response was also investigated. Lastly, effect of manufacturing method on hADSCs cell behaviour was examined. Moreover, scaffolds mechanical properties were investigated as well as their microstructure analyzed by micro-computed tomography (μCT).

The goal of this study was to show that the control over the glass composition, preincubation time and manufacturing method can prevent excessive ion release from borosilicate 3D porous scaffolds and consequently improve bioactivity and cell viability. Moreover, we introduced borosilicate 3D scaffolds with different porosities as a suitable candidate for bone tissue engineering. The studied scaffolds are promising as bone grafts that promote, support, and direct the new bone growth. Moreover, 3D printed scaffolds could allow manufacturing of custom-made implants with tailored porosity.

2. Materials and methods

2.1. Preparation of bioactive glass powders

B12.5 and B12.5-Mg-Sr were prepared from analytical grade (Na_2CO_3, NH_4H_2PO4, $(CaHPO_4)(2(H_2O))$, $CaCO_3$, MgO, $SrCO_3$, H_3BO_3 (Sigma Aldrich, St Louis, MO, USA), and Belgian quartz sand. The 60 g batches of B12.5 and B12.5-Mg-Sr were melted for 30 min at 1300 °C in a platinum crucible in LHT 02/17 LB Speed electric furnace (Nabertherm GmbH, Lilienthal, Germany) in air atmosphere. The batch was heated from room temperature to 800 °C using 10 °C/min heating rate and kept at 800 °C for 15 min to allow evaporation of volatile CO_2. Then the temperature was raised from 800 °C to 1300 °C using 10 °C/min heating rate and kept at 1300 °C for 30 min to homogenize the glass melt. The molten glasses were casted and then annealed for at least 6 h at 450 °C in electric muffle furnace (Nabertherm L 3/12). After annealing, glasses at room temperature were crushed, milled in a planetary ball mill (Fritsch GmbH, Idar-Oberstein, Germany), and sieved into less than 38 μm particles with sieves (Gilson Company, Inc., Ohio, USA). The nominal oxide compositions of the glasses are given in Table 1.

2.2. Scaffold manufacturing

Burn-off scaffolds were made by pressing mixture of glass powder and porogen inside a cylindrical mold. The ammonium bicarbonate, NH_4HCO_3 (Sigma-Aldrich, 99.5%, CAS No. 1066–33–7), was used as the porogen (70 vol%) and mixed with glass (30 vol%). The porogen is assumed to fully evaporate during the sintering, leaving pores behind.

3D printed scaffolds were made by robocasting using 3Dn-Tabletop printer (nScrypt Inc., Orlando, Florida, USA), and controlled via the Machine Tool 3.0 system software.

Firstly, the Pluronic solution, which acts as the binder, was made by mixing the Pluronic 127 (Sigma-Aldrich, CAS No. 9003–11–6) and distilled water in the ratio of 25:75 wt% respectively, in an ice bath, until the solution turned clear. The solution was then stored at 4 °C.

Secondly, the ink was made by mixing glass powder and Pluronic solution in the ratio of 30:70 wt% respectively, using Vibrofix VF1 electrical shaker (IKA®-Labortechnic, Staufen, Germany) at 2500 rpm. Mixing was done in intervals of 30 s mixing and then 30 s cooling in the ice bath. The mixing-cooling cycles were repeated at least 5 times until the ink was homogenous and no bubbles could be visually seen. The ink was loaded into Optimum® 3cc printing cartridge (Nordson EFD, Bedfordshire, England) and left for 1 h at room temperature to achieve right viscosity for 3D printing.

Finally, the cartridge was attached to the 3D printer and ink extruded through the SmoothFlow Tapered Tips with tip diameter of 0.41 mm (Nordson EFD Optimum® SmoothFlow™, Westlake, Ohio, USA) onto the acrylic sheets (Folex AG, Seewen, Switzerland). The material feed was set to 18.0–22.0 psi, to maintain a continuous flow during movement of the tip. After drying at room temperature for at least 24 h to reduce the risk of collapse, scaffolds were ready for sintering.

For cellular experiments, the burn-off scaffolds and 3D printed scaffolds were compared to the bulk of these same glasses. Bulk scaffolds were made by pressing the glass powder into a cylindrical mold with diameter and height of 5 mm. The compacted pellets were placed onto a ceramic plate for the sintering.

Bulk, burn-off and 3D printed scaffolds were sintered for 1 h at between 540 and 545 °C (Nabertherm LT 9/11/SKM electric muffle furnace) in an air atmosphere. Sintering allows fusing of glass particles, but also removes the porogen and binder from scaffolds. The sintering

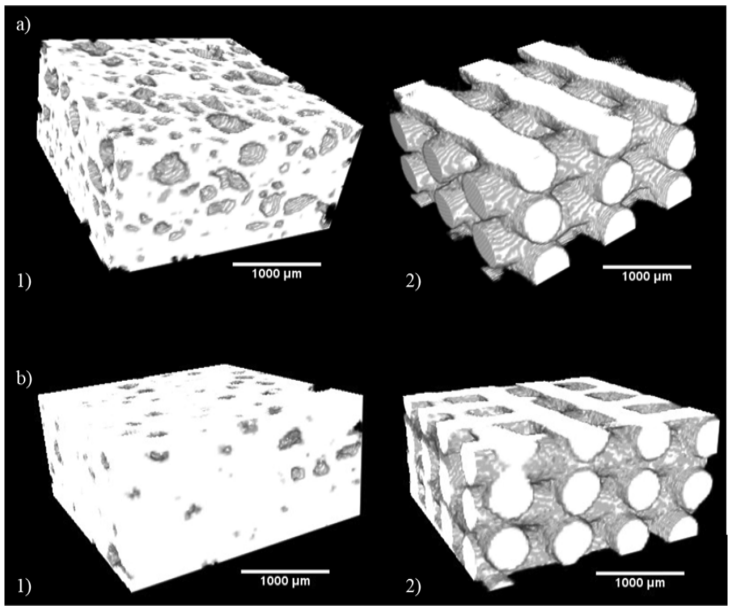

Fig. 1. 3D structure of scaffolds produced via 1) burn-off, 2) 3D printing of a a) B12.5, b) B12.5-Mg-Sr compositions.

Table 2
Average sizes of scaffolds used for static in vitro dissolution in TRIS and SBF.

	Burn-off		3D printed	
Type of scaffolds	Bottom diameter (mm)	Height (mm)	Bottom diameter (mm)	Height (mm)
B12.5	14.37 ± 0.16	4.3 ± 0.3	9.82 ± 0.17	4.45 ± 0.08
B12.5-Mg-Sr	12.59 ± 0.28	4 ± 0.39	8.41 ± 0.26	3.83 ± 0.11

process had three phases: 1) from room temperature to 300 °C at 1 °C/min, 2) from 300 °C to the sintering temperature at 5 °C/min and 3) staying at the sintering temperature for 1 h. Multistep, slow sintering is done to avoid sudden shrinkage which might cause cracking of the scaffolds. Sintered scaffolds were taken out after furnace cools down to room temperature and stored in a desiccator. Figure S1, presents the images of the produced scaffolds, post-sintering.

2.3. Material characterization

2.3.1. Porosity measurements

The estimation of the scaffolds' porosity was performed assuming that scaffolds are cylinder-shaped. The porosity was estimated using the following equation:

$$Porosity = (1 - \rho/\rho_0) \times 100\% \quad (1)$$

where the ρ_0 was the bulk density, and ρ was the apparent density (scaffolds mass divided by scaffold volume) of each scaffold. The porosities were obtained from at least 50 parallel samples per each glass composition and type and expressed as mean ± standard deviation (SD).

2.3.2. Micro-computed tomography (μCT)

Micro-computed tomography (μCT) was utilized to gain information about the scaffold 3D structures and these are shown in Fig. 1. Measurements were conducted with MicroXCT-400 (Carl Zeiss X-ray Microscopy, Inc., Pleasanton, California, USA) by having 80 kV tube voltage and 0.4x objective. The resulting pixel size was 16.7 μm. Scaffold structures were constructed from the obtained data with ImageJ software combined with 3D Viewer plugin. Images show that scaffolds produced via porogen burn-off had randomly sized and located round pores. 3D printed scaffolds were comprised of parallel filaments with constant spacing making interconnected porosity.

2.3.3. X-ray powder diffraction (XRD)

To evaluate if the 3D printed and porogen burn-off glass scaffolds stayed amorphous after sintering they were grounded to fine powder in a mortar and analyzed with a X-ray diffractometer (XRD). Measurements were conducted in the 10–60° 2θ diffraction angle range with MiniFlex™ (Rikagu, Tokyo, Japan).

2.3.4. Mechanical properties

Scaffolds produced via porogen burn-off had shrunk inhomogeneously during sintering. Thus, their top and bottom surfaces were ground flat with grit P800 SiC paper in Ethanol (96%, VWR Chemicals, CAS No. 64–17–5). Ground samples were dried overnight in a type B 8133 drying oven (Termaks, Bergen, Norway) at 37 °C.

For measurements burn-off and 3D printed scaffolds with diameter d≈ 11–14 mm and height h≈ 5–6 mm were used. Compression testing was conducted with Instron 4411 mechanical tester (Instron, Massachusetts, USA) by using a 0.5 mm/min deformation speed. 5 kN load cell was used for glass scaffolds. Highest compression values were taken from individual measurements to describe the compressive strength of glass scaffolds. The measurements were obtained from three parallel samples for each scaffold type and glass composition and expressed as mean ± standard deviation (SD).

2.3.5. Physico-chemical characterization

To study the dissolution behavior of the scaffolds and their bioactivity, they were immersed in in Tris(hydroxymethyl)aminomethane (TRIS) and Simulated Body Fluid (SBF), respectively. The average sizes of the scaffolds used for this characterization step are presented Table 2.

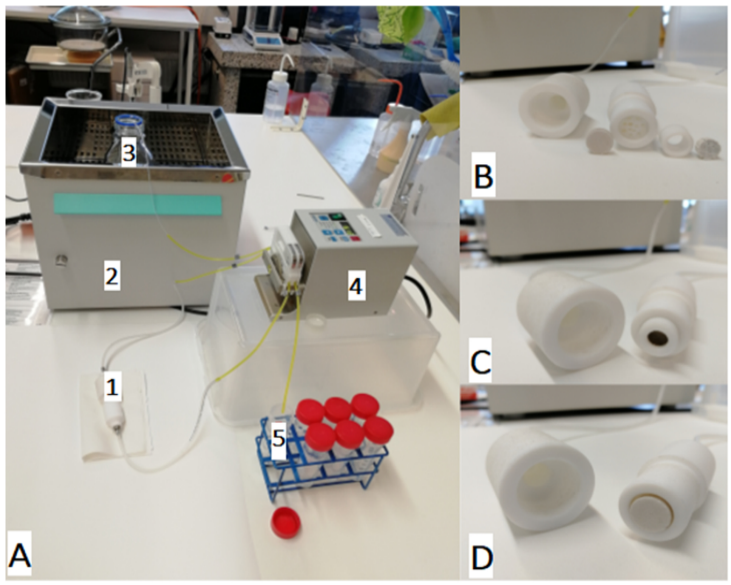

Fig. 2. Picture of the flow-through system. A) is the intact system: 1-reactor, 2-water bath, 3-bottle of SBF, 4-pump, 5-outflow; B is inner structure of reactor; C is a scaffold adjusted by a Teflon ring; D is a scaffold loaded into chamber.

2.3.6. Fourier transformation infrared spectroscopy (FTIR)

Sintered B12.5 and B12.5-Mg-Sr glass scaffolds were crushed into powders. FTIR measurements were conducted with a Spectrum One FTIR Spectrophotometer (PerkinElmer Inc., Massachusetts, USA) using the attenuated total reflectance (ATR) mode. 8 scan accumulations were performed in the 650–4000 cm^{-1} wavenumber range with a 4 cm^{-1} resolution. The spectra were baseline corrected and normalized to the peak with the highest intensity.

2.3.7. Dissolution in TRIS in static conditions

Dissolution of the scaffolds in TRIS was done to test the ions leaching, while the risk of ionic supersaturation was limited [34]. TRIS solution (50 mM) was prepared by mixing ultrapure TRIS (Sigma Aldrich, St Louis, MO, USA) and TRIS-HCl (Sigma Aldrich, St Louis, MO, USA) in pure water. The pH of the solution was adjusted to 7.4 at 37 °C. The solution was not refreshed over the course of the immersion test.

Burn-off and 3D printed scaffolds made from B12.5 and B12.5-Mg-Sr glass compositions were immersed in TRIS solution for up to 2 weeks in an incubator at 37 °C (Orbital incubator SI600, Stuart) with an orbital speed of 100 rpm. The volume of TRIS was calculated to maintain a mass/volume ratio constant at 20 mg/ml. At each timepoint (6, 24, 48, 72, 168, and 336 h), the pH of the immersion solution was measured at 37 °C using a S47-K SevenMultiTM pH-meter (Mettler-Toledo LLC, Ohio, USA). The ionic concentration was studied by Inductively Coupled Plasma – Optical Emission Spectroscopy (ICP-OES). After drying the samples 48 h at 37 °C, the mass loss ratio was calculated following the equation:

$$Massloss = (W_0 - W_t)/W_0 * 100 \quad (2)$$

Where the W_0 is the original mass before immersion, and W_t is the dry mass after each time of immersion.

This study was conducted on three parallel samples and two parallel blank samples, and the results are presented as mean ± SD.

2.3.8. Dissolution in SBF in static conditions

The samples in vitro bioactivity, related to the formation of HA and the change in ionic concentration, was studied in SBF, developed by Kokubo et al. and prepared following the methodology from the standard ISO/FDIS 23317. During the experiment, the solution was not refreshed to observe the precipitation of CaP.

Burn-off and 3D printed scaffolds made from B12.5 and B12.5-Mg-Sr glass compositions were immersed in SBF in the same way as TRIS immersion. The volume of SBF was calculated to maintain a mass/volume ratio constant at 20 mg/ml. At each timepoint (6, 24, 48, 72, 168, and 336 h), the pH of the solution was measured at 37 °C, the mass loss was calculated, and the ionic concentration was studied. This study was conducted on three parallel samples and two parallel blank samples, and the results are presented as mean ± SD.

2.3.9. Scanning electron microscope (SEM)

To assess the bioactivity and HA layer formation, SEM/EDX imaging was used to analyze scaffolds after 336 h of static immersion in SBF. For SEM analysis, the scaffold pieces were mounted in epoxy resin and polished with Struers Tegramin-30 automatic polishing machine up to 1 μm diamond suspension. Samples were carbon coated prior to analysis. Magnification of 250x, 15 kV acceleration voltage and back-scattered electrons were used for imaging. Thicknesses of the surface layers were obtained via image analysis with ImageJ from 10 different spots and the results are presented as mean ± SD.

2.3.10. Dissolution in SBF in dynamic conditions

The dynamic dissolution of burn-off and 3D printed scaffolds made from B12.5 and B12.5-Mg-Sr glass compositions, was evaluated in SBF with a flow-through system. Each scaffold was loaded separately in a home-made reactor, which was connected to the bottle of SBF solution on one end (inlet) and the outlet to tubes to collect the fluid. There was a detachable Teflon ring to adjust the cross-section of the reactor to match the size of the different type of scaffolds. The experiment for each sample was performed with SBF at 37 °C and at 0.4 ml/min flow rate for 74 h. At each timepoint, the pH of the outflow solution was measured, the outflow tube was removed and replaced with new container. For first three days the solution was collected 8 times per day during an 8-hour window. On the last day, the solution was collected 3 times during a

Table 3
Average porosity of scaffolds.

	Porosity (%)		
Type of scaffolds	Bulk	Burn-off	3D printed
B12.5	30.85 ± 8.53	72.5 ± 1.4	69.68 ± 3.19
B12.5-Mg-Sr	15.17 ± 7.38	60.4 ± 2.75	51.79 ± 5.77

Table 4
Average width and length of pores found in 3D printed scaffolds. Measured by optical microscope.

Type of scaffolds	Width (μm)	Length (μm)
B12.5 3D printed	280 ± 70	290 ± 60
B12.5-Mg-Sr 3D printed	192 ± 46	208 ± 57

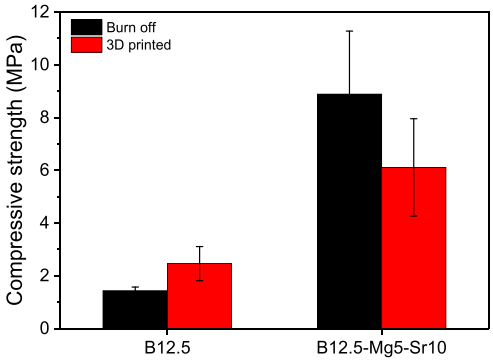

Fig. 3. Compressive strength at failure.

3-hour time window. The whole set-up is shown in Fig. 2. The analyses were conducted once on each sample and blank sample.

2.3.11. ICP analysis

The immersion solutions collected from static and dynamic in vitro dissolution in TRIS and SBF were diluted 10 times in 1 M high purity nitric acid for ion analysis. ICP-OES (Agilent technologies 5110, Santa Clara, CA, USA) was employed to quantify P^{3-} ($\lambda = 213.618$ nm), Ca^{2+} ($\lambda = 422.673$ nm), Mg^{2+} ($\lambda = 285.213$ nm), Si^{4+} ($\lambda = 250.690$ nm), B^{3+} ($\lambda = 249.772$ nm), Sr^{2+} ($\lambda = 421.552$ nm), and Na^{+} ($\lambda = 588.995$ nm) ion concentrations in the immersion solutions.

2.4. Effect of preincubation in TRIS and αMEM

Bulk, burn-off and 3D printed scaffolds with diameter d≈ 4.5 mm and height h≈ 4.5 mm, were immersed in TRIS and α-Minimum Essential Media (α-MEM) to investigate which preincubation time affects the ion release from the scaffolds.

One scaffold per each composition, scaffold type and timepoint, was immersed in TRIS solution for up to 6 days at 37 °C in incubator with an orbital speed of 100 rpm. The TRIS was refreshed at days 2 and 4 to mimic the changing of cell culture media. At each timepoint (day 1, 2, 4 and 6) and before refreshing, the samples for ICP measurement were collected and diluted 10 times in 1 M high purity nitric acid. Moreover, at each timepoint the pH of preincubation solution was measured. Because some samples were refreshed, the ICP and pH measurements of TRIS solution were conducted on one to three parallel samples and on one to three parallel blank samples, and the results are presented as mean ± SD.

Each scaffold, after immersion in TRIS, was immersed in α-Minimum Essential Media (α-MEM) (Gibco, Life Technologies, Carlsbad, CA, USA) containing glutamine supplemented with 1% penicillin/streptomycin (Gibco, Life Technologies, Carlsbad, CA, USA). After 24 h, preincubation solution was collected and diluted 10 times in 1 M high purity nitric acid. The ICP measurement of α-MEM were conducted once on each sample and once on blank sample.

Ion concentrations in collected TRIS and α-MEM preincubation solutions were measured as described in ICP analysis section. Scaffolds were removed from immersion solution, rinsed with ethanol and dried for 24 h before their mass was weighted. The volume of TRIS and α-MEM used for preincubation was calculated to maintain a mass/V ratio constant at 10 mg/ml.

2.5. Cell analysis with MC3T3-E1 and hADSCs

2.5.1. MC3T3-E1 and hADSCs expansion

Murine calvarial pre-osteoblastic MC3T3-E1 cells subclone four (ATCC, Manassas, VA, USA) were cultured in α-Minimum Essential Media (Gibco, Life Technologies, Carlsbad, CA, USA) containing glutamine supplemented with 10% Fetal Bovine Serum (FBS, Biosera, Marikina, Philippines) and 1% penicillin/streptomycin (Gibco, Life Technologies, Carlsbad, CA, USA). These, cells were used for initial evaluation and to develop a methodology.

Human ADSCs were isolated from subcutaneous abdominal tissue sample obtained from a female donor (age 49 years, BMI 21.4) at the Tampere University Hospital Department of Plastic Surgery with the donor's written informed consent and processed under ethical approval of the Ethics Committee of the Expert Responsibility area of Tampere University Hospital (R15161). The cells were isolated as described previously [35]. These cells, show greater translational potential which make them more clinically relevant compared to animal derived cells.

The mesenchymal origin of ADSCs was confirmed by surface marker expression analysis with flow cytometry [36] and ability of adipogenic and osteogenic differentiation [37] by Oil Red O and Alizarin Red staining, respectively. The cells were characterized as MSCs due to positive expression of CD73 (97%), CD90 (99%), and CD105 (99%), and low or negative expression of CD14 (1%), CD19 (0.6%), CD45 (2.6%), CD34 (8%) and HLA-DR (0.9%) [38,39] as well as accumulation of lipid droplets by Oil Red O and mineralized matrix deposition by Alizarin Red staining.

Human adipose-derived stem cells (hADSCs) were cultured in α-Minimum Essential Media (α-MEM) (Gibco, Life Technologies, Carlsbad, CA, USA) without nucleosides supplemented with 5% human serum (Serana Europe, Germany GmbH) and 1% penicillin/streptomycin (Gibco, Life Technologies, Carlsbad, CA, USA).

Both types of cells were cultured at 37 °C in a humidified atmosphere of 5% CO_2 balanced 95% air in incubator (Thermo Scientific forma stericycle i160 CO_2) until they reached over 80% confluence.

2.5.2. Preincubation of scaffolds before cell culturing

For this part of experiment scaffolds with average diameter of with height h= 4.2 ± 0.4 mm and diameter d= 4.4 ± 0.3 mm were used.

For cell tests with MC3T3-E1 cells, bulk B12.5 and B12.5-Mg-Sr scaffolds, were preincubated for either 1 or 6 days in TRIS always followed by 24 h in αMEM in incubator at 37 °C.

For cell test with hADSCs, bulk, burn-off and 3D printed scaffolds made from B12.5-Mg-Sr glass composition were preincubated for 2 days in TRIS and followed by 24 h in αMEM in incubator at 37 °C. For this test, only B12.5-Mg-Sr glass was studied. Each condition (bulk, burn-off, 3D printed) was studied in triplicate. Then, scaffolds were preincubated for 2 days in TRIS, followed by 24 h in αMEM in incubator at 37 °C. The volume of TRIS and α-MEM used for preincubation was calculated to maintain a mass/V ratio constant at 10 mg/ml. All scaffolds were sterilized for 3 h at 200 °C before preincubation.

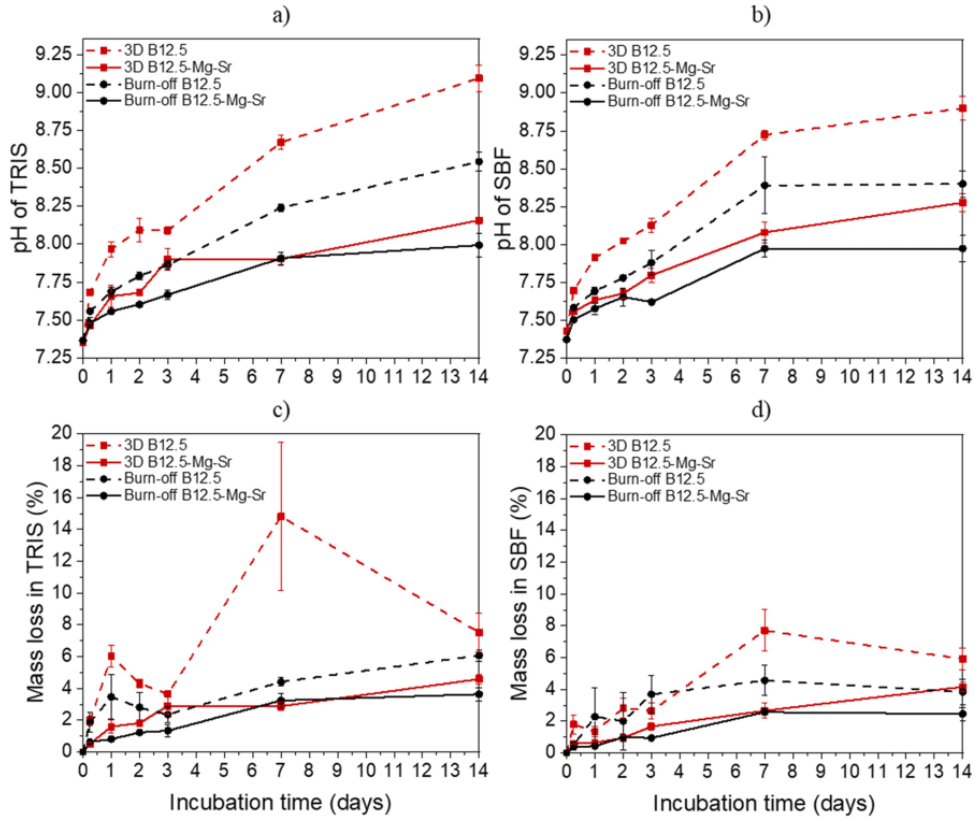

Fig. 4. a-b) pH of TRIS and SBF after static in vitro dissolution of scaffolds up to 14 days, c-d) mass loss of scaffolds after static in vitro dissolution in TRIS and SBF for up to 14 days.

2.5.3. Live/dead assay

Live/dead assay was used to detect cell viability in the proximity of the scaffolds and their dissolution by-products. Firstly, preincubated scaffolds were placed into 48 well plates (Thermo Scientific). For experiment with MC3T3-E1, 20.000 cells, passage 26–27 were seeded in 550 µl of α-MEM culture medium (containing glutamine, 10% FBS, 1% P/S) and cultured in contact with scaffolds for 24 h.

For cell experiments with hADSCs, 25.000 cells, passage 4 were seeded in 1 ml of α-MEM culture medium (no glutamine, 5% human serum, 1% P/S) and cultured in contact with scaffolds for 1, 3 and 7 days.

For both live/dead experiments, the positive control used was the Tissue Culture Polystyrene (TCPS) 48-wellplate seeded with cells, without scaffold.

At each timepoint, the cell culture media was collected and diluted 10 times in ultrapure water for ICP analysis. ICP measurements were conducted on three parallel samples and one blank sample and expressed as mean ± standard deviation (SD).

Next, wells with scaffolds were rinsed using Dulbecco′s Phosphate Buffered Saline, DPBS (Gibco, Life Technologies, Carlsbad, CA, USA) heated to 37 °C. The staining solution was prepared according to the Live & Dead Kit (Live/Dead Cell Double Staining Kit, SIGMA-ALDRICH, 04511), added to the wells and incubated for 30 mins at room temperature. Viable and necrotic MC3T3-E1 and ASCs cells were stained with 1% (v/v) of Calcein AM and 0,5% (v/v) Ethidium homodimer-1 solution. Finally, wells with scaffolds were rinsed with DPBS and cells were observed under the fluorescence microscope Olympus IX51 (Olympus Corporation, Japan).

3. Results and discussion

3.1. Characterization of the materials

3.1.1. Porosity

3D scaffolds with large pores (50–500 µm) and porosity between 50% and 90% are necessary for scaffold to be osteoconductive and allow tissue infiltration and regeneration crucial for proper bone tissue engineering [5,7]. Also, it is crucial that the scaffolds remain amorphous post-sintering. Table 3 present the overall porosity of the produced scaffolds (Eq.1) while Figure S2, presents the XRD diffraction pattern of the scaffold post sintering. From XRD analysis it is clear that no noticeable diffraction peaks can be noticed, indicating that the scaffolds remain amorphous. Regardless of the technique used, the porosities of B12.5 scaffolds were higher than that of B12.5-Mg-Sr scaffolds. This could be explained by enhanced sinterability of B12.5-Mg-Sr BAGs caused by addition of Mg and Sr [14,16]. Moreover, the porogen burn-off method can produce scaffolds with higher porosity compared to those produced by the 3D printing method, depending on design. While the ratio between glass particles and porogen was tailored to obtain similar porosity between the two techniques, one might expect that the size distribution and interconnection between pores will be lower in the case of the burn-off scaffolds when compared to scaffolds obtained by robocasting [29]. Most importantly, the scaffolds had porosity over 50% which is in line with the recommendation for tissue and cell migration

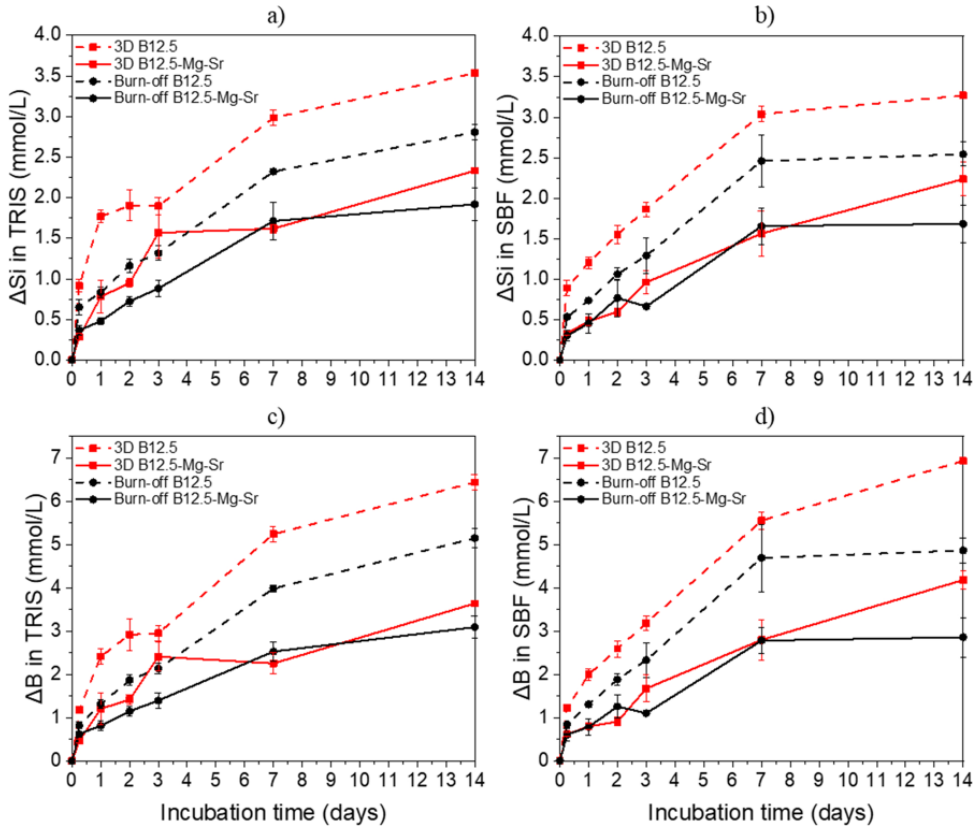

Fig. 5. Concentrations of a-b) Si and c-d) B after static in vitro dissolution in TRIS and SBF for up to 14 days. ΔElement = [Element] in TRIS/SBF in the presence of the sample – [Element] in TRIS/SBF initial solution.

inside the construct [4].

The sizes of pores in the 3D printing scaffolds are reported in the Table 4 and are all above the 100 μm required for the migration of MC3T3-E1 and mesenchymal stem cells, which have sizes between 20 and 50 μm and 13–30 μm, respectively. [40,41]. The pore sizes of scaffolds produced by porogen burn-off are quite inhomogeneous, ranging from micropores to pores of few millimeters.

Overall, scaffolds made from B12.5 and B12.5-Mg-Sr glass compositions meet the porosity and pore size required in bone tissue engineering. 3D printed scaffolds offer better pore size homogeneity when compared to those obtained by porogen burn-off. Moreover, interconnective porosity, as found in the 3D printed scaffolds, is known to permit cell migration inside of the scaffolds, diffusion of nutrients and removal of waste from the scaffold [42].

3.1.2. Mechanical properties

The mechanical properties of the implant should mimic the mechanical properties of the natural tissue. The compressive strengths of B12.5 scaffolds produced by the burn-off method and 3D printing were 1.5 ± 0.2 and 2.5 ± 0.7 MPa, respectively, as seen in the Fig. 3. Significantly higher values were obtained with B12.5-Mg-Sr composition, 8.9 ± 2.4 and 6.1 ± 1.8 MPa for scaffolds produced by burn-off and 3D printing, respectively. Addition of Mg to the glass composition lowers the glass viscosity which, consequently, improves the sintering properties and improves scaffolds strength [43,44]. Addition of Sr widen the sintering temperature window, which allows sintering at higher temperature above Tg. Moreover, the strength is greatly affected by the porosity. Thus, the increase in strength can also be linked to the lower porosities of B12.5-Mg-Sr scaffolds, as seen in Table 3 [9]. Summarizing, the strengths of sintered glass scaffolds were mostly within the 2–12 MPa strength of trabecular bone [45]. It has been reported that hip stems are subjected to 3–11 MPa loading and tibial bones to approximately 4 MPa stresses [46,47].

3.1.3. Static in vitro dissolution in TRIS and SBF

To study the effect of static in vitro dissolution and bioactivity, scaffolds were incubated in TRIS and SBF solution for up to 14 days. In vitro dissolution tests performed in TRIS aimed to assess the ions released from the glass during dissolution. In SBF, the ability of the released ions to saturate the solution, thus leading to the precipitation of HA, is being studied. Change in pH, mass loss and ion concentrations were investigated.

Fig. 2 presents the pH of TRIS and SBF solutions as a function of the incubation time for both glass compositions, manufactured into 3D printed and burn-off scaffolds. For all scaffold types and compositions, there is a rise in pH with increasing immersion time followed by stabilization around the 7th day (Fig. 4a-b). The initial increase in pH is related to the ion release of silicate and borosilicate glasses, as already shown in previous studies [14,15]. The stabilization in pH can be attributed to the solution becoming saturated with ions and subsequent formation of the HA layer [48]. The pH profile is similar in both TRIS and SBF. Immersion of B12.5 glass composition results in higher pH

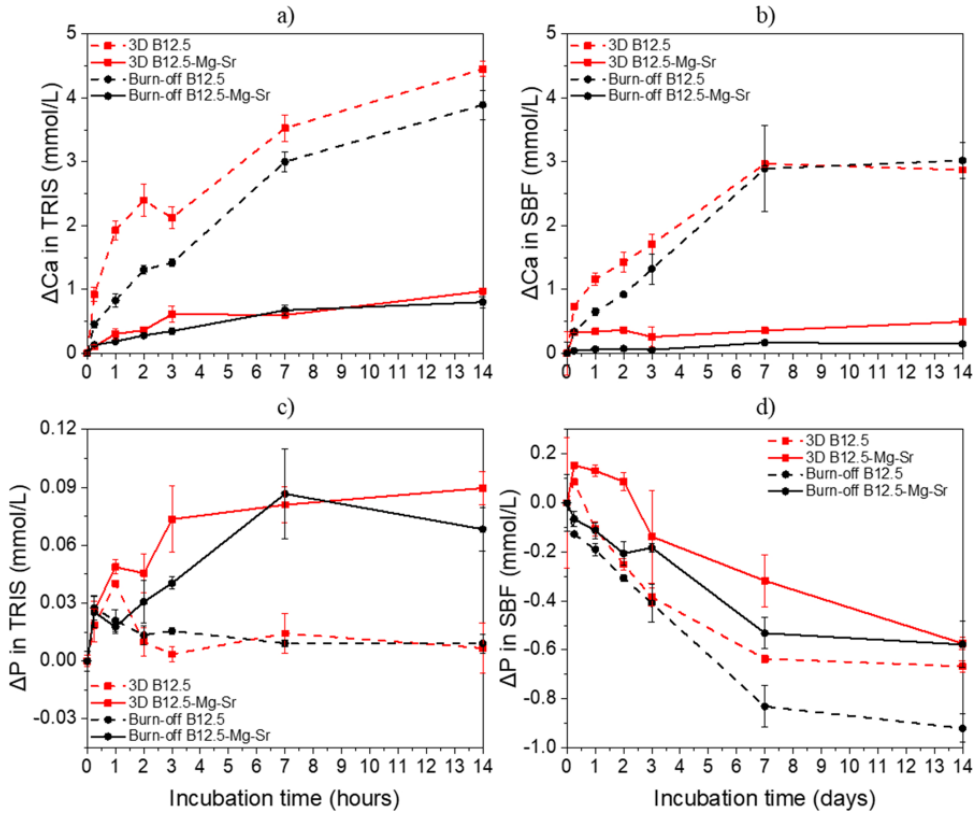

Fig. 6. Concentrations of a-b) Ca and c-d) P after static in vitro dissolution in TRIS and SBF for up to 14 days. ΔElement = [Element] in TRIS/SBF in the presence of the sample – [Element] in TRIS/SBF initial solution.

compared to B12.5-Mg-Sr in both solutions. The rise of pH is also more significant in 3D printed scaffolds than in burn-off scaffolds. The pH of the solution in all groups of scaffolds can increase to, or even exceed, pH= 8 after 7 days. This indicates that the scaffold dissolution is rapid and, if not carefully controlled, may be toxic for cells [49]. These results are also indicative of a faster dissolution of B12.5 scaffolds, resulting in rise of ions and consequently higher pH levels. B12.5-Mg-Sr scaffolds dissolve slower due to the stabilizing effect of Mg and Sr on glass network [15,16]. Substitution of SrO and MgO for CaO results in increase in BO_3 at the expense of BO_4 units [14]. Consequently, changing the ratio between bridging and non-bridging oxygen leading to stabilization of the borate network.

When compared, despite their overall porosity being similar (Tables 2), 3D printed scaffolds produce higher pH levels than burn-off scaffolds. It can be explained by a more interconnected porosity for the 3D printed scaffolds resulting in higher surface area in contact with the immersion solution.

Fig. 4c-d presents the mass loss (Eq.2) as a function of the incubation time for both glass compositions manufactured into 3D printed and burn-off scaffolds. The mass loss is observed for all scaffolds indicating that degradation occurred. Mass loss is significantly higher for B12.5 than for B12.5-Mg-Sr scaffolds. This agrees with in vitro dissolution test performed by Tainio et al., showing that substitution of CaO with SrO and/or MgO have stabilizing effect on borate network and help to decrease the dissolution rate [14]. Results also implies that the impact of composition is dominant over the scaffold preparation techniques. Moreover, 3D printed scaffolds tend to have larger mass loss compared to burn-off scaffolds. This is also in accordance with pH data and is most probably related to the higher surface area of the 3D printed scaffolds. The ion concentrations in TRIS and SBF after static in vitro dissolution were analyzed using ICP-OES. Si and B are backbone of the glass network and thus their release profiles inform about the glass dissolution trend. The release profiles of B and Si are quite identical in both SBF and TRIS solutions (Fig. 5).

For all scaffold types and compositions, there is a linear increase in Si^{4+} and B^{3+} ion release until 7th day after which it stabilizes significantly. Highest Si^{4+} and B^{3+} ion release is observed from B12.5 glass scaffolds. Moreover, the ion release is higher from 3D printed scaffolds compared to the burn-off scaffolds. These observations are in agreement with pH results and further confirm faster dissolution of B12.5 glass composition as well as faster dissolution of the 3D printed scaffolds.

The Ca and P release profiles (Fig. 6) are important as they give information about precipitation of HA-like layer, which is often seen as a first sign of bioactivity [50]. The release profile of Ca in TRIS and SBF is characterized by linear increase until 7th day, after which the release slows down (Fig. 6a-b).

Ca release in both TRIS and SBF is higher from B12.5 compared to B12.5-Mg-Sr scaffolds. It could be caused by significantly more Ca in B12.5 glass network. Moreover, the Ca release is highest for 3D printed scaffolds compared to the burn-off scaffolds. Although, this difference was not always significant.

In TRIS, the P^{3-} ion concentrations remains stable for the B12.5 scaffolds (Fig. 6c). However, it rises with increasing immersion time for the B12.5-Mg-Sr scaffolds. These results can be explained by

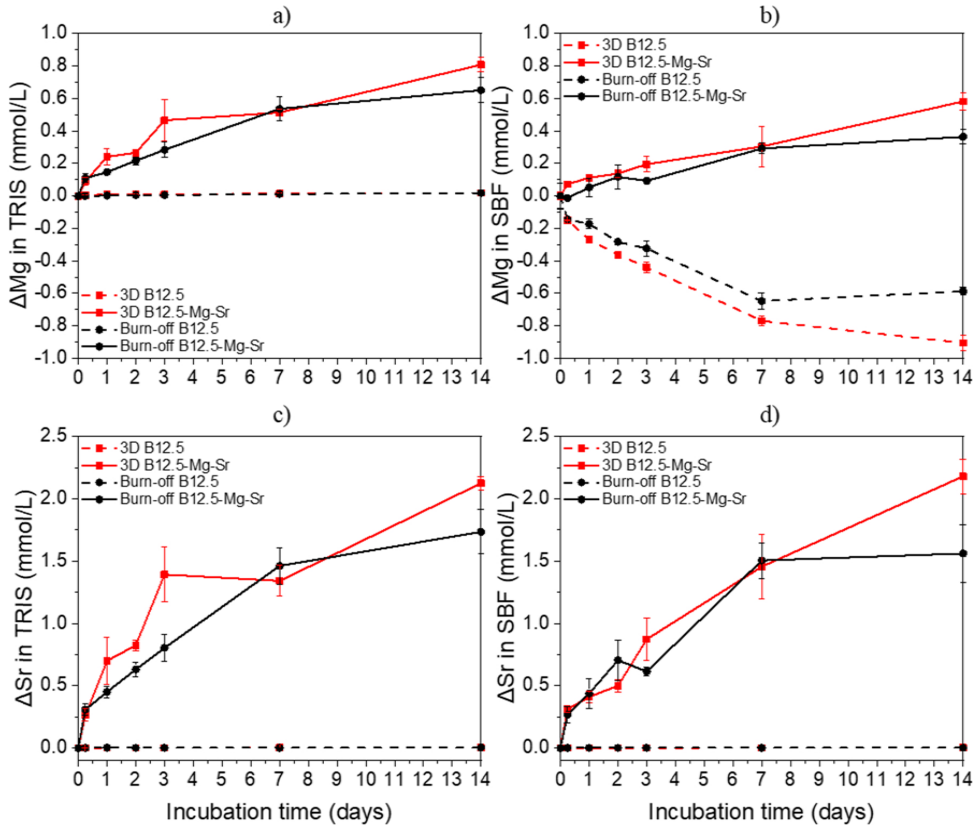

Fig. 7. Concentrations of a-b) Mg and c-d) Sr after static in vitro dissolution in TRIS and SBF for up to 14 days. ΔElement = [Element] in TRIS/SBF in the presence of the sample – [Element] in TRIS/SBF initial solution.

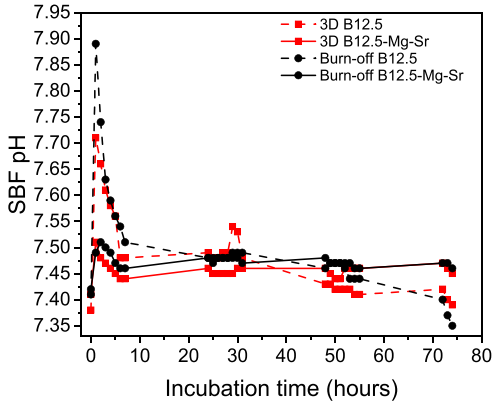

Fig. 8. pH of SBF after dynamic in vitro dissolution for up to 74 h.

simultaneous release and precipitation of phosphorus. Differences in P^{3-} ion release between 3D printed scaffolds and burn-off scaffolds in TRIS are not significant.

In SBF, simultaneous dissolution and precipitation of P, results in overall P consumption (Fig. 6d). This consumption reaches a plateau after day 7th. Moreover, P release for B12.5 groups were significantly lower. This can be linked to a slower HA precipitation when Ca is replaced with Mg and/or Sr containing silicate bioactive glasses as discussed in [15,16]. Finally, the P consumption, from the SBF, appears to be faster for the scaffolds produced by burn-off scaffolds. This consumption of P indicates precipitation of Ca-P layer, which is an indication of the scaffolds' bioactivity [50].

B12.5 glass composition does not contain MgO so as expected Mg was only released from B12.5-Mg-Sr glass composition in TRIS (Fig. 7a). In SBF, Mg concentration decreases significantly for B12.5 glass composition and raises slowly for B12.5-Mg-Sr composition over the course of the immersion in SBF (Fig. 7b). Burn-off scaffolds releases slightly less Mg^{2+} ions than 3D printed scaffolds in TRIS. However, in SBF the Mg concentration is smaller for 3D printed scaffolds. The slow release, and the decrease in some cases, of Mg concentration could be indicative that part of the Mg is consumed and incorporated into the reactive layer [16].

Finally, as expected from the glass composition, the Sr concentration remains null in the solution containing the B12.5 glass, whereas it rises with increasing immersion time for the scaffolds made from the B12.5-Mg-Sr glass composition (Fig. 7c-d). Burn-off scaffolds releases slightly more ions compared to 3D printed scaffolds. From past research, it is highly probable that part of the strontium is also incorporated in the reactive layer [15].

Summarizing, ICP results are in agreement with pH results and further confirm faster dissolution of B12.5 glass composition as well as faster dissolution of 3D printed scaffolds. This results are in accordance with previous reports, where slower dissolution rate and HA

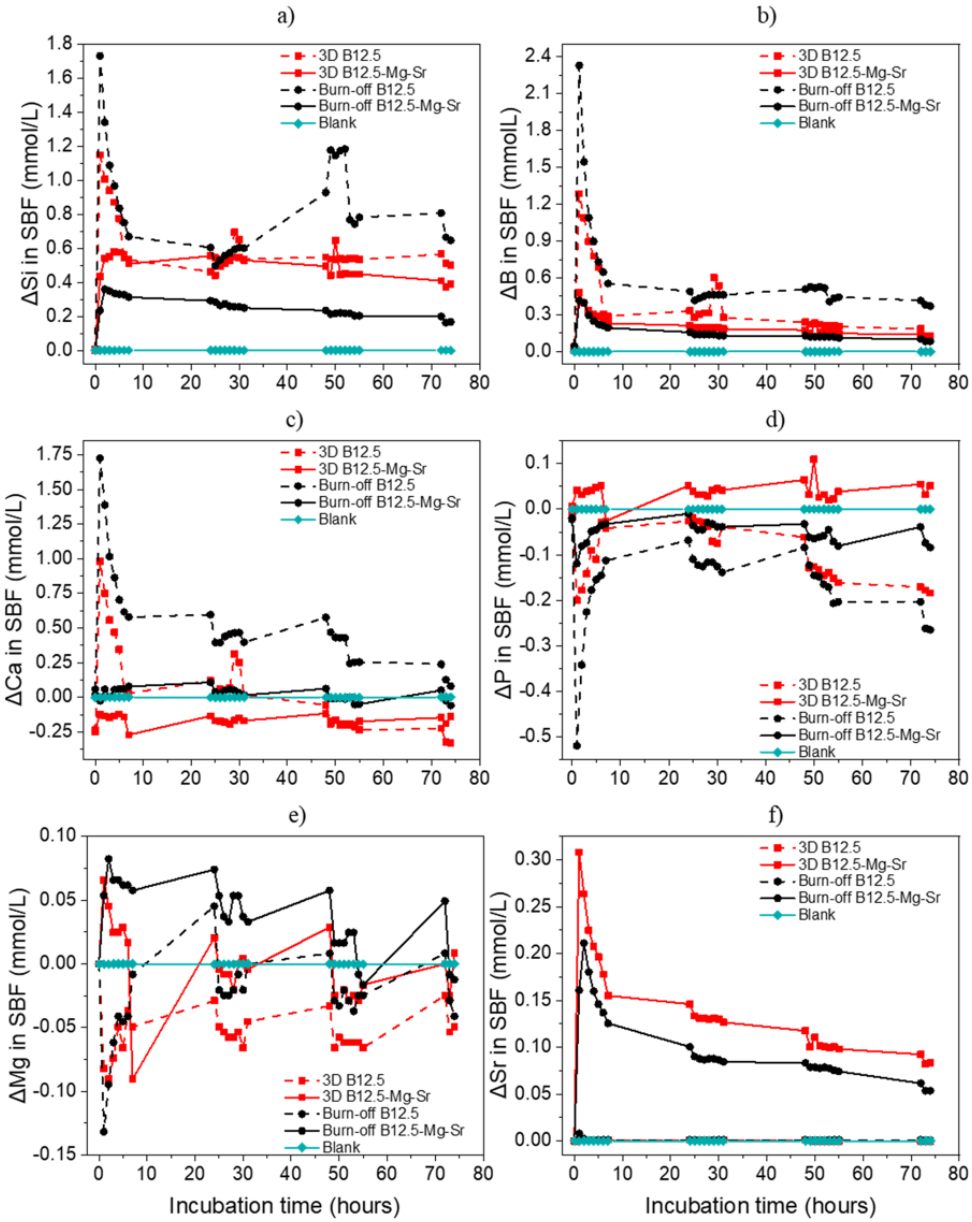

Fig. 9. Concentrations of a-f) Si, B, Ca, P, Mg and Sr in SBF after dynamic in vitro dissolution test with scaffolds for up to 74 h. ΔElement = [Element] in SBF in the presence of the sample – [Element] in SBF initial solution.

precipitation was observed with Mg and Sr containing silicate bioactive glasses [15,16].

Moreover, bioactivity of all scaffolds is indicated by HA precipitation, which is faster for B12.5 than for B12.5-Mg-Sr scaffolds. Finally, based on release profiles it seems that ions releases stabilize after 7th day. These results also agree with previous studies done with B12.5 and B12.5-Mg-Sr glass compositions [14].

3.1.4. Dynamic in vitro dissolution in in SBF

To investigate the effect of dynamic in vitro dissolution on scaffolds degradation and bioactivity, scaffolds were incubated in SBF solution for up to 72 h. Change in pH and ion concentrations were investigated. Fig. 8 presents the pH change in SBF as a function of the incubation time for both glass compositions, B12.5 and B12.5-Mg-Sr, manufactured into 3D printed and burn-off scaffolds. For all scaffolds, there is a drastic increase in pH after the first hour for all scaffolds and then the pH goes rapidly down and stabilizes after 7 h. The increase in pH is more pronounced for the B12.5 glass composition. No significant difference is seen between the B12.5-Mg-Sr scaffolds produced by either of the utilized techniques. The pH values in the dynamic conditions remain stable

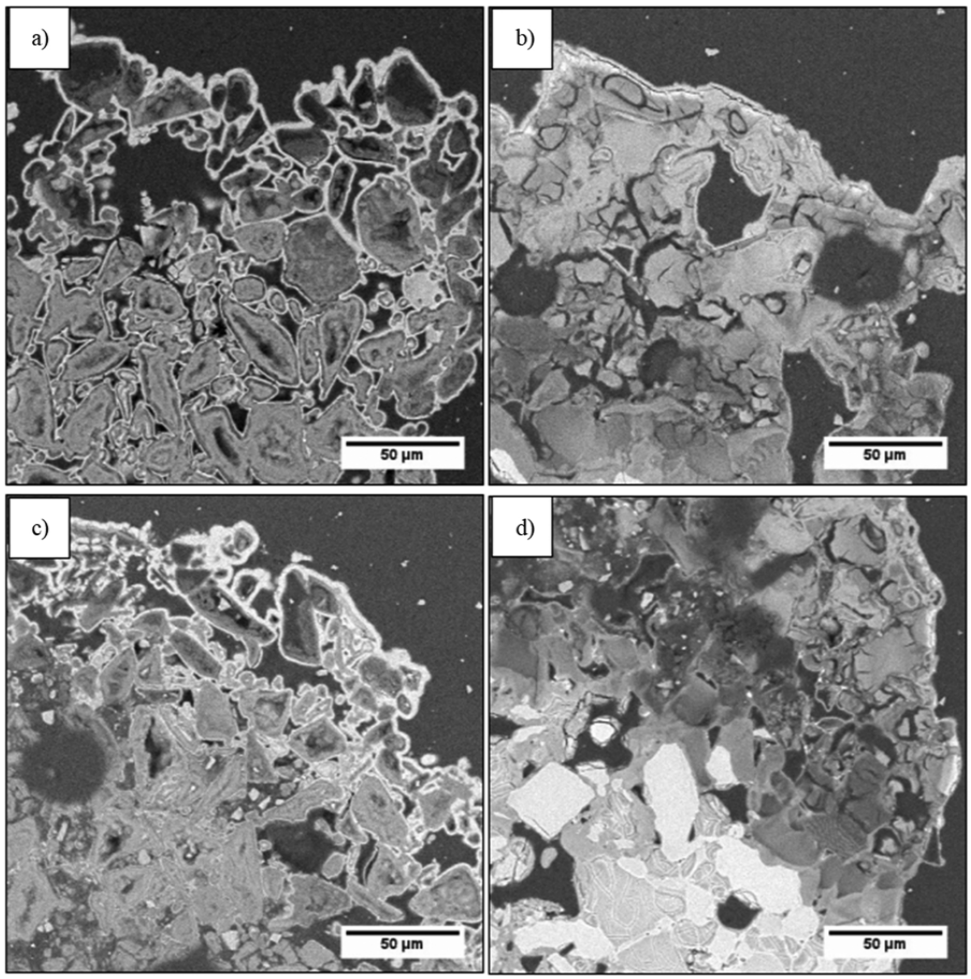

Fig. 10. SEM images of scaffolds after 336 h of immersion in SBF at 250x magnifications. SEM images of (a,c) B12.5 and (b,d) B12.5-Mg-Sr scaffolds produced via (a, b) burn-off and (c,d) 3D printing methods.

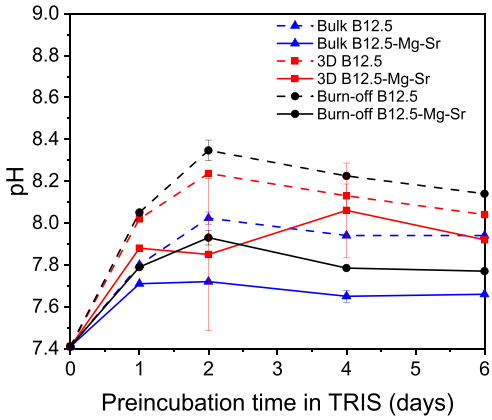

Fig. 11. pH of TRIS after preincubation with scaffolds for up to 6 days.

in the range of 7.4–7.5 for all the scaffolds. Only a burst of ions is seen within the first 6 h. These pH values are appropriate for the culture of cells.

The ion concentrations in SBF after dynamic in vitro dissolution were analyzed using ICP-OES (Fig. 9). The release profiles of Si and B scaffolds are characterized by initial burst of ions reaching its peak after 1 h. Ion concentrations decrease and stabilize after 7 h (Fig. 9a-b). This dissolution behavior is characteristic of dynamic condition and has been reported before [51]. The burst ion release is more significant for B12.5 scaffolds compared to B12.5-Mg-Sr scaffolds. Highest Si^{4+} ion release from B12.5 is observed from burn-off scaffolds, and with B12.5-Mg-Sr scaffolds from 3D printed scaffolds, respectively.

With B12.5-Mg-Sr composition, no significant difference between dissolution of the burn-off and 3D printed scaffolds is observed. The increased pH and Si release for the burn-off scaffold is unexpected based on the higher surface area of the 3D printed scaffolds. However, such discrepancy can be due to the ability of the liquid to flow through the various samples [29]. Indeed, the smaller pore size and lower interconnectivity between pores in the burn-off scaffolds could also lead to longer liquid reminiscence time in contact with the sample, thus leading

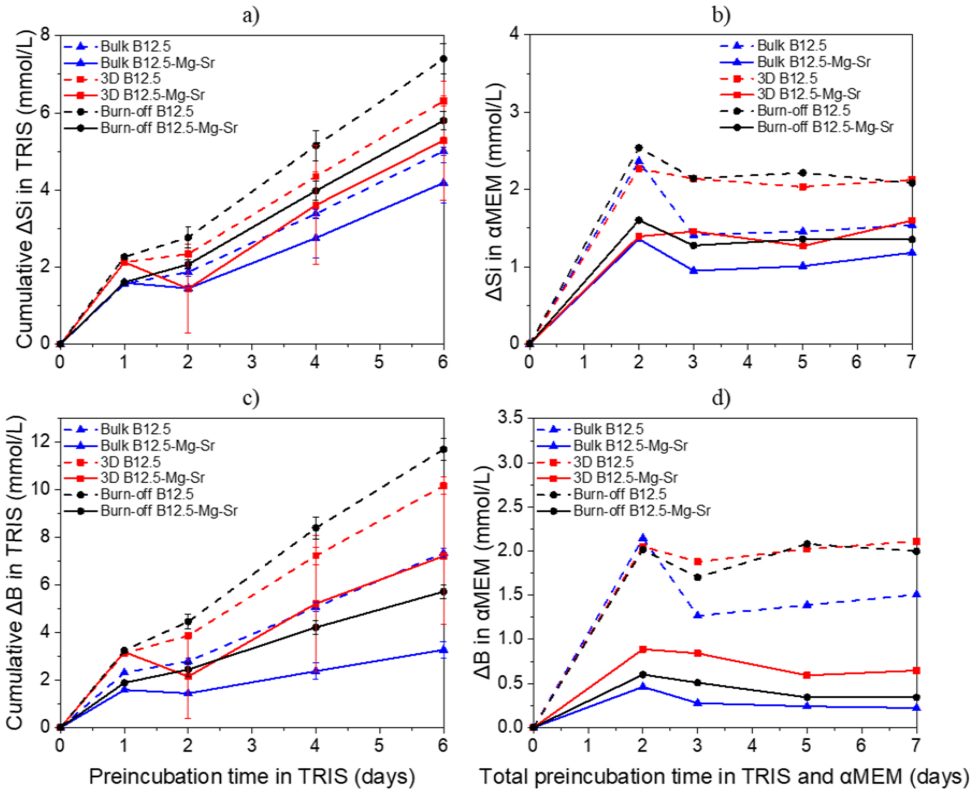

Fig. 12. Concentrations of a-b) Si and c-d) B in TRIS and αMEM culture medium after preincubation with scaffolds for up to 7 days. ΔElement = [Element] in TRIS/ αMEM in the presence of the sample – [Element] in TRIS/ αMEM initial solution.

to more extended degradation. This is of particular interest and to keep in mind in future investigation of scaffolds in a dynamic context.

Ca^{2+} ion concentration levels are highest for B12.5, and P^{3-} ion concentrations are highest for B12.5-Mg-Sr scaffolds (Fig. 9c-d). Ion release profiles of Ca^{2+} from B12.5 scaffolds are characterized by initial burst of ions during the first hour of immersion, followed by strong decrease and stabilization after 7 h. For B12.5-Mg-Sr glass, Ca^{2+} ion release profiles are mostly stable from the beginning of the immersion. Ion release profiles of P^{3-} is characterized by initial consumption of ions during first hours of immersion, followed by increase and stabilization after 7 h. Burn-off scaffolds produce higher Ca^{2+} ion concentration levels than 3D printed scaffolds. However, 3D printed scaffolds produce higher P^{3-} ion concertation levels than burn-off scaffolds.

As expected, Mg^{2+} and Sr^{2+} ion release is highest for B12.5-Mg-Sr scaffolds, since B12.5 glass composition does not contain these elements. Mg release (Fig. 9e) was not found to be stable, which could be explain by simultaneous release and precipitation of Ca-P reactive layer that can also include Mg [16]. Sr release profile is characterized by initial burst of ions, followed by strong decrease after 1 h and stabilization after 7 h (Fig. 9f). most likely due to the incorporation of Sr into the reactive layer. Moreover, 3D printed scaffolds release more Sr^{2+} ions that burn-off scaffolds.

Generally, ion concentrations are notably lower during dynamic in vitro dissolution compared (Fig. 9) to static in vitro dissolution (Figs. 5–7). This is in accordance with previous research reporting that dynamic conditions can help to avoid a rapid and drastic fluctuation of pH [51,49,52]. The initial burst release of ions is significantly higher for B12.5 compared to B12.5-Mg-Sr glass composition. After burst release, ion releases stabilize and are lower than in static condition. Moreover, dynamic conditions resemble human body environment more accurately than the static ones, as in physiological conditions fluids are constantly washed away [49]. In this respect, dynamic conditions could be more optimal for in vitro cell growth. Finally, consumption of Ca and P from immersion solution indicate, as seen in Fig. 6, that formation of most likely HA layer takes place.

3.1.5. SEM

SEM imaging was used to analyze scaffolds after 336 h of static immersion in SBF. The sintered scaffolds had high levels of internal microporosity (Fig. 10a, c) showing loose particles suggesting insufficient sintering of B12.5. Moreover, internal microporosity of B12.5-Mg5-Sr10 scaffolds seems to be more compact indicating Mg and Sr ability to promote sintering.

In all SEM images a bright layer appears at the surface of the grains exposed to the solution. This bright layer was found to be rich in calcium and phosphorus and was earlier found to be assigned to the precipitation of a reactive layer [9]. Elemental compositions of unreacted glass and formed surface layers for scaffolds produced via porogen burn-off and robocasting were analyzed and are presented in Table S3.

Furthermore, the FTIR spectra of the glass scaffolds pre and post-immersion were recorded and are reported in Figure S4. FTIR spectra confirm the precipitation of a reactive layer. The change in the molecular vibration is indicative of the typical dissolution of the glass network and precipitation of reactive layer within the HA domain.

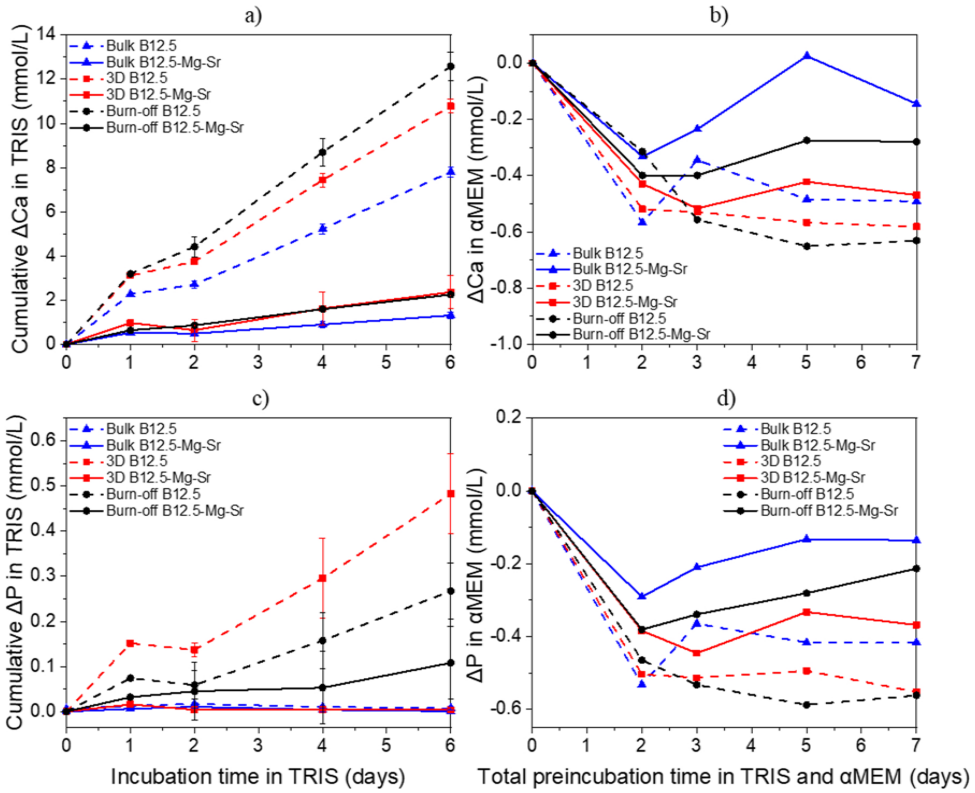

Fig. 13. Concentrations of a-b) Ca and c-d) P in TRIS and αMEM culture medium after preincubation with scaffolds for up to 7 days. ΔElement = [Element] in TRIS/ αMEM in the presence of the sample – [Element] in TRIS/ αMEM initial solution.

3.2. Cell analysis

3.2.1. Effect of preincubation on ion release

To investigate the effect of preincubation on ions release profiles, scaffolds were preincubated for up to 6 days in TRIS, following additional 24 h in αMEM. The pH levels of TRIS during preincubation are presented in Fig. 11.

There is an increase in pH for all scaffolds until 2 days except for bulk and 3D printed B12.5-Mg-Sr, where the increase stopped at 1 day. This indicates that the scaffold dissolution in TRIS is rapid. Then, the pH slightly decreased and stabilized. The pH peak of TRIS solution with the scaffolds is reached at pH≥ 8 for B12.5 and pH≥ 7.7 for B12.5-Mg-Sr scaffolds. Slower increase of pH with B12.5-Mg-Sr glass composition can be explained by stabilizing effect of Mg and Sr consequently, resulting in a slower dissolution rate of B12.5-Mg-Sr scaffolds and thus smaller pH levels.

For B12.5 glass composition, the pH rise was most pronounced for the burn-off scaffolds. For B12.5-Mg-Sr composition the pH rise was most pronounced for 3D printed scaffold. For both glass compositions, bulk scaffolds produced lower pH rise compared to other scaffold types. The difference between bulk, burn-off and 3D printed scaffolds could be explained by their different porosities (Table 3&4). Dissolution of scaffolds with higher porosity and consequently surface area, result in higher ion and pH levels and thus, dissolution of more porous and more reactive B12.5 scaffolds can result in higher pH levels compared to less porous/reactive B12.5-Mg-Sr scaffolds. Furthermore, 3D printed and burn-off scaffolds with higher porosity compared to bulk scaffolds also produced higher pH levels during dissolution. The ion concentrations in TRIS and αMEM after preincubation test were analyzed using ICP-OES (Fig. 12). The ICP results for Si and B were in accordance with measured pH levels; ion concentrations expressed higher for B12.5 than for B12.5-Mg-Sr scaffolds in TRIS and αMEM.

The release profiles of Si and B in TRIS were increasing linearly (Fig. 12a, c). Highest Si^{4+} and B^{3+} ion concentrations in TRIS were observed for B12.5 burn-off scaffolds, and lowest for B12.5-Mg-Sr bulk scaffolds.

In αMEM, the highest ion concentrations were observed for burn-off and 3D printed B12.5 scaffolds, and lowest for B12.5-Mg-Sr bulk scaffolds (Fig. 12b, d). Most importantly, after 2nd day of total preincubation time, Si^{4+} and B^{3+} ion concentrations in αMEM decrease and stabilize at day 3.

Ca^{2+} ion concentrations were highest for B12.5 composition when compared with B12.5-Mg-Sr scaffolds in TRIS, but lowest in αMEM (Fig. 13a-b).

P^{3-} ion concentrations were highest for B12.5-Mg-Sr scaffolds compared with B12.5 scaffolds in both TRIS and αMEM (Fig. 13c-d). The release profiles of Ca and P in TRIS increased linearly (Fig. 13a-c). Most importantly, after 48 h of total preincubation time, Ca^{2+} and P^{3-} ion concentrations in αMEM decrease and stabilize at day 3 (Fig. 13b-d). Moreover, highest Ca^{2+} and P^{3-} ion concentrations in TRIS and αMEM are observed for burn-off and bulk scaffolds, respectively.

Consumption of Ca and P in αMEM, indicate that precipitation of Ca-P rich layer precipitate already after 2 days of total preincubation time. The precipitation was faster for B12.5 scaffolds due to their faster dissolution [14] and consequently faster oversaturation of αMEM with ions.

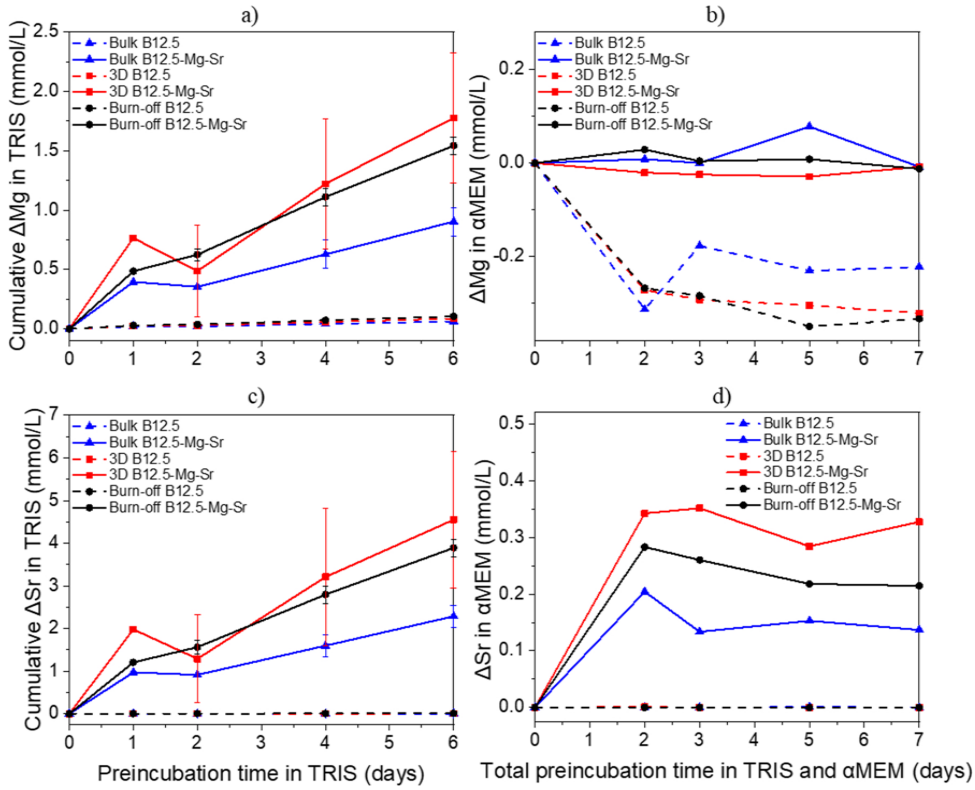

Fig. 14. Concentrations of a-b) Mg and c-d) Sr in TRIS and αMEM culture medium after preincubation with scaffolds for up to 7 days. ΔElement = [Element] in TRIS/ αMEM in the presence of the sample – [Element] in TRIS/ αMEM initial solution.

Mg^{2+} and Sr^{2+} ion concentrations, as expected from glass compositions, were highest for B12.5-Mg-Sr composition in both preincubation solutions. B12.5 scaffolds do not produce any Mg^{2+} and Sr^{2+} ion release (Fig. 14). Only in αMEM consumption of Mg from B12.5 scaffolds is observed (Fig. 14b). This consumption could be related to precipitation of reactive layer with incorporated Mg.

Mg^{2+} and Sr^{2+} ion release from B12.5-Mg-Sr scaffolds in TRIS were increasing linearly (Fig. 14a, c). In αMEM, Mg and Sr^{2+} ion release stabilized after 2 days of total preincubation (Fig. 14b, d). Highest Mg^{2+} and Sr^{2+} ion release in TRIS was observed for 3D printed scaffolds. In αMEM, highest Mg^{2+} and Sr^{2+} ion release was observed from bulk and 3D printed scaffolds, respectively.

In conclusion, ICP results tend to indicate that after 2 days of preincubation (1 day in TRIS and 1 day in αMEM) still exhibit significant ion release. At 3 days of total preincubation (2 days in TRIS and 1 day in αMEM) the ion release exhibits a plateau most likely related to the precipitation of hydroxyapatite. Therefore, it was concluded that 3 days of total preincubation is optimal to control the excess ion release. This is in accordance with literature review by Ciraldo et al., in which it was suggested that highly porous BAG scaffolds, with more than 21 wt% of Na_2O should be preincubated for more than 72 h before static cell culture [49].

3.2.2. Effect of glass composition on cell survival and ion release

MC3T3-E1 cells were used for initial evaluation of the impact of the glass composition on cell survival. For this experiment, bulk scaffolds were preincubated for 2 or 7 days in TRIS always followed by 24 h in αMEM.

Fig. 15 shows MC3T3-E1 cell viability images after 24 h of culture with B12.5 and B12.5-Mg-Sr bulk scaffolds. These scaffolds were preincubated two or seven days before culture. There were significantly more live cells in the bottom of wells with B12.5-Mg-Sr scaffolds compared to B12.5 after the pre-incubations (Fig. 15a-d). In fact, cell survival around B12.5-Mg-Sr glass scaffolds is comparable to cell survival in the control. Cell survival at the top of the scaffolds (Fig. 15A-D), was better with B12.5-Mg-Sr glass composition. Longer preincubation slightly improved cell survival with B12.5 glass composition. The effect of longer preincubation time on cell survival at the top of B12.5-Mg-Sr scaffolds did not seem significant.

Better cell survival with B12.5-Mg-Sr scaffolds could be due to stabilizing properties of Mg and Sr. It is expected that, less stabilized B12.5 glass dissolves faster, causing a rise in pH to levels that would be toxic for the cells. This ion release can be further decreased by longer preincubation of 7 days in TRIS.

Longer preincubation led to a better cell survival with B12.5 scaffolds but still not comparable to the control. Moreover, even after longer preincubation, B12.5-Mg-Sr glass still seemed less toxic for the cells than B12.5. The effect of preincubation time was not significant for B12.5-Mg-Sr glass composition, because shorter preincubation already prevented toxic ion burst released while maintaining an ion release of interest.

Cell survival at the top of the bulk scaffolds (Fig. 15A-D), is better with B12.5-Mg-Sr glass composition. Longer preincubation slightly improve cell survival with B12.5 glass composition. The effect of longer preincubation time on cell survival at the top of B12.5-Mg-Sr scaffolds is not significant.

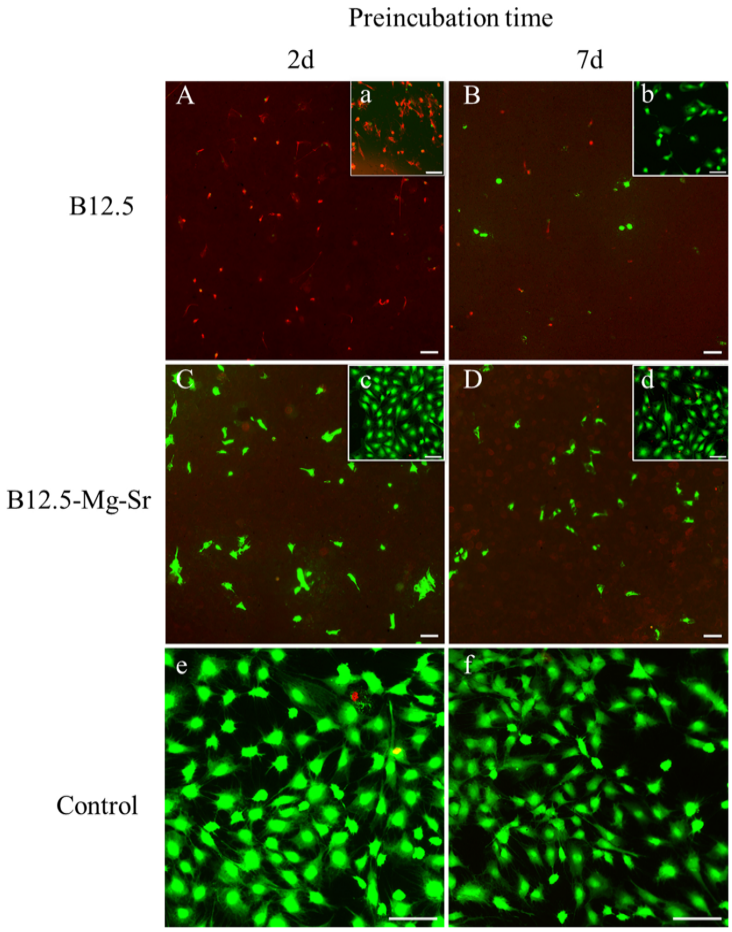

Fig. 15. Fluorescent images of MC3T3-E1 cells after 24 h of culture in αMEM culture medium. Images A-D show the top of the bulk scaffolds. Images a-f show the bottom of the wellplate. Viable (green) and necrotic (red) cells were stained with Calcein AM and Ethidium homodimer-1 respectively. Scale bar 100 μm.

The ion concentrations in αMEM after culture with cells were analyzed using ICP-OES (Fig. 16). Si^{4+} ion concentrations increased for both glass compositions and were higher than in the cell culture media (positive control; cells growing without scaffold presence). Longer preincubation time of 7 days resulted in smaller ion concentrations for both glass compositions.

However, this decrease is significant only for B12.5 scaffolds. In scaffolds preincubated for 2 days, B12.5-Mg-Sr glass composition produced slightly smaller Si^{4+} ion release. There is no difference between ion release from scaffolds preincubated for 7 days.

B^{3+} ion concentrations increased for both glass compositions and were significantly higher than in control cell culture media, which does not initially contain boron. Most importantly, even after both preincubation times, B12.5 scaffolds produce significantly larger B^{3+} ion release, whereas longer preincubation time of 7 days resulted in significant decrease in B^{3+} ion concentrations for B12.5 scaffolds. For B12.5-Mg-Sr scaffolds, no difference in ion release between different preincubation times were observed. It has been reported that B concentrations above 0.65 mmol were shown to decrease the growth and proliferation rate of bone marrow cells (BMSc) [53]. Similar results were reported by Brown et al. where B concentrations of 1.5 mmol in the culture medium inhibits cell proliferation [11]. In our study, the non-cumulative B concentration for B12.5 scaffolds were around 26 and 17 after 2 and 7 days of total preincubation time, respectively. The non-cumulative B concentration for B12.5-Mg-Sr bulk scaffolds were around 3.2 and 2.4 after 2 and 7 days of total preincubation time, respectively. This could explain why B12.5 scaffolds were more cytotoxic compared to B12.5-Mg-Sr scaffolds.

Ca^{2+} ion concentrations decreased with both glass composition scaffolds, and concentrations were smaller than in control cell culture media. Notably, for both preincubation times, B12.5 scaffolds produce significantly smaller Ca^{2+} ion concentrations. Longer preincubation time of 7 days results in larger ion concentrations for B12.5 scaffolds. Different preincubation times have no significant impact of Ca^{2+} ion release from B12.5-Mg-Sr scaffolds.

P^{3-} ion concentrations can be seen to decrease for B12.5-Mg-Sr and increase B12.5 scaffolds, respectively. Longer preincubation time of 7 days resulted in decrease of P^{3-} ion release from B12.5 scaffolds, while different preincubation times had no significant impact of P^{3-} ion release from B12.5-Mg-Sr scaffolds.

ICP results indicate that Ca consumption is faster with cell cultures in the presence of B12.5 scaffolds. Most probably, due to higher dissolution rate of B12.5, culture medium could be oversaturated with Ca faster, leading to faster precipitation of CaP compared to B12.5-Mg-Sr

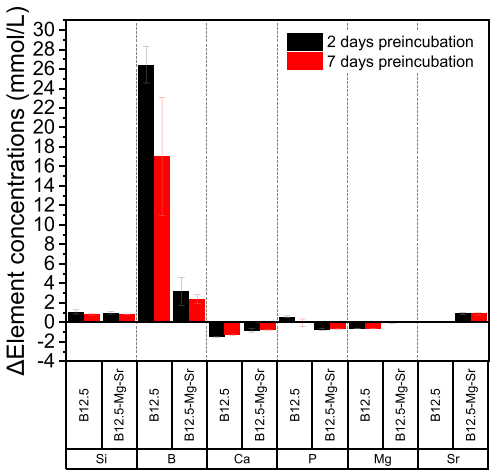

Fig. 16. Concentrations of Si, B, Ca, P, Mg and Sr in αMEM culture medium after culturing Bulk B12.5 and B12.5-Mg-Sr scaffolds for 24 h with the MC3T3-E1 cells as a function of time. ΔElement = [Element] in αMEM in the presence of the sample – [Element] in αMEM initial solution.

scaffolds. Moreover, content of Ca in B12.5 is significantly larger than in B12.5-Mg-Sr glass composition. However, P seems to be consumed slower with B12.5 than B12.5-Mg-Sr scaffolds. This could be due to P release from B12.5 being significantly larger than simultaneous P precipitation.

Since there is no Mg and Sr in B12.5 glass composition, their release is observed only for B12.5-Mg-Sr glass composition. With B12.5 scaffolds, Mg content decreases after 24 h of cell culture and Sr release stays at positive control level. This could be explained by precipitation of Mg from culture medium together with Ca-P layer. Longer preincubation time of B12.5-Mg-Sr and B12.5 scaffolds does not result in any significant change compared to shorter preincubation time.

In the study by Gentlemen et al. Sr concentrations between 5 and 23 ppm resulted in Saos-2 osteoblast cells activity and inhibited osteoclasts differentiation [54]. In our study, non-cumulative Sr release from 12.5-Mg-Sr scaffolds, after 2 and 7 days of total preincubation time, were significantly higher, around 78 ppm. Despite, that MC3T3-E1 cells shown better viability and survival with B12.5-Mg-Sr compared to B12.5 bulk scaffolds, which can indicate that levels of Sr around 78 ppm are not cytotoxic.

Overall, ion release from B12.5 and B12.5-Mg-Sr bulk scaffolds after 24 h cell culture with MC3T3-E1 corresponds with fluorescent microscopy images. Addition of Mg and Sr results in slower dissolution rate of B12.5-Mg-Sr glass as can be seen from B and Si release profiles. Precipitation of Ca and P into a probably HA-like layer indicates bioactivity of these glass compositions. Longer preincubation time does not affect ion release from B12.5-Mg-Sr scaffolds. However, it decreases Si^{4+}, B^{3+} and P^{3-} ion release from B12.5, which could explain why longer preincubation with B12.5 results in better cell survival. However, longer preincubation did not affect cell survival with B12.5-Mg-Sr scaffolds.

3.2.3. Effect of scaffolds manufacturing method on cell survival and ion release

Human ADSC were used to evaluate how different scaffolds manufacturing methods affected the cell survival. These cells, show greater translational potential which make them more clinically relevant compared to animal derived cells. With murine MC3T3-E1 cells, it was observed that all scaffolds made from B12.5-Mg-Sr glass composition seemed to provide better cell survival than B12.5 glass composition, hence only the former composition was utilized in the following experiments.

The Fig. 17 shows fluorescent microscope images of viable and necrotic cells after 1,3 and 7 days of culture with bulk, burn-off and 3D printed B12.5-Mg-Sr scaffolds. Moreover, based on preincubation results, preincubation of 2 days in TRIS and 24 h in αMEM was used. The cell density increased throughout the seven days of culturing, and there was no significant difference between the studied scaffold types (burn-off vs 3D printed). Scaffolds presence did not prevent the survival of the cells around it (Fig. 17a-l). On all the scaffolds tops, there is comparable number of alive cells (Fig. 17A-I). Only after 7 days of cell culture there was significantly more cells on the top of the bulk, than on other scaffolds. Moreover, cell migration inside the 3D printed scaffolds could also be observed. However, this was observed only beneath the top layer as imaging along the z-axis was limited.

Despite 3D printed scaffolds higher porosity, surface area and ion release concentrations, cell viability is comparable with positive control and other scaffold types. This indicates that B12.5-Mg-Sr glass composition is a promising candidate for 3D printing scaffolds with interconnected porosity. However, this result should be further confirmed by studying the proliferation of the cells more deeply.

Next, the ion concentrations in αMEM after cell culture were analyzed using ICP-OES (Fig. 18). Si^{4+} and B^{3+} ion release concentrations were increasing over course of cell culture (Fig. 18 a-b). Si^{4+} ion concentrations were not significantly different between scaffold types (Fig. 18a). 3D scaffolds produce higher B^{3+} ion concentration compared to bulk and burn-off scaffolds (Fig. 18b). These results indicate that 3D printed scaffolds dissolve faster, most probably due to their higher surface area connected with their high porosity.

It has been reported that B concentration of $\leq$ 0.65 mmol in the culture medium supports the proliferation and function of MLO-A5 cells (H. [53]. However, extensive B release, in vitro, has been shown to result in cells death [11]; H. [53]; Q. [12]. B concentrations above 0.65 mmol were shown to decrease the growth and proliferation rate of bone marrow cells (BMSc) (H. [53]. Similar results were reported by Brown et al. where B concentrations of 1.5 mmol in the culture medium inhibits cell proliferation [11]. In our study, the non-cumulative B concentration at each timepoint was always below 8 mmol/L. Nevertheless, despite potential cytotoxicity, B12.5-Mg-Sr scaffolds have been shown to support of hADSCs viability and proliferation.

Ca release was highest from 3D scaffolds and lowest from bulk scaffolds (Fig. 18c). P^{3-} ion concentrations are decreasing linearly, with lowest ion release from 3D scaffolds and highest ion release from bulk scaffolds (Fig. 18d). Ca and P consumption indicate Ca-P reactive layer deposition. Consumption was biggest for 3D printed scaffolds, most probably due to their higher dissolution rate. This leads to faster oversaturation of culture media with P^{3-} ions, and thus greater precipitation. Moreover, low concentration of Ca between 2 and 4 mmol has been shown to support osteoblast proliferation. Higher Ca concentration between 6 and 8 mmol has been shown to favor osteoblast differentiation and mineralization. Whereas Ca concentrations higher than 10 mmol were shown to be cytotoxic [55]. In our study, non-cumulative Ca concentration for all scaffold types were between 1.8 and 2.6 mmol and has also been shown to support hADSCs proliferation. Mg^{2+} and Sr^{2+} ion release (Fig. 18e-f) was highest from 3D printed scaffolds and lowest from bulk scaffolds.

Summarizing, 3D scaffolds release highest concentrations of B^{3+}, Ca^{2+}, Mg^{2+} and Sr^{2+} ions probably due to their highest porosity and surface area. However, these ion levels are low enough to provide cell survival comparable with other less porous scaffolds.

4. Conclusions

Bioactive borosilicate glass scaffolds, made from B12.5 and B12.5-Mg-Sr compositions, were successfully produced using heat sintering of packed particles to produce a "bulk" scaffold, 3D printing and porogen burn-off manufacturing methods. The consumption of P^{3-} and Ca^{2+}

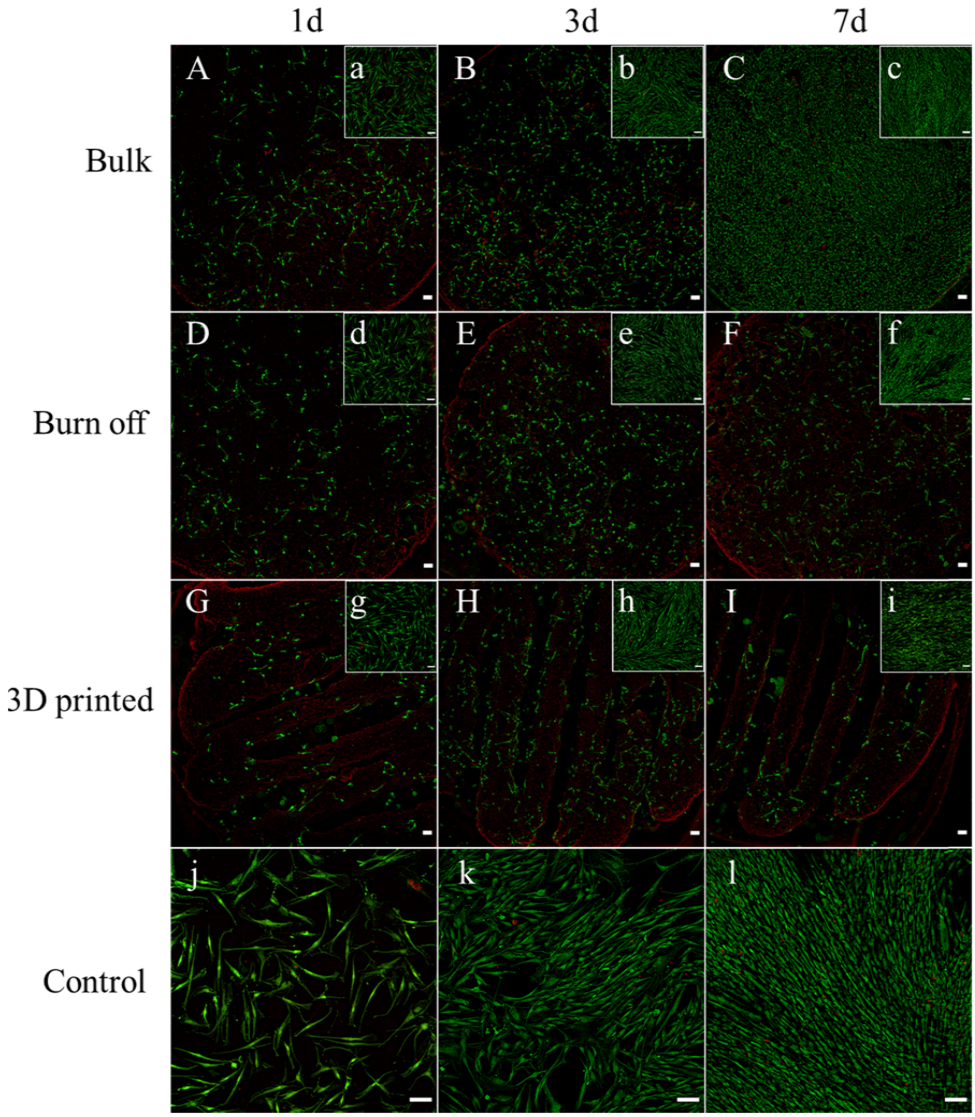

Fig. 17. Fluorescent images of hADSCs cells after 1,3 and 7 days of culture in αMEM culture medium. Images A-I show the top of bulk, burn-off and 3D printed scaffolds. Images a-l show the bottom of the wellplate. Viable (green) and necrotic (red) cells were stained with Calcein AM and Ethidium homodimer-1 respectively. Part of the red lines are product of autofluorescence from scaffolds. Scale bar 100 μm.

ions during immersion in SBF suggest the formation of a HA-like layer, indicating scaffolds bioactivity. Moreover, the studied 3D printed, and burn-off scaffolds met porosity and pore size requirements for favorable for bone tissue engineering applications. Moreover, the 3D printed scaffolds exhibited interconnected porosity, more homogenous pore sizes, and overall better reproducibility.

Scaffolds made from B12.5-Mg-Sr glass composition dissolved in TRIS and precipitated Ca and P in SBF in a slower way compared to B12.5 scaffolds. This could be attributed to stabilizing effect of MgO and SrO substitution for CaO on borate network. This had a significant effect on MC3T3-E1 cell survival and proliferation. It was shown that only B12.5-Mg-Sr glass composition supported cell survival. However, toxicity of B12.5 scaffolds due to high ion release, in static cell culture, could be resolved using dynamic cell culture.

Furthermore, 3D printed and burn-off scaffolds, with higher porosity compared to bulk scaffolds, exhibited faster dissolution in TRIS. These are attributed to greater surface area resulting from higher porosity. Most importantly, when hADSCs were cultured with B12.5-Mg-Sr bulk, burn-off and 3D printed scaffolds, cells survival was comparable to control cell culture without scaffolds. Thus, differences in dissolution and precipitation rate between these scaffolds were not significant. Moreover, migration of hADSCs beneath the top layer in the 3D printed scaffolds was also observed.

Additionally, preincubation of scaffolds in TRIS and αMEM was shown to be an effective way to decrease burst release of ions during cell culture with cells. Total preincubation period of 3 days was chosen to be

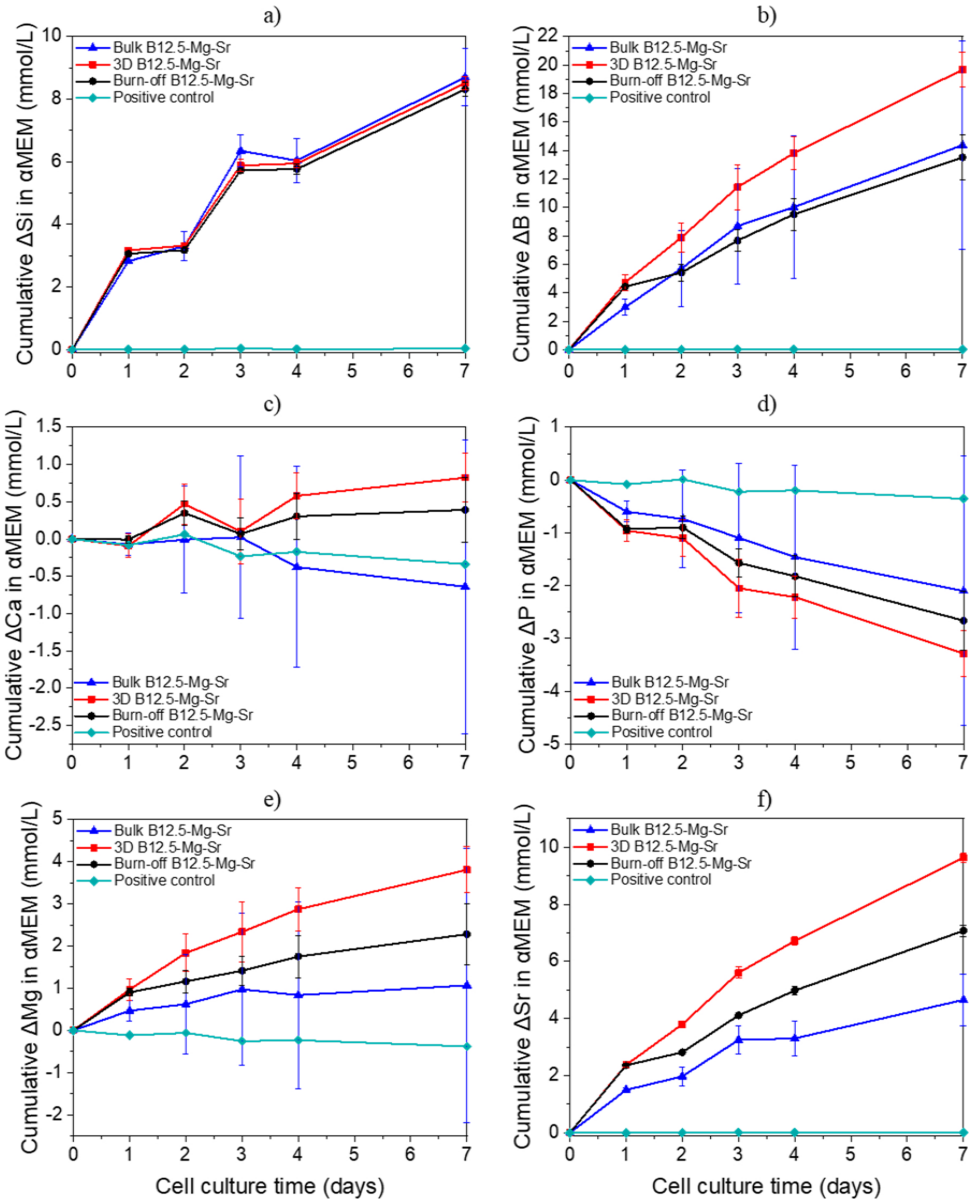

Fig. 18. Concentrations of a-f) Si, B, Ca, P, Mg and Sr in αMEM culture medium after 1, 3 and 7 days of hADSCs culture with Bulk, Burn-off and 3D printed B12.5-Mg-Sr scaffolds as a function of time. ΔElement = [Element] in αMEM in the presence of the sample – [Element] in αMEM initial solution.

optimal.

3D printed scaffolds made from B12.5-Mg-Sr glass composition were developed to be bioactive, with high interconnected porosity with good pore size and optimal dissolution rate, allowing better hADSCs cell survival. The B12.5-Mg-Sr 3D printed scaffolds met the requirements of the structural properties and reproducibility. Based on these results, the future research will be focused on 3D printed B12.5-Mg-Sr scaffolds. To further improve the properties and functionality of these constructs, they could be combined for example with a cellularized collagen gel to produce a hybrid scaffold. Additionally, the ability of hADSCs to differentiate towards osteogenic lineage when cultured with hybrid scaffolds will be studied.

CRediT authorship contribution statement

Agata Szczodra: Conceptualization, Methodology, Validation, Formal analysis, Investigation, Data curation, Writing – original draft, Visualization **Jenna M. Tainio**: Conceptualization, Methodology, Validation, Writing – review & editing **Amel Houaoui**: Conceptualization, Methodology, Validation, Formal analysis, Investigation, Data curation, Writing – original draft, Writing – review & editing, Visualization **Hongfei Liu:** Methodology, Validation, Formal analysis, Investigation,

Data curation, Writing – review & editing, Visualization **Juuso Pohjola:** Conceptualization, Methodology, Validation, Formal analysis, Investigation, Data curation **Susanna Miettinen:** Conceptualization, Methodology, Validation, Resources, Writing – review & editing ***Delia S. Brauer:*** Conceptualization, Methodology, Validation, Writing – review & editing, Project administration, Funding acquisition **J. Massera:** Conceptualization, Methodology, Validation, Resources, Writing – original draft, Writing – review & editing, Supervision, Project administration, Funding acquisition.

Declaration of Competing Interest

The authors declare the following financial interests/personal relationships which may be considered as potential competing interests: Agata Szczodra, Jonathan Massera reports financial support was provided by Academy of Finland. Jenna Tainio, Juuso Pohjola reports financial support was provided by German Academic Exchange Service.

Data Availability

Data will be made available on request.

Acknowledgments

Authors would like to thank the Academy of Finland (research grant #331924) for financial support of the AS as well as the DAAD-Finland mobility program (grant #295962) for the mobility of JT and JP to Jena university.

Appendix A. Supporting information

Supplementary data associated with this article can be found in the online version at doi:10.1016/j.mtcomm.2023.105984.

References

[1] M. Brink, The influence of alkali and alkaline earths on the working range for bioactive glasses, J. Biomed. Mater. Res. 36 (1) (1997) 109–117, https://doi.org/10.1002/(SICI)1097-4636(199707)36:1<109::AID-JBM13>3.0.CO;2-D.

[2] S. Fagerlund, J. Massera, M. Hupa, L. Hupa, T–T–T behaviour of bioactive glasses 1–98 and 13–93, J. Eur. Ceram. Soc. 32 (11) (2012) 2731–2738, https://doi.org/10.1016/j.jeurceramsoc.2011.10.040.

[3] J. Massera, S. Fagerlund, L. Hupa, M. Hupa, Crystallization mechanism of the bioactive glasses, 45S5 and S53P4, J. Am. Ceram. Soc. 95 (2) (2012) 607–613, https://doi.org/10.1111/j.1551-2916.2011.05012.x.

[4] M.N. Rahaman, D.E. Day, B. Sonny Bal, Q. Fu, S.B. Jung, L.F. Bonewald, A. P. Tomsia, Bioactive glass in tissue engineering, Acta Biomater. 7 (6) (2011) 2355–2373, https://doi.org/10.1016/j.actbio.2011.03.016.

[5] L.-C. Gerhardt, A.R. Boccaccini, Bioactive glass and glass-ceramic scaffolds for bone tissue engineering, Materials 3 (7) (2010) 3867–3910, https://doi.org/10.3390/ma3073867.

[6] H. Jodati, B. Yılmaz, Z. Evis, A review of bioceramic porous scaffolds for hard tissue applications: effects of structural features, Ceram. Int. 46 (10) (2020) 15725–15739, https://doi.org/10.1016/j.ceramint.2020.03.192.

[7] V. Karageorgiou, D. Kaplan, Porosity of 3D biomaterial scaffolds and osteogenesis, Biomaterials 26 (27) (2005) 5474–5491, https://doi.org/10.1016/j.biomaterials.2005.02.002.

[8] A. Yao, D. Wang, W. Huang, Q. Fu, M.N. Rahaman, D.E. Day, In vitro bioactive characteristics of borate-based glasses with controllable degradation behavior, J. Am. Ceram. Soc. 90 (1) (2007) 303–306, https://doi.org/10.1111/j.1551-2916.2006.01358.x.

[9] M. Fabert, N. Ojha, E. Erasmus, M. Hannula, M. Hokka, J. Hyttinen, J. Rocherullé, I. Sigalas, J. Massera, Crystallization and sintering of borosilicate bioactive glasses for application in tissue engineering, J. Mater. Chem. B 5 (23) (2017) 4514–4525, https://doi.org/10.1039/C7TB00106A.

[10] W. Huang, D.E. Day, K. Kittiratanapiboon, M.N. Rahaman, Kinetics and mechanisms of the conversion of silicate (45S5), borate, and borosilicate glasses to hydroxyapatite in dilute phosphate solutions, J. Mater. Sci.: Mater. Med. 17 (7) (2006) 583–596, https://doi.org/10.1007/s10856-006-9220-z.

[11] R.F. Brown, M.N. Rahaman, A.B. Dwilewicz, W. Huang, D.E. Day, Y. Li, B.S. Bal, Effect of borate glass composition on its conversion to hydroxyapatite and on the proliferation of MC3T3-E1 cells, J. Biomed. Mater. Res. Part A 88A (2) (2009) 392–400, https://doi.org/10.1002/jbm.a.31679.

[12] Q. Fu, M.N. Rahaman, B.S. Bal, L.F. Bonewald, K. Kuroki, R.F. Brown, Silicate, borosilicate, and borate bioactive glass scaffolds with controllable degradation rate for bone tissue engineering applications. II. In vitro and in vivo biological evaluation, J. Biomed. Mater. Res. Part A 95A (1) (2010) 172–179, https://doi.org/10.1002/jbm.a.32823.

[13] Narayan, R., Colombo, P., Halbig, M., & Mathur, S. (Eds.). (2012). *A*dvances in Bioceramics and Porous Ceramics V. John Wiley & Sons, Inc. https://doi.org/10.1002/9781118217504.

[14] J.M. Tainio, D.A.A. Salazar, A. Nommeots-Nomm, C. Roiland, B. Bureau, D. R. Neuville, D.S. Brauer, J. Massera, Structure and in vitro dissolution of Mg and Sr containing borosilicate bioactive glasses for bone tissue engineering, J. Non-Cryst. Solids 533 (2020), 119893, https://doi.org/10.1016/j.jnoncrysol.2020.119893.

[15] J. Massera, L. Hupa, Influence of SrO substitution for CaO on the properties of bioactive glass S53P4, J. Mater. Sci.: Mater. Med. 25 (3) (2014) 657–668, https://doi.org/10.1007/s10856-013-5120-1.

[16] J. Massera, L. Hupa, M. Hupa, Influence of the partial substitution of CaO with MgO on the thermal properties and in vitro reactivity of the bioactive glass S53P4, J. Non-Cryst. Solids 358 (18–19) (2012) 2701–2707, https://doi.org/10.1016/j.jnoncrysol.2012.06.032.

[17] P. Naruphontjirakul, O. Tsigkou, S. Li, A.E. Porter, J.R. Jones, Human mesenchymal stem cells differentiate into an osteogenic lineage in presence of strontium containing bioactive glass nanoparticles, Acta Biomater. 90 (2019) 373–392, https://doi.org/10.1016/j.actbio.2019.03.038.

[18] M.E. Santocildes-Romero, A. Crawford, P. v Hatton, R.L. Goodchild, I.M. Reaney, C.A. Miller, The osteogenic response of mesenchymal stromal cells to strontium-substituted bioactive glasses, J. Tissue Eng. Regen. Med. 9 (5) (2015) 619–631, https://doi.org/10.1002/term.2003.

[19] J. Liu, S.C.F. Rawlinson, R.G. Hill, F. Fortune, Strontium-substituted bioactive glasses in vitro osteogenic and antibacterial effects, Dent. Mater. 32 (3) (2016) 412–422, https://doi.org/10.1016/j.dental.2015.12.013.

[20] P. Naruphontjirakul, A.E. Porter, J.R. Jones, In vitro osteogenesis by intracellular uptake of strontium containing bioactive glass nanoparticles, Acta Biomater. 66 (2018) 67–80, https://doi.org/10.1016/j.actbio.2017.11.008.

[21] S. Hesaraki, M. Alizadeh, H. Nazarian, D. Sharifi, Physico-chemical and in vitro biological evaluation of strontium/calcium silicophosphate glass, J. Mater. Sci. Mater. Med. 21 (2) (2010) 695–705, https://doi.org/10.1007/s10856-009-3920-0.

[22] A. Hoppe, B. Sarker, R. Detsch, N. Hild, D. Mohn, W.J. Stark, A.R. Boccaccini, In vitro reactivity of Sr-containing bioactive glass (type 1393) nanoparticles, J. Non-Cryst. Solids (2014), https://doi.org/10.1016/j.jnoncrysol.2013.12.010.

[23] L. Hupa, S. Fagerlund, J. Massera, L. Björkvik, Dissolution behavior of the bioactive glass S53P4 when sodium is replaced by potassium, and calcium with magnesium or strontium, J. Non-Cryst. Solids 432 (2016) 41–46, https://doi.org/10.1016/j.jnoncrysol.2015.03.026.

[24] Ż. Ciosek, K. Kot, D. Kosik-Bogacka, N. Łanocha-Arendarczyk, I. Rotter, The effects of calcium, magnesium, phosphorus, fluoride, and lead on bone tissue, Biomolecules 11 (4) (2021) 506, https://doi.org/10.3390/biom11040506.

[25] L.Y. He, X.M. Zhang, B. Liu, Y. Tian, W.H. Ma, Effect of magnesium ion on human osteoblast activity, Braz. J. Med. Biol. Res. 49 (7) (2016), https://doi.org/10.1590/1414-431×20165257.

[26] S. Bose, S. Tarafder, S.S. Banerjee, N.M. Davies, A. Bandyopadhyay, Understanding in vivo response and mechanical property variation in MgO, SrO and SiO2 doped β-TCP, Bone 48 (6) (2011) 1282–1290, https://doi.org/10.1016/j.bone.2011.03.685.

[27] Q. Fu, M.N. Rahaman, H. Fu, X. Liu, Silicate, borosilicate, and borate bioactive glass scaffolds with controllable degradation rate for bone tissue engineering applications. I. Preparation and in vitro degradation, J. Biomed. Mater. Res. Part A 95A (1) (2010) 164–171, https://doi.org/10.1002/jbm.a.32824.

[28] D. Ke, S. Tarafder, S. Vahabzadeh, S. Bose, Effects of MgO, ZnO, SrO, and SiO2 in tricalcium phosphate scaffolds on in vitro gene expression and in vivo osteogenesis, Mater. Sci. Eng.: C. 96 (2019) 10–19, https://doi.org/10.1016/j.msec.2018.10.073.

[29] F. Baino, E. Fiume, J. Barberi, S. Kargozar, J. Marchi, J. Massera, E. Verné, Processing methods for making porous bioactive glass-based scaffolds—a state-of-the-art review, Int. J. Appl. Ceram. Technol. 16 (5) (2019) 1762–1796, https://doi.org/10.1111/ijac.13195.

[30] Y. Niu, L. Guo, J. Liu, H. Shen, J. Su, X. An, B. Yu, J. Wei, J.-W. Shin, H. Guo, F. Ji, D. He, Bioactive and degradable scaffolds of the mesoporous bioglass and poly(<scp>l</scp> -lactide) composite for bone tissue regeneration, J. Mater. Chem. B 3 (15) (2015) 2962–2970, https://doi.org/10.1039/C4TB01796J.

[31] K. Rezwan, Q.Z. Chen, J.J. Blaker, A.R. Boccaccini, Biodegradable and bioactive porous polymer/inorganic composite scaffolds for bone tissue engineering, Biomaterials 27 (18) (2006) 3413–3431, https://doi.org/10.1016/j.biomaterials.2006.01.039.

[32] D.W. Hutmacher, S. Cool, Concepts of scaffold-based tissue engineering—the rationale to use solid free-form fabrication techniques, J. Cell. Mol. Med. 11 (4) (2007) 654–669, https://doi.org/10.1111/j.1582-4934.2007.00078.x.

[33] C. Shuai, W. Yang, P. Feng, S. Peng, H. Pan, Accelerated degradation of HAP/PLLA bone scaffold by PGA blending facilitates bioactivity and osteoconductivity, Bioact. Mater. 6 (2) (2021) 490–502, https://doi.org/10.1016/j.bioactmat.2020.09.001.

[34] S. Fagerlund, L. Hupa, M. Hupa, Dissolution patterns of biocompatible glasses in 2-amino-2-hydroxymethyl-propane-1,3-diol (Tris) buffer, Acta Biomater. 9 (2) (2013) 5400–5410, https://doi.org/10.1016/j.actbio.2012.08.051.

[35] L. Kyllönen, S. Haimi, B. Mannerström, H. Huhtala, K.M. Rajala, H. Skottman, G. K. Sándor, S. Miettinen, Effects of different serum conditions on osteogenic differentiation of human adipose stem cells in vitro, Stem Cell Res. Ther. 4 (1) (2013) 17, https://doi.org/10.1186/scrt165.

[36] M. Patrikoski, M. Juntunen, S. Boucher, A. Campbell, M.C. Vemuri, B. Mannerström, S. Miettinen, Development of fully defined xeno-free culture

system for the preparation and propagation of cell therapy-compliant human adipose stem cells, Stem Cell Res. Ther. 4 (2) (2013) 27, https://doi.org/10.1186/scrt175.

[37] L. Hyväri, M. Ojansivu, M. Juntunen, K. Kartasalo, S. Miettinen, S. Vanhatupa, Focal adhesion kinase and ROCK signaling are switch-like regulators of human adipose stem cell differentiation towards osteogenic and adipogenic lineages, Stem Cells Int. 2018 (2018) 1–13, https://doi.org/10.1155/2018/2190657.

[38] P. Bourin, B.A. Bunnell, L. Casteilla, M. Dominici, A.J. Katz, K.L. March, H. Redl, J. P. Rubin, K. Yoshimura, J.M. Gimble, Stromal cells from the adipose tissue-derived stromal vascular fraction and culture expanded adipose tissue-derived stromal/stem cells: a joint statement of the International Federation for Adipose Therapeutics and Science (IFATS) and the International Society for Cellular Therapy (ISCT), Cytotherapy 15 (6) (2013) 641–648, https://doi.org/10.1016/j.jcyt.2013.02.006.

[39] M. Dominici, K. le Blanc, I. Mueller, I. Slaper-Cortenbach, F.C. Marini, D.S. Krause, R.J. Deans, A. Keating, D.J. Prockop, E.M. Horwitz, Minimal criteria for defining multipotent mesenchymal stromal cells. The International Society for Cellular Therapy position statement, Cytotherapy 8 (4) (2006) 315–317, https://doi.org/10.1080/14653240600855905.

[40] J. Ge, L. Guo, S. Wang, Y. Zhang, T. Cai, R.C.H. Zhao, Y. Wu, The size of mesenchymal stem cells is a significant cause of vascular obstructions and stroke, Stem Cell Rev. Rep. 10 (2) (2014) 295–303, https://doi.org/10.1007/s12015-013-9492-x.

[41] H. Sudo, H.A. Kodama, Y. Amagai, S. Yamamoto, S. Kasai, In vitro differentiation and calcification in a new clonal osteogenic cell line derived from newborn mouse calvaria, J. Cell Biol. 96 (1) (1983) 191–198, https://doi.org/10.1083/jcb.96.1.191.

[42] Iordache, F. (2019). Bioprinted scaffolds. In Materials for Biomedical Engineering (pp. 35–60). Elsevier. https://doi.org/10.1016/B978–0-12–816901-8.00002-X.

[43] M. Diba, F. Tapia, A.R. Boccaccini, L.A. Strobel, Magnesium-containing bioactive glasses for biomedical applications, Int. J. Appl. Glass Sci. 3 (3) (2012) 221–253, https://doi.org/10.1111/j.2041-1294.2012.00095.x.

[44] M.T. Souza, M.C. Crovace, C. Schröder, H. Eckert, O. Peitl, E.D. Zanotto, Effect of magnesium ion incorporation on the thermal stability, dissolution behavior and bioactivity in Bioglass-derived glasses, J. Non-Cryst. Solids 382 (2013) 57–65, https://doi.org/10.1016/j.jnoncrysol.2013.10.001.

[45] Q. Fu, E. Saiz, M.N. Rahaman, A.P. Tomsia, Bioactive glass scaffolds for bone tissue engineering: state of the art and future perspectives, Mater. Sci. Eng.: C. 31 (7) (2011) 1245–1256, https://doi.org/10.1016/j.msec.2011.04.022.

[46] X. Liu, M.N. Rahaman, G.E. Hilmas, B.S. Bal, Mechanical properties of bioactive glass (13-93) scaffolds fabricated by robotic deposition for structural bone repair, Acta Biomater. 9 (6) (2013) 7025–7034, https://doi.org/10.1016/j.actbio.2013.02.026.

[47] L. Olah, K. Filipczak, Z. Jaegermann, T. Czigany, L. Borbas, S. Sosnowski, P. Ulanski, J.M. Rosiak, Synthesis, structural and mechanical properties of porous polymeric scaffolds for bone tissue regeneration based on neat poly (ε-caprolactone) and its composites with calcium carbonate, Polym. Adv. Technol. 17 (11–12) (2006) 889–897, https://doi.org/10.1002/pat.768.

[48] A. Li, Y. Lv, H. Ren, Y. Cui, C. Wang, R.A. Martin, D. Qiu, In vitro evaluation of a novel pH neutral calcium phosphosilicate bioactive glass that does not require preconditioning prior to use, Int. J. Appl. Glass Sci. 8 (4) (2017) 403–411, https://doi.org/10.1111/ijag.12321.

[49] F.E. Ciraldo, E. Boccardi, V. Melli, F. Westhauser, A.R. Boccaccini, Tackling bioactive glass excessive in vitro bioreactivity: preconditioning approaches for cell culture tests, Acta Biomater. 75 (2018) 3–10, https://doi.org/10.1016/j.actbio.2018.05.019.

[50] J.R. Jones, Reprint of: Review of bioactive glass: from Hench to hybrids, Acta Biomater. 23 (2015) S53–S82, https://doi.org/10.1016/j.actbio.2015.07.019.

[51] M. Arango-Ospina, L. Hupa, A.R. Boccaccini, Bioactivity and dissolution behavior of boron-containing bioactive glasses under static and dynamic conditions in different media, Biomed. Glass 5 (1) (2019) 124–139, https://doi.org/10.1515/bglass-2019-0011.

[52] A. Rámila, M. Vallet-Regı, Static and dynamic in vitro study of a sol–gel glass bioactivity, Biomaterials 22 (16) (2001) 2301–2306, https://doi.org/10.1016/S0142-9612(00)00419-1.

[53] H. Fu, Q. Fu, N. Zhou, W. Huang, M.N. Rahaman, D. Wang, X. Liu, In vitro evaluation of borate-based bioactive glass scaffolds prepared by a polymer foam replication method, Mater. Sci. Eng.: C. 29 (7) (2009) 2275–2281, https://doi.org/10.1016/j.msec.2009.05.013.

[54] E. Gentleman, Y.C. Fredholm, G. Jell, N. Lotfibakhshaiesh, M.D. O'Donnell, R. G. Hill, M.M. Stevens, The effects of strontium-substituted bioactive glasses on osteoblasts and osteoclasts in vitro, Biomaterials 31 (14) (2010) 3949–3956, https://doi.org/10.1016/j.biomaterials.2010.01.121.

[55] S. Maeno, Y. Niki, H. Matsumoto, H. Morioka, T. Yatabe, A. Funayama, Y. Toyama, T. Taguchi, J. Tanaka, The effect of calcium ion concentration on osteoblast viability, proliferation and differentiation in monolayer and 3D culture, Biomaterials 26 (23) (2005) 4847–4855, https://doi.org/10.1016/j.biomaterials.2005.01.006.

IV

BOROSILICATE BIOACTIVE GLASSES WITH ADDED MG/SR ENHANCES HUMAN ADIPOSE-DERIVED STEM CELLS OSTEOGENIC COMMITMENT AND ANGIOGENIC PROPERTIES

by

Jenna M. Tainio, Sari Vanhatupa, Susanna Miettinen and Jonathan Massera

Submitted for publication 26th of January 2024